Applications of Continuum Damage Mechanics to Fatigue and Fracture

David L. McDowell, editor

ASTM

STP 1315

STP 1315

Applications of Continuum Damage Mechanics to Fatigue and Fracture

David L. McDowell, editor

ASTM Publication Code Number (PCN):
04-013150-30

ASTM
100 Barr Harbor Drive
West Conshohocken, PA 19428-2959
Printed in the U.S.A.

Library of Congress Cataloging-in-Publication Data

Applications of continuum damage mechanics to fatigue and fracture / David L. McDowell, editor.
(STP : 1315)
"Symposium on Applications of Continuum Damage Mechanics to Fatigue and Fracture was held in Orlando, Florida, on 21 May 1996 . . . sponsored by ASTM Committee E8 on Fatigue and Fracture."
Includes bibliographical references and index.
ISBN 0-8031-2473-2
1. Fracture mechanics—Congresses. 2. Materials—Fatigue—Congresses. I. McDowell, David L., 1956– . II. ASTM Committee E-8 on Fatigue and Fracture. III. Symposium on Applications of Continuum Damage Mechanics to Fatigue and Fracture (1996 : Orlando, Fla.) IV. Series: ASTM special technical publication : 1315.
TA409.A67 1997
620.1'126—dc21 97-36339
CIP

Photocopy Rights

Peer Review Policy

Each paper published in this volume was evaluated by three peer reviewers. The authors addressed all of the reviewers' comments to the satisfaction of both the technical editor(s) and the ASTM Committee on Publications.

The quality of the papers in this publication reflects not only the obvious efforts of the authors and the technical editor(s), but also the work of these peer reviewers. The ASTM Committee on Publications acknowledges with appreciation their dedication and contribution of time and effort on behalf of ASTM.

Printed in Ann Arbor, MI
October 1997

Foreword

The Symposium on Applications of Continuum Damage Mechanics to Fatigue and Fracture was held in Orlando, Florida, on 21 May 1996. The symposium was sponsored by ASTM Committee E8 on Fatigue and Fracture. David L. McDowell, Georgia Institute of Technology, presided as symposium chairman and is editor of this publication.

Contents

Overview

ASTM Special Technical Publications relate a long tradition of fundamental contributions to the disciplines of fatigue life prediction and fracture mechanics, with an emphasis on the understanding of the physics of these phenomena and development of appropriate experimental techniques. Some of the earliest, most significant contributions to fracture mechanics, for example, were relayed through ASTM symposia and resulting publications. The discipline of continuum damage mechanics (CDM), essentially the application of internal state variable concepts of nonequilibrium continuum thermodynamics of solids, has received increasing international attention in addressing fatigue and fracture issues in broad classes of materials. To date, CDM has received most attention abroad with particularly significant advances in Europe. One of the primary goals of the *Symposium on Applications of Continuum Damage Mechanics to Fatigue and Fracture*, held 21 May 1996 in Orlando, Florida was to summarize the state-of-the-art in application of damage mechanics to fatigue and fracture problems. As the field advances and its domain of fruitful applications are better understood, it is envisioned that the fatigue and fracture communities will embrace it to address many complex issues such as crack tip process zone mechanics, size and constraint effects, interaction of multiple damage modes, length scale issues in mechanics of fatigue and fracture, and so on.

There are several important characteristics of CDM. In this approach, various forms of distributed damage are represented by smooth, continuous field quantities. As damage accumulates, the elastic and/or elastic-plastic stiffness degrades. The evolution of damage is typically specified through a set of first order rate equations. Multiple damage mechanics may be coupled with the thermomechanical deformation response. The CDM constitutive description is inevitably integrated within a computationally-based framework along with the governing equations of conservation of mass, momentum and energy, so that notions of "global" parameters which have prevailed in the early years of fracture and fatigue mechanics yield to more detailed, mechanistic local descriptions. The limitations of global approaches, which are recognized as efficient engineering tools, therefore, will be much better understood with the advent of more and more CDM applications. In some cases, computational CDM approaches will form the basis for materials design and selection for given applications.

It is instructive to contrast CDM with "micromechanics," another contemporary treatment of heterogeneous materials such as composites. Micromechanics typically involves application of continuum elasticity or plasticity theories to each of the individual constituents, with volume averaging over a unit cell or a representative volume element to achieve an equivalent homogeneous description at a higher length scale. The derivation of void growth theories in ductile elasto-plastic solids is a good example, as is the theory of multiple microcracked brittle solids based on Green's functions. In some cases, micromechanics involves a local analysis of a dominant deformation or failure mechanism, without volume averaging; these solutions are sometimes useful in tailoring particular features of material microstructure to impart improved resistance to deformation or failure. They can also provide detailed information regarding the driving forces for evolution of damage. CDM may incorporate micromechanics results into its overall structure, as in the case of the aforementioned void growth theories, but has greater

breadth of scope, also potentially incorporating statistical mechanics aspects of evolution of damage and experimentally measured/inferred information. In fact, the overall framework of CDM, based on the use of internal state variables to represent evolving structure of the material, appeals strongly to irreversible statistical thermodynamics. CDM relations can also be constructed from experiments, which can yield information regarding the proper choice of internal state variables and their evolution. Invariably, experiments form the basis for validating CDM models built up from micromechanics approaches at lower length scales. Hence, CDM is typically a hybrid approach, blending observation with some degree of empiricism along with idealized analyses of specific mechanisms.

These features render the framework of CDM useful for applications involving distributed defects in the presence of nonlinearities of various sorts such as inelastic flow, distributed frictional effects, and complex many-body interaction problems at various length scales. These sorts of problems are extremely difficult to pose properly for analytic micromechanical solution, notwithstanding whether the solution can be reasonably obtained for even well-posed problems. CDM is often useful as a constitutive framework for structural analysis, including *changes* of average local properties with evolution of damage.

In some cases where micromechanics solutions are abundant and where certain average properties are assumed, these solutions may be *explicitly* incorporated into CDM. Indeed, this is highlighted in some of the composites papers presented at this Symposium.

Some of the more difficult challenges facing CDM are shared with other constitutive equations in continuum theories which seek to model effects of distributed sources of irreversible behavior. For example, local theories of CDM are subject to dependence upon the details of the numerical mesh and degree of refinement. Some current research aims to introduce material length scales which are associated with the mesh, or to introduce nonlocal effects through gradient terms in the CDM formulation or through mesh averaging procedures. Weighting the influence of distributed damage at the microscale on the collective macroscale stiffness and evolution of damage is a challenge as well.

Effective medium approaches have been well-established in micromechanics to model the change of stiffness associated with a given state of damage. However, the evolution of damage remains a fertile subject for new developments. Generalization of energy release rate concepts to distributed damage is a natural feature of CDM, but distribution effects which depend strongly on nearest neighbor or second nearest neighbor spacing and clustering of defects have not been fully incorporated. Furthermore, many constitutive laws for engineering materials require a description of the effects of damage occurring at multiple length scales, with couplings between these scales. A good example is the influence in in situ matrix heterogeneity, microstructure and residual stresses on load transfer, and interface damage in composites. Defects are rarely observed to be periodically distributed in the material; rigorous treatment of nonuniformly distributed defects requires tools not yet fully developed in CDM.

A number of technologies have already benefited from the use of CDM, such as constraint effects in ductile fracture, modeling formability and impact damage, dynamic fracture, time dependent crack growth, fatigue crack initiation, creep-fatigue interaction and distributed damage in composites. Potential areas of application that might interest readers of this STP abound. These include, among others, crack tip process zone studies in fracture, crack growth history effects, validity limits of fracture mechanics (LEFM, EPFM and TDFM), fracture in heterogeneous materials, tailoring microstructures and reinforcement architectures of advanced materials for fracture and fatigue resistance, and modeling process-induced damage during primary forming, machining, solidification, or welding/joining.

Among the authors of this volume are some of the pioneers of CDM as applied to fatigue and fracture problems involving both monolithic and composite materials. This field first

emerged from development of continuum theories for creep damage evolution in the late 1950s, and its development flourished in the European community. Within the past few decades, it has received increased attention in the fields of fracture and fatigue of materials. This realm of applications are the focus of this Special Technical Publication.

This Symposium sought to explore the state-of-the-art in CDM model development as well as its industrial usage, both in the United States and abroad. The integration of CDM into tools for assessing effects of processing, deformation and constraint on fracture was one arena of direct applicability to recent ASTM E8 technical thrusts. Applications involving the use of standard and nonstandard experiments to characterize CDM parameters were also an area of exploration.

The papers in this STP are organized into several categories. The first set of papers deal with various aspects of modeling damage in composite materials. Some of the papers concern effects of high temperature environmental degradation, fatigue and viscous damage in metal and ceramic matrix composites. Theories are introduced which account for anisotropy, matrix microcracking, and delamination of composite layups. Here, we see examples of the use of micromechanics and experimental observations to construct useful damage mechanics relations for composites, including evolution of damage as well as relations for stiffness degradation.

A second set of papers deals with some of the issues related to the scaling of effects of distributed damage on behavior at a higher length scale, for example, macroscopic. Special attention is focused on the dependence of the evolution of damage on nonuniformity of its distribution. Finally, a set of papers deals with various application examples of CDM, including particle erosion damage, fracture of weldments, and impact damage. We trust that this Special Technical Publication will provide valuable insight into the capabilities of CDM, as well as its future possibilities for fruitful application to the subjects of fracture and fatigue.

David L. McDowell

Georgia Institute of Technology, Atlanta, GA 30332-0405; symposium chairman and editor.

Damage Mechanics of Composites

Serge Kruch[1] *and Steven M. Arnold*[2]

Creep Damage and Creep-Fatigue Damage Interaction Model for Unidirectional Metal-Matrix Composites

REFERENCE: Kruch, S. and Arnold, S. M., "**Creep Damage and Creep-Fatigue Damage Interaction Model for Unidirectional Metal-Matrix Composites,**" *Applications of Continuum Damage Mechanics to Fatigue and Fracture, ASTM STP 1315*, D. L. McDowell, Ed., American Society for Testing and Materials, 1997, pp. 7–28.

ABSTRACT: A multiaxial, isothermal, continuum damage mechanics model for creep and creep-fatigue interaction of a unidirectional metal-matrix composite (MMC) volume element is presented. The model is phenomenological, stress based, and assumes a single scalar internal damage variable with directional-dependent evolution. The present creep damage model is an extension of the Leckie-Hayhurst creep damage model to unidirectional MMCs and is shown when taken to its isotropic limit, to directly simplify to this previously developed and validated isotropic creep damage model. This extension is accomplished by introducing into the isochronous damage function physically meaningful stress invariants that reflect the local stress and material orientation within a metallic, transversely isotropic material (for example, hexagonally packed unidirectional metal-matrix composite). These invariants are included based on the anticipation that the associated stress may strongly influence void growth at the fiber-matrix interface (as this interface is postulated to play a role, on the mesostructural scale, analogous to that of grain boundaries on the microstructural scale and interfacial degradation); and, consequently may correlate with a creep rupture mechanism based on interfacial degradation through diffusion-related void growth.

Creep-fatigue interaction is accomplished by directly adding together the mechanical effects of creep and fatigue damage. A uniaxial parametric study is performed under pure creep and creep-fatigue conditions, to demonstrate the sensitivity of the various material parameters and the capability of the formulation in attempting to characterize a class of composite materials. Specifically, two interaction regions will be examined, the first being important for low-frequency loading cycles (<5 Hz) and is termed "creep-dominated" interaction; whereas the second is for high-frequency loading cycles with a non-zero mean stress, and is termed "fatigue-dominated" interaction. Results are presented in the form of *S-N* and damage accumulation curves.

KEYWORDS: continuum damage mechanics, cracking, fatigue (materials), fracture (materials), metal-matrix composites, creep (materials), composite materials

Many approaches have been proposed in the literature to describe the degradation and failure of structures under creep and fatigue conditions. The most notable are the linear elastic fracture mechanic (LEFM) and the continuum damage mechanic (CDM) approaches. LEFM can be applied to analyze the influence and evolution of macroscopic defects within a structure, where the defect is characterized from a geometrical point of view, see Fig. 1. Alternatively, the CDM approach allows one to describe the material's progressive deterioration (damage), for example, nucleation, growth and coalescence of micro-defects, from a virgin state (no damage) to the

[1] Research engineer, Office National d'Études et de Recherches Aérospatiales, B. P. 72-92322 Chatillon Cédex, France.

[2] Research engineer, NASA Lewis Research Center, Cleveland, OH 44135.

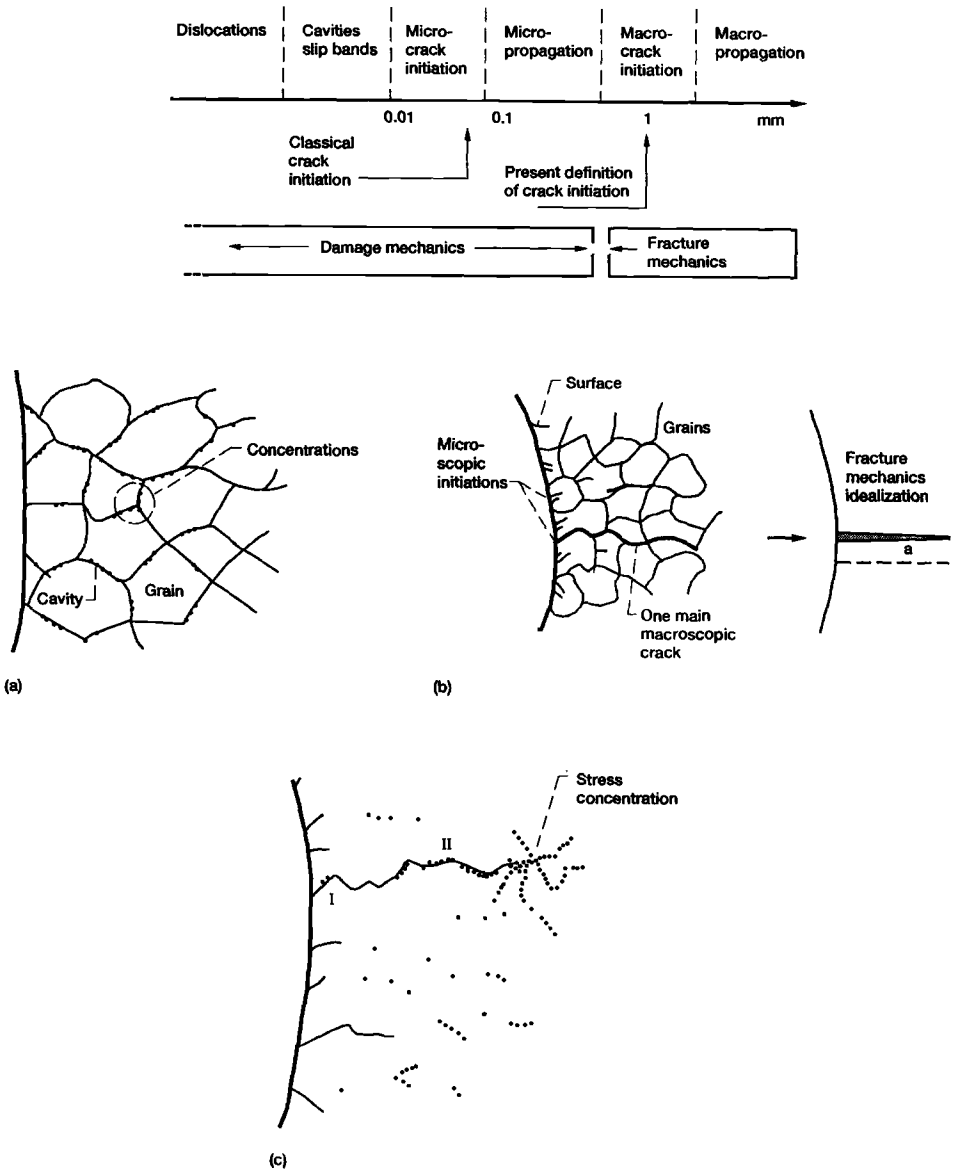

FIG. 1—*Schematic of different damage modes and the associated scale in a monolithic metal:* (a) *creep damage—coalescence of cavities and intergranular defects;* (b) *fatigue damage—nucleation of slip bands, microcracks, and transgranular defects; and* (c) *creep/fatigue damage—interaction of intergranular and transgranular defects.*

final state, corresponding generally to macrocrack initiation and propagation (or the "breaking up" of the representative volume element). Consequently, the life limiting macroscopic properties such as rupture strength, fatigue life, or creep rupture lifetime of the material can be predicted.

The tracking, or description, of the evolution of damage is accomplished by introducing

special thermodynamic (internal) field variables representing, in an appropriate statistical sense, the local distribution and density of defects. Numerous damage theories, both micromechanical [*1–6*] and phenomenological [*7–11*], for example, have been proposed and discussed in the literature. There is great diversity in the mathematical nature of the damage variables (for example, a scalar [*7,12,13*], vectors [*14,15*], and tensors [*12,16,17*]) and thus the damage theories; this stems from the difficulty in directly measuring "damage" macroscopically and the degree of approximation with which the internal variables describe the salient aspects of the macroscopic effects of the microdefect kinematics. For a number of excellent review articles and books on this subject, see Refs *7*, *12*, *18*, and *25*.

In this paper, we analyze the behavior of unidirectional, continuously fiber-reinforced, hexagonally packed, metal-matrix composites (MMCs), using recently developed phenomenological, stress-based isothermal, transversely isotropic creep, fatigue and creep/fatigue CDM models, with a scalar internal damage variable [*26,27*], the evolution of which is directionally dependent. Because, the transversely isotropic fatigue damage model was previously described in detail [*28*], our attention will be focused on the transversely isotropic extension of the Leckie-Hayhurst creep damage model to unidirectional MMCs and the behavior of both anisotropic creep and fatigue models under conditions of creep-fatigue damage interaction. Specifically, two such interaction regions will be examined, the first is important for low-frequency loading cycles (<5 Hz) and is called creep-dominated interaction, whereas, the second is for high-frequency loading cycles with a non-zero mean stress, called fatigue-dominated interaction.

The paper begins by summarizing the proposed mathematical structure of both the transversely isotropic creep and fatigue damage evolution laws, their associated material parameters, and the approach taken to achieve creep/fatigue interaction. Next, a brief parametric study of the creep damage model is conducted in order to establish which material parameters associated with creep will significantly influence the subsequent creep-fatigue interaction analyses. The creep damage analyses are performed under both uniaxial and multiaxial situations, whereas the creep-fatigue interaction cases are subjected to only uniaxial load histories. All results presented are related to the prediction of the lifetime of a volume element subjected to cyclic loading, and were obtained with the computer code DAMAGE developed at ONERA.

Damage Models

Material (lattice) defects can be classified roughly with respect to their geometry into (1) point defects (for example, vacancies, interstitial and impurity atoms), (2) line defects (dislocations), (3) plane defects (slip planes and cracks), and (4) volume defects (cavities and inclusions). Numerous ways are available to define the internal variables associated with these defects and damage processes. Each definition, however, must correspond to some method of measurement and implies a given approach, either a micromechanical or phenomenological one. The phenomenological point of view, utilizing the concept of effective stress [*12,29*] with an equivalence in strain, is taken throughout this paper. Figure 1 clearly illustrates the damage mechanics for the three cases of interest, that is, creep, fatigue, and creep-fatigue interaction for monolithic metals. In Fig. 1*a*, the two primary damage mechanisms [*30,31*], nucleation and growth of integranular defects (typically by a diffusion process), are illustrated schematically when the material is subjected to a pure creep loading condition. Hayhurst [*32*] has shown that it is possible to make some connection between the equations obtained from a materials science approach and the more macroscopic ones developed under the framework of CDM. The fatigue crack initiation and growth process is illustrated in Fig. 1*b*, with the damage (D_F) being associated, macroscopically, with the initiation and propagation of transgranular defects (for example, slip bands and microcracks), and Fig. 1*c* depicts the interaction of intergranular and transgranular defects. It is surmized, within the pertinent domain where creep-fatigue interac-

tion is applicable, that the presence of cavities allow for easier crack propagation and that the increase in stress intensity at a crack tip causes an increase in the propensity of nucleation and coalescence of voids.

Figure 2 is the extension of Fig. 1 to the "mesoscale" and illustrates the various mesostructural damage mechanisms that might result when a representative volume element (RVE) on the mesostructural scale (Fig. 3) of a given composite material is subjected to creep, fatigue, and creep-fatigue loadings, respectively. Here, damage mechanisms similar to those on the microstructural scale are postulated to occur on the mesostructural scale; the surface or interface of a constituent (the fiber) plays the role (on the mesostructural scale) of the grain boundary of a constituent (grain) on the microscopic scale. Furthermore, because of the internal structure of the material, a sufficient number of defects will be present, thus allowing a theoretically consistent continuum representation of both creep and fatigue damage to be constructed. The mathematical extension of the creep damage model (proposed by Leckie [*33,34*] and Leckie

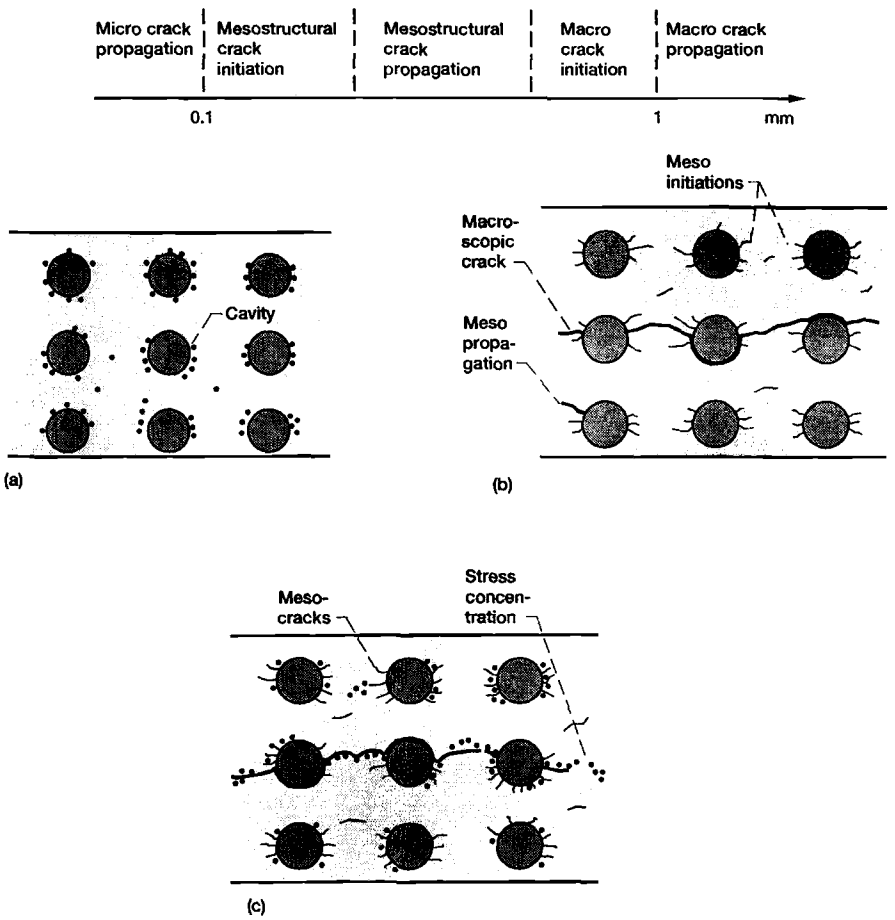

FIG. 2—*Schematic of different damage modes and the associated scale in a metallic composite. Fibers on mesostructural scale are analogous to grain boundaries on microstructural scale:* (a) *creep damage by way of intergranular void growth;* (b) *fatigue damage—initiation and propagation of transgranular defects; and* (c) *creep fatigue—interaction of intergranular and transgranular defects.*

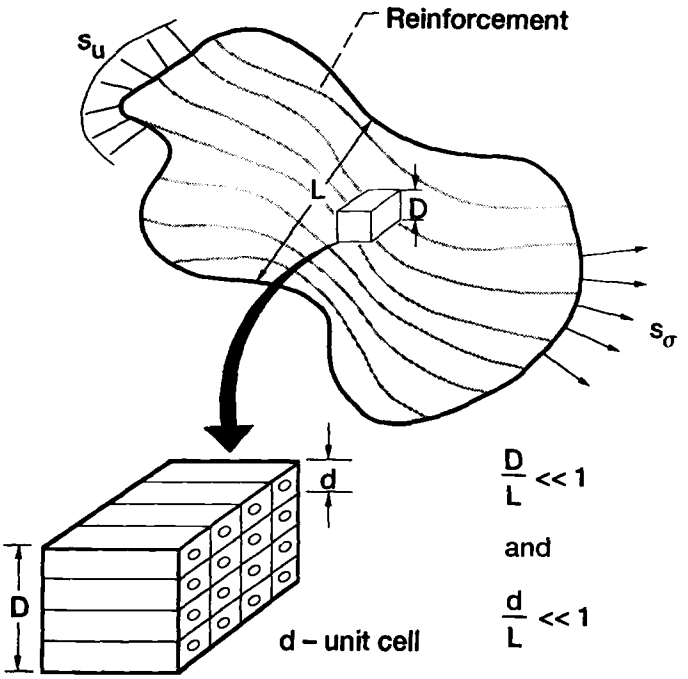

FIG. 3—*Nonrigorous definition of representative volume element.*

and Hayhurst [*8,13*]) and the NLCDR (nonlinear cumulative damage rule) fatigue model (developed at ONERA [*10,11,18,19,25–27,29*]), both valid for isotropic monolithic metals, is accomplished by introducing into the pertinent damage functions, appropriate stress invariants [*35,36*] representing stress states that are likely to strongly influence the various damage mechanisms in metallic composites. These physically meaningful invariants (I_1, I_2, and I_3) represent the maximum transverse shear stress (and thus implicitly the maximum transverse stress), longitudinal shear stress, and the maximum normal deviatoric stress in the fiber direction, respectively, and are defined as (see Refs *35* and *37*)

$$I_1 = J_2 - D_{ij}s_{jk}s_{ki} - \frac{1}{4}(D_{ij}s_{ij})^2 \tag{1}$$

$$I_2 = D_{ij}s_{jk}s_{ki} - (D_{ij}s_{ij})^2 \tag{2}$$

$$I_3 = (D_{ij}s_{ij})^2 \tag{3}$$

with

$$J_2 = \frac{1}{2}s_{ij}s_{ij},\ D_{ij} = d_i d_j \qquad s_{ij} = \sigma_{ij} - \frac{1}{3}\delta_{ij}\sigma_{kk}$$

and d_i (i = 1,2,3) are the components of a unit vector denoting the local fiber direction.

It is well known that the direction-oriented creep and fatigue damage modes of interest here in a monolithic material suggest the need for a direction-dependent damage variable (for ex-

ample, a vector or tensor). Here, however, based on the strong initial anisotropy of the unidirectional composite, it is assumed that a scalar damage measure is sufficient provided the evolution of damage is directionally dependent and associated with the preferred direction of the material, as any load-induced damage anisotropy is expected to be dominated by the degree of initial transverse isotropy of the composite material. For example, if the composite is loaded in the fiber direction, the evolution of damage would be small relative to the case in which the composite is loaded normal to the fiber. However, because of the assumed scalar measure, the distribution of damage would be identical in all directions. Thus, the accumulation but not the magnitude of damage would be dependent upon the preferred direction of the material. Such an assumption, could potentially lead to errors in the life prediction of structures subjected to highly nonproportional loadings, particularly if components of stress in the plane of isotropy vary greatly.

Pure Creep

The transversely isotropic creep damage model used in this study is based on an extension of the Leckie and Hayhurst model [*36,38*] where the anisotropic isochronous failure surface is defined as

$$\Delta = \Delta(\sigma_{ij}^{d}) = \beta J_1 + (1 - \alpha - \beta)\Sigma + \alpha S \tag{4}$$

in which the hydrostatic state of stress (J_1), maximum transverse shear (Σ), and longitudinal shear (S) stress are assumed to be the dominant damage measures and are defined as

$$J_1 = \sigma_{ii} \tag{5}$$

$$\Sigma = \sqrt{I_1} \tag{6}$$

$$S = \sqrt{I_2} \tag{7}$$

These invariants are included based on the anticipation that the associated stress may strongly influence void growth at the fiber-matrix interface (as this interface is postulated to play a role, on the mesostructural scale, analogous to that of grain boundaries on the microstructural scale and interfacial degradation); and, consequently may correlate with a creep rupture mechanism based on interfacial degradation through diffusion-related void growth.

This specific functional form for Δ given in Eq 4 will reduce, in the isotropic limit $\left(D_{ij} = \frac{1}{3}\delta_{ij}\right)$, to the original Leckie-Hayhurst surface, expressed as

$$\hat{\Delta} = \hat{\Delta}(\sigma) = \gamma J_0 + \beta J_1 + (1 - \gamma - \beta)\hat{\Sigma} \tag{8}$$

when $\alpha = 0$, $\gamma = 0$, and $\hat{\Sigma} = \sqrt{3J_2}$. The validity of this assumed form, as well as any other form, must be determined experimentally as discussed by Robinson et al. [*36*] and Leckie [*33,34*]. The damage evolution law [*8,33*], extended now (through the isochronous failure surface) to account for initially transversely isotropic material symmetry (for example, hexagonally packed unidirectional metallic composite materials), is given by

$$\frac{dD_c}{dt} = \left(\frac{\Delta}{A}\right)^{r}(1 - D_c)^{-k} \tag{9}$$

where Δ is given in Eq 4, D_c is the creep damage variable, and A, r, and k are material parameters. Note, that here the exponent, k, is assumed to be a constant, thus implying linear accumulation of creep damage even though the evolution of damage may be nonlinear. The influence of these material parameters on the evolution of creep damage will be illustrated in the subsequent results section.

The results of creep-like cyclic tests (for example, high frequency-low amplitude or high amplitude-low frequency) have shown the need to include some factor relating the response time of the material versus that of the rate of loading. For example, when a material is subjected to a high frequency loading with a mean stress equal to zero, the material damage induced by creep is negligible, thereby leading to the case of "pure" fatigue damage. However, if the material is subjected to a high frequency and a low or medium amplitude with a high mean stress, the damage induced by creep is dominant. Thus, a new material parameter (τ), representing a delay time for the applied load, and a "delayed" stress (σ_{ij}^d) were introduced into the formulation, to account for the lag time between load application and material response [*26*]; that is, the effects of viscosity. The definition of σ_{ij}^d is given by the following differential equation

$$d\sigma_{ij}^d = \frac{\sigma_{ij} - \sigma_{ij}^d}{\tau} dt \tag{10}$$

For low-frequency load histories, the delayed stress is the real (or applied) stress, whereas for high-frequency load histories, the delayed stress is equal to the mean stress.

Pure Fatigue

In this section, the requisite multiaxial representation is given for the recently extended NLCDR [*12*] fatigue damage evolutionary law and the associated anisotropic damage surfaces. For a detailed explanation of the capability and features of this anisotropic (that is, transversely isotropic) damage evolution and life (ADEAL) model, see Refs *28*, *38*, and *39*. The pure fatigue damage evolutionary law (valid for materials that possess initial transversely isotropic material symmetry) is defined as

$$dD_F = [1 - (1 - D_F)^{1+\beta}]^{\alpha} \left[\frac{\hat{F}_m}{(1 - D_F)}\right]^{\beta} dN \tag{11}$$

with

$$\alpha = 1 - a \frac{\langle \Phi_{fl} \rangle}{\langle \Phi_u \rangle} \tag{12}$$

and, $\sigma_{fl_L} = \sigma(0)_{fl_L}(1 - 3bP)$, $M_L = M_{0L}(1 - 3cP)$; where a,b,c, β, $\sigma(0)_{fl_L}$, σ_{u_L}, and M_{0L} are material constants and the notation

$$\langle X \rangle = \begin{pmatrix} 0, X < 0 \\ X, X \geq 0 \end{pmatrix} \tag{13}$$

defines the Macauley bracket. Note that one additional modification, besides the inclusion of a preferred direction, has been introduced into the preceding fatigue damage model; a hydrostatic stress measure P, that is, $P = \zeta\sigma_{H_{\max}} + (1 - \zeta)\sigma_{H_{avg}}$, that combines both the Sines and

Crossland criteria. This alternate hydrostatic measure (P), based on the macrohydrostatic stress field, is felt to be required as a judgment as the most applicable criteria cannot be made at this time due to the lack of experimental data on MMCs.

Also, having introduced the most pertinent damage-producing stress measures (through the physically meaningful stress invariants, I_1, I_2, and I_3), the fatigue limit surface, Φ_{fl}, and the static fracture surface, Φ_u, are defined as

$$\Phi_u = 1 - \left(\frac{\max}{t} F_{(u)}(\sigma_{ij}(t)) \right) \tag{14}$$

$$\Phi_{fl} = \frac{1}{2} \frac{\max}{t_0} \frac{\max}{t} F_{(fl)}(\sigma_{ij}(t) - \sigma_{ij}(t_0)) - 1 \tag{15}$$

and the normalized stress amplitude as

$$\hat{F}_m = \frac{1}{2} \frac{\max}{t} \frac{\max}{t_0} F_{(m)}(\sigma_{ij}(t) - \sigma_{ij}(t_0)) \tag{16}$$

where the general form for $F_{(fl),(u)}$, or $_{(m)}$ may be expressed as

$$F_{(\,)} = \sqrt{\frac{1}{(\,)_L^2} \left\{ (4\omega_{(\,)}^2 - 1) I_1 + \frac{4\omega_{(\,)}^2 - 1}{\eta_{(\,)}^2} I_2 + \frac{9}{4} I_3 \right\}} \tag{17}$$

and σ_{fl_L}, σ_{u_L}, M_L, ω_{fl}, ω_u, ω_m, η_{fl}, η_u, and η_m are material parameters (some of them varying with the mean stress) that describe the initial anisotropy of the surfaces. Note that the subscripts, L and T, denote the longitudinal (along the fiber) and transverse (normal to the fiber) directions, respectively. Also in the preceding equations, t_0 is the time at the beginning of the load cycle and t is some time during the load cycle, where the intent is to find the maximum value for the given loading history.

Creep-Fatigue Interaction

Analytically, the creep-fatigue interaction is represented using the effective stress concept, by assuming that the mechanical effects of creep and fatigue damage can be added directly, that is

$$\begin{gathered} dD = dD_c + dD_F \\ dD = f_c(\sigma, T, D, \ldots) + f_F(\sigma, \sigma_m, T, D, \ldots) \end{gathered} \tag{18}$$

where f_c and f_F represent the characteristic functions of creep (for example, see Eq 9) and fatigue (for example, see Eq 11), respectively, and $D = D_c + D_F$. Thus, the two functions (f_c and f_F) can be determined independently from pure tensile creep and pure high-frequency fatigue tests. The conditions under which accumulation of both macroscopic effects would take place (for example, low frequency or loadings with hold times) are then predicted by integrating numerically the preceding equations. This approach has been shown to give reasonable results for several monolithic (isotropic) materials [*12,40,41*].

The implementation of this approach is shown schematically as

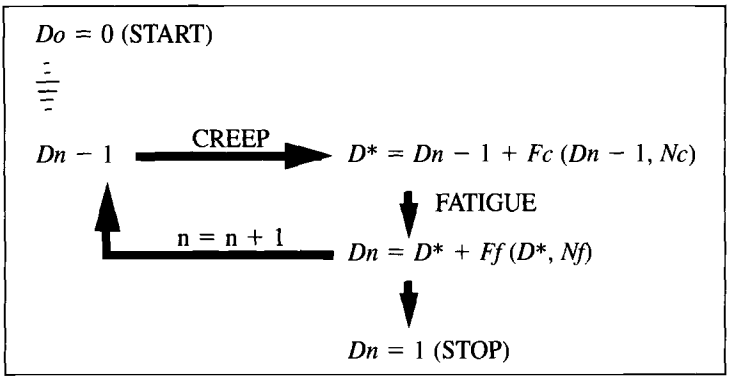

where one load cycle of fatigue is taken as the reference cycle and then divided into a discrete number of time steps. The damage in creep is computed for each time step and the total damage for one cycle in creep is computed. At the end of each reference cycle, the damage induced is then computed by combining both damages in fatigue and creep. This creep-fatigue damage interaction is then computed step by step at each time (or cycle) increment, where the integration of both damage criteria is accomplished using a Runge-Kutta algorithm.

Results

Pure Creep

Here, the uniaxial simplification of the anisotropic creep damage model is presented and a parametric study conducted to illustrate the influence of the pertinent material parameters, as well as fiber orientation, the global behavior of a volume element subjected to a constant uniaxial state of stress. The isochronous failure surface of Eq 4 becomes

$$\Delta = \{\beta + (1 - \alpha - \beta)A_1 + \alpha A_2\}\sigma \tag{19}$$

where

$$A_1 = \frac{\sqrt{[12 - 16\cos(\theta)^2 - 4\sin\theta^2 + (2\cos(\theta)^2 - \sin\theta^2)^2]}}{6} \tag{20}$$

$$A_2 = \frac{\sqrt{[(4\cos(\theta)^2 + \sin\theta^2 - (2\cos(\theta)^2 - \sin\theta^2)^2)]}}{3} \tag{21}$$

and the integration of the damage evolution law, Eq 9, gives

$$D = 1 - \left[1 - \frac{t}{t_{cr}}\right]^{\left(\frac{1}{k+1}\right)} \tag{22}$$

where t_{cr} (the creep rupture time) is defined as

$$t_{cr} = \frac{1}{(k+1)}\left(\frac{\Delta}{A}\right)^{-r} \tag{23}$$

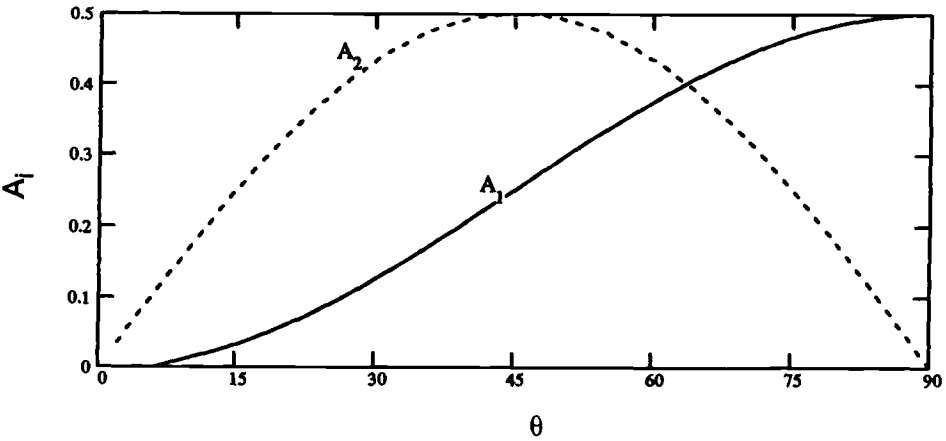

FIG. 4—*The angle dependency of the longitudinal shear* (A_1), *transverse shear* (A_2) *components.*

Clearly, the influence of fiber orientation (θ) relative to the applied load direction is completely contained within the coefficients, A_1 and A_2. Both A_1 and A_2 are depicted in Fig. 4 as a function of Angle θ, where, for example, $\theta = 0$ and 90° indicate loading parallel and transverse to the fiber direction, respectively. Similarly, Parameters α and β determine the longitudinal shear and hydrostatic stress influence, respectively, on the driving stress, Δ. Assuming $\alpha = \beta = 0$, then $\Delta = A_1\sigma$ and Fig. 4 clearly illustrate that no creep damage would occur along the fiber direction and that maximum damage would occur when the load is transverse to the fiber direction. An example of a stress versus rupture time (S versus t) plot (for three fiber orientation angles) substantiating this conclusion is shown in Fig. 5, given the reasonable baseline creep damage parameters in Table 1 (having SI units and not representing any specific material). Similar qualitative trends have been observed experimentally in that creep rupture times for laminates loaded in the fiber direction ($\theta = 0°$) are substantially longer (one to three orders of magnitude) than those loaded transverse to the fiber direction ($\theta = 90°$), even when the lon-

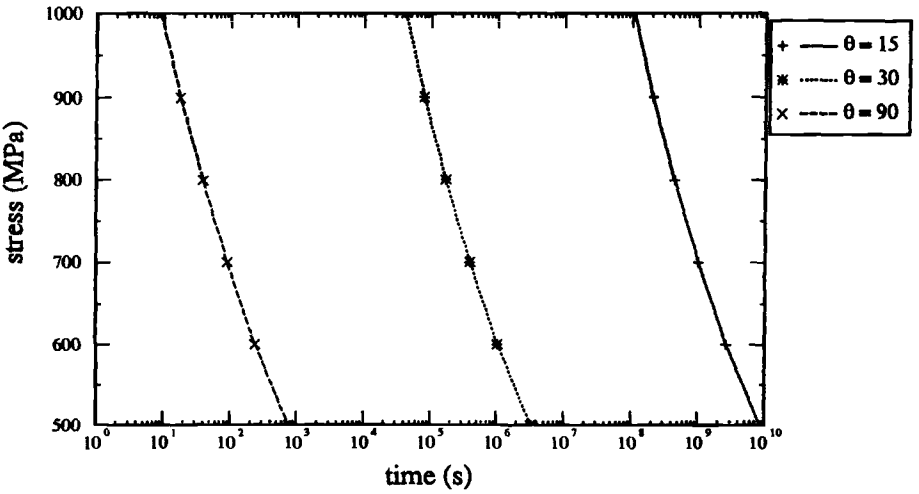

FIG. 5—*Degradation of* S-t *response with fiber orientation.*

TABLE 1—*Baseline creep and fatigue material parameters.*

Creep	Fatigue
$\alpha = 0.05$	$\sigma_{fl} = 175.0$
$\beta = 0.0$	$M_L = 1350.0$
	$\sigma_{u_L} = 700.0$
$r = 6.3$	$\beta = 3.0$
$A = 3173.0$	$a = 0.1$
$k = 15.0$	$\eta = 2.0$
$\tau = 0.15$	$\omega = 5.0$

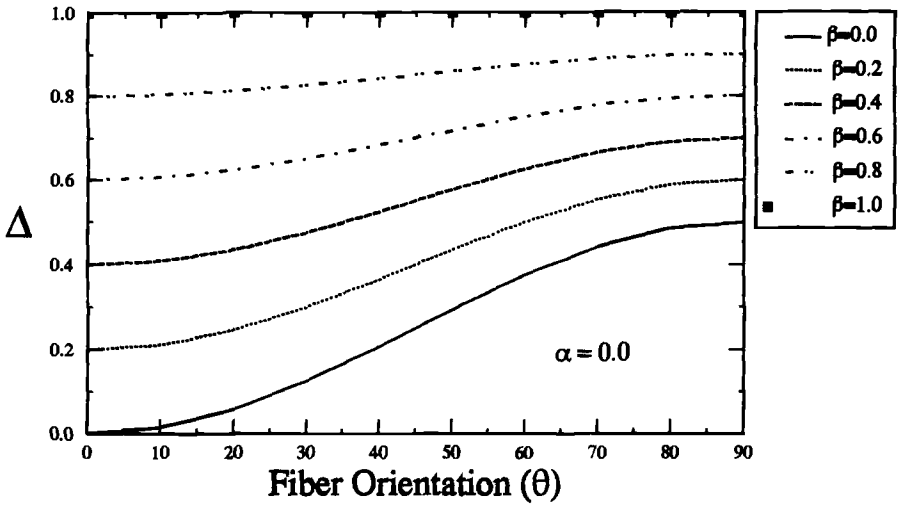

FIG. 6—*Effect of varying the beta parameter on the isochronous function.*

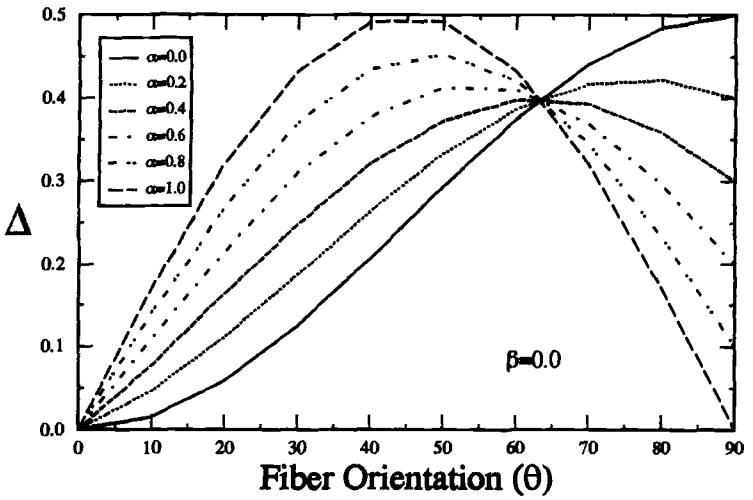

FIG. 7—*Effect of varying the alpha parameter on the isochronous function.*

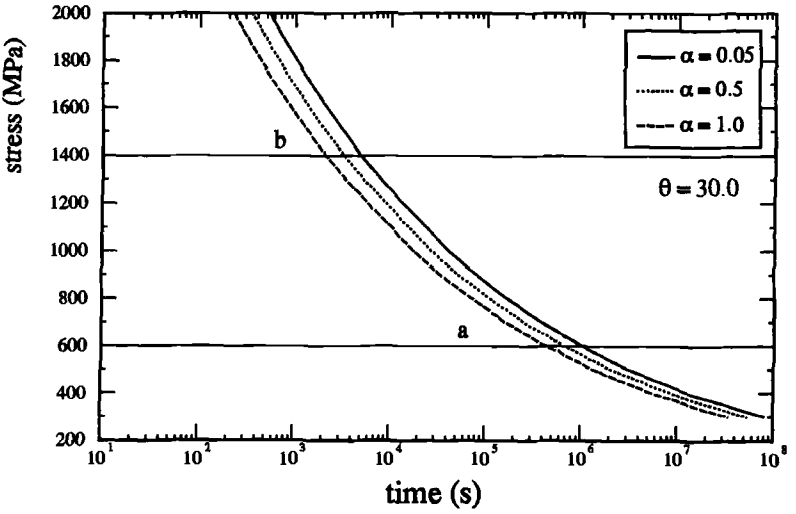

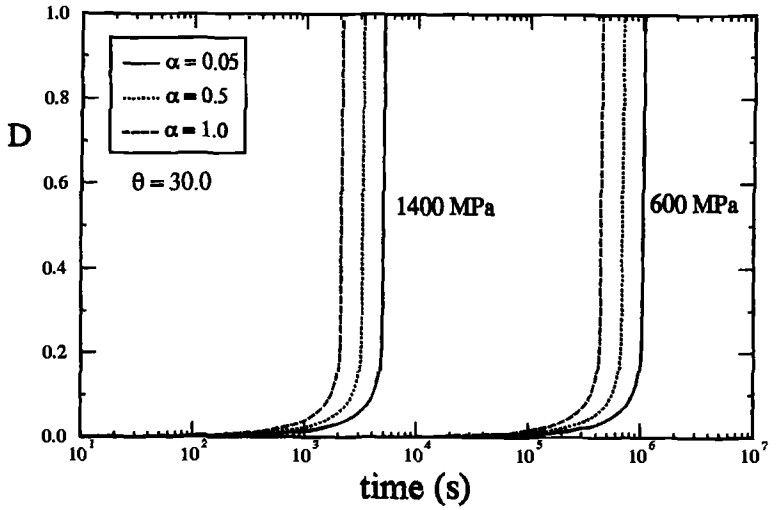

FIG. 8—*Influence of the longitudinal shear parameter (alpha) on the* S-t *and* D-t *responses.*

gitudinal applied load is an order of magnitude larger than that imposed transverse to the fibers, see Figs. 16 and 19 of Ref *42* for an example given for an SCS-6/TIMETAL 21S composite system. Increasing β primarily impacts the difference between longitudinal and transverse creep damage in that, for example, if $\beta = 1$, $\Delta = 0$; whereas, if $\beta = 1$, no angle dependence would

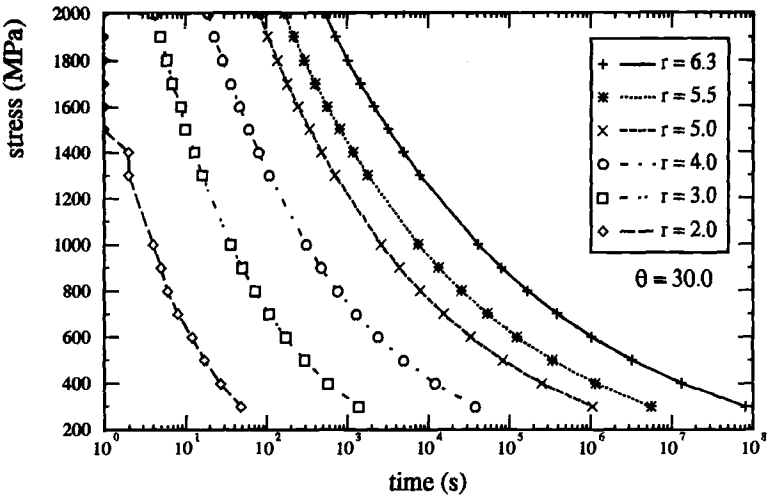

FIG. 9—*Variation of creep exponent,* r.

be detected; that is, $\Delta = \sigma$ (see Fig. 6). Holding β fixed at zero and varying α, we see that the fiber orientation at which maximum creep damage occurs shifts from ($\theta = 90°$, $\alpha = 0$) to a minimum of ($\theta = 45°$, if $\alpha = 1.0$ and $\beta = 0.0$), see Fig. 7. However, in Fig. 8, we see that for a fixed orientation, for example, $\theta = 30°$, the influence of α on the *S-t* curve and the damage evolution is relatively minimal. Finally, examining Eqs 17 and 18, it is apparent that the material parameters, *A* and *r*, predominately influence the time to rupture (see Figs. 9 and 10) whereas *k* impacts greatly the nonlinearity of the evolution of damage, see Fig. 11(*bottom*), while having minimal influence on the corresponding *S-t* response (see Fig. 11(*top*)).

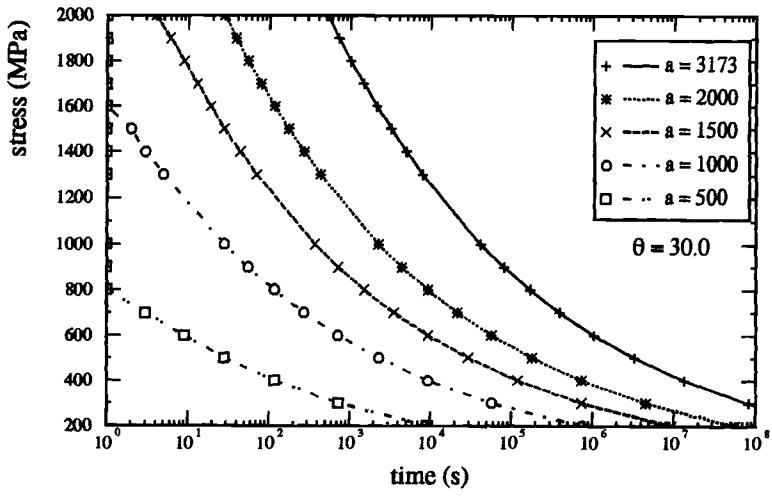

FIG. 10—*Variation of Parameter* A.

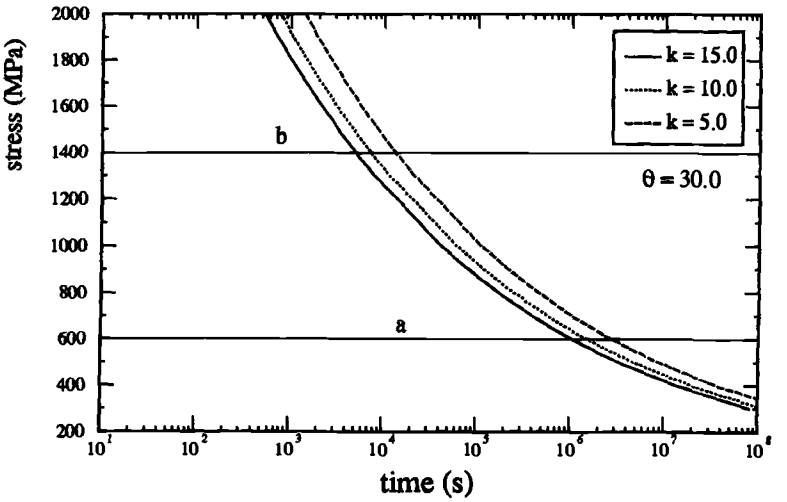

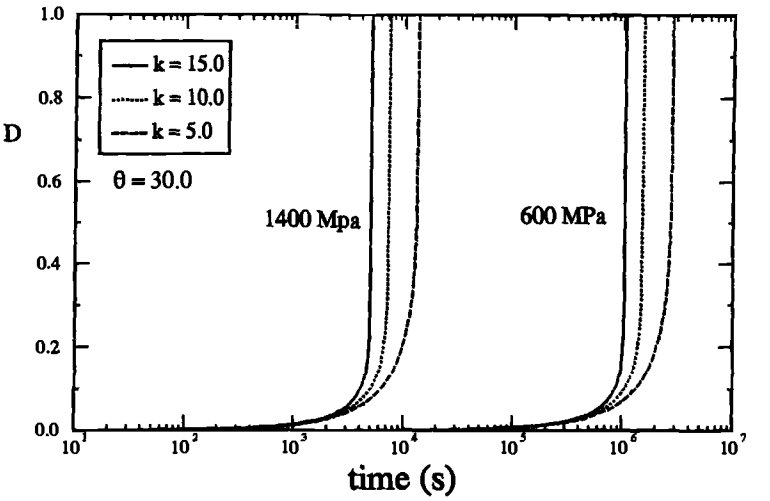

FIG. 11—*Variation of Exponent* k.

Pure Fatigue

A complete parametric study demonstrating the flexibility of the recently developed transversely isotropic fatigue damage model was presented in Ref *28*, the results presented here are restricted to classical Whöler curves for different fiber orientations relative to the applied load direction (see Fig. 12). The curves in Fig. 12 and subsequent figures are generated using the

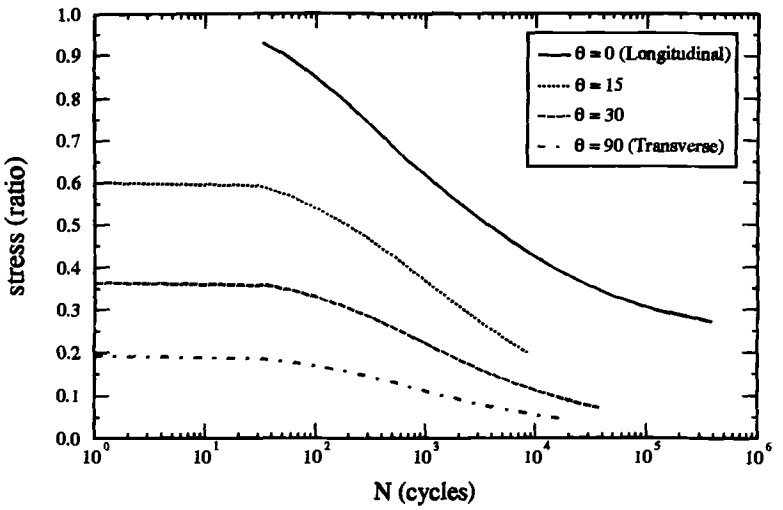

FIG. 12—S-N *curve given almost pure fatigue conditions.*

baseline fatigue and creep parameters given in Table 1 and the sinusoidal cycle with a high-frequency (ν = 25 Hz) and zero mean stress (S_m = 0.0), except where noted, that is

$$S = S_m + S_a \sin(2\pi\nu t) \tag{24}$$

where

$$S = \frac{\sigma}{\sigma_{u_L}},\ S_m = \frac{\sigma_m}{\sigma_{u_L}},\ S_a = \frac{\sigma_a}{\sigma_{u_L}}$$

As observed in previous work, the fatigue strength decreases as fiber orientation increases until it reaches a minimum (for these sets of material parameters) under transverse loading, that is, θ = 90°. Again, this qualitative trend is in keeping with experimental observations made for a number of titanium matrix composite systems (for example, see Fig. 10 in Ref *39* and Fig. 22 in Ref *43*). The actual magnitudes are almost identical to those previously obtained (see Fig. 4 in Ref *38*) since under these conditions, the effective stress (Δ) for creep is almost zero and consequently the resulting creep damage is inactive.

Creep-Fatigue Interaction: Fatigue Dominated

Two classes of creep-fatigue interactions will be examined. In this section, we will consider the case of a volume element of material subject to a high-frequency load cycle with and without zero mean stress. In Fig. 13, the equivalent *S-N* curves (for a fiber orientation of 30°, S_m = 0.0, r = 5.5, and ν = 25 Hz) for pure creep, pure fatigue, and creep-fatigue interaction responses are presented to illustrate the influence of the various damage measures and their interactions. Clearly, for all stress amplitudes, the fatigue damage mechanism dominates the creep-fatigue interaction curve; however, at lower stress amplitudes (where sufficient time elapses), creep damage does begin to play a role and so the creep-fatigue interaction response deviates from

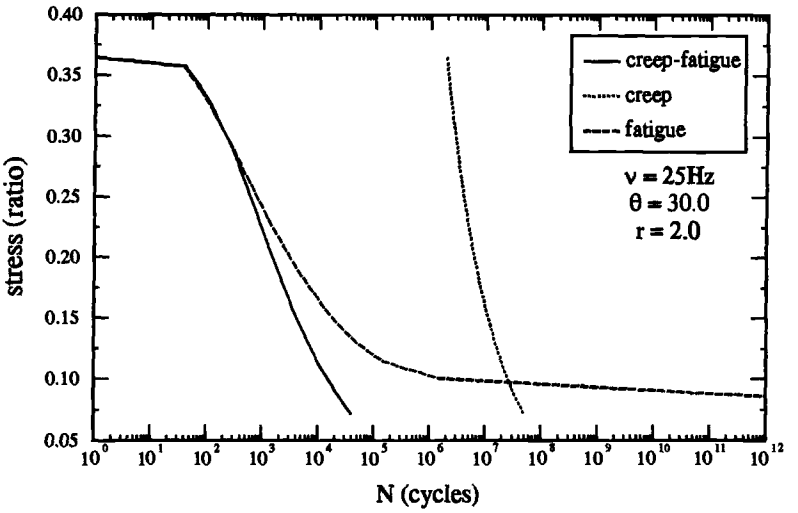

FIG. 13—*Illustration of fatigue-dominated load history.*

that of pure fatigue. Also, note an important theoretical consequence resulting from the presence of a creep damage mechanism in the creep-fatigue interaction response curve; that is, the complete elimination of the fatigue endurance limit. It is primarily these types of interaction effects that prompted the development of more sophisticated fatigue damage models as discussed in Ref *38*.

The preceding creep damage sensitivity study indicated that both Parameters r and A had a similar and significant (potentially 3 to 5 orders of magnitude) impact on creep rupture life times. Consequently, the influence of changing r (from 5.5 to 2.0) on the resulting *S-N* curve for two different frequencies (that is, 5 and 25 Hz) and three fiber orientations is illustrated in Fig. 14. Here, we see for a given frequency a significant reduction in life, as expected, for all nonzero fiber orientations, when the creep damage is enhanced by reducing r from 5.5 to 2.0. Also, from Fig. 14, one can easily see the detrimental influence of decreasing the frequency of loading when a material is highly susceptible to creep damage (for example, r = 2.0). Note that the present fatigue model purposely has no frequency dependence, therefore, any difference in response can be totally attributed to the increased influence of the creep damage mechanism.

Another important influencing factor is mean stress. In Fig. 15, we plot the normalized stress amplitude versus cycles to failure for six sinusoidal load histories, that is, σ_m = 0.0, 100, and 200 MPa at two frequencies each (that is, ν = 5 and 25 Hz). As expected, imposing a higher tensile mean stress results in an overall shorter life. Clearly, this mean stress influence is further enhanced, as demonstrated in Fig. 15, due to creep-fatigue interaction effects as the load frequency is decreased from ν = 25 to 5 Hz. This is particularly evident at the higher tensile mean stress of 200 MPa.

Creep-Fatigue Interaction: Creep Dominated

Creep-dominated creep-fatigue interaction will occur when a volume of material is subjected to a low-frequency cyclic load. This class of behavior is clearly illustrated in Fig. 16, when as before (see Fig. 13) we plot the equivalent *S-N* response under pure creep, pure fatigue, and creep-fatigue interaction, given an orientation of 30°, S_m = 0.0, r = 2.0, and ω = 0.25 Hz. In

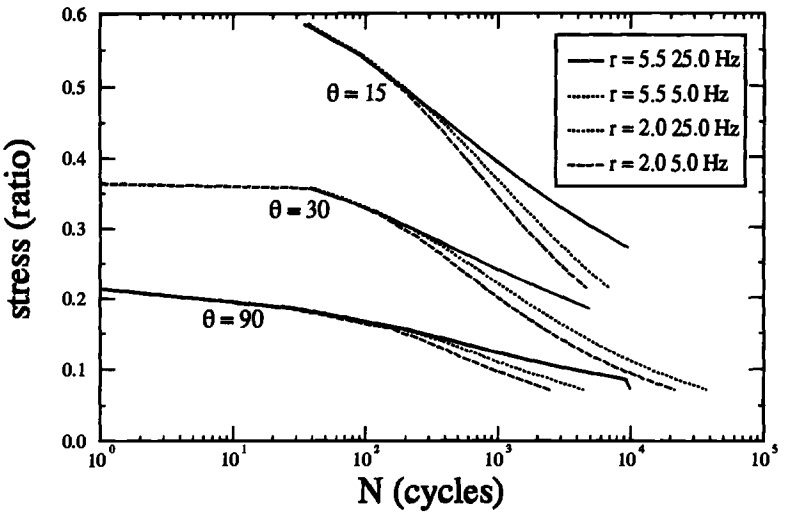

FIG. 14—*Effect of frequency and fiber orientation on the creep-fatigue interaction given,* r = *5.5 and 2.0.*

Fig. 16, it is obvious that the creep-fatigue interaction response curve essentially follows that of the pure creep response, except in the higher stress regime where the lives are predicted to be slightly shorter than those due to pure creep alone. Again, note the loss of the apparent fatigue endurance limit.

The parameter (τ) that heretofore has not been examined can significantly influence the creep damage accumulation and thus the creep-fatigue interaction. The influence of τ on the creep and creep-fatigue interaction *S-N* response is illustrated in Fig. 17, for a fiber orientation of

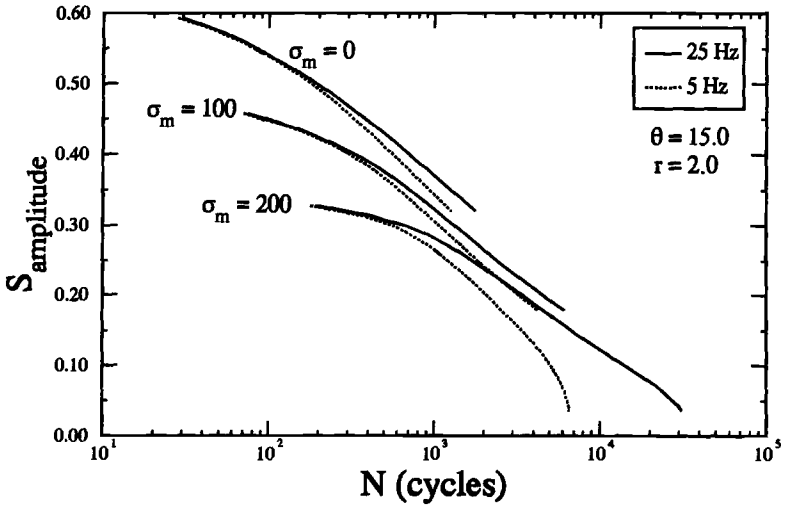

FIG. 15—*Effect of mean stress and frequency on the creep-fatigue interaction effects.*

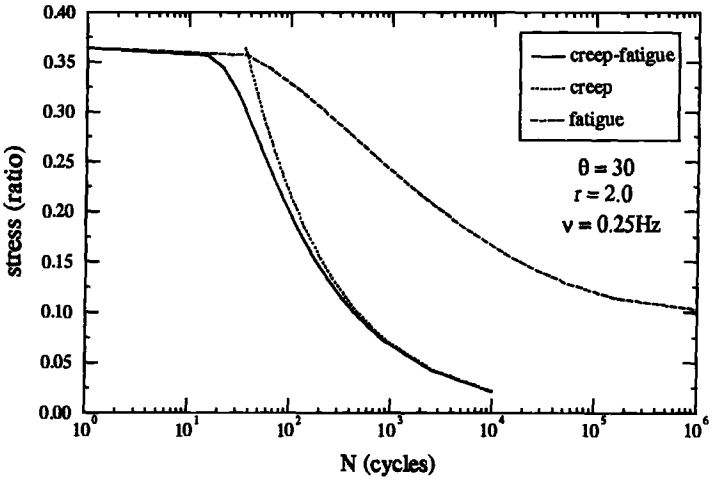

FIG. 16—*Illustration of creep-dominated load history.*

15°, a low frequency of 0.25 Hz, and a creep exponent r of 2.0, with all other parameters being equal to the baseline parameters given in Table 1. As an example, consider the predicted lives at the normalized stress amplitude of 0.4. Here, we see approximately a 27% increase in pure creep life for over a threefold increase in τ (that is, $\tau = 0.15$ to $\tau = 0.5$) while only an 18% increase is observed for the case when creep-fatigue interaction is incorporated in the analysis. This decreased influence in creep-fatigue interaction is due to the fact that the fatigue stress versus time history is unaffected by τ, whereas the creep stress versus time is significantly impacted by changes in τ; as illustrated in Fig. 18. The influence of τ (see Fig. 18) is such that increasing τ decreases the maximum stress amplitude affecting the creep damage evolution and

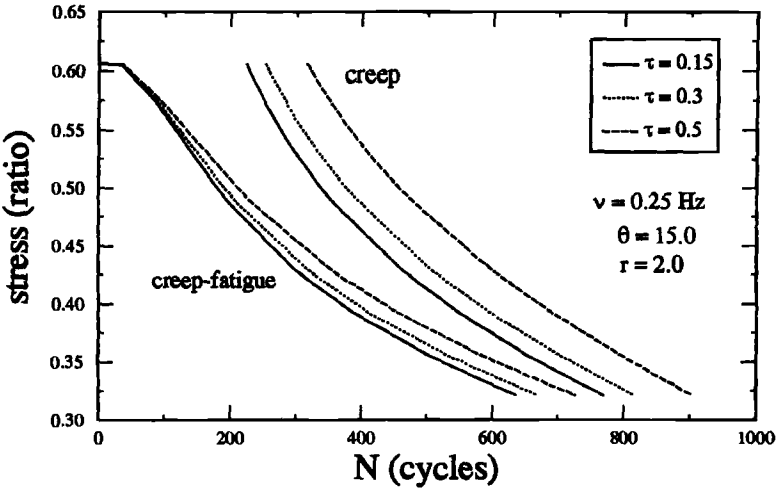

FIG. 17—*Effect of delay stress (τ) on creep and creep-fatigue interaction.*

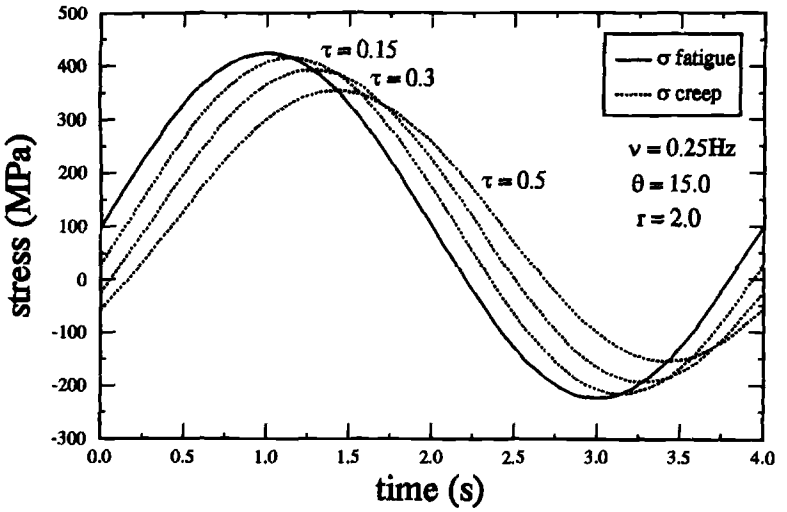

FIG. 18—*Effect of delay stress parameter on fatigue and creep stress history.*

shifts the phasing of that maximum so as to delay it; thus, the name "delay stress" (σ_{ij}^{d}). Similarly, given a fixed τ value (for example, $\tau = 0.5$) and increasing the frequency of loading from 0.25 to 1 Hz, one can see in Fig. 19 that the reduction in maximum stress amplitude is increased. Consequently, as we continue to increase the frequency of loading, the significance of creep damage accumulation (irrespective of the chosen parameters) is minimized, that is, we move into the realm of "fatigue-dominated" creep-fatigue interaction.

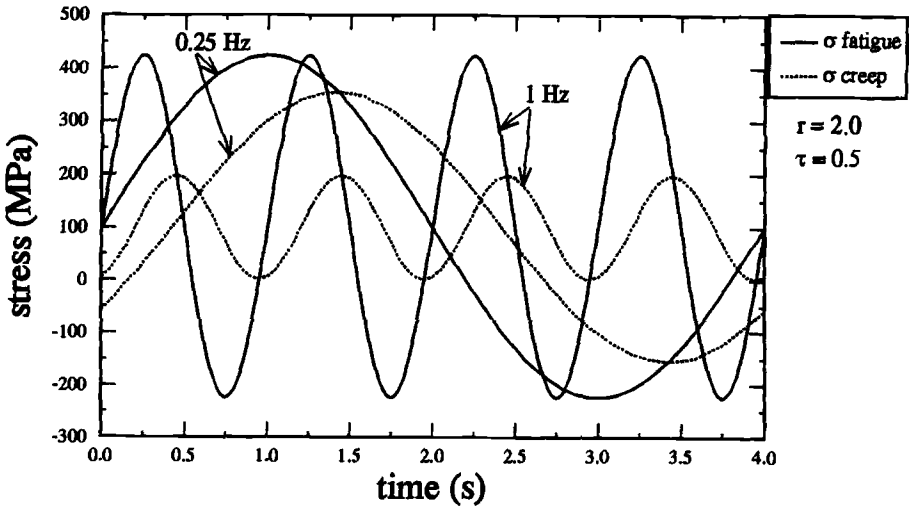

FIG. 19—*Interaction of delay stress and loading frequency on the fatigue and creep stress histories.*

Conclusion

A multiaxial, isothermal, continuum damage mechanics model for creep and creep-fatigue interaction of a unidirectional metal-matrix composite volume element has been presented. The model is phenomenological, stress based, and assumes a single scalar internal damage variable, the evolution of which is directionally dependent. The present creep damage model is an extension of the Leckie-Hayhurst creep damage model to unidirectional MMCs and when taken to its isotropic limit, will directly simplify to this previously developed and validated isotropic creep damage model. The extension was accomplished by introducing into the isochronous damage function physically meaningful stress invariants that reflect the local stress and material orientation within a metallic, transversely isotropic material (for example, hexagonally packed unidirectional metal-matrix composite). These invariants were included based on the anticipation that the associated stress state may strongly influence void growth at the fiber-matrix interface (as this interface is postulated to play a role, on the mesostructural scale, analogous to that of grain boundaries on the microstructural scale and interfacial degradation); and, consequently may correlate with a creep rupture mechanism based on interfacial degradation through diffusion-related void growth.

Creep-fatigue interaction was accomplished by directly adding together the mechanical effects of creep and fatigue damage. A uniaxial parametric study was performed under pure creep and creep-fatigue conditions, to demonstrate the sensitivity of the various material parameters and determine the capability of the formulation to characterize a class of composite materials. Specifically, two interaction regions were examined, the first (termed creep-dominated interaction) is important for low-frequency loading cycles (<5 Hz); whereas the second (termed fatigue-dominated interaction) is for high-frequency loading cycles with a nonzero mean stress. Results were presented in the form of *S-N* and damage accumulation curves and suggest that the proposed creep, fatigue, and creep-fatigue interaction model is capable of representing a wide range of behavior. Experimental correlation and validation of the proposed model is anticipated in the future.

References

[1] Eshelby, J. D., "The Determination of the Elastic Field of an Ellipsoidal Inclusion and Related Problems," *Proceedings*, Royal Society, Vol. A241, 1957, pp. 376–396.

[2] Mura, T., *Micromechanics of Defects in Solids*, M. Nijhoff, The Hague, The Netherlands, 1982.

[3] Budiansky, B., "Micromechanics II," *Proceedings*, 10th U. S. National Congress of Applied Mechanics, J. P. Lamb, Ed., American Society of Mechanical Engineers, New York, 1987, pp. 25–32.

[4] Krajcinovic, D. and Sumarac, D., "Micromechanically Based Damage Models," *Proceedings*, 10th U. S. National Congress of Applied Mechanics, J. P. Lamb, Ed., American Society of Mechanical Engineers, New York, 1987, pp. 115–123.

[5] Nemat-Nasser, S., "Micromechanically Based Constitutive Modeling of Inelastic Response of Solids," *Constitutive Models of Deformation*, J. Chandra and R. P. Srlvastava, Eds., Society for Industrial and Applied Mechanics Publ., 1987, pp. 120–129.

[6] Sanchez-Palencia, E. and Zaoui, A., *Homogenization Techniques for Composite Media*, Springer, Berlin, 1987.

[7] Kachanov, L. M., *Introduction to Continuum Damage Mechanics*, Martinus Nijhoff, Dordrecht, The Netherlands, 1986.

[8] Leckie, F. A. and Hayhurst, D. R., "Creep Rupture in Structures," *Proceedings*, Royal Society, London, Vol. 340A, 1974, pp. 323–347.

[9] Janson, J., "A Continuum Damage Approach to the Fatigue Process," *Engineering Fracture Mechanics*, Vol. 10, 1978, pp. 651–657.

[10] Chaboche, J. L. and Lesne, P. M., "A Non-Linear Continuous Fatigue Damage Model," *Fatigue Fracture Engineering and Materials Structures*, Vol. 11, No. 1, 1988, pp. 1–7.

[11] Chaboche, J. L., "Phenomenological Aspects of Continuum Damage Mechanics," *Materials and Engineering Design: The Next Decade*, B. F. Dyson and D. P. Hayhurst, Eds., Institute of Metals, Brookfield, VT, 1989, pp. 352–365.
[12] Lemaitre, J. and Chaboche, J. L., *Mechanics of Solid Materials*, Cambridge University Press, Cambridge, MA, 1990.
[13] Hayhurst, D. R., "Creep Rupture Under Multiaxial State of Stress," *Journal of the Mechanics and Physics of Solids*, Vol. 20, No. 6, 1972, pp. 381–390.
[14] Krajcinovic, D. and Fonseka, G. U., "The Continuous Damage Mechanics of Brittle Materials—Parts I and II," *Journal of Applied Mechanics*, Vol. 48, No. 4, 1981, pp. 809–815.
[15] Talreja, R., "A Continuum Mechanics Characterization of Damage in Composite Material," *Proceedings*, Royal Society, London, Vol. A399, 1985, pp. 195–216.
[16] Leckie, F. A. and Onat, E. T., "Tensorial Nature of Damage Measuring Internal Variables," IUTAM Symposium on Physical Non-Linearities in Structural Analysis, J. A. Hult and J. Lemaitre, Eds., Springer, 1980, pp. 140–155.
[17] Murakami, S. and Ohno, N., "A Continuum Theory of Creep and Creep Damage," *Creep in Structures*, A. R. S. Ponter, Ed., Third IUTAM Symposium, Springer-Verlag, New York, 1981, pp. 422–453.
[18] Caboche, J. L., "Continuum Damage Mechanics: Part I—General Concepts," *Journal of Applied Mechanics*, Vol. 55, No. 3, 1988, pp. 59–64.
[19] Chaboche, J. L., "Continuum Damage Mechanics: Part II—Damage Growth, Crack Initiation and Crack Growth," *Journal of Applied Mechanics*, Vol. 55, No. 3, 1988, pp. 65–72.
[20] Krajcinovic, D., "Continuum Damage Mechanics," *Applied Mechanics Reviews*, Vol. 37, No. 1, 1984, pp. 1–6.
[21] Krajcinovic, D., "Damage Mechanics," *Mechanics of Materials*, Vol. 8, 1989, pp. 117–197.
[22] Hult, J., "Continuum Damage Mechanics (CDM)—A New Design Tool," *Materials and Engineering Design: The Next Decade*, B. F. Dyson and D. R. Hayhurst, Eds., Institute of Metals, London, 1989, pp. 199–204.
[23] Rabotnov, Y. N., *Creep Problems in Structural Members*, North Holland, Amsterdam, 1969.
[24] Rabier, P. J., "Some Remarks on Damage Theory," *International Journal of Engineering Science*, Vol. 27, No. 1, 1989, pp. 29–54.
[25] Lesne, P. M. and Savalle, S., "A Differential Damage Rule with Microinitiation and Micropropagation," *Recherche Aerospatiale*, No. 2, 1987, pp. 33–47.
[26] Lesne, P. M. and Cailletaud, G., "Creep-Fatigue Interaction under High Frequency Loading," Fifth International Conference in Mechanical Behavior of Materials, Beijing, China, ONERA TP 1987–66, 1987.
[27] Chaboche, J. L., "Fracture Mechanics and Damage Mechanics: Complementary of Approaches," *Proceedings*, International Conference on Numerical Methods in Fracture Mechanics, San Antonio, Pineridge Press, Swansea, ONERA TP 1987–25, 1987, pp. 308–324.
[28] Arnold, S. M. and Kruch S., "A Differential Continuum Damage Mechanics Model for Fatigue of Unidirectional Metal Matrix Composite," *International Journal of Damage Mechanics*, Vol. 3, 1994, pp. 170–191.
[29] Chaboche, J. L., "Continuous Damage Mechanics—Tool to Describe Phenomena Before Crack Initiation," *Nuclear Engineering and Design*, Vol. 64, 1981, pp. 233–247.
[30] Greenwood, G., "Creep Life and Ductility," *Proceedings*, International Congress on Metals, Cambridge, Microstructure and the Design of Alloys 2, 1973, p. 91.
[31] Dyson, B. F., "Constrained Cavity Growth, Its Use in Quantifying Recent Creep Fracture Experiments," *Canadian Metals Quarterly*, Vol. 18, 1979, p. 31.
[32] Hayhurst, D. R., "On the Role of Creep Continuum Damage in Structural Mechanics," *Engineering Approaches to High Temperature Design*, Wilshire and Owen, Eds., Pineridge Press, Swansea, 1983.
[33] Lecike, F. A., "The Constitutive Equations of Continuum Creep Damage Mechanics," *Philosophical Transactions*, Royal Society, London, Vol. A288, 1978, pp. 27–47.
[34] Leckie, F. A., "The Micro and Macro Mechanics of Creep Rupture," *Engineering Fracture Mechanics*, Vol. 25, No. 5/6, 1986, pp. 505–521.
[35] Robinson, D. N. and Duffy, S. F., "Continuum Deformation Theory for High Temperature Metallic Composites," *Journal of Engineering Mechanics*, ASCE, Vol. 116, No. 4, 1990, pp. 832–844.
[36] Robinson, D. N., Binienda, W. K., and Miti-Kavuma, M., "Creep and Creep Rupture of Strongly Reinforced Metallic Composites," *Journal of Engineering Mechanics*, ASCE, Vol. 118, No. 8, 1992, pp. 1646–1660, or NASA CR 185286, 1990.
[37] Arnold, S. M., "A Transversely Isotropic Thermoelastic Theory," NASA TM 101302, 1989.
[38] Arnold, S. M. and Kruch, S., "Differential Continuum Damage Mechanics Models for Creep and Fatigue of Unidirectional Metal Matrix Composite," NASA TM 105213, Cleveland, OH, 1991.

[*39*] Arnold, S. M. and Wilt, T. E., "A Deformation and Life Prediction of a Circumferentially Reinforced SiC/Ti 15-3 Ring," *Proceedings*, ASME Tenth Biennial Conference on Reliability, Stress Analysis and Failure Prevention, R. J. Schaller, Ed., DE-Vol. 55, 1994, pp. 231–238.

[*40*] Chaboche, J. L., "Une Loi Differentielle d'Endommagement de Fatigue avec Cumulation non Lineaire," *Revue Francaise de Mechanique*, No. 50-51, 1974, English translation in Annales de l'ITBTP, 1977.

[*41*] Lemaitre, J. and Plumtree, A., "Application of Damage Concepts to Predict Creep-Fatigue Failures," *Journal of Engineering Materials and Technology*, Vol. 101, 1979, pp. 284–292.

[*42*] Khobaib, M., John, R., and Ashbaugh, N. E., "Sustained Load Behavior of SCS-6/TIMET-AL 21S Composite," *Life Prediction Methodology for Titanium Matrix Composites, ASTM STP 1253*, W. S. Johnson, J. M. Larsen, and B. N. Cox, Eds., American Society for Testing and Materials, West Conshohocken, PA, 1996, pp. 185–207.

[*43*] Arnold, S. M. and Castelli, M. G., "What Constitutes a Model Material? A LeRC Structural Fatigue Branch Perspective," *HITEMP Review 1995*, NASA CP 10178, Cleveland, OH, 1995.

David H. Allen,[1] *James W. Foulk,*[1] *Kayleen L. E. Helms,*[1] *and Dimitris C. Lagoudas*[1]

A Model for Predicting the Effect of Environmental Degradation on Damage Evolution of Metal-Matrix Composites

REFERENCE: Allen, D. H., Foulk, J. W., Helms, K. L. E., and Lagoudas, D. C., "**A Model for Predicting the Effect of Environmental Degradation on Damage Evolution of Metal-Matrix Composites,**" *Applications of Continuum Damage Mechanics to Fatigue and Fracture, ASTM STP 1315*, D. L. McDowell, Ed., American Society for Testing and Materials, 1997, pp. 29–45.

ABSTRACT: A life prediction model is being developed by the authors for application to continuous fiber metal-matrix composites (MMCs). The specific systems considered in this study are silicon-carbide fibers imbedded in titanium matrix. Due to multiple nonlinearities, the model utilizes a computationally based framework derived from thermodynamics and continuum mechanics. Matrix inelasticity, damage evolution, and environmental degradation due to oxidation-related effects are also included within the model. To computationally implement the model, the finite element method is used with an evolutionary analysis of a unit cell accomplished via a time-stepping algorithm. Matrix inelasticity is modeled with the Bodner anisotropic hardening viscoplastic model. Damage growth such as fiber-matrix debonding, surface cracking, and matrix cracking is modeled via the inclusion of cohesive zone elements in the unit cell. The locations of these elements are chosen to correspond with experimentally observed damage. As environmental degradation varies in form, depending on the specific system, it is accounted for by including either an outer surface layer that is embrittled due to oxidation or degraded material properties that result from oxygen-induced changes in microstructure.

The current paper outlines the formulation utilized by the authors to solve this problem, and recent results are discussed. Specifically, results are given for a four-ply unidirectional composite subjected to monotonic and fatigue loadings. In both cases, environmental degradation influences the initiation and evolution of damage.

KEYWORDS: metal-matrix composites, oxidation, damage, fracture (materials), environmental degradation, life prediction, fatigue (materials), continuum damage mechanics, cracking

Over the last three decades, metal-matrix composites (MMCs) have been considered as candidate materials for a variety of advanced technological applications. MMCs have the potential to provide improved elevated-temperature performance as compared to the capabilities of currently available monolithic metals or polymer-matrix composites. Unfortunately, continuous fiber MMCs have found only limited applications due to a variety of shortcomings that generally lead to low fracture toughness and limited life [*1*]. These limitations have resulted in considerable investigation by the research community, but full solutions have yet to be achieved.

Titanium metal-matrix composites (TMCs) have been developed for use in a variety of elevated-temperature aerospace applications. These include the National AeroSpace Plane

[1] Professor, graduate research assistant, graduate research and teaching assistant, and associate professor, respectively, Center for Mechanics of Composites, Texas A&M University, College Station, TX 77843–3141.

(NASP), Integrated High Performance Turbine Engine Technology (IHPTET), and the High Speed Civil Transport (HSCT). TMCs are being considered because they provide improved performance at elevated temperatures, high specific strength, and high ductility as compared to other currently available materials [2]. Unfortunately, in most circumstances, TMCs have failed to reach production primarily because they have been found to have relatively short life in elevated-temperature environments.

Two particular candidate metastable beta-titanium alloys have received the most interest over the past 10 to 15 years. Both alloys are usually used with continuous silicon-carbide fiber reinforcement. Unfortunately, when exposed to temperatures in excess of 550°C, the first of these materials, Ti-15-3, was found to undergo severe oxidation that in turn induces premature failure. In an effort to develop a more oxygen-resistant titanium matrix, Ti-β21S was developed as a more promising matrix material. In the past five to six years, this matrix material has been the focus of many research efforts. Of all of the metastable titanium alloys, Ti-β21S is considered to be the most oxidation-resistant [3]. However, this material also experiences premature failure when subjected to fatigue loading at elevated temperatures.

Recent Research

Many previous research efforts have attempted to model the behavior of MMCs. Several suggested approaches have been based on micromechanics schemes [4–7]. These methods utilize approximate techniques such as the concentric cylinder model to determine effective composite properties that can then be used in conjunction with a mechanical finite element code to model MMC behavior. A second approach for modeling fatigue behavior has been to utilize a linear life fraction technique to determine the number of cycles to failure for a given maximum applied stress [8,9]. This technique, which does not require a full finite element analysis, involves determination of (1) local stresses via codes like METCAN [8] and (2) linear relation constants obtained empirically from experimental observation. In conjunction with these approaches, several computer codes have been developed to aid in life prediction of MMCs. A full review of many of these codes was recently completed [10]. In addition, detailed literature searches on TMCs are given in two recent publications [11,12].

To effectively model MMC behavior, several specific factors have been investigated, including (1) the effects of thermal gradients [13,14]; (2) the effects of fiber and interfacial layer morphologies on matrix response [15]; (3) the type of reinforcement used, especially long brittle fibers [16,17]; and (4) the effects of an inelastic matrix and damage evolution [18–20]. As a result of much study, it has been determined that two essential components for successful modeling of continuous fiber-reinforced MMCs are the incorporation of (1) an inelastic matrix model to accurately capture time-dependent behavior and (2) a damage evolution model to accurately predict unloading [21].

Since environmental effects play a substantial role in MMC behavior, several attempts have been made to incorporate environmental effects into proposed modeling efforts. Specific efforts include the use of an Arhennius-type expression in an attempt to include environmental damage due to oxidation in life prediction [22]. A diffusion-based model has predicted oxidation and subsequent oxidation-induced damage in MMCs [23–25]. Utilizing a diffusion-based oxidation model in conjunction with a micromechanics unit cell approach, TMC behavior has also been modeled with some success [26,27].

For modeling of the two most popular titanium systems, most methods have assumed fibers to be thermoelastic and have modeled Ti-15-3 and Ti-β21S stress-strain behavior using the Bodner-Partom thermoviscoplastic model [28], although others have been proposed [29]. Although the material parameters for Ti-β21S were determined by Neu [30]; the original constants were found to deviate from the experimentally observed cyclic loading behavior. Some researchers also suggested revisions to the original constants to increase isotropic hardening

effects [*31*]. In an attempt to capture the cyclic behavior of Ti-β21S, Neu and Bodner have recently developed a revised set of material parameters that vary exponentially as a function of hardening [*32*]. These new parameters are utilized in the current paper.

Experimental Observations

Titanium-15-3

Despite the fact that Ti-15-3's microstructure remains relatively stable at elevated temperatures, it is extremely susceptible to oxidation. In fact, after two h at 650°C, Ti-15-3 forms a considerable oxide layer of primarily rutile TiO_2 as shown in Fig. 1. Unfortunately, this oxide layer is extremely porous, brittle, and nonprotective. Under mechanical loading, surface cracks quickly initiate in the oxide and continue to propagate towards the metallic substrate; thereby inducing other damage mechanisms that eventually lead to an earlier failure than would be observed in an inert environment.

Titanium-β21S

Although Ti-β21S has superior oxidation resistance when compared to Ti-15-3, rapid degradation of mechanical properties has been observed at elevated temperatures. This degradation of mechanical properties can be indirectly attributed to oxidation dissolution [*33,34*]. Unlike Ti-15-3, Ti-β21S has been observed to form a thin, protective oxide layer, approximately 3 μm thick after 72 h at 700°C, as shown in Fig. 2. In fact, Ti-β21S is far superior to all other titanium alloys in experimentally observed weight gain measurements. Unfortunately, weight gain is measured in days, while a significant degradation of mechanical properties can occur within hours or perhaps even minutes.

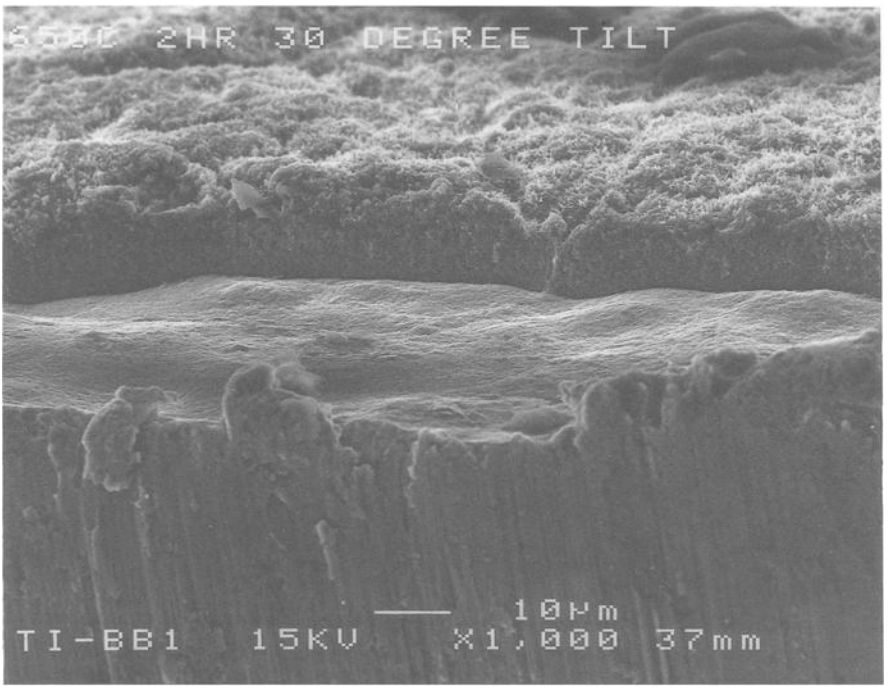

FIG. 1—*Oxide layer in Ti-15-3 at 650°C after 2 h.*

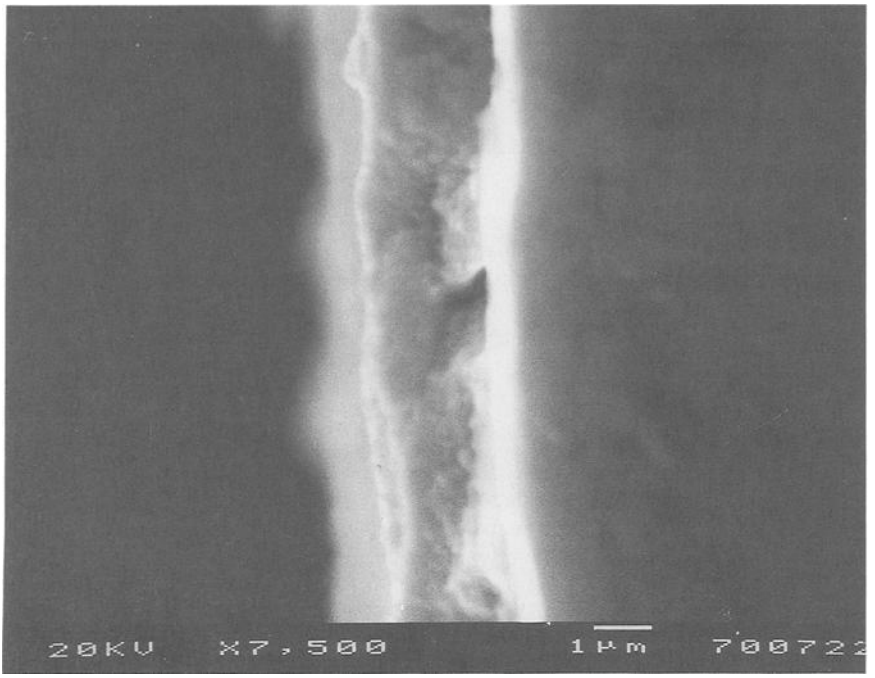

FIG. 2—*Oxide layer in Ti-β21S at 700°C after 72 h.*

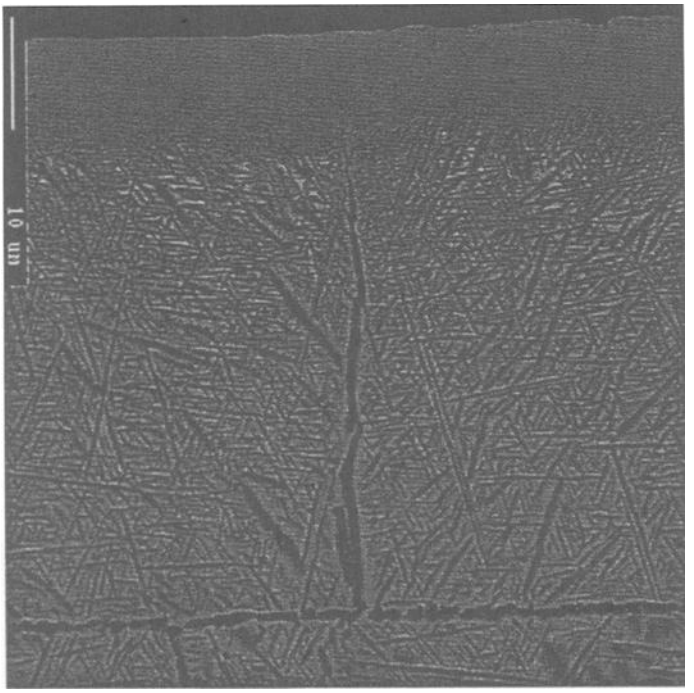

FIG. 3—*Distribution of alpha grains in Ti-β21S near the surface at 700°C after 24 h.*

We have experimentally observed a high concentration of alpha phase near the surface of Ti-β21S during oxidation. The alpha phase forms along the grain boundaries and coarsens away from the surface, as shown in Fig. 3. These observations have been noted by previous research efforts [*33*]. Apparently, oxygen quickly diffuses into the surface layer at elevated temperatures and acts as an alpha stabilizer that encourages the formation of the small Widmanstatten alpha phase both within and along the large beta grains [*33*]. With this phase change, a severe loss of ductility has been observed [*35,36*]. In fact, this embrittled region has been found to develop within seconds with less than 1% weight gain at 800°C [*37*]. This embrittlement is similar to that found in alpha-beta titanium alloys. Previous studies of oxidation effects on alpha-beta titanium alloys have indicated that even low-level oxygen concentrations in the alpha phase significantly affect slip plane movement due to interstitially located oxygen atoms. Due to the limited available slip systems, alpha-beta titanium alloys experience a loss of ductility accompanied by an increase in stiffness [*38*]. In alpha-beta alloys, any alpha microstructures other than equiaxed are generally susceptible to ductility loss at elevated temperatures [*39*]. Even the fatigue crack growth rate of alpha-beta alloys has been shown to increase with decreasing alpha phase grain size [*40*].

Failure of the composite is apparently caused by a succession of separate damage events. In the unoxidized case, damage initiates in the form of matrix radial cracks emanating from fibers [*41*]. Under continued loading, fiber cracks are assumed to form that will ultimately lead to the failure of the part. In the oxidized case, damage is first observed in the form of large substrate cracks along grain boundaries due to embrittlement caused by oxygen-induced microstructural changes. This damage mechanism is then followed by the formation of smaller surface cracks in the brittle thin oxide layer. These surface cracks form perpendicular to the load, as shown in Fig. 4. In [90] laminates, surface cracks lead to fiber/matrix debonding and eventual failure

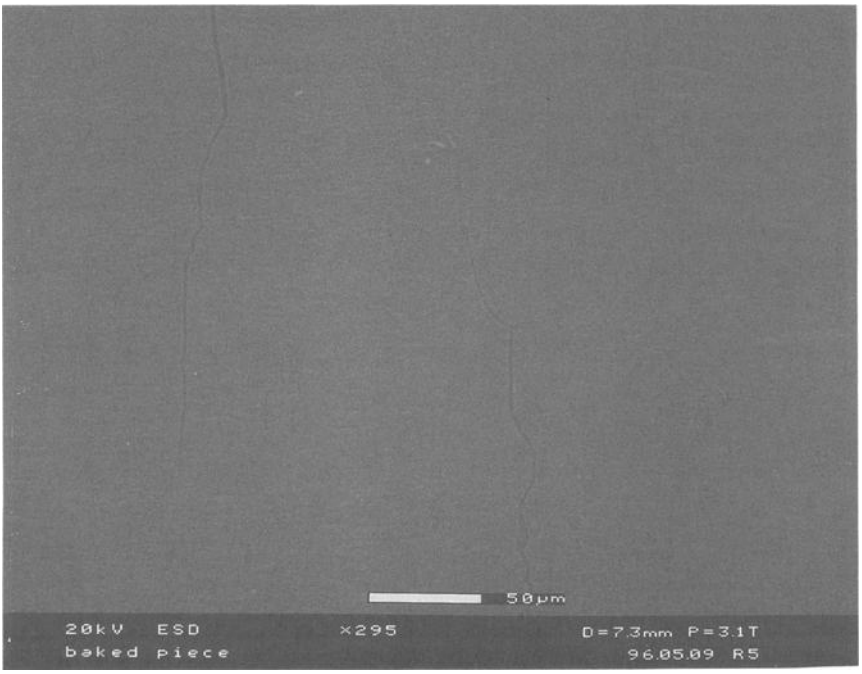

FIG. 4—*Surface cracks in a SCS-6/Ti-*β*21S pre-oxidized (for 72 h) specimen loaded monotonically at 750°C.*

of the composite. In contrast, surface cracks in [0] laminates propagate to and around the first row of fibers. This fiber bridging causes the stress in the fiber to exceed the maximum allowable fiber stress and, in turn, causes failure. These mechanisms are then followed by radial cracking and, ultimately, failure is caused by fiber breakage. Although final failure occurs similarly in the unoxidized case, it occurs much sooner in the oxidized specimens.

Several experimental studies have noted the impact of environment on fatigue life [*5,9,22,42–44*]. In out-of-phase (OP) fatigue testing, for example, the one damage mechanism that has been observed is surface cracking due to oxidation-induced embrittlement. This damage mechanism, along with fiber/matrix debonding, has been found to eventually lead to failure. In addition, material properties such as static moduli and coefficients of thermal expansion have been observed to degrade during high-temperature fatigue in a non-inert environment [*43,45,46*].

Computational Damage Evolution Model

Thermomechanical Model

In spite of the observed environmental effects, few attempts have been made to include the effect of environment on damage evolution. The approach presented here utilizes continuum thermomechanics to analyze a unit cell, as shown in Fig. 5. To model oxidation effects on MMCs, two approaches are used herein. In the case where oxidation occurs quickly, such as Ti-15-3, an oxide layer that is considered to be brittle is included within the model, as shown in Fig. 6. In the slower oxidation case where the oxide layer is thin but the layer beneath is embrittled, such as Ti-β21S, it is assumed that three layers of degraded material exist at the free surface of the unit cell, as shown in Fig. 7. These layers are modeled as brittle (elastic) layers with reduced fracture toughness. It is beyond the scope of this paper to cover the formulation of the model in detail. However, we will review the pertinent equations here, and the interested reader is referred to Refs *20* and *26* for more complete coverage of this approach.

The analysis of the metal-matrix composite is accomplished by satisfying the conservation of linear momentum

$$\sigma_{ji,j} = 0 \tag{1}$$

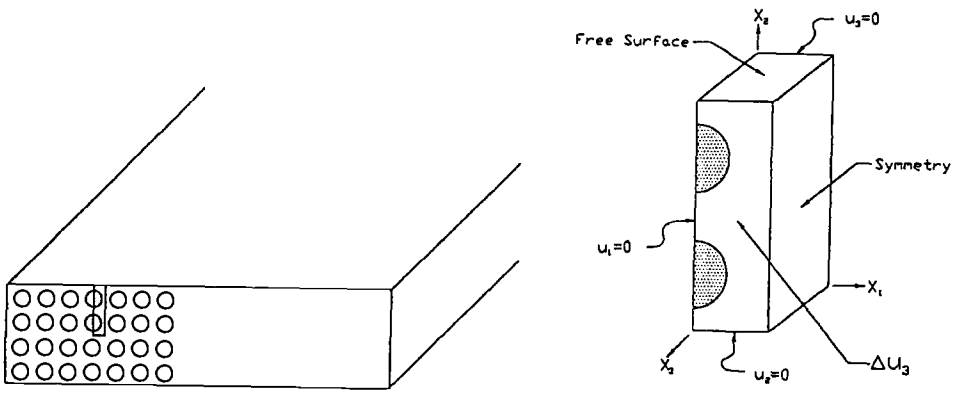

FIG. 5—*Depiction of four-ply unidirectional composite and unit cell.*

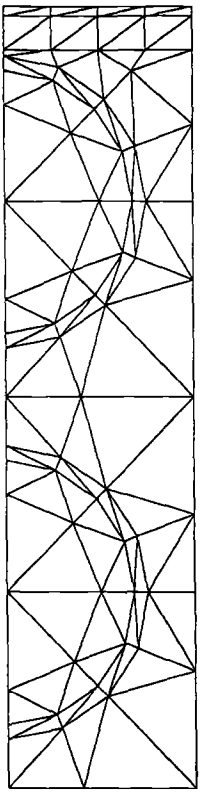

FIG. 6—*Two-dimensional finite element mesh with surface oxide layer.*

where $\sigma_{ij} = \sigma_{ij}(x_k,t)$ is the stress tensor, and body forces and inertial terms are neglected. Furthermore, angular momentum is trivially satisfied by the assumption that the stress tensor is symmetric. Equation 1 is adjoined with strain-displacement equations

$$\varepsilon_{ij} = \frac{1}{2}(u_{i,j} + u_{j,i}) \tag{2}$$

where $u_i = u_i(x_k,t)$ is the displacement field, and $\varepsilon_{ij} = \varepsilon_{ij}(x_k,t)$ is the strain tensor for infinitesimal displacements. Finally, the thermomechanical constitutive equations are given by

$$\sigma_{ij} = D_{ijkl}(\varepsilon_{kl} - \varepsilon_{kl}^{PC} - \varepsilon_{kl}^{I} - \varepsilon_{kl}^{T}) \tag{3}$$

where D_{ijkl} is the elastic modulus tensor, ε_{kl}^{PC} is the phase change eigenstrain to be described later, ε_{kl}^{I} is the inelastic strain tensor, and ε_{kl}^{T} is the thermal strain tensor. The thermal strain tensor is assumed to be a function of the temperature, which is obtained from a solution of the conservation of energy, which is assumed to be uncoupled in the current model [*47*]. The inelastic strain tensor and additional internal variables are assumed to be governed by internal variable evolution laws of the form

$$\dot{\alpha}_{ij}^{\eta} = \Omega_{ij}^{\eta}(\varepsilon_{kl},\varepsilon_{kl}^{I},T,\alpha_{kl}^{\mu}) \quad \eta = 1, \ldots, n; \ \mu = 1, \ldots, n \tag{4}$$

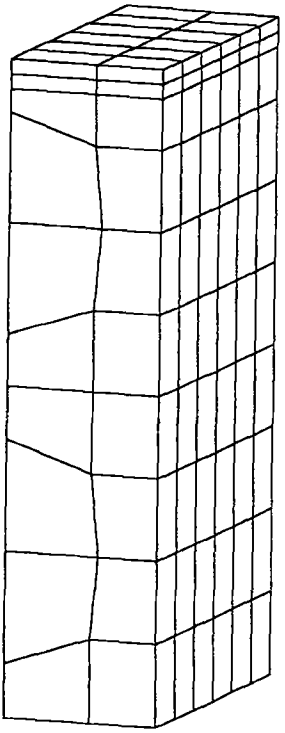

FIG. 7—*Three-dimensional finite element mesh for modeling surface embrittlement. (Top three layers of elements have degraded material properties.)*

where n is the number of internal variables. In the current research, the so-called anisotropic Bodner model is utilized [*28*]. This model has been selected partly because it has been shown to be accurate for titanium [*32*] but also because the material parameters do not appear to be available for other models.

In the current paper, the properties in the fiber are assumed to be thermoelastic ($\varepsilon_{ij}^I \equiv 0$). Assuming that the temperature field is known (from conservation of energy), the preceding field equations can be cast with appropriate mechanical boundary conditions to produce a well-posed boundary value problem.

The thermomechanical model proceeds from the application of continuum thermomechanics to a thermoviscoplastic medium [*47*]. Due to the nonlinearities introduced by the thermoviscoplastic constitutive model, analytic solutions are not practical for most geometries and loading conditions. Therefore, the solutions are obtained computationally via the finite element method.

The details of the formulation are given in Refs *20* and *14*. Briefly, the conservation of momentum (Eq 1) is cast into a weak variational principle in terms of the primary variable $u_i = u_i(x_k,t)$. This variational principle is incrementalized in time, and the strain-displacement (Eq 2) and constitutive equations (Eq 3) are substituted to obtain a field problem that can be discretized for a typical finite element. Due to the fact that internal variable evolution equations (Eq 4) are ordinary differential equations, the variational principle must be incrementalized in time, and the solution is obtained by incrementing the boundary conditions with time. Due to the nonlinearity of evolution Eq 4 as well as the cohesive zone model to be described later

(they are actually numerically stiff), extremely small time steps are required in order to obtain accurate solutions, so that for cyclic loading the solution is computationally intensive. As described in the section on crack growth, this problem may be exacerbated by instabilities introduced during periods of crack propagation.

Crack Growth Model

The evolution of damage in the unit cell is accomplished by implementing cohesive zone elements into the finite element algorithm. This procedure is not only numerically efficient, but it is also physically attractive. The cohesive zone model utilizes a nonconvex quasi-potential to produce a smooth transition from displacement continuity along predetermined internal surfaces to traction-free internal boundaries, thereby affecting crack growth. This procedure has been utilized recently by several researchers [*20,48–50*] to successfully model the evolution of damage in metals and MMCs. Most recently, Allen and co-workers [*21,51*] have used this procedure to model interactions between multiple damage modes.

In the current paper, one of the models developed by Tvergaard [*49*] is used. The cohesive zone model proceeds from the definition of a quasi-potential

$$\Phi(u_n,u_t) \equiv \int_0^{\lambda} F(\lambda')d\lambda' \tag{5}$$

where

$$F(\lambda) \equiv \frac{27}{4}\sigma_{\max}(\lambda - 2\lambda^2 + \lambda^3) \tag{6}$$

and

$$\lambda \equiv [(u_n/\delta_n)^2 + (u_s/\delta_s)^2 + (u_t/\delta_t)^2]^{1/2} \tag{7}$$

where u_n, u_s, and u_t are, respectively, the normal and tangential components of crack opening displacement in the cohesive zone, as shown in Fig. 8. Furthermore, the function, $F(\lambda)$, is graphically depicted in Fig. 9, wherein the material parameter, $\sigma_{\max}$, is depicted. In addition,

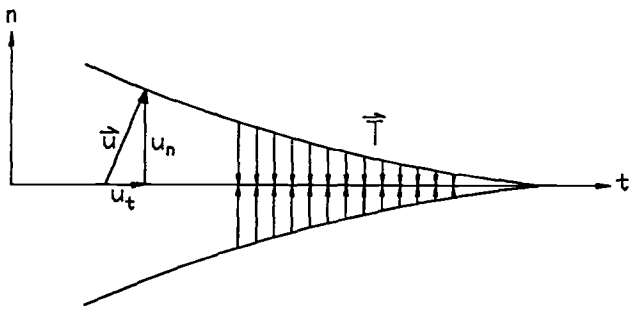

FIG. 8—*A two-dimensional depiction of the crack opening displacements and surface tractions in the cohesive zone.*

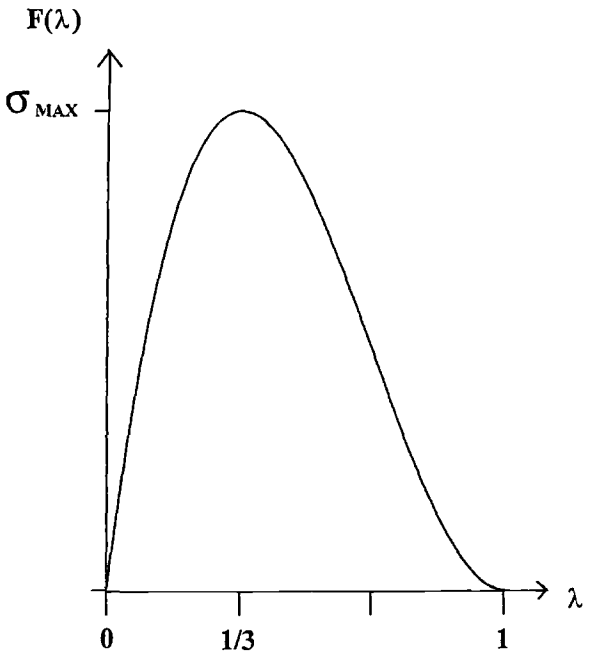

FIG. 9—*Graphical depiction of the function,* F(λ).

δ_n, δ_s, and δ_t are material parameters. The resulting normal and tangential components of the tractions along the cohesive zone are

$$T_n = \frac{\partial \Phi}{\partial u_n} = \frac{F(\lambda)}{\lambda} \frac{u_n}{\delta_n} \tag{8}$$

$$T_s = \alpha_s \frac{\partial \Phi}{\partial u_s} = \alpha_s \frac{F(\lambda)}{\lambda} \frac{u_s}{\delta_s} \tag{9}$$

$$T_t = \alpha_t \frac{\partial \Phi}{\partial u_t} = \alpha_t \frac{F(\lambda)}{\lambda} \frac{u_t}{\delta_t} \tag{10}$$

respectively, where α_s and α_t are the material properties relating normal to shear strength. The cohesive zone model description is completed by the constraint that

$$\lambda \geq 1 \Rightarrow T_n = T_s = T_t = 0 \tag{11}$$

For both loading and unloading, T_n, T_s, and T_p are one-to-one relationships. In addition, due to the tensile nature of the modeling, penetration was not considered in the analysis.

The preceding formulation has been shown to produce a framework that is consistent with the notion of an energy release rate that is critical for crack growth [*52,53*]. This model has been implemented to the computational algorithm used in this paper, so that the code may be utilized to predict crack growth wherever interface elements are placed in the finite element mesh.

Model Predictions

The first MMC considered was a $[90]_4$ SiC/Ti-15-3 laminate. This was accomplished with the use of a two-dimensional generalized plane-strain analysis that was possible because the surface cracks form normal to the load direction. Using the same unit cell as shown in Fig. 6, an analysis has been performed for a monotonically increasing displacement applied normal to the fiber direction. As shown in Fig. 10, this analysis has been performed for two cases: (1) a specimen that is assumed to be unoxidized and (2) a specimen that is assumed to have been pre-oxidized with a surface oxide layer of 50 μm thickness. It is seen in the figure that the average stress-strain behavior of the composite is deteriorated in the oxidized case. The reason for this can be explained by viewing Fig. 11, wherein the crack length is plotted versus time. Although both the oxidized and unoxidized specimens experience discontinuous crack growth, the development of surface cracks in the oxidized specimen tends to shed load to the interior of the composite, thereby causing interface debonding to occur somewhat earlier in the oxidized specimen. This effect is demonstrated in Fig. 12, wherein the evolution of interface radial stress shows unloading in the crack wake and an increased loading ahead of the crack tip as the interface crack propagates. It is our belief that this mechanism has a substantial impact on the life of the composite.

Next a pre-oxidized $[0]_4$ Ti-β21S was considered. Once again, the surface cracks form nor-

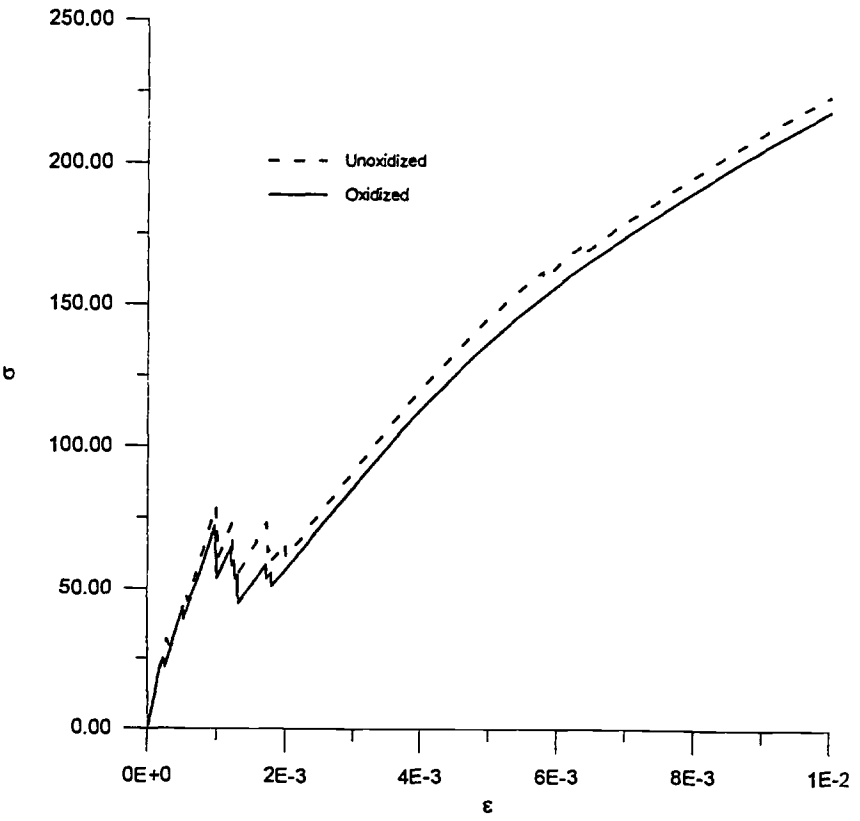

FIG. 10—*Comparison of model for oxidized and unoxidized SiC/Ti-15-3 $[90]_4$ cases.*

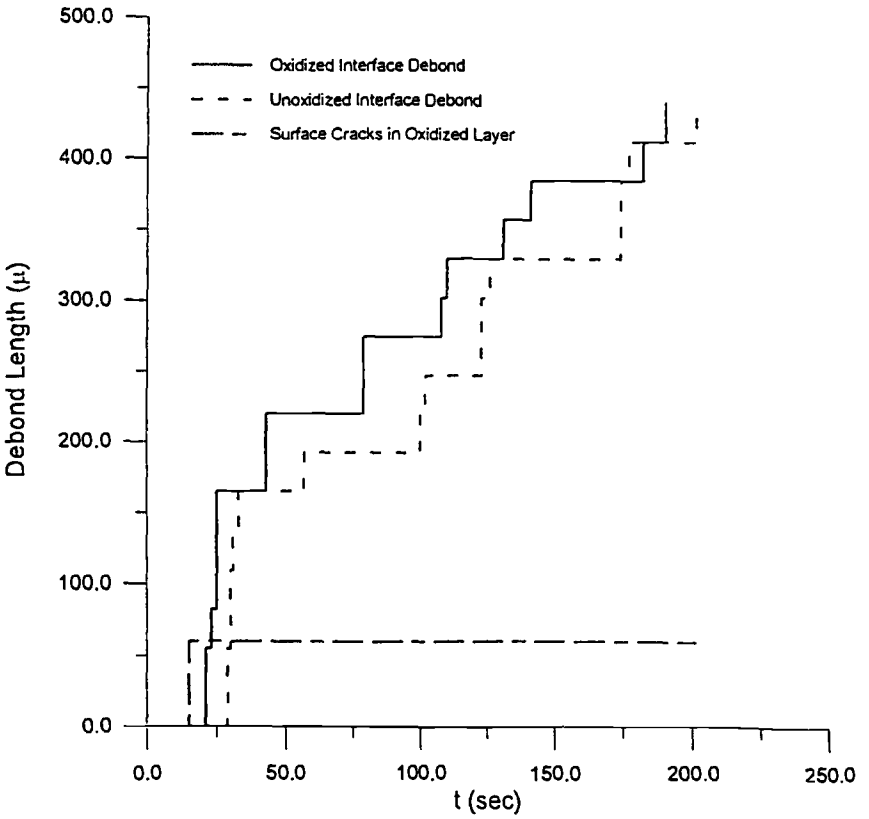

FIG. 11—*Predicted crack growth for oxidized and unoxidized SiC/Ti-15-3 $[90]_4$ cases.*

mal to the loading direction [*21*]. Prior to the development of the surface cracks, a two-dimensional generalized plane-strain analysis can be performed, but the development of these cracks leads to symmetry constraints that require the use of a full three-dimensional analysis. This complication forced the modification of our in-house code, SADISTIC [*20*]. We have now implemented three-dimensional continuum and planar cohesive zone elements to the code. In addition, it was necessary to implement three-dimensional versions of the elastic and thermoviscoplastic constitutive subroutines, as well as the cohesive zone model. These have all been accomplished and are utilized in the analyses performed herein.

In order to demonstrate the necessity to include microcracking in the analyses, we have performed one solution for a $[0]_4$ without damage in the unit cell as shown in Fig. 7. As shown in Fig. 13, the macroscopically averaged strain reaches shakedown after approximately 80 load cycles. Since this does not occur in the experimental results [*41*], it is suggested that further ratchetting can only be modeled if progressive damage is incorporated into the analyses.

To support this assumption, damage was included in another analysis of the same unit cell under monotonic loading in the fiber direction. Preliminary results were obtained by using an elastic model for the matrix. A surface crack quickly propagated through the embrittled region and was blunted by the nondegraded interior. Under continued monotonic loading, fiber bridging is observed. Immediately following, the maximum allowable fiber stress is reached and failure occurs. Due to the brittle nature of the surface, the macroscopically averaged stress-strain behavior only captures the fiber bridging and fiber breakage, as shown in Fig. 14.

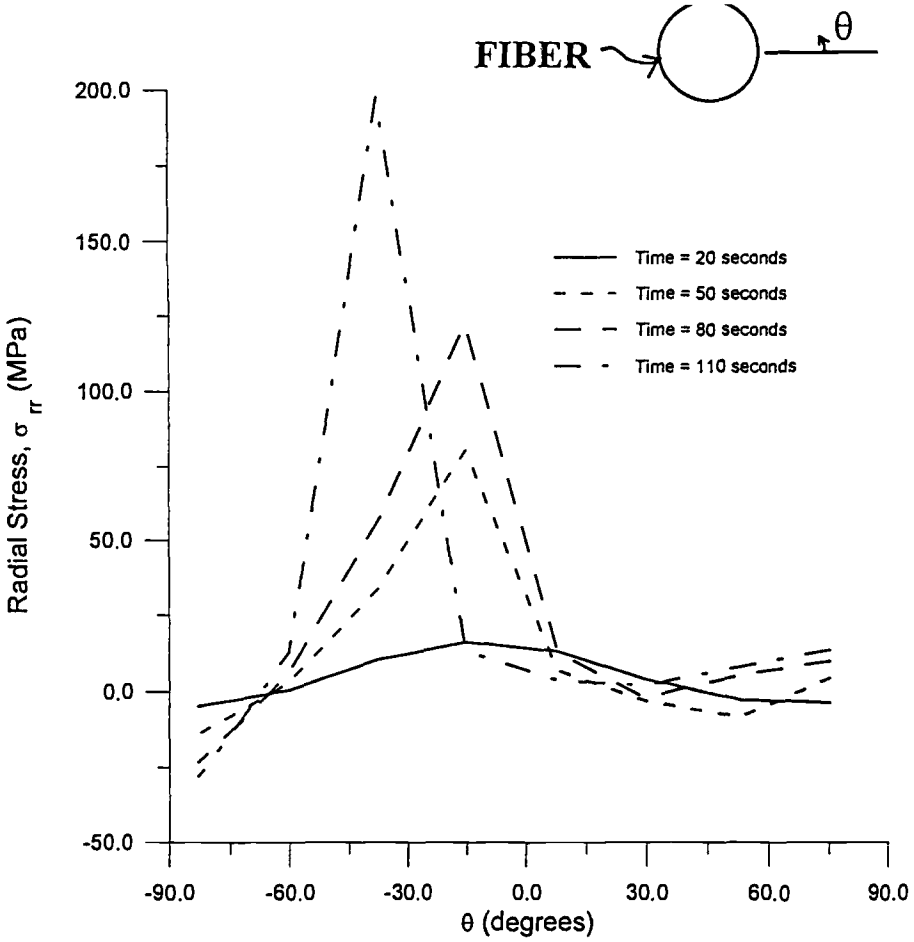

FIG. 12—*Predicted evolution of interface radial stress in the oxidized SiC/Ti-15-3 $[90]_4$ case.*

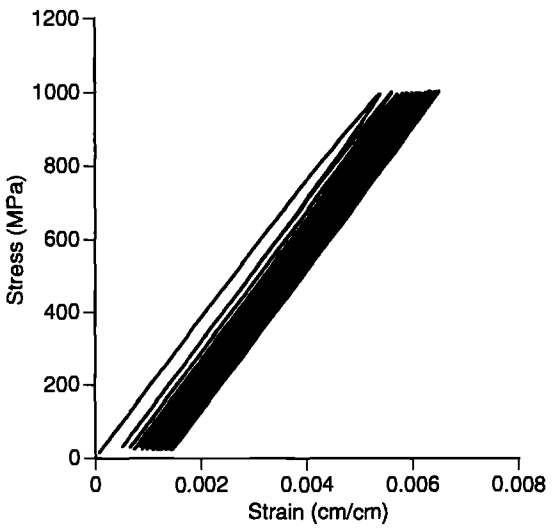

FIG. 13—*Predicted average stress versus strain without damage for cyclic loading of SCS-6/Ti-β21S $[0]_4$ at 650°C (first 80 cycles).*

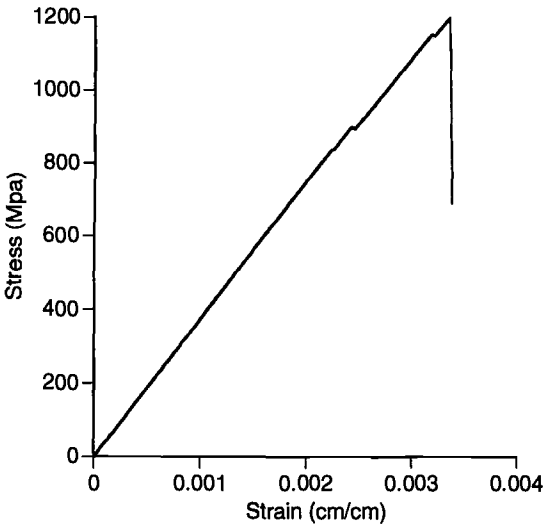

FIG. 14—*Predicted average stress versus strain with damage for monotonic loading of SCS-6/Ti-β21S* $[0]_4$ *at 650°C.*

Conclusion

Results have been obtained herein for MMCs with and without oxygen-induced surface layer embrittlement. The results indicate that load sheds more quickly to the interior of the composite producing failure sooner in the pre-oxidized cases performed. Furthermore, additional results reported herein for predicting cyclic response suggest that the method described in this paper may be suitable for predicting MMC behavior under cyclic fatigue. Pursuit of such results will be the subject of continued research by the authors.

Acknowledgment

The authors are grateful to the Air Force Office of Scientific Research for providing funding for this research under Grant No. F49620-94-1-0341. We also wish to thank Lockheed Aerospace Corporation–Fort Worth Division for providing the SCS-6/Ti-β21S specimens used in this research.

References

[*1*] Larsen, J. M., Russ, S. M., and Jones, J. W., "Possibilities and Pitfalls in Aerospace Applications of Titaniumm Matrix Composites," *Proceedings*, NATO AGARD Conference on Characterization of Fibre Reinforced Titanium Metal Matrix Composites, Bordeaux, France, Sept. 1993.

[2] Ashley, S., "Boeing 777 Gets a Boost from Titanium," *Mechanical Engineering*, July 1993, pp. 60–65.

[*3*] Bania, P. J., "Beta Titanium Alloys and Their Role in the Titanim Industry," *Beta Titanium Alloys in the 1990's*, D. Eylon, R. R. Boyer, D. A. Koss, Eds., The Minerals, Metals & Materials Society, Warrendale, PA, 1993, pp. 3–13.

[*4*] Coker, D., Ashbaugh, N. E., and Nicholas, T., "Analysis of the Thermomechanical Behavior of [0] and [0/90] SCS-6/TIMETAL21S Composites," *Proceedings*, ASME Winter Annual Meeting, American Society of Mechanical Engineers, New York, 1993.

[5] Neu, R. W., "Thermomechanical Fatigue Damage Mechanism Maps for Metal Matrix Composites," *Thermo-Mechanical Fatigue Behavior of Materials: 2nd Volume, ASTM STP 1263*, M. J. Verrilli and M. G. Castelli, Eds., American Society for Testing and Materials, Philadelphia, 1995.

[6] Newaz, G., "Evaluation and Modeling of Mechanical Response and Strength of MMC in Compression," private communication, 1994.

[7] Tamin, M. N., Zheng, D., and Ghonem, H., "Time-Dependent Behavior of Continuous-Fiber-Reinforced Metal Matrix Composites: Modelling and Applications," *Journal of Composites Technology and Research*, submitted for publication.

[8] Nicholas, T. and Russ, S. M., "Response of a [0/90] SCS-6/Timetal 21S Composite to Isothermal and Thermomechanical Fatigue," *Proceedings, Structural Testing Technology at High Temperature—II*, The Society for Experimental Mechanics, Bethel, CT, Nov. 1993, pp. 155–164.

[9] Mall, S. and Portner, B., "Characterization of Fatigue Behavior in Cross-Ply Laminate SCS-6/Ti-15-3 Metal Matrix Composite at Elevated Temperature," *Journal of Engineering Materials and Technology*, Oct. 1992, pp. 409–415.

[10] Kroupa, J. L., Neu, R. W., Nicholas, T., Coker, D., Robertson, D. D., and Mall, S., "A Comparison of Analysis Tools for Predicting the Inelastic Cyclic Response of Cross-Ply Titanium Matrix Composites," *Proceedings*, ASTM Symposium on Life Prediction Methodology for Titanium Matrix Compoaites, Hilton Head, SC, 22–24 March 1994.

[11] Allen, D. H., Eggleston, M. R., and Hurtado, L. D., "Recent Research on Damage Development in SiC/Ti Continuous Fiber Metal Matrix Composites," *Fracture of Composites*, E. A. Armanios, Ed., in *Key Engineering Materials*, Vols. 120–121, Trans Tech Publications, Zurich, 1996, pp. 257–289.

[12] Nicholas, T., Zuiker, J., and Pernot, J., "Characterization of Titanium Matrix Composites," NASP Technical Memorandum 1199, National Institute for the Mechanics and Life Prediction of High Temperature Composites, Vol. I, April 1995.

[13] Aboudi, J., Pindera, M.-Z., and Arnold, S. M., "Elastic Response of Metal Matrix Composites with Tailored Microstructures to Thermal Gradients," *International Journal of Solids and Structures*, Vol. 31, No. 10, 1994, pp. 1393–1428.

[14] Jeong, G. S., Allen, D. H., and Lagoudas, D. C., "Residual Stress Evolution Due to Cool Down in Viscoplastic Metal Matrix Composites," *International Journal of Solids and Structures*, Vol. 31, No. 19, 1994, pp. 2653–2677.

[15] Pindera, M.-J., Freed, A. D., and Arnold, S. M., "Effects of Fiber and Interfacial Layer Morphologies on the Thermoplastic Response of Metal Matrix Composites," *International Journal of Solids and Structures*, Vol. 30, No. 9, 1993, pp. 1213–1238.

[16] Du, Z. Z. and McMeeking, R. M., "Creep Models for Metal Matrix Composites with Long Brittle Fibers," *Journal of the Mechanics and Physics of Solids*, Vol. 43, No. 5, May 1995, pp. 701–726.

[17] Du, Z. Z., McMeeking, R. M., and Schmauder, S., "Transverse Yielding and Matrix Flow Past the Fibers in Metal Matrix Composites," *Mechanics of Materials*, Vol. 21, No. 2, Aug. 1995, pp. 159–167.

[18] Lissenden, C. J., Herakovich, C. T., and Pindera, M.-J., "Inelastic Deformation of Metal Matrix Composites," Applied Mechanics Program Report Am-93-03, School of Engineering and Applied Science, University of Virginia, Charlottesville, 1993.

[19] Aboudi, J., "Micromechanical Prediction of Initial and Subsequent Yield Surfaces of Metal Matrix Composites," *International Journal of Plasticity*, Vol. 6, 1990, pp. 471–484.

[20] Allen, D. H., Jones, R. H., and Boyd, J. G., "Micromechanical Analysis of a Continuous Fiber Metal Matrix Composite Including the Effects of Matrix Viscoplasticity and Evolving Damage," *Journal of the Mechanics and Physics of Solids*, Vol. 42, No. 3, 1994, pp. 502–529.

[21] Allen, D. H., Helms, K. L. E., Hurtado, D. L., and Lagoudas, D. C., "Prediction of Damage Evolution in Continuous Fiber Metal Matrix Composites Subjected to Fatigue Loading," *Proceedings*, Symposium on Recent Developments in Engineering Science, Society of Engineering Science (SES) 32nd Annual Technical Meeting, New Orleans, 29 Oct.–1 Nov. 1995, submitted for publication.

[22] Neu, R. W. and Nicholas, T., "Thermomechanical Fatigue of SCS-6/Timetal 21S Under Out-of-Phase Loading," *Proceedings*, 1993 ASME Winter Annual Meeting, New Orleans, American Society of Mechanical Engineers, 28 Nov.–3 Dec. 1993.

[23] Lagoudas, D. C., Ma, X., Miller, D. A., and Allen, D. H., "Modelling of Oxidation in Metal Matrix Composites," *International Journal of Engineering Science*, accepted for publication.

[24] Xu, S., Lagoudas, D. C., and Allen, D. H., "Impact on Surface Oxidation on Damage Evolution in Metal Matrix Composites," *Micromechanics and Constitutive Modeling of Composite Materials*, H. M. Zbeb, I. Demir, and H.-T. Zhu, Eds., AMD-Vol. 202, MD-Vol. 01, American Society of Mechanical Engineers, 1995, pp. 77–101.

[25] Lagoudas, D. C., Allen, D. H., and Ma, X., "Modeling of Surface Oxidation and Oxidation Induced Damage in Metal Matrix Composites," *Computational Material Modeling, AD-Vol. 42, PVP-Vol.*

294, A. K. Noor and A. Needleman, Eds., American Society of Mechanical Engineers, New York, 1994, pp. 245–264.

[*26*] Wittig, L. A. and Allen, D. H., "Modeling the Effect of Oxidation on Damage in SiC/Ti-15-3 Metal Matrix Composites," *Journal of Engineering Materials and Technology*, Vol. 116, July 1994, pp. 421–427.

[*27*] Hurtado, L. D. and Allen, D. H., "Effect of Oxidation on Damage Evolution in Titanium Matrix MMC's," *Proceedings*, Symposium on Inelasticity and Micromechanics in Metal Matrix Composites, Twelfth U.S. National Congress of Applied Mechanics, Seattle, 26 June–1 July 1994.

[*28*] Chan, K. S., Bodner, S. R., and Lindholm, U. S., "Phenomenological Modeling of Hardening and Thermal Recovery in Metals," *Journal of Engineering Materials and Technology*, Jan. 1988, pp. 1–8.

[*29*] Arnold, S. M., Saleeb, A. F., and Castelli, M. G., "A Fully Associative, Non-Linear Kinematic, Unified Viscoplastic Model for Titanium Based Matrices," NASA Technical Report TM-106609, Cleveland, OH, March 1994.

[*30*] Neu, R. W., "Nonisothermal Material Parameters for the Bodner-Partom Model," *Proceedings*, ASME Winter Annual Meeting, New Orleans, American Society of Mechanical Engineers, 28 Nov.–3 Dec. 1993.

[*31*] Zuiker, J. R. and Sanders, B. P., "Analysis of Pinned Joints in Viscoplastic Monolithic Plates," *Numerical Implementation and Application of Constitutive Models in the Finite Element Method*, J. A. Sherwood, Ed., ASME-AMD-XX, American Society of Mechanical Engineers, New York, submitted for publication.

[*32*] Neu, R. W. and Bodner, S. R., "Determination of the Material Constants of Timetal 21S for a Constitutive Model," internal report, Wright Laboratory Materials Directorate, Wright-Patterson AFB, OH, Sept. 1995.

[*33*] Wallace, T. A., Wiedemann, K. E., and Clark, R. K., "Oxidation Characteristics of Beta-21S in Air in the Temperature Range 600 to 800°C," NASA Technical Memorandum 104217, NASA, Hampton, VA, 1992.

[*34*] Ignatov, D. V., Model, M. S., Sokyriansky, L. F., and Shinyaev, A. Y., *Titanium Science and Technology*, Vol. 4, R. I. Jaffee and H. M Borte, Eds., Plenum Press, New York, 1973, p. 2535.

[*35*] Parris, W. M. and Bania, P. J., "Oxygen Effects on the Mechanical Properties of TIMETAL 21S," *Proceedings*, Seventh World Conference on Titanium, San Diego, June 1992, The Minerals, Metals, & Materials Society, Warrendale, PA.

[*36*] Imam, M. A. and Feng, C. R., "Effects of Oxygen on Microstructure and Properties of Timetal 21S," *Microstructure/Property Relationships of Titanium Alloys*, S. Ankem and J. A. Hall, Eds., The Minerals, Metals, & Materials Society, Warrendale, PA, 1994, pp. 107–114.

[*37*] Wallace, T. A., Bird, R. K., and Wiedemann, K. E., "The Effect of Oxidation on the Mechanical Properties of Beta-21S," *Beta Titanium Alloys in the 1990's*, D. Eylon, R. R. Boyer, and D. A. Koss, Eds., The Minerals, Metals, & Materials Society, Warrendale, PA, 1993, pp. 115–126.

[*38*] Welsch, G. and Bunk W., "Deformation Modes of the α-Phase of Ti-6Al-4V as a Function of Oxygen Concentration and Aging Temperature," *Metallurgical Transactions A*, Vol. 13A, May 1982, pp. 889–899.

[*39*] Rath, B. B., Damkroger, B. K., Imam, M. A., and Edwards, G. R., "High Temperature Ductility Loss in Titanium Alloy—A Review," *Microstructure/Property Relationships of Titanium Alloys*, S. Ankem and J. A. Hall, Eds., The Minerals, Metals & Materials Society, Warrendale, PA, 1994, pp. 3–15.

[*40*] Chan, K. S., "Microstructure/Fatigue Crack Growth Relationships in Titanium Alloys and Aluminides," *Microstructure/Property Relationships of Titanium Alloys*, S. Ankem and J. A. Hall, Eds., The Minerals, Metals & Materials Society, Warrendale, PA, 1994, pp. 303–313.

[*41*] Foulk, J. W., Helms, K. L. E., and Allen, D. H., "A Computational Finite Element Analysis for Predicting the Effects of Environmental Degradation on Life in Metal Matrix Composites," *Proceedings*, Symposium on Recent Developments in Engineering Science, Society of Engineering Science (SES) 32nd Annual Technical Meeting, New Orleans, 29 Oct.–1 Nov. 1995.

[*42*] Ghonem, H., Wen, Y., and Zheng, D., "An Interactive Simulation Technique to Determine the Internal Stress States in Fiber Reinforced Metal Matrix Composites," *Materials Science and Engineering*, Vol. A177, 1994, pp. 125–134.

[*43*] Castelli, M. G., "Thermomechanical Fatigue Damage/Failure Mechanisms in SCS-6/Timetal 21S $[0/90]_S$ Composite," *Composites Engineering*, submitted for publication.

[*44*] Revelos, W. C., Jones, J. W., and Dolley, E. J., "Thermal Fatigue of a SiC/Ti-15 Mo-2.7 Nb-3 Al-0.2 Si Composite," *Characterization of Titanium Matrix Composites: Volume II—Mechanical Behavior and Damage Tolerance of TMC's*, NASP Technical Memorandum 1199, National Institute for the Mechanics and Life Prediction of High Temperature Composites, J. Larsen, B. Sanders, M. L. Gambone, and M. Khobaib, Eds., June 1995, pp. 76–115.

[45] Castelli, M G., "Isothermal Damage and Fatigue Behavior of SCS-6/TIMETAL 21S $[0/90]_S$ Composite at 650°C," Contractor Report 195345, NASA, Cleveland, OH, June 1994.
[46] Castelli, M. G., "An Advanced Test Technique to Quantify Thermomechanical Fatigue Damage Accumulation in Composite Materials," *Journal of Composites Technology and Research*, Oct. 1994.
[47] Allen, D. H., "A Review of the Theory of Thermomechanical Coupling in Inelastic Solids," *Applied Mechanics Reviews*, American Society of Mechanical Engineers, Vol. 44, No. 8, 1991, pp. 361–373.
[48] Needleman, A., "A Continuum Model for Void Nucleation by Inclusion Debonding," *Journal of Applied Mechanics*, Vol. 54, 1987, pp. 525–531.
[49] Tvergaard, V., "Micromechanical Modeling of Fibre Debonding in a Metal Reinforced by Short Fibres," *Proceedings, Inelastic Deformation of Composite Materials*, G. J. Dvorak, Ed., Springer-Verlag, New York, 1990, pp. 99–111.
[50] Tvergaard, V. and Hutchinson, J. W., "The Influence of Plasticity on Mixed Mode Interface Toughness," *Journal of the Mechanics and Physics of Solids*, Vol. 41, No. 6, 1993, pp. 1119–1135.
[51] Lo, D. C. and Allen, D. H., "Modeling of Delamination Damage Evolution in Laminated Composites Subjected to Low Velocity Impact," *International Journal of Damage Mechanics*, Vol. 3, No. 4, Oct. 1994, pp. 378–407.
[52] Constanzo, F. and Allen, D. H., "A Continuum Mechanics Approach to Some Problems in Subcritical Crack Propagation," *International Journal of Fracture*, Vol. 63, No. 1, 1993, pp. 27–57.
[53] Constanzo, F. and Allen, D. H., "A Continuum Thermodynamics Analysis of Cohesive Zone Models," *International Journal of Engineering Science*, accepted for publication.

Jinghong Fan[1]

In Situ Damage Progression in General Layup Composites

REFERENCE: Fan, J., **"In Situ Damage Progression in General Layup Composites,"** *Applications of Continuum Damage Mechanics to Fatigue and Fracture, ASTM STP 1315*, D. L. McDowell, Ed., American Society for Testing and Materials, 1997, pp. 46–64.

ABSTRACT: In this paper, a methodology for progressive matrix cracking-delamination interaction is proposed. Two damage variables and a five-layer equivalent constraint model (ECM) are introduced. After a mesoscopic stress analysis is conducted for the ECM, concepts of continuum damage mechanics are applied to obtain the effective moduli by the approach proposed by Fan and Zhang in 1993. The critical matrix cracking densities at which the transition from matrix cracking to delamination occurs are found to be dependent on the number of plies of the weakest layer and almost independent of the layups. These numerical results of general layups are consistent with those obtained by Nairn and Hu in 1992 for cross-ply laminates. Results also show connections between the calculated energy release rates with the experimental data of the least required energy for damage initiation of T300/976 composite beams.

KEYWORDS: continuum damage mechanics, cracking, fatigue (materials), fracture (materials), constraint effects, general layup composites, in situ damage effective factor, mesoscopic analysis, macroscopic analysis, five-layer model

The predominant characteristics of damage progression in laminated composites are the important internal constraint effects that exist between different layers. These effects can be better understood if we look at the experimental results given by Timmer and Hahn [*1*]. Their tests were conducted on a quasi-isotropic $[0°{\pm}45°/90°]_{3s}$ laminate of AS4/3501-6 graphite/epoxy composites. Matrix cracking in the 90° layers occurred first, followed by matrix cracking in the −45° layers, but there was no matrix cracking at all in the 45° layers. To find the reason for this phenomenon, the constraint conditions of 45° layers and −45° layers were checked. From their tests, we could see that the 45° layer and −45° layer were constrained directly by the strongest 0° layers and the weakest 90° layers, respectively. The much stronger internal constraint effects on the 45° layers than that on the −45° layers make damage initiation difficult in the 45° layer.

In the past 20 years, there have been intensive research activities in damage analysis of composite materials. Different damage models have been proposed such as various kinds of shear lag models, variational approaches, a self-consistent scheme, an approximate elasticity approach, an internal variable method, and an approximate elasticity approach. The reader is suggested to refer to Ref 2. Here, only selected papers are reviewed to save the space. In the 1970s, Garrett and Bailey [*3*] and Highsmith and Reifsnider [*4*] used one-dimensional shear-lag models to consider stiffness reduction in cross-ply laminates due to transverse matrix cracking. The internal constraint effects on damage progression of the 90° plies were quantified

[1] Professor and visiting scholar from the Department of Engineering Mechanics, Chongging University; The George W. Woodruff School of Mechanical Engineering, Georgia Institute of Technology, Atlanta, GA 30332-0405.

under the assumption that the applied stress is transferred to the 90° plies from the constraining layers through shear deformation. In the formulation, some adjustable parameter related to the shear transfer layer was needed. Flaggs [*5*] developed a two-dimensional shear-lag model for investigating the constraint effects of $\pm\theta^{\circ}$ layers on 90° layers. The initiation strain of transverse matrix cracking in the 90° layer was predicted well, but the evolution of matrix cracking was not considered. Hashin [*6–8*] developed a variational approach for the analysis of the $[0^{\circ}/90^{\circ}_{n}]_{s}$ laminate. In this work, the constraint effect was found to be dependent on the ply elastic moduli and ply thickness. Hashin's methodology has been proved to be an essential contribution in micromechanics-based damage analysis, and several recent works such as Praveen and Reddy [*9*], Varna and Berglund [*10*], and Narin [*11*], and Narin and Hu [*12*] are the extensions of Hashin's. However, the premise of Hashin's approach is based on cross-ply laminates. Therefore, an extension of this scheme to general layups appears to be intractably complicated. Pagano [*13,14*] developed a method for layer and inter-layer stress analysis based on the Reissner variational principle. This work currently has been applied to delamination and matrix cracking of cross-ply layups [*15*]. Other work, such as Gudmundson and Zhang [*16*], used known analytical solutions such as a row of cracks in a finite isotropic medium for damage analysis of cross-ply and angle-ply layups, but these analytical solutions are of limited applicability to composite laminates. There are also several models for delamination analysis [*17–20*]. However, these models were mostly developed for fixed geometry of cracks, and the interactive damage evolution between matrix cracking and delamination are seldom investigated. This situation is more clearly described by Lagace [*21*], "Clear procedure do not exist to predict the observed interacting growth of in-plane and out-of-plane damage modes and for the prediction of the overall load-carrying capability of the configuration." Choi, Downs, and Chang [*22*] developed an empirical relationship for the internal constraint effects. However, some of their model prediction is higher than the test data, some is lower. There is no definite trend.

In summary, most existing damage models are only suitable for cross-ply layups and without considering interactive damage progression. Since cross-ply laminates are of limited use in engineering applications, new approaches that can analysis in situ damage progression of general layup composites are technically important. In this paper, a new methodology for damage analysis of an arbitrary ply of general layups is proposed. This approach is centered about the internal constraint effects through an introduction of the five-layer equivalent constraint damage model. Theoretical development is based on continuum damage mechanics by the introduction of two damage variables and by obtaining the effective properties of damaged layers through a volume averaging procedure to determine the in situ damage effective factors. Numerical results for T300/976 graphite/epoxy (Gr/Ep) are then introduced and discussed.

A Five-Layer Equivalent Constraint Model (ECM)

The central problem of modeling general layup composites is to develop a method for damage analysis of a generic ply, k, with a ply angle, $\theta^{(\kappa)}$, between the ply coordinate axis, $x_i^{(k)}$, and the laminate coordinate axis, X_I (Fig. 1). If this can be done, then the damage analysis for any other ply can be dealt with similarly. To focus our effort, this work will concentrate on this damage analysis. In this regard, two things are important to make this analysis much simpler. One is to develop an equivalent constraint model to replace the complicated laminate structure for investigating the constraint effects. The other is to emphasize the important role of the ply coordinates, $x_i^{(k)}$ (with a prime in the subscript, or with x, y as coordinates that are also used to denote the local coordinates for convenience, see Fig. 1), in the analysis of an arbitrary ply, k. Actually, this generic ply, k, as any other ply can be viewed as "a local 90° layer" with respect to its ply coordinate system $x_i^{(k)}$.

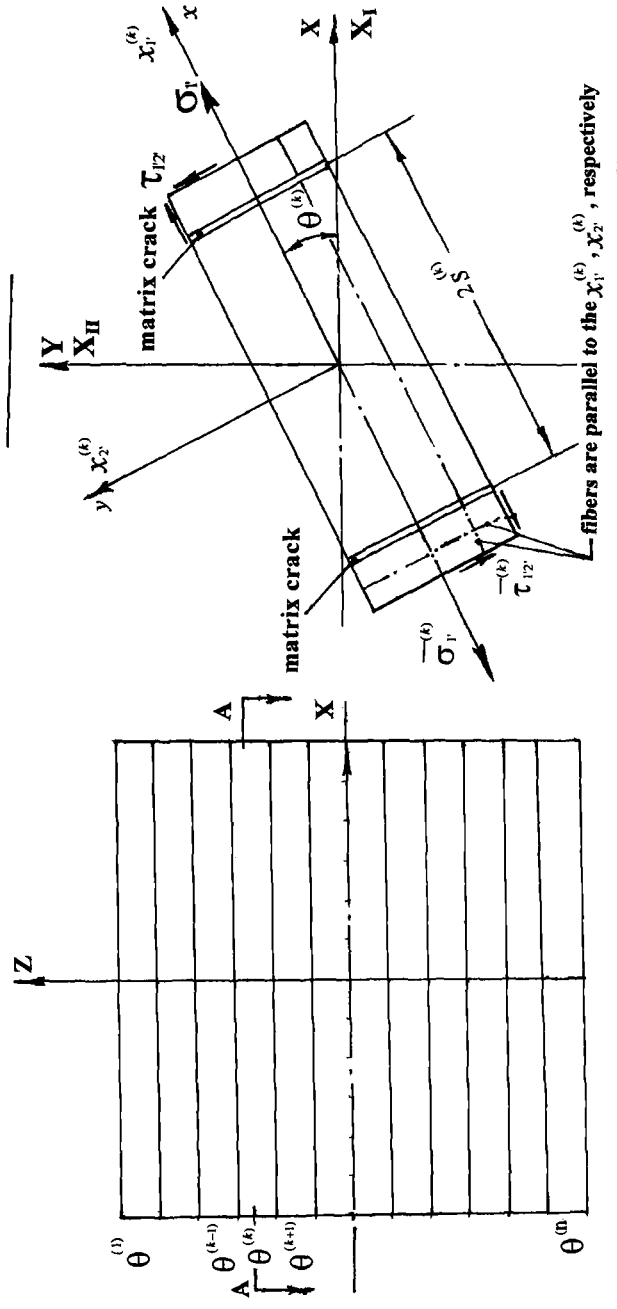

FIG. 1—*A generic ply,* k, *is viewed as a "local 90° layer" with respect to its ply coordinates,* $x_{1'}^{(k)}$.

TABLE 1—*Layup effects on the least required damage initiation energy,* $E^{initiation}$, *(data obtained from test curves of Fig. 13 of Chou et al.* [22].

Layup Type	Material Type	Layups	$E^{initiation}$, J/m[a]
A	T300/976 Gr/Ep	$[0_3^\circ/90_3^\circ/0_3^\circ/90_{1.5}^\circ]_s$	415
B	T300/976 Gr/Ep	$[0_4^\circ/\pm 45_4^\circ/90_2^\circ]_s$	190
C	T300/976 Gr/Ep	$[0_6^\circ/\pm 45_4^\circ/90_5^\circ]_s$	55
D	T300/976 Gr/Ep	$[90_3^\circ/0_3^\circ/90_3^\circ]$	75

[a] Line loading is assumed to calculate the impact energy.

A scrutiny of the experimental results in Ref *1* and the test data in Table 1 that are obtained from the test curves of Ref *22* suggests an approximate correlation between the internal constraint effects and layups. First, the internal constraint effects highly depend on the geometry of the weakest ply under consideration. The thicker the 90° layers, the less the required energy for damage initiation (see the comparison between the Layups B and C). Second, the very important role of the adjacent layer on the damage initiation in the weakest layer can be observed. The stronger the adjacent layer, the larger damage resistance can be obtained through constrained forces offered by adjacent layers (see the test result of Timmer and Hahn [*1*] and Layup A of Table 1). In addition, these constraint effects depend weakly on the geometry of the remote constraint layers. To emphasize the important roles of the weakest layer and the adjacent layer, these layers are totally included in the five-layer model. More specifically, all the geometric and material parameters of the weakest layer and the adjacent layers, such as the thickness ($h^{(k-1)}$, $h^{(k)}$, $h^{(k+1)}$), ply angles ($\theta^{(k-1)}$, $\theta^{(k)}$, $\theta^{(k+1)}$), and stiffness ($\bar{Q}_{ij}^{(k-1)}$, $\bar{Q}_{ij}^{(k)}$, $\bar{Q}_{ij}^{(k+1)}$), are considered in the five-layer ECM. However, the remaining layers will be handled in an approximate manner. This is because experimental results show relatively weak dependence of the constraint effects on remote layers, and also because of the advantages regarding a compromise of relative accuracy and simplicity. Specifically, all remaining plies above and below the adjacent layers of ply groups $(k-1)$ and $(k+1)$, respectively, will be lumped into two equivalent homogeneous anisotropic layers, that is, an upper group, I_k, and a lower group, II_k. In general, this consideration results in a five-layer ECM for a generic damaged layer, k. The five layers are: the kth ply itself, two adjacent layers $(k-1)$ and $(k+1)$, and the remote equivalent layers, I_k and II_k (see Fig. 2).

Since the analysis for the kth ply is performed as the analysis for a "local 90° layer" with respect to its ply coordinate system, $x_i^{(k)}$, it is advantageous to express the stiffness of the five layers also related to these ply coordinates. To do so, coordinate transformations from corresponding coordinates such as $x_{i'}^{(k+1)}$ and $x_{i'}^{(k-1)}$ to the local coordinate system, $x_{i'}^{(k)}$, are necessary. For the two remote equivalent constraint layers, it is convenient to obtain their average stiffness, $\bar{Q}_{ij}^{(Ik)}$ and $\bar{Q}_{ij}^{(IIk)}$, with respect to the laminate coordinates, X_I, first, and then integrally transform to the ply coordinate system, $x_i^{(k)}$. It may be noted that the five-layer ECM can be degenerated to a four-layer or a three-layer ECM when the generic kth layer approaches or becomes the top (or bottom) layer.

Quantitative Measures for Internal Constraint Effects

In this paper, the theory of the overall moduli of a cracked body contributed by several researchers, namely, Valuenko and Kachanov [*23*], Budiansky and O'Connell [*24*], and Horii and Nemat-Nasser [*25*], is applied to formulate the basic relationship between damage param-

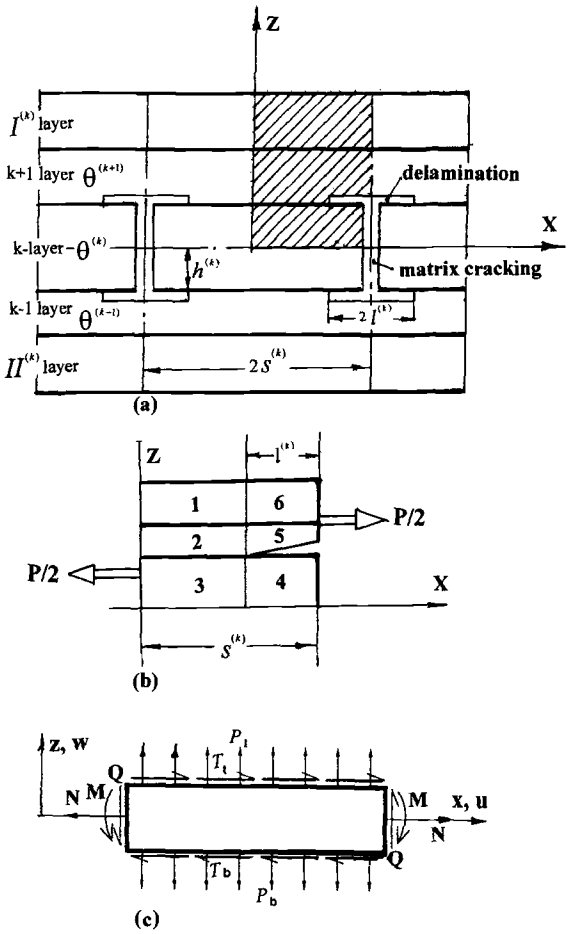

FIG. 2—*Five-layer equivalent constraint model (ECM) and the representative unit cell:* (a) *five layer-model* (b) *a quarter of the unit cell, and* (c) *a generic sublaminate.*

eters and the effective moduli of the damaged layers. Following this theory, the overall compliance tensor, $\bar{S}_{ijkl}$, of a cracked body can be expressed as

$$\bar{S}_{ijkl} = S^0_{ijkl} + \bar{H}_{ijkl} \tag{1}$$

Here, Superscript 0 denotes components of material without damage, thus S^0_{ijkl} is the original compliance tensor of the homogeneous media. $\bar{H}_{ijkl}$ is the increase of compliance induced by damage whose values depend on crack distribution and configuration. This is an elegant theory, since it can be used for a body with finite volume under general loading. However, the premise of this theory is that the media must be homogeneous. This premise makes it difficult to directly apply this theory to laminates because laminates are highly inhomogeneous media with layers in different directions. Due to this fundamental difficulty, to the author's knowledge, there has been no relationship between this elegant theory and damage analysis of laminated composites until the work given by the present author and his co-workers for cross-ply and $[\pm\theta_m/90_n]_S$ layups [26–29].

In this work, each individual ply is considered as an effective homogeneous anisotropic media with matrix crack and delamination. Consequently, the theory can be suitably applied to any individual ply separately. Employing the truncated notation related to the ply coordinate system, $x_{i'}^{(k)}$, one expresses the relationship of average stress and average strain, as well as Eq 1, respectively, as

$$\bar{\sigma}_{i'}^{(k)} = \bar{Q}_{i'j'}^{(k)} \bar{\varepsilon}_{j'}^{(k)} \tag{2a}$$

$$\bar{S}_{i'j'}^{(k)} = S_{i'j'}^{0(k)} + \bar{H}_{i'j'}^{(k)} \tag{2b}$$

where $\bar{Q}_{i'j'}^{(k)}$ is the effective in-plane stiffness matrix of the damaged ply, the determination of which is the main concern of this formulation. For the damage mode of transverse matrix cracking and local delamination with respect to its local coordinate, $x_{i'}^{(k)}$ (see Fig. 1), it can be proved that only $\bar{H}_{1'1'}^{(k)}$ and $\bar{H}_{6'6'}^{(k)}$ are not zero, and we have

$$S_{1'1'}^{(k)} = S_{1'1'}^{0(k)} + \bar{H}_{1'1'}^{(k)},\ S_{6'6'}^{(k)} = S_{6'6'}^{0(k)} + \bar{H}_{6'6'}^{(k)},\ S_{2'2'}^{(k)} = S_{2'2'}^{0(k)},\ S_{1'2'}^{(k)} = S_{1'2'}^{0(k)}$$

Furthermore, using the relationship between $S_{i'j'}^{(k)}$ and $\bar{Q}_{i'j'}^{(k)}$ for an orthotropic lamina (see Eqs 2.60 of Ref *30*), the effective stiffness matrix can be obtained as follows

$$\begin{bmatrix} Q_{1'1'}^{(k)} & Q_{1'2'}^{(k)} & 0 \\ Q_{2'1'}^{(k)} & Q_{2'2'}^{(k)} & 0 \\ 0 & 0 & Q_{6'6'}^{(k)} \end{bmatrix} = \begin{bmatrix} Qo_{1'1'}^{(k)} & Qo_{1'2'}^{(k)} & 0 \\ Qo_{2'1'}^{(k)} & Qo_{2'2'}^{(k)} & 0 \\ 0 & 0 & Qo_{6'6'}^{(k)} \end{bmatrix} - \begin{bmatrix} Qo_{1'1'}^{(k)} \Lambda_{1'1'}^{(k)} & Qo_{1'2'}^{(k)} \Lambda_{1'1'}^{(k)} & 0 \\ Qo_{1'2'}^{(k)} \Lambda_{1'1'}^{(k)} & \dfrac{(Qo_{1'2'}^{(k)})^2 \Lambda_{1'1'}^{(k)}}{Qo_{1'1'}^{(k)}} & 0 \\ 0 & 0 & Qo_{6'6'}^{(k)} \Lambda_{6'6'}^{(k)} \end{bmatrix} \tag{3}$$

in which the $\Lambda_{i'j'}^{(k)}$ directly relate to $\bar{H}_{1'1'}^{(k)}$ and $\bar{H}_{6'6'}^{(k)}$ as follows

$$\Lambda_{1'1'}^{(k)} = \frac{Q_{1'1'}^{0(k)} \bar{H}_{1'1'}^{(k)}}{1 + Q_{1'1'}^{0(k)} W_{1'1'}^{(k)}},\ \Lambda_{6'6''}^{(k)} = \frac{Q_{6'6''}^{0(k)} \bar{H}_{6'6'}^{(k)}}{1 + Q_{6'6'}^{0(k)} W_{6'6'}^{(k)}}$$

The second matrix of Eq 3 denotes the stiffness reductions caused by damage. From the expressions of their components, we see that the reduced stiffnesses are expressible by means of just two factors, $\Lambda_{1'1'}^{(k)}$ and $\Lambda_{6'6'}^{(k)}$. It is important to notice that these two factors depend not only on the in situ damage state, but also on the internal constraint effects. This is because these factors correlate the average stress and average strain according to (see Eqs 2*a* and 3)

$$\Lambda_{1'1'}^{(k)} = 1 - \frac{\bar{\sigma}_{1'}^{(k)}}{Q_{1'1'}^{0} \bar{\varepsilon}_{1'}^{(k)} + Q_{1'2'}^{0} \bar{\varepsilon}_{2'}^{(k)}} \tag{4a}$$

$$\Lambda_{6'6'}^{(k)} = 1 - \frac{\bar{\sigma}_{6'6'}^{(k)}}{Q_{6'6'}^{0} \bar{\gamma}_{6'6'}^{(k)}} \tag{4b}$$

On the other hand, the constraint forces applied at the contact surfaces will change the average stress and average strain in the *k*th ply and, in turn, these constraint effects will change the

values of these factors. Therefore, these factors are functions of the in situ internal constraint conditions. From the preceding discussions, we see the two factors that determine the constraint effects through the second matrix of Eq 3. Therefore, it will be taken as quantitative measures for the internal constraint effects on all-ply stiffness reductions of an arbitrary ply. These measures are renamed as IDEF, short for the in situ damage effective factors. Since all quantities used later are related to the ply coordinates, $x_i^{(k)}$, the prime in the subscript will be dropped from now on.

Determination of the In Situ Damage Effective Factors (IDEFs)

In this work, a unit cell that represents a specific distribution and configuration of damage state within the kth ply is taken from the five-layer ECM (Fig. 2). Two damage variables are introduced. They are the normalized matrix crack density, $C_d^{(k)} = t/S^{(k)}$, and the normalized delamination length, $D^{(k)dl} = l^{(k)}/S^{(k)}$, where t denotes ply thickness, and $l^{(k)}$ and $S^{(k)}$ are one half of the local delamination length and one half of the interval between two transverse matrix cracks, respectively, as can be seen in Fig. 2*a*. The important thing is to carry on a homogenization process to obtain the effective in-plane stiffness matrix, $\bar{Q}_{i'j'}^{(k)}$ through the determination of the IDEF. A meso/macroscopic approach is then introduced for this purpose. From a mesoscopic point of view, the task is to determine the stress and strain distribution in the unit cell under applied loading. The stress analysis for this unit cell involves a formulation of approximate boundary value problems (BVP) for fixed geometries. From a macroscopic point of view, the homogenization process is realized through a volume average of mesoscopic stress and strain in the damaged ply. Having had the distributions of the stress, $\sigma_y^{(k)}$, and strain, $\varepsilon_y^{(k)}$, in the ply, k, the volume average of stress and strain over the volume, $v^{(k)}$, can be obtained by the following volume averages

$$\bar{\sigma}_x^{(k)} = \frac{1}{v^{(k)}} \int_{v^{(k)}} \sigma_x^{(k)}\, dv \quad \bar{\varepsilon}_x^{(k)} = \frac{1}{v^{(k)}} \int_{v^{(k)}} \varepsilon_x^{(k)}\, dv \tag{5a,b}$$

$$\bar{\sigma}_{xy}^{(k)} = \frac{1}{v^{(k)}} \int_{v^{(k)}} \sigma_{xy}^{(k)}\, dv, \quad \bar{\varepsilon}_y^{(k)} = \frac{1}{v^{(k)}} \int_{v^{(k)}} \varepsilon_y^{(k)} \tag{5c,d}$$

$$\bar{\gamma}_{xy}^{(k)} = \frac{1}{v^{(k)}} \int_{v^{(k)}} \gamma_{xy}^{(k)}\, dv \tag{5e}$$

Now, by substituting the average stress and strain into Eqs 4*a* and *b*, explicit closed-form solutions for the IDEF can be obtained. To exemplify the proposed approach and to avoid lengthy mathematical descriptions, in the following discussion, a problem of transverse matrix cracking-local delamination interaction of a symmetric five-layer ECM under the tensile applied loading will be analyzed. The unsymmetric analysis will be published elsewhere.

Matrix Cracking-Local Delamination Interaction for a Symmetric Five-Layer ECM

Here, local delamination denotes the interfacial cracks originate from transverse matrix cracks in the "local 90°-ply." Plane-strain conditions are assumed, and strain in the thickness direction is neglected. In this case, only one quarter of that model is needed for mesoscopic

analysis. This quarter is shown in a shield area in Fig. 2 and can be divided into six sublaminates in which Sublaminates 3, 4 denote the 90° layers. Sublaminates 2, 5 are the adjacent layers, and Sublaminates 1, 6 are the homogeneous remote layers (Fig. 2*b*). The analysis for each sublaminate will be conducted by the first-order plate theory. This stress analysis was used previously for a two-layer unit cell by Armanios et al. [*17*]. Following their formulation, a generic sublaminate is shown in Fig. 2*c*. Where resultants of tensile stress, shear stress, and bending moment are denoted by N, Q, and M, respectively. The peel and interlaminal shear stresses are denoted by P and T, with t and b subscripts for the top and bottom surfaces, respectively. The basic equations are listed as follows.

Displacement Field—Let u and w denote displacements relative to the x and z axes, and U and W represent the axial midplane stretching and transverse displacement, respectively, and β is the rotation. The displacement field is described as

$$u(x,z) = U(x) + z\beta(x),\ w(x,z) = W(x) \tag{6a,b}$$

ε_z is neglected and w is zero along the center horizontal line of the unit cell, therefore, transverse displacement, w, and its derivative $w_{,x}$, are zero in Sublaminates 1, 2, 3, and 4.

Equilibrium Equations—The z-axis is located at the central line between two transverse cracks. The equilibrium equations take the form (see Fig. 2*c*)

$$N_{,x} + T_t - T_b = 0,\ Q_{,x} + P_t - P_b = 0,\ M_{,x} - Q + \frac{h}{2}(T_t + T_b) = 0 \tag{7a,b,c}$$

in this paper, the Subscripts ,x and ,xx following a variable such as $N_{,x}$, $N_{,xx}$ denote the first and second derivatives of N with respect to the x-coordinate, respectively.

Constitutive Equations in Terms of Forces and Moments—

$$N = A_{11}U_{,x} + B_{11}\beta_{,x},\ Q = A_{55}(\beta + w_{,x}),\ M = B_{11}U_{,x} + D_{11}\beta_{,x} \tag{8a,b,c}$$

Where A_{ij}, B_{ij}, and D_{ij} are the stretching, coupling, and bending stiffness of the classical laminate theory, respectively.

Now, analyses will be conducted through the following three groups: Group I includes Sublaminates 1, 2, and 3; Group II contains Sublaminates 5 and 6; and Group III refers to Sublaminate 4. The common procedure for formulating governing equations is to obtain relationships between interfacial forces (T_t, T_b) and displacements (β, U, w) through combining Eqs 7*a* and *c* with Eqs 8*a*, *b*, and *c*). Then, continuity conditions of displacements and reciprocal relationships of forces at the interfaces of Groups I and II are used to obtain governing equations for $\beta^{(i)}$ ($i = 1 - 5$). For Group III, there is only one layer. Its governing equations for $M^{(4)}$ can be easily obtained. Let the exponential parameters represent the eiginvalues, λ, ω, and δ, for Groups I, II, and III, respectively, with the main results as follows.

(a) Group I: Sublaminates 1, 2, and 3—The governing equations are

$$\begin{bmatrix} a_{11} & a_{12} & a_{13} \\ a_{21} & a_{22} & a_{23} \\ a_{31} & a_{32} & a_{33} \end{bmatrix} \begin{Bmatrix} \beta^{(1)}_{,xx} \\ \beta^{(2)}_{,xx} \\ \beta^{(3)}_{,xx} \end{Bmatrix} - \begin{bmatrix} A^{(1)}_{55} & 0 & 0 \\ 0 & A^{(2)}_{55} & 0 \\ 0 & 0 & A^{(3)}_{55} \end{bmatrix} \begin{Bmatrix} \beta^{(1)} \\ \beta^{(2)} \\ \beta^{(3)} \end{Bmatrix} = 0 \tag{9}$$

The first matrix is a symmetric matrix. Its elements, a_{ij}, are explicitly expressed in Appendix I. Suppose $\beta^{(i)} = \beta_0^{(i)} e^{\lambda x}$ $(i = 1,2,3)$, one obtains the following characteristic equations with $\overline{\lambda} = \lambda^2$

$$A\overline{\lambda^3} + B\overline{\lambda^2} + C\overline{\lambda} + D = 0 \tag{10a}$$

$$A = a_{11}a_{22}a_{33} + 2a_{12}a_{13}a_{23} - a_{12}^2 a_{33} - a_{23}^2 a_{11} - a_{13}^2 a_{22} \tag{10b}$$

$$B = -(a_{11}a_{22}A_{55}^{(3)} + a_{22}a_{33}A_{55}^{(1)} + a_{11}a_{33}A_{55}^{(2)} - a_{13}^2 A_{55}^{(2)} - a_{23}^2 A_{55}^{(1)} - a_{12}^2 A_{55}^{(3)}) \tag{10c}$$

$$C = a_{11}A_{55}^{(2)}A_{55}^{(3)} + a_{22}A_{55}^{(1)}A_{55}^{(3)} + a_{33}A_{55}^{(1)}A_{55}^{(2)},\ D = -A_{55}^{(1)}A_{55}^{(2)}A_{55}^{(3)} \tag{10d,e}$$

The numerical calculations for carbon fiber-reinforced polymeric-matrix composites show that the six eigenvalues, $\pm\lambda_1$, $\pm\lambda_2$, and $\pm\lambda_3$, are all real, and the eigenvectors are $\alpha_j\{p_j^1, p_j^2, 1\}^T$ with α_j to be determined by boundary conditions and

$$\begin{Bmatrix} p_j^1 \\ p_j^2 \end{Bmatrix} = \frac{-\lambda_j^2}{(a_{11}\lambda_j^2 - A_{55}^{(1)})(a_{22}\lambda_j^2 - A_{55}^{(2)}) - a_{12}^2\lambda_j^4} \begin{Bmatrix} (a_{22}a_{13} - a_{12}a_{23})\lambda_j^2 - a_{13}A_{55}^{(2)} \\ (a_{11}a_{23} - a_{12}a_{13}\lambda_j^2 - a_{23}A_{55}^{(1)} \end{Bmatrix} \tag{11}$$

Since $W_{,x} = 0$, from Eq 8*b*, we have $Q = A_{55}\beta$. Therefore, shear deformation is recognized through the rotation, β. Furthermore, because the z-axis is taken at the symmetric vertical line of the unit cell (see Figs. 2*a* and *b*), Q is anti-symmetric and, in turn, β is antisymmetric about the z-axis. Mathematically, it reads

$$Q(x) = -Q(-x),\ \beta(x) = -\beta(-x) \tag{12a,b}$$

Combining this equation with the solution of Eq 9 turns out

$$\begin{Bmatrix} \beta_{(1)} \\ \beta_{(2)} \\ \beta_{(3)} \end{Bmatrix} = \sum_{j=1}^{3} \alpha_i \begin{Bmatrix} p_j^1 \\ p_j^2 \\ 1 \end{Bmatrix} \sinh(\lambda_j x) \tag{13}$$

(b) Group II: Sublaminates 5 and 6—Using the continuity condition at the interface between Sublaminate 5 and 6 and noticing the fact that $T_b^{(5)} = 0$, $P_b^{(5)} = 0$, $T_t^{(6)} = 0$, $P_t^{(6)} = 0$, the governing equation can be derived as

$$\begin{bmatrix} b_{11} & b_{12} \\ b_{12} & b_{22} \end{bmatrix} \begin{Bmatrix} \beta_{,xx}^{(5)} \\ \beta_{,xx}^{(6)} \end{Bmatrix} + \frac{A_{55}^{(1)} A_{55}^{(2)}}{A_{55}^{(1)} + A_{55}^{(2)}} \begin{bmatrix} -1 & 1 \\ 1 & -1 \end{bmatrix} \begin{Bmatrix} \beta^{(5)} \\ \beta^{(6)} \end{Bmatrix} = 0 \tag{14a}$$

where b_{11}, b_{12}, and b_{22} can be found in Appendix I. Assuming $\beta_j = \beta_j^0 e^{\omega x}$, the characteristic equation is obtained as

$$(b_{11}b_{22} - b_{12}^2)\omega^4 - \frac{A_{55}^{(1)} A_{55}^{(2)}}{A_{55}^{(1)} + A_{55}^{(2)}} (b_{11} + b_{22} - 2b_{12})\omega^2 = 0 \tag{14b}$$

The four eigenvalues are all real and can be written as follows

$$\omega_{1,2} = \pm\sqrt{\frac{A_{55}^{(1)}A_{55}^{(2)}(b_{11} + b_{22} - 2b_{12})}{(A_{55}^{(1)} + A_{55}^{(2)})(b_{11}b_{22} - b_{12}^2)}},\ \omega_{3,4} = 0 \tag{15a,b}$$

The related eigenvector is $\{q, 1\}^T$, with

$$q = -\frac{b_{12}(A_{55}^{(1)} + A_{55}^{(2)})\omega_j^2 + A_{55}^{(1)}A_{55}^{(2)}}{b_{11}(A_{55}^{(1)} + A_{55}^{(2)})\omega_j^2 - A_{55}^{(1)}A_{55}^{(2)}} \tag{16}$$

The solutions for Eq 14*a* are

$$\begin{Bmatrix} \beta^{(5)} \\ \beta^{(6)} \end{Bmatrix} = \theta_1 \begin{Bmatrix} q \\ 1 \end{Bmatrix} e^{\omega_1 x} + \theta_2 \begin{Bmatrix} q \\ 1 \end{Bmatrix} e^{-\omega_1 x} + \theta_3 \begin{Bmatrix} 1 \\ 1 \end{Bmatrix} \tag{17}$$

(c) Group III: Sublaminate 4—From Eqs 8*a*, *b*, and *c* and the boundary condition, we obtain

$$N_{ij}^{(4)} = 0 \tag{18}$$

$$M_{,xx}^{(4)} - \frac{A_{55}^{(4)}}{D_{11}^{(4)}} M^{(4)} = 0 \tag{19}$$

$$M^{(4)} = \Psi_1 e^{\delta x} + \Psi_2 e^{-\delta x} \tag{20}$$

with

$$\delta = \pm\sqrt{\frac{A_{55}^{(4)}}{D_{11}^{(4)}}}$$

Constants in Eqs 13, 17, and 20 are determined through boundary conditions at the boundary of the unit cell, $x = s^{(k)}$, and continuity conditions at $x = s^{(k)} - 1^{(k)}$ between sublaminates (see Fig. 2*b*). Combining these solutions with Eqs 7*a*, *b*, and *c* and Eqs 8*a*, *b*, and *c*, all interfacial forces, moment, and force resultants can be determined. Specific results are expressed as follows

$$N_x^{(1)} = \alpha_1\eta_1 \cosh(\lambda_1 x) + \alpha_2\eta_2 \cosh(\lambda_2 x) + \alpha_3\eta_3 \cosh(\lambda_3 x) + A_{11}^{(1)}\alpha_4 \tag{21a}$$

$$N_x^{(2)} = \alpha_1\eta_4 \cosh(\lambda_1 x) + \alpha_2\eta_5 \cosh(\lambda_2 x) + \alpha_3\eta_6 \cosh(\lambda_3 x) + A_{11}^{(2)}\alpha_5 \tag{21b}$$

$$N_x^{(3)} = -\alpha_1(\eta_1 + \eta_4) \cosh(\lambda_1 x) - \alpha_2(\eta_2 + \eta_5) \cosh(\lambda_2 x) - \alpha_3(\eta_3 + \eta_6) \cosh(\lambda_3 x) + A_{11}^{(3)}\alpha_6 \tag{21c}$$

$$N_x^{(5)} = \frac{0.5\, A_{11}^{(2)}\, P}{A_{11}^{(1)} + A_{(11)}^{(2)}} \tag{21d}$$

$$N_x^{(6)} = \frac{0.5\, A_{11}^{(1)}\, P}{A_{11}^{(1)} + A_{(11)}^{(2)}} \tag{21e}$$

where P is the applied loading, $\alpha_i (i = 1 - 6)$, $\eta_l, (l = 1 - 6)$ are explicitly expressed in Appendix II.

A Closed-Form Expression for the IDEF

For the case of matrix cracking-local delamination, the plane-strain conditions are assumed, resulting in $\bar{\varepsilon}_y = 0$ and $\bar{\varepsilon}_{xy} = 0$. In this case, only Λ_{11} is needed. When using Eq 4*a* to calculate

the IDEF, the compatibility conditions of average strain between different layers are used, that is

$$\bar{\varepsilon}_x^{(k)} = \bar{\varepsilon}_x^{(k+1)} = \bar{\varepsilon}_x^{(lk)} = \frac{\bar{N}_x^{(lk)}}{A_{11}^{(lk)}} \tag{22}$$

This allows one to replace $\bar{\varepsilon}_x^{(k)}$ with $\bar{N}_x^{(lk)}/A_{11}^{(lk)}$. It turns out that

$$\Lambda_{11}^{(k)} = 1 - \frac{A_{11}^{(lk)}\bar{N}_x^{(k)}}{A_{11}^{(k)}\bar{N}_x^{lk}} \tag{23}$$

$$\bar{N}_x^{(k)} = \left(\int_0^{s^{(k)}-t^{(k)}} N_x^{(3)}\,dx + \int_{s^{(k)}-t^{(k)}}^{s^{(k)}} N_x^{(4)}\,dx\right)\Big/ S^{(k)} \tag{24a}$$

$$\bar{N}_x^{(lk)} = \left(\int_0^{s^{(k)}-t^{(k)}} N_x^{(1)}\,dx + \int_{s^{(k)}-t^{(k)}}^{s^{(k)}} N_x^{(6)}\,dx\right)\Big/ S^{(k)} \tag{24b}$$

Substituting Eqs 18 and 21*a*, *c*, and *e* into Eqs 24*a* and *b* and, in turn, into Eq 23, we obtain

$$\Lambda_{11}^{(k)} = \frac{(1 + \Phi_1)[D^{(k)dl} + \Phi_2 D^{(k)mc} F_1(\chi)]}{1 + \Phi_1[D^{(k)dl} + \Phi_2 D^{(k)mc} F_1(\chi)]} \tag{25}$$

where Φ_1, Φ_2, and F_1 are functions of layups, geometric, and material parameters of the five layers. Their explicit forms are expressed in Appendix II. $D^{(k)mc}$ is another type of damage parameter for matrix crack density whose relationship with C_d can be expressed as $D^{(k)mc} = C_t h^{(k)}/t$. The independent variable, χ, in the function, $F(\chi)$, is defined as

$$\chi \equiv \frac{1 - D^{(k)dl}}{D^{(k)mc}} \tag{26}$$

that is a combined damage parameter of matrix cracking and delamination. The appearance of damage parameters, χ, $D^{(k)dl}$, and $D^{(k)mc}$, in the expression of the IDEF, $\Lambda_{11}^{(k)}$, denotes that the IDEF can be applied to investigate interactions of different damage modes.

Damage Evolution Law

If damage only occurs in the weakest 90° layer, the energy release rate for matrix cracking and delamination, respectively, are [*26*]

$$G^{(k)mc} = -h^{(k)} \frac{\partial \bar{Q}_{ij}^{(k)}}{\partial D^{(k)mc}} \bar{\varepsilon}_i^{(k)} \bar{\varepsilon}_j^{(k)}, \qquad r = 1,2...N \tag{26a}$$

$$G^{(k)dl} = -h^{(k)} \frac{\partial \bar{Q}_{ij}^{(k)}}{\partial D^{(k)dl}} \bar{\varepsilon}_i^{(k)} \bar{\varepsilon}_j^{(k)}, \qquad r = 1,2...N \tag{26b}$$

where $\bar{\varepsilon}_i^{(r)}$ are the average strains in the rth ply. From Eqs 26*a* and *b* and Eq 5, the energy release rates, $G^{(k)dl}$ and $G^{(k)mc}$, can be obtained from the derivatives of the IDEF with respect to $D^{(k)dl}$ and $D^{(k)mc}$, respectively. These derivatives obtained from Eq 25 are

$$\partial\Lambda_{11}/\partial D^{mc} = \frac{(1 + \Phi_1)\Phi_2[F_1 - xF_{1,x}]}{(1 + \Phi_1[D^{dl} + \Phi_2 D^{mc}F_1])^2} \tag{27a}$$

$$\partial\Lambda_{11}/\partial D^{dl} = \frac{(1 + \Phi_1)[1 - \Phi_2 F_{1,x}]}{(1 + \Phi_1[D^{dl} + \Phi_2 D^{mc}F_1(x)])^2} \tag{27b}$$

where $F_{1,x}$ denotes the derivative of $F(x)$. Based on these calculations, the level of available fracture energies under the current constraint conditions is evaluated and arranged in hierarchical order for delamination versus matrix cracking modes, with individual accounting for each damaged ply. The Griffith energy principle is used in developing criteria for the damage initiation and progression of matrix cracking and delamination. These criteria are

for matrix cracking

$$G^{(k)mc} = G_R^{mc} \tag{28a}$$

for delamination

$$G^{(k)dl} = G_R^{dl} \tag{28b}$$

The quantities in the left-hand side of Eqs 28*a* and *b* denote energy release rate (or available fracture energy), and those in the right-hand side denote critical energy release rate (or required fracture energy for cracking). The damage scenario is generated by gradually incrementing the load amplitudes, tracking the comparative ratios between levels of available and required fracture energies, and switching to new damage configurations for which the criterion of damage evolution has been satisfied.

Numerical Results and Verification

The approach developed in this work is based on the IDEF concept via a meso/macroscopic analysis. This approach was applied to cross-ply laminate using an improved shear lag analysis for a three-layer constraint model and verified extensively by comparison with experimental results (more than 15 figures of comparison can be seen in Refs *2*, *26–28*). The present work has been developed to apply this approach to general layup composites by proposing a five-layer constraint model with a more fine mesoscopic analysis than the shear lag analysis used previously. However, the verification for the new formulation is difficult due to the fact that there are very limited experimental results for general layup composites as well as for interactive damage progression. The consideration here is to use the experimental results [*22*] obtained by Choi, Downs, and Chang for verification of the predicted layup effects, and the calculated results given by Harin and Hu [*12*] for the predicted interactive damage progression. These verifications are not quite satisfactory because the conditions for comparison are difficult to be the same as we can see later. However, in the present numerical analysis, all material constants are taken for T300/976 graphite/epoxy (Gr/Ep) composites [*22*] that are used for the experiments of Choi et al. These constants are E_{11} = 156 GPa, $E_{22} = E_{33}$ = 9.09 GPa, $G_{12} = G_{13}$ = 6.96 GPa, G_{23} = 3.24 GPa, $\nu_{12} = \nu_{13}$ = 0.228, and ply thickness: t = 0.132 mm.

Following the assumption of Nairn and Hu [*20*], the critical energy release rates for matrix cracking and delamination are assumed to be the same. The values used are

$$G_R^{dl} = G_R^{mc} = 2.28 \cdot 10^{-4} \text{ MPa/m}^2 \tag{28c}$$

Figures 3 through 6 are obtained by the method proposed in this work. Figure 3 shows load-carrying curves versus normalized transverse matrix cracking density for $[0_3^\circ/90_3^\circ/0_3^\circ/90_{1.5}^\circ]_s$. At the first stage, the required applied stress for transverse matrix cracking is lower than that for delamination. Matrix cracking is then initiated and developed after the applied loading reaches the required loading for initiation of transverse matrix cracking. When the matrix crack density reaches the critical transverse crack density at the transition point, more applied stress is required for further matrix cracking than for initiation of delamination. It turns out that the transition from matrix cracking to delamination occurs at that point. Figure 4 shows the critical matrix cracking densities for delamination initiation as functions of the number of 90° plies. Since the ply thickness is fixed, the number is proportional to the thickness of the 90° plies. In agreement with Eq 19, it can be seen from the figure that as the thickness of the 90° layer increases, the critical damage density decreases. The interesting thing is that the decaying curves for the previous three layups are almost coincident with each other. This interesting phenomena was predicted by Narin and Hu (Fig. 5 of Ref *12*) for cross-ply layups. Although constraint effects have little affect on the critical crack density, it has a significant effect on the load at which the critical density is reached as we can see later. When the number of the 90° layer decreases from 5.5 to 1.5, the normalized critical matrix crack density increases from 0.22 to 0.805, which corresponds to an increase from 5.8 cracks per centimetre to 28. This result means that when the 90°-layer group becomes very thin, the transition from matrix cracking to delamination becomes very difficult. The calculated results show that when the number, n, is less than 1, the transition from transverse matrix cracking to interlaminar local delamination does not occur.

Figure 5 shows the internal constraint effects on the critical applied stresses at which initiation of matrix-cracking and the transition from matrix cracking to delamination occur, respectively. In the figure, three laminates with the same thickness of 90° layers are placed in such a way that the anisotropic constraint effects on the 90° layer monotonically increase from the left laminate $[0_3^\circ/90_3^\circ/-45_3^\circ/90_{1.5}^\circ]_s$, through the middle laminate $[0_4^\circ/\pm 45_4^\circ/90_{1.5}^\circ]_s$ to the right one $[0_3^\circ/90_3^\circ/0_3^\circ/90_{1.5}^\circ]_s$. From Fig. 5, we can see that the critical stresses are also monotonically

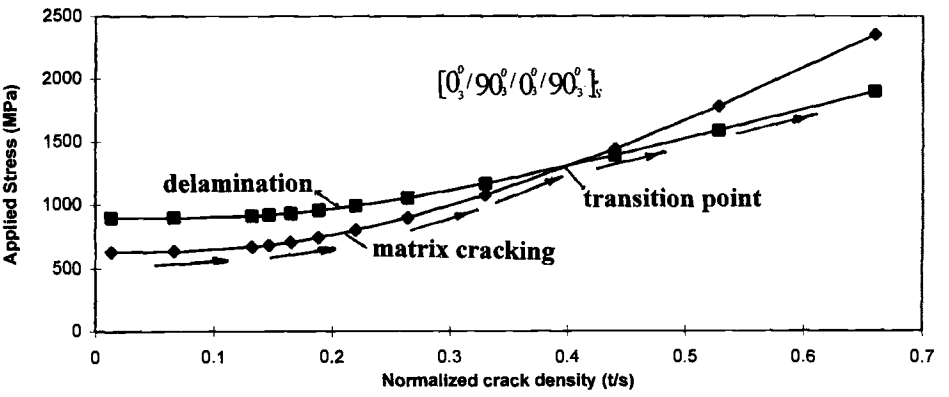

FIG. 3—*Applied stress for initiation of delamination and for continued microcracking.*

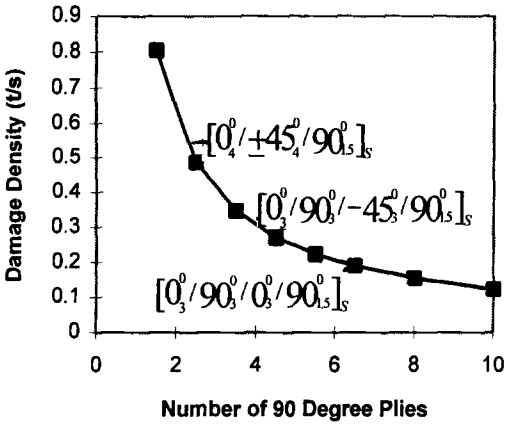

FIG. 4—*The critical damage densities for delamination initiation as functions of the number of 90° plies.*

increasing from the left to the right. These results illustrate that the higher the anisotropic constraint effects, the higher the required applied stresses for matrix-cracking initiation and for the transition from matrix cracking to delamination.

Figure 6 shows energy release rates of matrix cracking versus normalized matrix cracking densities for the three kinds of layups under the applied tensile stress of 100 MPa. The curves in this figure can be used to explain results in Figs. 3 and 5. In fact, this figure shows that as the matrix cracking density increases, the available fracture energy decreases up to a very small value at the transition point. This is because when the matrix damage density approaches the transition point, the distance between the two cracks is short, and interactions between matrix cracks become intensive. These interactions cause the available fracture energy to be reduced and requires a larger applied stress for continued matrix cracking. In relation to Fig. 5, curves in Fig. 6 show that if a layer is constrained more strenuously by neighboring layers, it has less available fracture energy for damage initiation, and therefore requires more applied stress for matrix cracking and more stress for the transition from matrix cracking to delamination. For instance, Layup A in Table 1, that is $[0_3^0/90_3^0/0_3^0/90_{1.5}^0]_s$, has the largest damage resistance, or the greatest required initiation energy, $E^{\text{initiation}}$. This is because the highest constraint effects

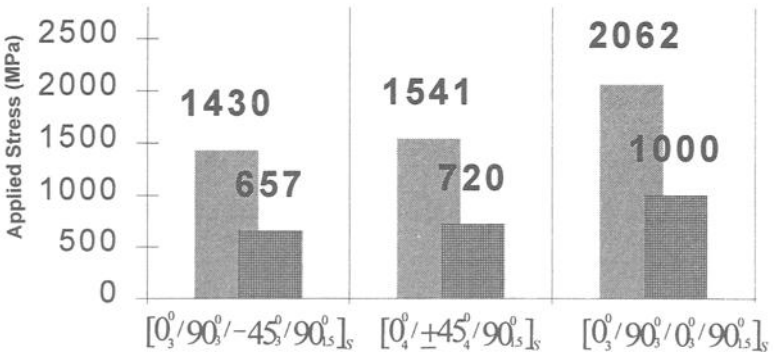

FIG. 5—*The critical stresses for initiation of matrix cracking and delamination.*

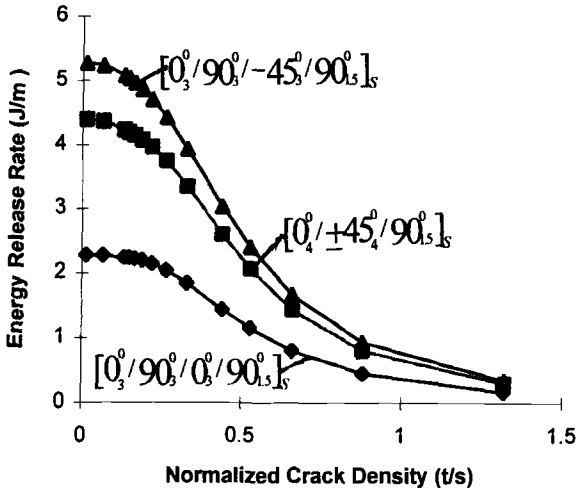

FIG. 6—*Comparison of energy release rates for continued matrix cracking of three layups.*

of that kind of layup cause its available fracture energy for a fixed applied stress to be the smallest.

Table 2 shows the available fracture energy, G^{mc}, for matrix-cracking initiation under applied tensile stress of 400 MPa. Since the required energy, $E^{\text{initiation}}$, in Table 1 was obtained through impact bending, the two kinds of results cannot be used for direct quantitative comparison. However, Tables 1 and 2 are for the same material and layups, and their values may show some connections. In fact, in Table 2 the ratio of the available fracture energy, G^{mc}, according to the order, D, C, B, A, is 6.6:2.46:1.33:1. The ratio of $E^{\text{initiation}}$ for the required initiation energy according to the same order, D, C, B, A, is 1:1.36:2.18:7.55. This comparison shows that the inverse ratio of the required energy, $E^{\text{initiation}}$, in Table 1 is roughly proportional to the ratio of available fracture energy in Table 2. This comparison seems reasonable due to the following reason. For an idealized elasticity body and fixed critical energy release rate, G_R^{mc}, the lower the available fracture energy, $G^{mc}|_{\sigma=const}$, under fixed applied stress, the higher the required supply energy, $E^{\text{initiation}}$, to make G^{mc} reach the value of G_R^{mc}. Therefore, the values of the two types of energies, $G^{mc}|_{\sigma=const}$ and $E^{\text{initiation}}$, should be approximate inverse.

Conclusions

1. Two internal variables, namely, normalized matrix crack density and delamination length, are introduced in this work. The effective stiffness matrix of a damaged ply is expressed through the introduced parameter's IDEF, based on the inhomogeneity theory of cracked bodies that were developed by Valuenko and Kachanov, Budiansky and O'Connell, and Horii and Nemat-

TABLE 2—*Layup effects on available fracture energy,* G^{mc}, *for applied tensile stress, 400 MPa.*

Layup Type	Material Type	Layups	G_0^{mc}, J/m^2
A	T300/976 Gr/Ep	$[0_3^\circ/90_3^\circ/0_3^\circ/90_{1.5}^\circ]_s$	36.5
B	T300/976 Gr/Ep	$[0_4^\circ/\pm 45_4^\circ/90_2^\circ]_s$	97.9
C	T300/976 Gr/Ep	$[0_6^\circ/\pm 45_4^\circ/90_3^\circ]_s$	241
D	T300/976 Gr/Ep	$[90_3^\circ/0_3^\circ/90_3^\circ]$	181

Nasser. The homogeneous process of the cracked body is carried out by a volume average process of stress and strain in the damaged ply at hand.

2. A methodology of interactive damage progression has been developed for general layup composites by accounting for internal constraint effects. These important effects are analyzed by proposing a five-layer ECM for the ply at hand. Considering any generic ply as a "local 90° layer" and embedding it in a five-layer ECM, the IDEF, proposed by Fan and Zhang in 1993, is extended to an arbitrary layer with transverse matrix cracking-local delamination interaction. The introduced IDEF can be considered as a quantitative measure for the anisotropic constraint effects on interactive damage interaction of an arbitrary layer.

3. By proposing a meso/macroscopic method for the analysis of a unit cell in the five-layer model, the IDEF of an arbitrary ply can be determined. In the mesoscopic analysis, a boundary value problem involved continuity conditions at the interface between sublaminates, and boundary conditions at the crack surface are solved for the symmetric ECM under the normal applied stress. From this, the sequential anisotropic stiffness reductions, the available fracture energy for competing damage modes, as well as the initiation, transition, and progression of damage modes can be determined and predicted. This methodology is exemplified by investigating the progressive matrix cracking-local delamination interaction.

4. With this unique approach, the intractable problem of laminate inhomogeneity effects on interactive damage progression can be handled in a systematic manner. More specifically, this approach can be reduced to solve different boundary problems to determine the IDEF for the problems at hand. This situation is very similar to fracture mechanics analysis where the main problem is to determine stress intensity factors. Future work will include the solution of several important boundary value problems to obtain the related IDEF expressions, such as symmetric and unsymmetric five-layer analysis without using the assumption of plane-strain conditions.

Acknowledgment

The author would like to thank Professor Y. Jack Weitsman for his valuable suggestions and support. Contributions from Dr. J. Zhang are sincerely appreciated.

APPENDIX I[2]

$$a_{11} = D_{11}^{(1)} - \frac{(B_{11}^{(1)})^2}{A_{11}^{(1)}} + \frac{A_{11}^{(1)}(A_{11}^{(2)} + A_{11}^{(3)})}{A_{11}^{(1)} + A_{11}^{(2)} + A_{11}^{(3)}} \left(\frac{B_{11}^{(1)}}{A_{11}^{(1)}} + \frac{h^{(1)}}{2}\right)^2 \tag{29}$$

$$a_{12} = \frac{1}{A_{11}^{(1)} + A_{11}^{(2)} + A_{11}^{(3)}} \left(B_{11}^{(1)} + \frac{h^{(1)}}{2} A_{11}^{(1)}\right)\left(h^{(2)} A_{11}^{(3)} + \frac{h^{(2)}}{2} A_{11}^{(2)}\right) \tag{30}$$

$$a_{13} = \frac{h^{(3)} A_{11}^{(3)}(B_{11}^{(1)} + 0.5\, h^{(1)} A_{11}^{(1)})}{2(A_{11}^{(1)} + A_{11}^{(2)} + A_{11}^{(3)})} \tag{31}$$

$$a_{22} = D_{11}^{(2)} + \frac{(h^{(2)})^2(4\, A_{11}^{(1)}A_{11}^{(3)} + A_{11}^{(2)}A_{11}^{(3)} + A_{11}^{(1)}A_{11}^{(2)})}{4(A_{11}^{(1)} + A_{11}^{(2)} + A_{11}^{(3)})} \tag{32}$$

$$a_{23} = \frac{h^{(3)} A_{11}^{(3)} h^{(2)}}{4(A_{11}^{(1)} + A_{11}^{(2)} + A_{11}^{(3)})} (2\, A_{11}^{(1)} + A_{11}^{(2)}) \tag{33}$$

[2] Equations $B_{11}^{(2)} = B_{11}^{(3)} = 0$ are used in these expressions.

$$a_{33} = D_{11}^{(3)} + \frac{(h^{(3)})^2 A_{11}^{(3)}(A_{11}^{(1)} + A_{11}^{(2)})}{4(A_{11}^{(1)} + A_{11}^{(2)} + A_{11}^{(3)})} \tag{34}$$

$$b_{11} = D_{11}^{(2)} + \frac{A_{11}^{(1)}A_{11}^{(2)}}{(A_{11}^{(1)} + A_{11}^{(2)})} \frac{(h^{(2)})^2}{4} \tag{35}$$

$$b_{12} = \frac{h^{(2)}}{2} \frac{A_{11}^{(1)}A_{11}^{(2)}}{(A_{11}^{(1)} + A_{11}^{(2)})} \left(\frac{h^{(1)}}{2} + \frac{B_{11}^{(1)}}{A_{11}^{(1)}} \right) \tag{36}$$

$$b_{22} = D_{11}^{(1)} - \frac{(B_{11}^{(1)})^2}{A_{11}^{(1)}} + \frac{A_{11}^{(1)}A_{11}^{(2)}}{(A_{11}^{(1)} + A_{11}^{(2)})} \left(\frac{h^{(1)}}{2} + \frac{B_{11}^{(1)}}{A_{11}^{(1)}} \right)^2 \tag{37}$$

APPENDIX II

In the following, Layer I^k corresponds to Layer 1, Layer $(k + 1)$ to Layer 2, and Layer k to Layer 3.

$$C_0 = A_{11}^{(Ik)} + A_{11}^{(k+1)} + A_{11}^{(k)} \qquad C_1 = A_{11}^{(k+1)} + A_{11}^{(k)} \tag{38, 39}$$

$$C_2 = A_{11}^{(Ik)} + A_{11}^{(k+1)} \qquad C_3 = 0.5\, A_{11}^{(k+1)} + A_{11}^{(k)} \tag{40, 41}$$

$$C_4 = 0.5\, h^{(k)} h_{11}^{(k)} \qquad C_5 = \left(\frac{h^{(Ik)}}{2} C_1 - B_{11}^{Ik} \right) \tag{42, 43}$$

$$C_6 = B_{11}^{(Ik)} + \frac{h^{(Ik)}}{2} A_{11}^{(Ik)} \qquad C_7 = 0.5\, h^{(k+1)}(A_{11}^{(Ik)} - A_{11}^{(k)}) \tag{44, 45}$$

$$\gamma_1 = \frac{p_1^1 C_5 + p_1^2 h^{(k+1)} C_3 + C_4}{C_0} \qquad \gamma_2 = \frac{p_2^1 C_5 + p_2^2 h^{(k+1)} C_3 + C_4}{C_0} \tag{46, 47}$$

$$\gamma_3 = \frac{p_3^1 C_5 + p_3^2 h^{(k+1)} C_3 + C_4}{C_0} \tag{48}$$

$$\eta_1 = B_{11}^{(Ik)} p_1^1 \lambda_1 + A_{11}^{(Ik)} \lambda_1 \gamma_1 \tag{49}$$

$$\eta_2 = B_{11}^{(Ik)} p_2^1 \lambda_2 + A_{11}^{(Ik)} \lambda_2 \gamma_2 \tag{50}$$

$$\eta_3 = B_{11}^{(Ik)} p_3^1 \lambda_3 + A_{11}^{(Ik)} \lambda_3 \gamma_3 \tag{51}$$

$$\eta_4 = \frac{A_{11}^{(k+1)} \lambda_1 (C_4 - p_1^1 C_6 - p_1^2 C_7)}{C_0} \tag{52}$$

$$\eta_5 = \frac{A_{11}^{(k+1)} \lambda_2 (C_4 - p_2^1 C_6 - p_2^2 C_7)}{C_0} \tag{53}$$

$$\eta_6 = \frac{A_{11}^{(k+1)} \lambda_3 (C_4 - p_3^1 C_6 - p_3^2 C_7)}{C_0} \tag{54}$$

$$\alpha_1 = \frac{(p_2^1 p_3^2 - p_3^1 p_2^2)\sinh(\lambda_2(s-l))\sinh(\lambda_3(s-l))}{\Delta} \frac{A_{11}^{(3)} N}{A_{11}^{(1)} + A_{11}^{(2)} + A_{11}^{(3)}} \tag{55}$$

$$\alpha_2 = \frac{-(p_1^1 p_3^2 - p_3^1 p_1^2)\sinh(\lambda_1(s-l))\sinh(\lambda_3(s-l))}{\Delta} \frac{A_{11}^{(3)} N}{A_{11}^{(1)} + A_{11}^{(2)} + A_{11}^{(3)}} \tag{56}$$

$$\alpha_3 = \frac{(p_1^1 p_2^2 - p_2^1 p_1^2)\sinh(\lambda_1(s-l))\sinh(\lambda_2(s-l))}{\Delta} \frac{A_{11}^{(3)} N}{A_{11}^{(1)} + A_{11}^{(2)} + A_{11}^{(3)}} \tag{57}$$

$$\alpha_4 = \alpha_5 = \alpha_6 = \frac{N}{A_{11}^{(1)} + A_{11}^{(2)} + A_{11}^{(3)}} \tag{58}$$

$$\begin{aligned}\Delta = {} & \sinh(\lambda_1(s-l))\sinh(\lambda_2(s-l))\sinh(\lambda_3(s-l)) \\ & [(p_1^1 p_2^2 - p_1^2 p_2^1)(\eta_3 + \eta_6)\coth(\lambda_3(s-l)) + (p_2^1 p_3^2 - p_3^1 p_2^2)(\eta_1 + \eta_4) \\ & \coth(\lambda_1(s-l)) + (p_1^2 p_3^1 - p_1^1 p_3^2)(\eta_2 + \eta_5)\coth(\lambda_2(s-l))]\end{aligned} \tag{59}$$

$$x = \frac{1 - D^{dl}}{D^{mc}}, \quad \Phi_1 = \frac{A_{11}^{(k)}}{A_{11}^{lk} + A_{(11)}^{(k+1)}} \tag{60, 61}$$

$$\Phi_2 = \frac{A_{11}^{(k)}(A_{11}^{lk} + A_{11}^{(k+1)})(p_{12} + p_{13} + p_{23})}{2(A_{11}^{(lk)} + A_{11}^{(k+1)} + A_{11}^{(k)})} \tag{62}$$

$$p_{12} = p_1^1 p_2^2 - p_1^2 p_2^1 \tag{63}$$

$$p_{13} = p_1^2 p_3^1 - p_1^1 p_3^2 \tag{64}$$

$$p_{23} = p_2^1 p_3^2 - p_3^1 p_2^2 \tag{65}$$

$$F_1(x) = \frac{1}{(\eta_1 + \eta_4)p_{23}\coth(\lambda_1 h_{(k)}x) + (\eta_2 + \eta_5)p_{13}\coth(\lambda_2 h_{(3)}x) + (\eta_3 + \eta_6)p_{23}\coth(\lambda_3 h_{(3)}x)} \tag{66}$$

References

[1] Timmer, J. L. and Hahn, H. T., "The Effect of Preloading on Fatigue Damage in Composites," *Mechanics of Composites Review*, Wright Patterson AFB, Dayton, OH, 1993, pp. 144–153.

[2] Fan, J. and Zhang, J., "In-site Damage Evolution and Micro/Macro Transition for Laminated Composites," *Composite Sciences and Technology*, Vol. 47, 1993, pp. 107–118.

[3] Garrett, K. W. and Bailey, J. E., "Multiple Transverse Fraction in 90° Cross-ply Laminates of a Glass Fiber-Reinforced Polyester," *Journal of Materials*, Vol. 12, 1977, pp. 157–168.

[4] Highsmith, A. L. and Reifsnider, K. L., "Stiffness Reduction Mechanisms in Composite Laminates," *Damage in Composite Materials, ASTM STP 775*, K. L. Reifsnider, Ed., American Society for Testing and Materials, Philadelphia, 1982, pp. 103–117.

[5] Flaggs, D. L., "Prediction of Tensile Matrix Failure in Composite Laminates," *Journal of Composite Materials*, Vol. 19, 1985, pp. 29–50.

[6] Hashin, Z., "Analysis of Cracked Laminates: A Variational Approach," *Mechanics of Materials*, 1985, pp. 121–136.

[7] Hashin, Z., "Analysis of Stiffness Reduction of Cracked Cross-Ply Laminates," *Engineering Fracture Mechanics*, Vol. 25, 1986, pp. 771–778.

[8] Hashin, Z., "Analysis of Cracked Laminates under Tension," *Journal of Applied Mechanics*, 1987, pp. 872–879.

[9] Praveen, G. N. and Reddy, J. N., "Stiffness Reduction in Composite Laminates due to Transverse Matrix Cracks," Recent Advance in Engineering Sciences, *Proceedings*, Thirty-first Annual Meeting Society of Engineering Science, College Station, TX, 1994, p. 6.

[10] Varna, J. and Berglund, L., "Multiple Transverse Cracking and Stiffness Reduction in Cross-Ply Laminates," *Journal of Composite Technology and Research*, 1991, pp. 97–106.

[11] Nairn, J. A., "The Strain Energy Release Rate of Composite Microcracking: Variational Approach," *Journal of Composite Materials*, 1989, Vol. 23, pp. 29–50.

[12] Nairn, J. A. and Hu, S., "The Initiation and Growth of Delaminations Induced by Matrix Microcracks in Laminated Composites," *International Journal of Fracture*, Vol. 57, 1992, pp. 1–24.

[13] Pagano, N. H., "Stress Fields in Composite Laminates," *International Journal of Solids and Structures*, Vol. 14, pp. 385–400.

[14] Pagano, N. J. and Soni, S. R., "Global-Local Laminate Variational Model," *International Journal of Solids and Structures*, Vol. 19, 1983, pp. 207–228.

[15] Schoeppner, G. A. and Pagano, N. J., "Stress Fields and Energy Release Rates in Cross-Ply Laminates," submitted for publication.

[16] Gudmundson, P. and Zhang, W., "An Analytical Model for Thermoelastic Properties of Composite Laminates Containing Transverse Matrix Cracks," *International Journal of Solids and Structures*, Vol. 30, 1993, pp. 3211–3231.

[17] Armanios, E. A. and Rehfield, L. W., "Sublaminate Analysis of Interlaminar Fracture in Composites: Part I: Analytical Model, Part: II—Applications," *Journal of Composite Technology and Research*, Vol. 11, 1989, pp. 135–146 and 147–153.

[18] O'Brien, T. K., "Characterization of Delamination Onset and Growth in a Composite Laminate," *Damage in Composite Materials, ASTM STP 775*, K. L. Reifsnider, Ed., American Society of Testing and Materials, Philadelphia, 1982, pp. 140–167.

[19] Crossman, F. W. and Wang, A. S. D., "The Dependence of Transverse Cracking and Delamination on Ply Thickness in Graphite/Epoxy Laminates," *Damage in Composite Materials, ASTM STP 775*, K. L. Reifsnider, Ed., American Society for Testing and Materials, Philadelphia, 1982, pp. 118–139.

[20] Whitney, J. M., "Stress Analysis of a Mode I Edge Delamination Specimen for Composite Materials," *AIAA Journal*, Vol. 24, 1986, pp. 1163–1168.

[21] Lagace, P. A., "Delamination: From Initiation to Final Failure," *Proceedings*, Ninth International Conference of Composite Materials, Vol. 1, 1993, pp. 120–122.

[22] Choi, H. Y., Downs, R. J., and Chang, F. K., "A New Approach Toward Understanding Damage Mechanisms and Mechanics of Laminated Composites Due to Low-Velocity Impact. Part I—Experiments, Part II—Analysis," *Journal of Composite Materials*, Vol. 25, 1991, pp. 992–1011 and 1013–1038.

[23] Valuenko, A. A. and Kachanov, M. L., "Continuum Theory of Medium with Cracks," *Mekhanika Tverdogo Tela*, Vol. 4, 1971, pp. 159–166.

[24] Budiansky, B. and O'Connell, R. J., "Elastic Moduli of a Cracked System," *International Journal of Solids and Structures*, Vol. 12, 1976, pp. 81–97.

[25] Horii, H. and Nemat-Nasser, S., "Overall Moduli of Solids with Microcracks: Load Induced Anisotropy," *Journal of the Mechanics and Physics of Solids*, Vol. 31, 1983, pp. 155–177.

[26] Zhang, J., Fan, J., and Soutis, C., "Analysis of Multiple Matrix Cracking in $[\pm\theta_n]_s$ Composite Laminates: Part I: In-Plane Stiffness Properties," *Composites*, Vol. 23, 1992, pp. 291–298.

[27] Zhang, J., Fan, J., and Soutis, C., "Analysis of Multiple Matrix Cracking in $[\pm\theta_n]_s$ Composite Laminates: Part 2: Development of Transverse Ply Cracks," *Composites*, Vol. 23, 1992, pp. 299–304.

[28] Zhang, J., Soutis, C., and Fan, J., "Strain Energy Release Rate Associated with Local Delamination in Cracked Composite Laminates," *Composites*, Vol. 25, 1994, pp. 851–862.

[29] Zhang, J., Soutis, C., and Fan, J., "Effects of Matrix Cracking and Hygro-thermal Stresses on the Strain Energy Release Rate for Edge Delamination Composites," *Composites*, Vol. 25, 1994, pp. 27–35.

[30] Jones, R. H., *Mechanics of Composite Materials*, Scripta Book Co., Washington, DC, 1975.

Thomas E. Wilt,[1] *Steven M. Arnold,*[2] *and Atef F. Saleeb*[3]

A Coupled/Uncoupled Computational Scheme for Deformation and Fatigue Damage Analysis of Unidirectional Metal-Matrix Composites

REFERENCE: Wilt, T. E., Arnold, S. M., and Saleeb, A. F., **"A Coupled/Uncoupled Computational Scheme for Deformation and Fatigue Damage Analysis of Unidirectional Metal-Matrix Composites,"** *Applications of Continuum Damage Mechanics to Fatigue and Fracture, ASTM STP 1315*, D. L. McDowell, Ed., American Society for Testing and Materials, 1997, pp. 65–82.

ABSTRACT: A fatigue damage computational algorithm utilizing a multiaxial, isothermal, continuum-based fatigue damage model for unidirectional metal-matrix composites has been implemented into the commercial finite element code MARC using MARC user subroutines. Damage is introduced into the finite element solution through the concept of effective stress that fully couples the fatigue damage calculations with the finite element deformation solution. Two applications using the fatigue damage algorithm are presented. First, an axisymmetric stress analysis of a circumferentially reinforced ring, wherein both the matrix cladding and the composite core were assumed to behave elastic-perfectly plastic. Second, a micromechanics analysis of a fiber/matrix unit cell using both the finite element method and the generalized method of cells (GMC). Results are presented in the form of *S-N* curves and damage distribution plots.

KEYWORDS: continuum damage mechanics, cracking, fatigue (materials), fracture (materials), metal-matrix composites, coupled deformation damage, uncoupled deformation damage, finite element methods

In advanced engine designs, materials that allow higher operating speeds and longer durability in addition to decreased weight are desirable. The use of metal-matrix composites (MMCs) may provide these benefits. For example, titanium metal-matrix composite (TMC) rotors are projected to have significant benefits in terms of increased rotor speeds and lower weight, as compared to the nickel and titanium rotors currently in service. However, to fully realize the benefits offered by MMCs, computationally efficient design and life prediction methods must be developed. Analysis of typical aerospace structures subjected to complex thermomechanical load histories requires the use of computational approaches such as the finite element method. In this regard, it is desirable to develop a life prediction algorithm that can be used in conjunction with the finite element method.

Historically, two basic approaches have been used in predicting the life of structures; uncoupled or fully coupled deformation-damage methods. A typical uncoupled analysis consists of obtaining the stress state for each element from a finite element analysis, and then, using the stress state data as input to a fatigue damage model, the number of cycles to the initiation of a crack are predicted. Subsequently, a "local" fracture mechanics approach is then used to propagate the crack. For example, a new finite element mesh is constructed to model the crack-

[1] Research engineer, University of Akron, Akron, OH 44325.
[2] Research engineer, NASA Lewis Research Center, Cleveland, OH 44135.
[3] Professor, Civil Engineering, University of Akron, Akron, OH 44325.

tip zone using a series of double nodes. The propagation of the crack is then controlled by a strain energy release rate criteria in conjunction with a node release scheme.

An alternative to the uncoupled method is a fully coupled deformation and damage method. By utilizing the concept of effective stress/strain equivalence, the effects of damage are accounted for in the finite element solution. Through the degradation of the material properties, as will be described in the computational scheme section, for a specified increment in damage, the individual finite element material properties are degraded and the subsequent finite element analysis then calculates the corresponding stress redistribution caused by the damage. This sequence of material degradation (representing damage) followed by re-analysis to capture stress redistribution effects is repeated until structural failure.

This is the approach taken in the present study. Specifically, the computational scheme developed uses MARC, a nonlinear finite element code in which the fatigue damage algorithm is coupled to MARC through the use of provided user subroutines. In the next section, the requisite fatigue damage equations are presented. In the following section, the computationally coupled fatigue damage algorithm will be outlined. Finally, two applications of the computational scheme will be presented. The first example is a reinforced MMC ring, representing a typical engine component, and the results will be presented in terms of the evolution of damage in the ring cross section. The second example is a micromechanics analysis of a fiber-matrix representative volume element (RVE). The damage distribution in the matrix will be shown.

Fatigue Damage Formulation

The fatigue damage calculations utilize a recently developed multiaxial, isothermal, continuum damage mechanics model for the fatigue of unidirectional metal-matrix composites [*1*]. The model is phenomenological, stress-based, and assumes a single scalar internal damage variable. Note that for an initially anisotropic material, the evolution of the damage, although a scalar, is directionally dependent. As will be shown, this directional dependence is accounted for in the terms, $\hat{F}_m$, Φ_{fl}, and Φ_u. The present multiaxial, isothermal, continuum damage model for unidirectional metal-matrix composites may be expressed as [*1*]

$$\int_{D_{k-1}}^{D_k} dD = \int_0^N [1 - (1 - D)^{\beta+1}]^{\alpha} \left[\frac{\hat{F}_m}{1 - D}\right]^{\beta} dN \tag{1}$$

N is the number of cycles at the current stress state (σ_k) and the increment in damage, ($D_k - D_{k-1}$), where D_k and D_{k-1} is the amount of damage at the current and previous increments, respectively. The quantity, α, that is a function of the current stress state is defined as

$$\alpha = 1 - a \frac{\langle \Phi_{fl} \rangle}{\langle \Phi_u \rangle} \tag{2}$$

where $\langle\ \rangle$ are the Macauley brackets. In Eq 2, the fatigue limit surface, Φ_{fl}, and the static fracture surface, Φ_u, are defined as

$$\Phi_{fl} = \frac{1}{2} \frac{\max}{t_0} \frac{\max}{t} F_{(fl)}(\sigma_{ij}(t) - \sigma_{ij}(t_0)) - 1 \tag{3}$$

$$\Phi_u = 1 - \frac{\max}{t} F_{(u)}(\sigma_{ij}(t)) \tag{4}$$

Note, the case, $\langle \Phi_u \rangle = 0$, indicates static fracture, which is failure, making it unnecessary to perform the fatigue calculations. Thus, having to consider the possibility of α being undefined

is unnecessary. As will be discussed in the following section, the finite element is considered to have failed completely. The case, $\langle \Phi_{fl} \rangle = 0$, indicates that the current stress state is below the fatigue limit and thus α is set equal to 1. This presents a special case when integrating the fatigue damage expression, Eq 1, and will be considered later in this section.

The quantity, $\hat{F}_m$, the normalized stress amplitude, is defined as

$$\hat{F}_m = \frac{1}{2} \frac{\max}{t} \frac{\max}{t_0} F_{(m)}(\sigma_{ij}(t) - \sigma_{ij}(t_0)) \tag{5}$$

In the preceding equations, t_0 is the time at the beginning of the current load cycle, and t is some time during the load cycle. The general form for $F_{(fl),(u),\text{ or }(m)}$ may be expressed as

$$F_{(\,)} = \sqrt{\frac{1}{(\,)_L^2} \left\{ (4\omega_{(\,)}^2 - 1) I_1 + \frac{4\omega_{(\,)}^2 - 1}{\eta_{(\,)}^2} I_2 + \frac{9}{4} I_3 \right\}} \tag{6}$$

It is here in Eq 6 where the evolution of the damage becomes directionally dependent. This simply amounts to the assumption of partial anisotropy, where the "extent" (magnitude) of damage is affected by the directionality of the stress state. Specifically, the directional dependence enters through the quantities, $I_1, I_2, I_3, \omega_{(\,)}$, and $\eta_{(\,)}$. The quantities, I_1, I_2, I_3, are invariants having the form

$$\begin{aligned} I_1 &= \frac{1}{2} S_{ij} S_{ij} - d_i d_j S_{jk} S_{ki} + \frac{1}{4} (d_i d_j S_{ij})^2 \\ I_2 &= d_i d_j S_{jk} S_{ki} - (d_i d_j S_{ij})^2 \\ I_3 &= (d_i d_j S_{ij})^2 \end{aligned} \tag{7}$$

that are a function of the current deviatoric stress state, S_{ij}^k, as well as the vector, d_i, that defines the materials' fiber orientation. In addition, the terms, $\omega_{(\,)}$ and $\eta_{(\,)}$, represent the ratios of longitudinal to transverse normal and shear stresses, respectively. Note, the longitudinal direction is parallel to the fiber direction and transverse is perpendicular to the fiber direction. For initially transversely isotropic materials, $\omega_{(\,)}$ and $\eta_{(\,)}$ are > 1, and for isotropic materials, $\omega_{(\,)}$ and $\eta_{(\,)}$ are $= 1$.

For a current state of stress, σ_k, which is above the fatigue limit, that is, $\alpha \neq 1$ (integrating Eq 1) results in an expression for the number of cycles, N, that is

$$N = \frac{([1 - (1 - D_k)^{\beta+1}]^{1-\alpha} - [1 - (1 - D_{k-1})^{\beta+1}]^{1-\alpha})}{\hat{F}_m^{\beta}(1 - \alpha)(\beta + 1)} \tag{8}$$

Note that D_{k-1} is the total amount of damage at the beginning of the load block and D_k is the total amount of damage at the end of this load block.

In the present computational scheme, since the damage increment is controlled, both D_k and D_{k-1} are known. That is, $D_k = D_{k-1} + \Delta D$ where ΔD is the user-specified increment in damage. Thus, Eq 8 is used to predict the increment in the number of cycles for each element, N^e, due to the increment in damage.

To calculate the number of cycles to failure for an initial damage amount, D_{k-1}, let $D_k = 1$, which results in the following

$$N_F = \frac{(1 - [1 - (1 - D_{k-1})^{\beta-1}]^{1-\alpha})}{\hat{F}_m^{\beta}(1 - \alpha)(\beta + 1)} \tag{9}$$

As will be shown in the following section, it is also necessary to rewrite Eq 8 in terms of the damage D_k, that is

$$D_k = 1 - \left(1 - \left\{[1 - (1 - D_{k-1})^{(\beta+1)}]^{1-\alpha} + (1 - \alpha)(\beta + 1)\hat{F}_m^{\beta} N\right\}^{\frac{1}{1-\alpha}}\right)^{\frac{1}{\beta+1}} \tag{10}$$

Now, consider the case in which the current stress state is below the fatigue limit, that is, $\langle \Phi_{fl} \rangle = 0$, which leads to $\alpha_k = 1$. Thus, Eq 1 takes the form

$$\int_{D_{k-1}}^{D^k} \frac{(1 - D)^{\beta}}{1 - (1 - D)^{\beta+1}} \, dD = \int_0^N \hat{F}_m^{\beta} dN \tag{11}$$

Upon integrating Eq 11, the increment in cycles, N, with initial damage, D_{k-1}, may be expressed as

$$N = \left(\frac{\log[1 - (1 - D_k)^{\beta+1}] - \log[1 - (1 - D_{k-1})^{\beta+1}]}{\hat{F}_m^{\beta}(\beta + 1)}\right) \tag{12}$$

Alternatively, the following expression for the damage, D_k, may be expressed as

$$D_k = 1 - \{1 - [1 - (1 - D_{k-1})^{\beta+1}] \exp((\beta + 1)\hat{F}_m^{\beta} N)]\}^{\frac{1}{\beta+1}} \tag{13}$$

For the number of cycles to failure, let $D_k = 1$

$$N_F = \frac{-\log[1 - (1 - D_{k-1})^{\beta+1}]}{\hat{F}_m^{\beta}(\beta + 1)} \tag{14}$$

The effect of damage is included in the finite element stress analysis by utilizing the concept of "effective stress" [2] and the hypothesis of strain equivalence [3,4]. Thus, the effect of damage may be accounted for by either using the effective stress, that is, increasing the stress, or by simply degrading the elastic and plastic material properties to represent the material softening due to damage. Material softening is used in the present approach with the degraded elastic constitutive matrix calculated by

$$[\bar{C}] = (1 - D_k)[C] \tag{15}$$

and similarly, the plastic material properties, for example, yield stress, σ_y, is given by

$$\bar{\sigma}_y = (1 - D_k)\sigma_y \tag{16}$$

Computational Scheme

General Framework

The present version of the fatigue damage algorithm utilizes *average* quantities in the damage calculations. For example, the stresses for each integration point are determined and then all integration points are averaged to give one stress state for each element. All subsequent damage calculations use these average quantities. However, the program was written in a sufficiently

general form so that all of the damage calculations may be performed at each integration point with minimal modifications. Specifically, all that is required is increased dimensions for various storage arrays. Note that, because of the scalar nature of the damage parameter used here, together with the assumptions previously discussed, the task of local (constitutive) level integration is simply reduced to the use of the "exact" closed-form expressions given in the preceding section.

A flowchart of the developed life prediction scheme is shown in Fig. 1. The deformation analysis is the actual finite element run. First, note there are two levels of failure criteria checks; element level and structural level. The element level includes a static fracture surface check that is part of the fatigue damage model (Eq 4). Additional criteria may be included such as a check on total mechanical strains, etc. If an element violates one of these failure criteria, that element is considered to have "failed" and its damage, D, is set equal to the maximum amount of damage allowed. As shown in Fig. 1, for a coupled analysis, the damage calculations are terminated and a deformation analysis is rerun in order to account for the stress redistribution

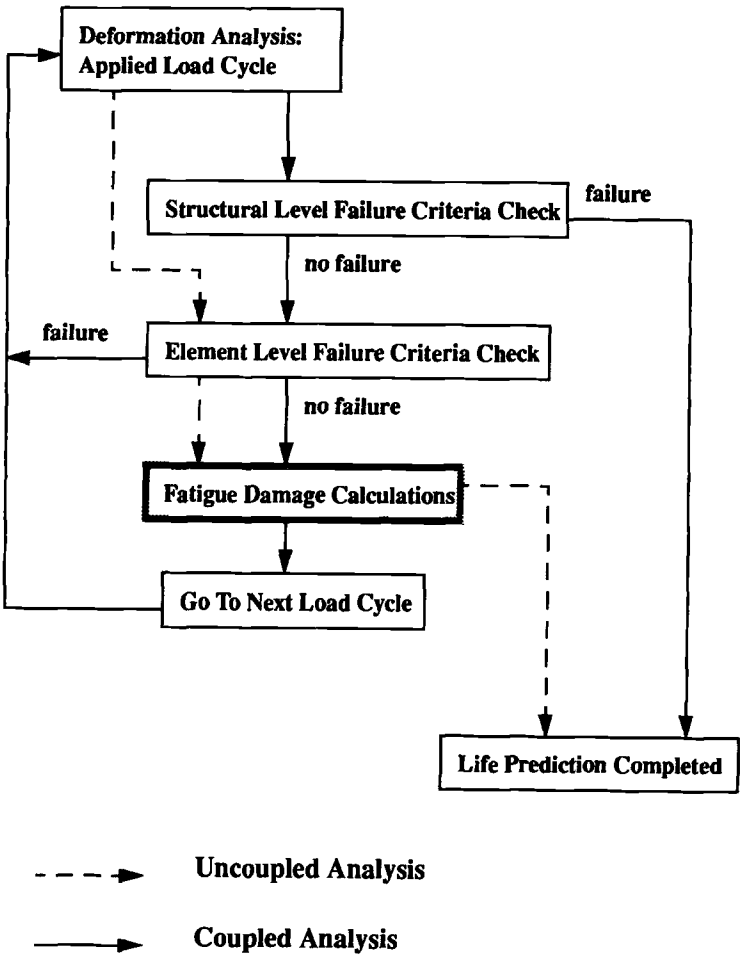

FIG. 1—*Coupled/uncoupled life prediction scheme.*

due to that element's failure. For an uncoupled analysis, when element failure occurs, the analysis does not loop back and perform another deformation analysis; instead, it continues to the next element and performs the damage calculations. The structural level criteria monitors the global response of the structure. This could take the form of a check upon selected nodal displacements that, if they violate a specified displacement criteria, the structure is considered to have failed. For example, the tip displacement of a turbine blade may be required to stay within a given tolerance. Again, note that for an uncoupled analysis no structural failure criteria check is performed since the present fatigue damage algorithm assumes that the structure, when subjected to the initial "applied" load cycle, is in a completely undamaged state.

The applied load cycles just mentioned are those actually defined by the user through the finite element input data file. In addition, the number of load increments per applied cycle must be specified by the user. This is necessary so that the program can internally monitor when a given applied load cycle has been completed and begin the damage calculation phase. The number of load increments used in the load cycle usually depends on the nonlinearity of the structural response and requires experience on the part of the user. At each increment during the applied load cycle, the average stress (strain is optional) state for each element is stored. At the last load increment of the current applied load cycle, the DAMAGE subroutine is called to perform the fatigue damage calculations, see Fig. 2.

When DAMAGE is entered for each element, various element quantities, such as α, Φ_{fl}, Φ_u, $\hat{F}_m$, are calculated and stored. When DAMAGE has been called for the last element in the mesh, the fatigue damage calculations are performed. Figure 2 shows the general algorithm for the fatigue damage calculations.

Presently, the damage calculations are controlled by the increment in damage, ΔD. The user specifies the allowable increment in damage, for example, $\Delta D = 0.15$, (15%). In CALCN, using Eq 9 or Eq 12, based upon the new value of damage and the given element's stress state, the number of cycles to failure, N_F^e, is calculated and stored. Next a "sorting" subroutine, SORTN, is called (see Fig. 2) to determine which element has the minimum number of cycles to failure and is chosen as the "controlling element," that is

$$N_{F\min} = \min N_F^e \qquad e = 1 \rightarrow numel \tag{17}$$

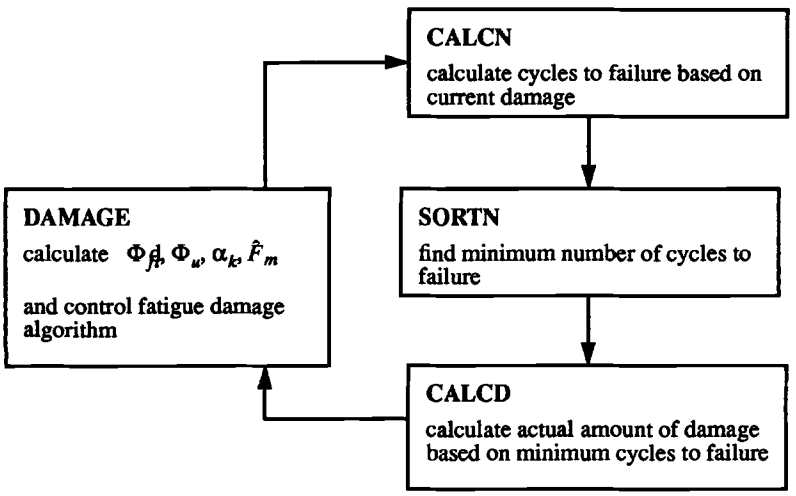

FIG. 2—*Fatigue damage calculations.*

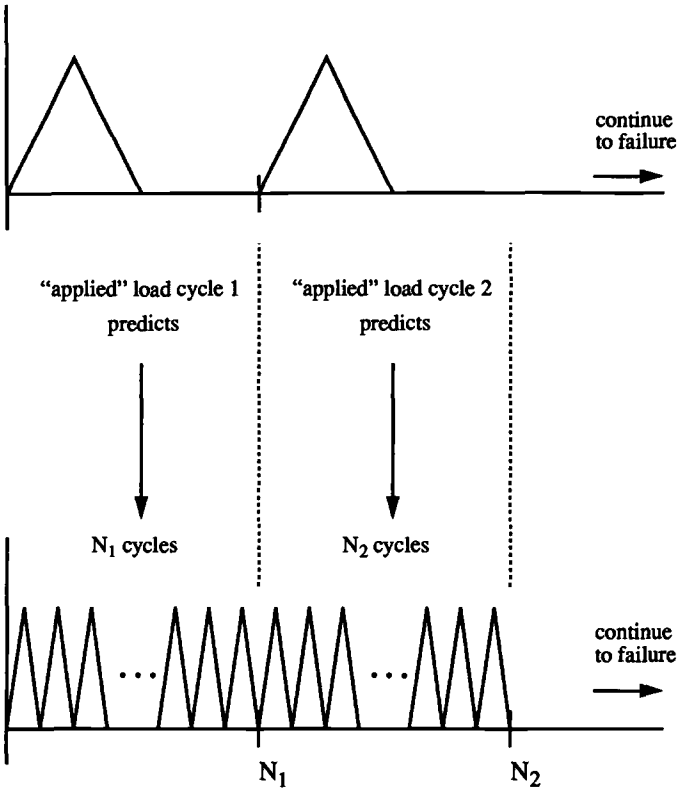

FIG. 3—*Cycle scheme for a coupled analysis.*

Once the controlling number of cycles has been determined, the corresponding, actual amount of damage, D_k^e, in all of the remaining elements must be recalculated. This is performed in subroutine CALCD using Eq 10 or 13. Note that since the damage was incremented by a specified amount, the controlling element's damage is already known.

Figure 3 shows the cycle scheme used in the code. Recall that the "applied" load cycle is the actual load history that is applied and used in the finite element analysis. The subsequent cycles, shown in dashed lines, are the predicted cycles corresponding to $N_{F\min}$ that is determined in SORTN. Here, it is assumed that the stress state in each element remains constant during the predicted $N_{F\min}$ cycles and at the end of $N_{F\min}$, each element has incurred an amount of damage as calculated in CALCD. Note for a coupled analysis, the next applied load cycle is run in the finite element analysis to account for the stress redistribution due to the new damage state in each element (that is, D_k^e) and again a new $N_{F\min}$ is predicted. This sequence of applied load cycle and predicted cycles is repeated until the structure has failed. For an uncoupled analysis, only one sequence, that is, only one applied load cycle, is performed. The resulting $N_{F\min}$ would be used to merely indicate the location of damage initiation.

In preparation for the subsequent applied load cycle, the element material properties are degraded according to the newly calculated element damage, D_k^e. Finally, a subroutine, PATSTR, was also written that generates PATRAN [5] element results files. These files contain damage distributions at specified increments during the fatigue damage analysis. In addition, output files containing a summary table of the current number of fatigue cycles and remaining

cycles to failure for each element, and a summary table showing the damage evolution in each element are also generated.

Some general comments on the fatigue damage algorithm need to be made. First, once an element attains the user specified maximum allowable damage, the element is assumed to fail and is no longer considered in any subsequent damage calculations. In the example presented in the next section, a cutoff value of 95% was specified based upon preliminary experience with difficulty in achieving global convergence when the element stiffness was reduced below 5%. Further investigation of convergence difficulties needs to be addressed. Second, in the present fully coupled damage-deformation analysis, a perfect plasticity model was used. This idealization eliminates the need to account for cyclic hardening, and the corresponding update of the internal variables, which may occur during a specific block of fatigue cycles. In order to accurately account for the hardening, a projection/update of the internal variables through the load block would be required. In addition, it is usually assumed that the fatigue damage calculations are applied to a "stabilized" stress redistribution. Thus, when hardening is present, more than one applied load cycle may be necessary in order to achieve the stabilized stress redistribution.

MARC Implementation

As an example, the present fatigue damage algorithm was implemented into the finite element code MARC. Please note that based upon the discussion in the previous section, it should be apparent that the fatigue damage algorithm was developed in a form that is independent of the specific finite element code that is used. Most commercial finite element codes provide capabilities similar to those described here with regards to MARC.

MARC provides various user subroutines [*6*] that allow implementation of constitutive models, failure criteria, new elements, etc. By using a few select MARC user subroutines, the continuum-based fatigue damage model has been coupled with the nonlinear finite element solution scheme. The primary MARC user subroutine required is ELEVAR. In addition, when using the plasticity model contained in MARC, the subroutines HOOKLW and ANPLAS are used to degrade the elastic and plastic material properties, respectively. In this study, the user subroutine HYPELA was also used to implement the Bodner-Partom viscoplastic model into MARC.

The subroutine ELEVAR is called at the end of each load increment once global convergence has been attained, and is intended to be used to output element quantities at the end of a given increment. In this algorithm, ELEVAR is used to store the current converged stress state for each element during the applied load cycle. The meaning of applied load cycle is the same as discussed earlier in the previous section. This is done through the MARC subroutines HOOKLW, for the elastic constants, and ANPLAS, for the anisotropic yield stress ratios using Eqs 17 and 18. Again, HOOKLW and ANPLAS are used when the MARC plasticity model is used. For the Bodner-Partom viscoplastic model, similar calculations are performed within the HYPELA routine.

Example Applications

A Cladded MMC Ring Insert

As stated previously, one of the primary motivations of this research is to establish a computationally efficient method for predicting the fatigue life of typical aerospace components. This includes the ability to predict the location of damage initiation and to be able to track the propagation of damage throughout the structure. With this in mind, the fatigue damage algorithm was applied to a cladded MMC ring. The reasons for choosing this specific structure are

TABLE 1—*Material properties for plastic deformation model (MPa).*

SiC/Ti 15-3 COMPOSITE MATERIAL
Elastic
$E_1 = 183959, E_2 = E_3 = 114457, \nu_{12} = 0.28, \nu_{13} = \nu_{23} = 0.32$
Inelastic
$\sigma_y = 276, \frac{\sigma_{y1}}{\sigma_y} = 5, \frac{\sigma_{y2}}{\sigma_y} = \frac{\sigma_{y3}}{\sigma_y} = 1$
MATRIX MATERIAL (Ti 15-3)
Elastic
$E = 74466, \nu = 0.32$
Inelastic
$\sigma_y = 514$

NOTE—The subscript, 1, denotes fiber direction.

twofold. First, it represents a MMC rotor insert currently under consideration in advanced engine designs. Secondly, because of its axisymmetric geometry and load conditions, qualitative stress distributions are known a priori. For example, maximum circumferential stress in the core occurs at its inner diameter and likewise for the cladding, thus providing some intuitive feel for where damage initiation will occur as well as how it may propagate.

The composite core was described by Hill's anisotropic elastic-plastic constitutive model available in MARC [*6*], while the matrix cladding was assumed to be isotropic and elastic perfectly-plastic. The elastic and inelastic material parameters required for the deformation analysis are given in Table 1, while the associated material parameters for the fatigue damage model are given in Table 2. Note that the matrix cladding utilizes the isotropic form of the fatigue damage model, that is, $\omega_u = \omega_{fl} = \omega_m = \eta_u = \eta_{fl} = \eta_m = 1$, whereas the composite core is represented by the transversely isotropic form of the model. The finite element model, representing the cross section of the ring, Fig. 4, consisted of 225 nodes and 64 eight-node axisymmetric elements (MARC element No. 28). A uniform pressure load was applied along the inner diameter of the ring.

With regards to the deformation analysis, burst pressure predictions have been previously made and compared to limited experimental data [*7,8*]. Very good correlation was observed, thus providing a level of confidence in the finite element modeling of the ring.

TABLE 2—*Material properties for fatigue model* [7] *(MPa).*

SiC/Ti 15-3 COMPOSITE MATERIAL	
$\sigma_u = 10694$	$\omega_u = 5.5$
$\sigma_{fl} = 1972$	$\omega_{fl} = 12.482$
$\beta = 1.842$	$\omega_m = 11.8$
$a = 0.012$	$\eta_u = \eta_{fl} = \eta_m = 1.0$
$M = 22371$	
MATRIX MATERIAL (Ti 15-3)—ISOTROPIC SIMPLIFICATION	
$\sigma_u = 6081$	$\omega_u = 1.0$
$\sigma_{fl} = 965$	$\omega_{fl} = 1.0$
$\beta = 2.27$	$\omega_m = 1.0$
$a = 0.0365$	$\eta_u = \eta_{fl} = \eta_m = 1.0$
$M = 6205$	

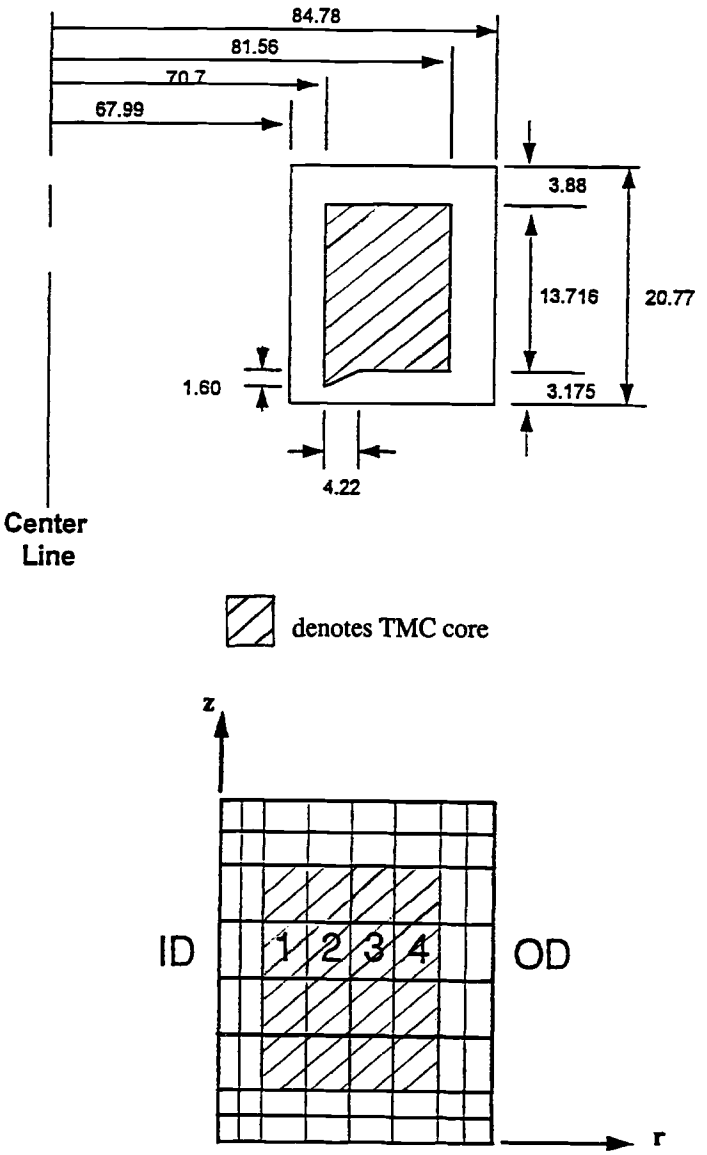

FIG. 4—*Cladded MMC ring geometry and finite element model:* (top) *actual ring geometry (dimensions are in mm) and* (bottom) *idealized ring geometry.*

Two types of fatigue life analyses were performed, namely, an uncoupled and a coupled analysis. The uncoupled life prediction results were obtained by taking four elements, labeled 1, 2, 3 and 4 in Fig. 4 (*bottom*), in the radial direction of the composite core of the ring. It was assumed that the stress state was relatively constant in the z-direction, thus one element would represent all of the elements in a column of the composite core. In the uncoupled analysis, no fatigue calculations were performed on the elements associated with the matrix cladding because of the initially low stress levels in the matrix cladding causing infinite fatigue lives to be

calculated. A finite element analysis was run in which the ring was subjected to a cyclic pressure load. During the analysis, the stress state history for each of the four elements was stored. The stress history for a given element (1, 2, 3, or 4) was then used to predict the corresponding fatigue life for that element. Since only a single cycle was used, no stress redistribution effects, due to damage, were accounted for in the uncoupled analysis. Figure 5 (*top*) shows the results of the uncoupled fatigue damage analysis. As expected, since Element 1 has the highest stress

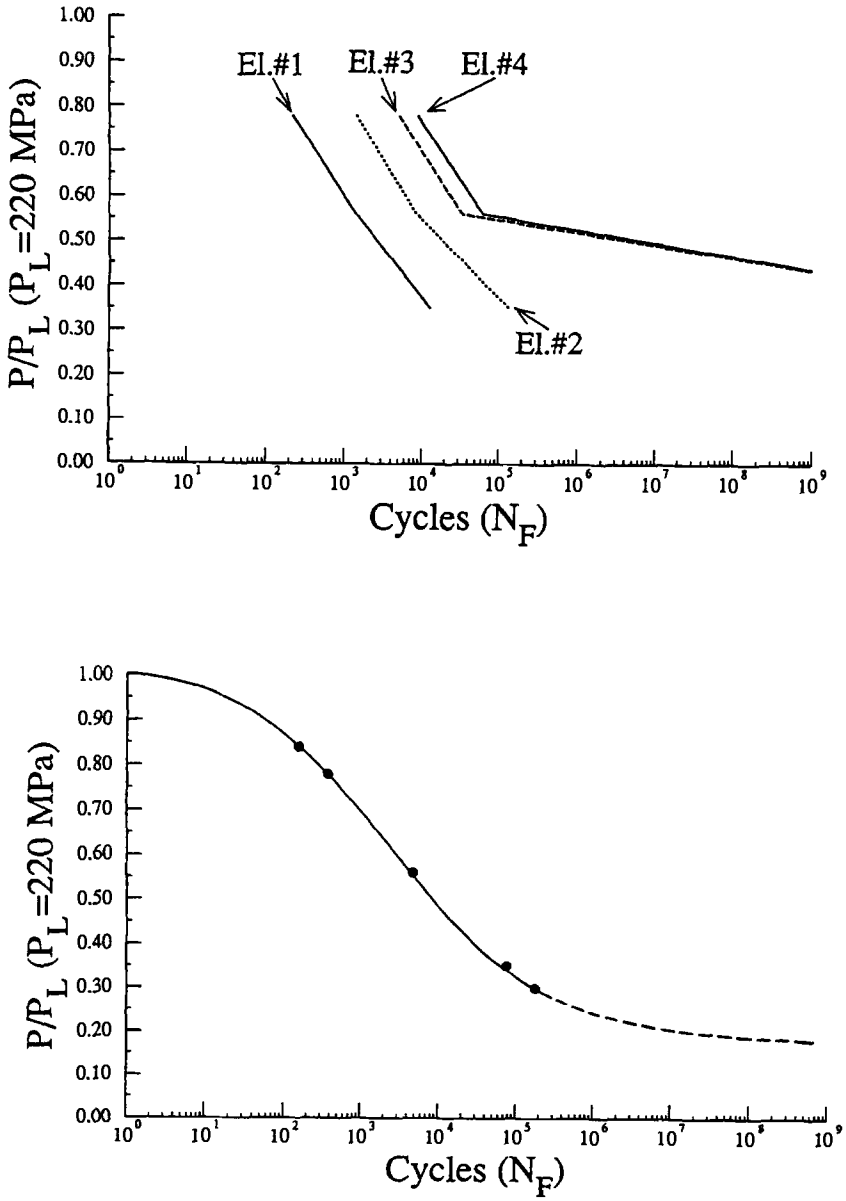

FIG. 5—*Life prediction for uncoupled* (top) *and coupled* (bottom) *analysis.*

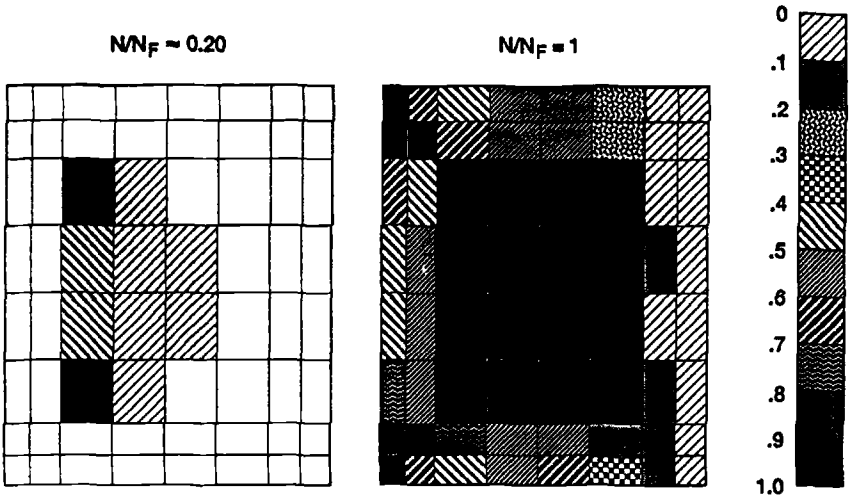

FIG. 6—*Fatigue damage distribution in ring cross section:* (left) $N/N_F \approx 0.2$ *and* (right) $N/N_F \approx 1.0$. *Cycles to failure,* $N_F = 155$.

state, it correspondingly has the shortest fatigue life. Thus, damage is predicted to initiate along the composite core inner diameter.

The fully coupled life prediction analysis follows the algorithm presented in the previous section that takes into account the effects of stress redistribution due to the propagation of damage. Now in the coupled analysis, finite lives and damage are predicted for the cladding, due to stress redistribution effects. Figure 5 (*bottom*) shows the fully coupled deformation and fatigue damage analysis results. The solid circles are analysis results obtained using the present fully coupled algorithm. A smooth solid line is drawn through these points to obtain the *S-N* curve. Note the dashed part of the *S-N* curve indicates an "extrapolation" since no analysis was run at a P/P_L less than 0.30. Upon comparison, one observes that at pressures close to the burst pressure, the fatigue life predicted by the coupled analysis is close to that of the uncoupled analysis, since at high stress levels, once the damage initiates in the core, "structural" failure of the ring occurred rapidly. On the other hand, at low stress levels, the fatigue life as predicted by the coupled analysis is longer than that predicted from the uncoupled analysis at the inside diameter. This difference may be viewed as the effect of propagation of the damage in the ring cross section. This propagation is caused by the stress redistribution effects that are automatically captured by performing a fully coupled deformation and fatigue damage analysis.

Finally, Fig. 6 shows two selected damage distribution plots in the ring cross section produced by the coupled fatigue damage analysis for $P/P_L = 0.85$. Note that in Fig. 6 (*left*), the damage initiates along the inner diameter of the composite core. In addition, the first elements to completely fail are located in the inner radius "corners" of the TMC core. Therefore, the assumption used in the uncoupled analysis of a uniform stress state in the z–direction for a given column of core elements was not appropriate. Conversely, in Fig. 6 (*right*) structural failure of the ring is depicted (that is, the composite core has completely failed) and due to stress redistribution, the matrix cladding has accumulated significant amounts of damage.

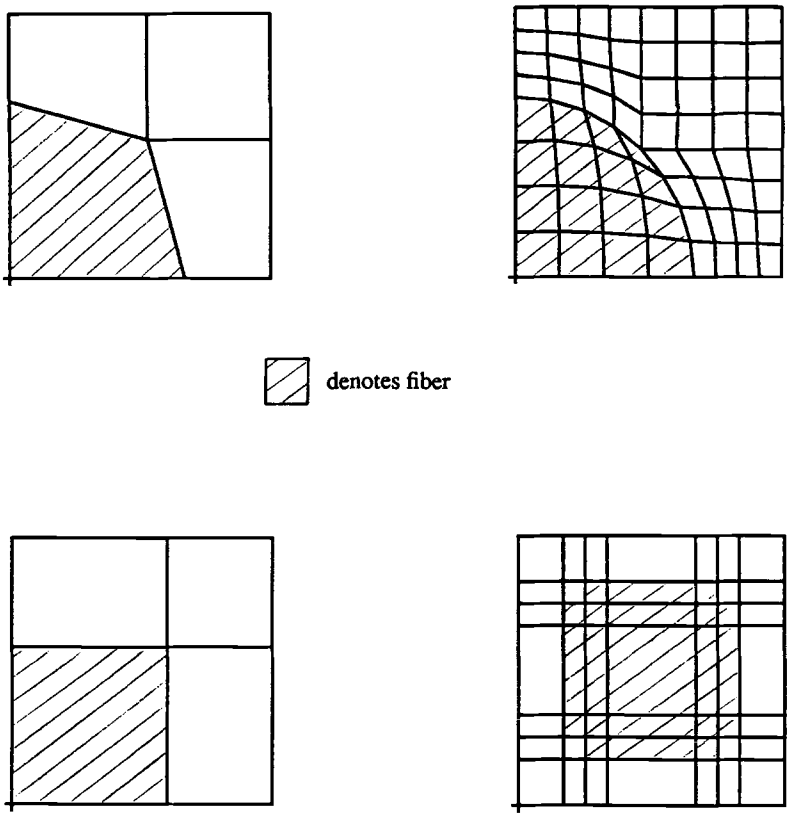

FIG. 7—*Finite element mesh* (top) *and GMC* (bottom) *RVEs.*

Micromechanical Failure Analysis

The second application is on the microscale in which a fiber/matrix unit cell representing a square pack, 35% fiber volume ratio (FVR), SiC/Ti-15-3 composite was analyzed. Two approaches were used to model and analyze the unit cell. The first approach utilized a finite element representation in which the unit cell was idealized using two mesh discretizations, consisting of 4 and 64 eight-node three-dimensional elements, Fig. 7. For the deformation response, the Bodner-Partom viscoplastic model was characterized for the Ti-15-3 matrix material (see Table 3) and the fiber utilized a simple isotropic linear elastic model (see Table 4).

TABLE 3—*Material properties for viscoplastic deformation model (MPa) SiC fiber material.*

Elastic
$E = 399910$, $\nu = 0.25$
Inelastic
$D_0 = 0$, $Z_0 = Z_1 = m = n = Q = 1$

TABLE 4—*Material properties for viscoplastic deformation model (MPa) Ti 15-3 matrix material.*

Elastic
$E = 74466$, $\nu = 0.32$
Inelastic
$D_0 = 1000$, $Z_0 = Z_1 = 120$
$m = 10$, $n = 3$, $Q = 1$

The Bodner-Partom viscoplastic model was implemented into MARC using the HYPELA user subroutine. The fatigue damage model, taken in its isotropic form, was characterized for the Ti-15-3 matrix constituent.

The second approach utilized the generalized method of cells, GMC, developed by Aboudi [*9*]. GMC is a continuum-based micromechanics model that provides closed-form expressions for the macro response of the composite in terms of the individual constituents (phases). The GMC model and the fatigue damage algorithm have been incorporated into the stand-alone micromechanics analysis code, MAC [*10*]. MAC has the ability to analyze a material volume element subjected to various thermal, mechanical (stress or strain control), and thermomechanical load histories, and wherein different integration algorithms and a variety of constitutive models can be selected. Previous work [*11*] has shown the accuracy and computational efficiency of GMC with respect to deformation analysis. Part of this work, and future research, is to determine if GMC also provides accurate and computationally efficient fatigue damage predictions.

The analysis consisted of stress-controlled cyclic loads applied in the longitudinal direction with respect to the unit cell. All four unit cells (both finite element and GMC) produced identical

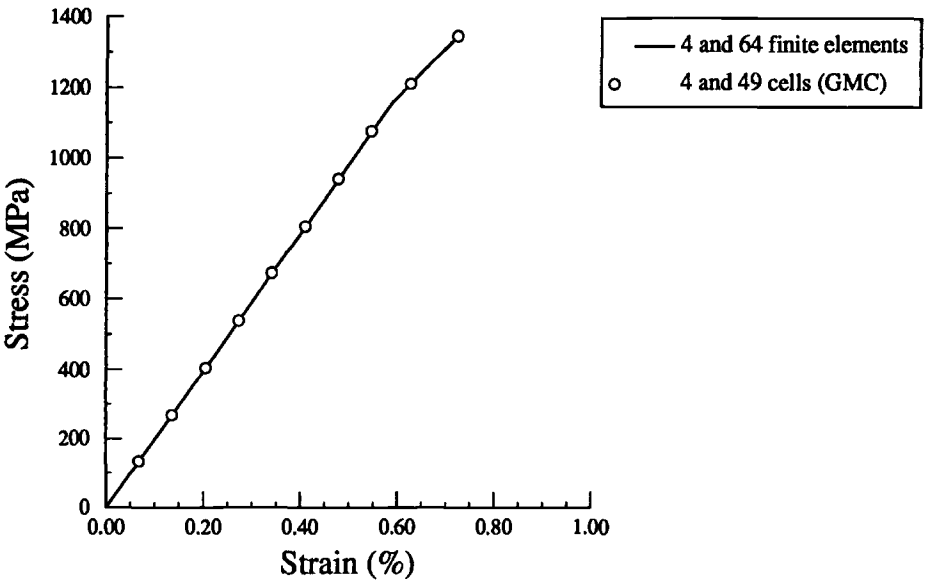

FIG. 8—*Longitudinal stress versus strain response: finite element and GMC.*

TABLE 5—*Fatigue lives for a 35% fiber volume fraction SCS-6/Ti-15-3 composite loaded longitudinally.*

	Fatigue Life, Cycles					
	Finite Element			GMC		
Load, MPa	4	64	Difference, %	4-Cell	49-Cell	Difference, %
1345	2939	2858	3.0	2497	2494	0.2
1207	4957	4859	2.0	4245	4234	0.25
931	21497	20992	2.4	20459	20098	2.
793	64496	62366	3.4	61235	59843	2.3

longitudinal macro stress-strain responses, as shown in Fig. 8. However, the predicted longitudinal fatigue lives are different, see Table 5. An example macrolongitudinal *S-N* curve produced with the 64 finite element model is shown in Fig. 9. Note, that if the SCS-6 fiber is taken to have a constant ultimate tensile strength (UTS) value, the lower stress amplitude lives in Fig. 9 are run outs. Consequently, in order to agree with the experimentally determined fatigue lives, a fiber UTS model that degrades as a function of time and temperature is required, Fig. 10. All the lives indicated in Table 5 were generated using this time-dependent fiber UTS model. Referring to Table 5, note that the 4 and 64 finite element unit cells give results that are consistently within 2 to 3% of each other for all stress levels, and the 4 and 49 cell GMC results are within 0.2 to 2% of each other. This shows that for the longitudinal response the 4 finite element unit cell produces results that are comparable to the 64 finite element unit cell. Similarly, the 4-cell GMC representative volume element (RVE) gives results that are as accurate as the 49-cell GMC RVE. Table 6 shows a comparison between the 4 finite element unit cell versus the 4-cell GMC RVE and the 64 finite element unit cell versus the 49-cell GMC

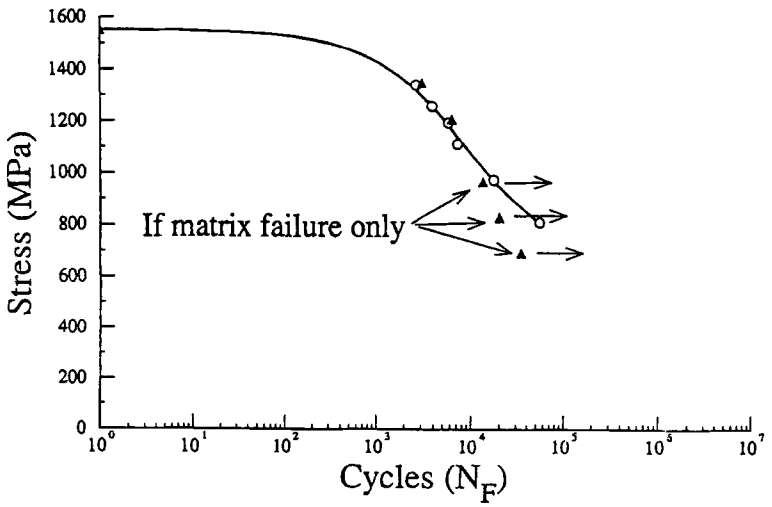

FIG. 9—*Life prediction for SiC/Ti-15-3 composite.*

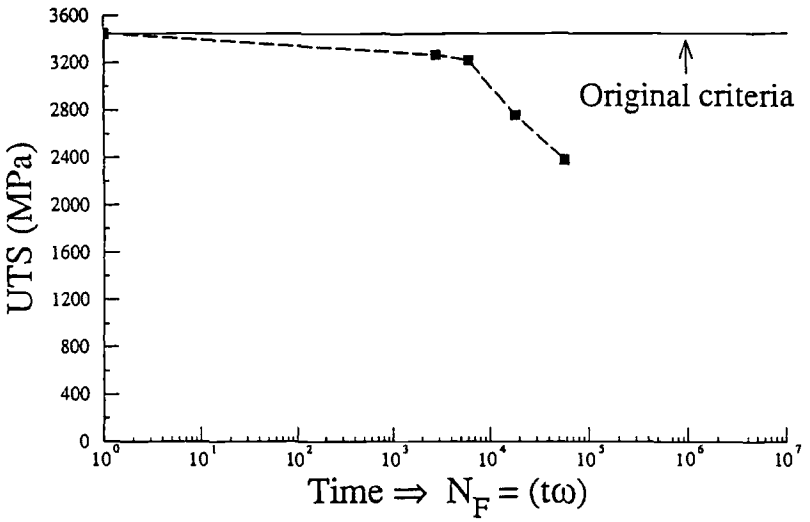

FIG. 10—*Fiber constituent ultimate tensile strength (UTS) failure diagram.*

RVE. Note that at the higher stress amplitudes (1345 and 1207 MPa), the relative differences are on the order of 14 to 17%, while at the lower stress amplitudes (931 and 793 MPa), there is a relative difference of 4 to 5%.

Figure 11 shows the damage distribution for the fatigue analysis having a maximum stress amplitude of 1345 MPa. The damage distributions were taken just before failure of the unit cell (that is, fiber fracture). Figure 11 shows the corresponding damage distributions for both the 4 and 64 finite element unit cells and the GMC 4-cell and 49-cell RVE models.

Conclusions

A coupled/uncoupled deformation and fatigue damage algorithm has been presented. The algorithm utilizes a multiaxial, isothermal, stress-based, transversely isotropic continuum fatigue damage model in which the fatigue damage calculations are coupled with the nonlinear finite element solution using the concept of effective stress. Incorporated in the life prediction scheme are failure criteria checks at both the element and structural level. The algorithm has been applied to a cladded MMC ring insert representing a typical aerospace component and results have been presented in terms of *S-N* curves along the damage distribution plots over the ring cross section. The fatigue damage results presented are qualitative in nature since no

TABLE 6—*Fatigue lives for a 35% fiber fraction SCS-6/Ti-15-3 composite loaded longitudinally.*

	Fatigue Life, Cycles					
Load, MPa	4 Finite Element	4-Cell GMC	Difference, %	64 Finite Elements	49-Cell GMC	Difference, %
1345	2939	2497	17.7	2858	2494	14.5
1207	4957	4245	16.7	4859	4234	14.7
931	21497	20459	5.0	20992	20098	4.0
793	64496	61235	5.3	62366	59843	4.0

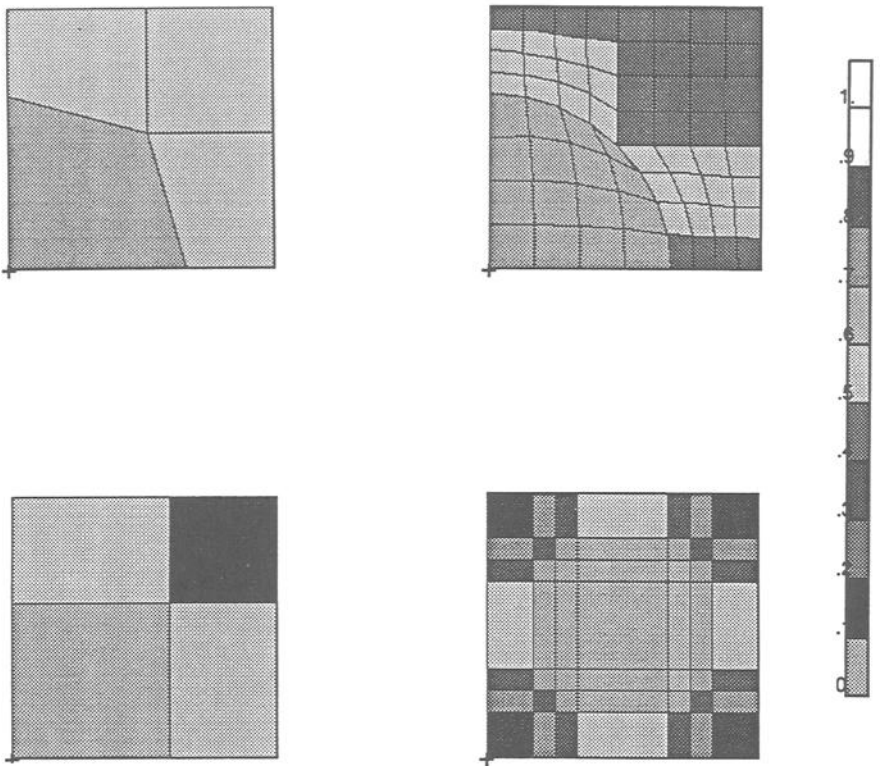

FIG. 11—*Representative damage states: finite element and GMC unit cells.*

experimental results are currently available. However, full-scale burst pressure and fatigue tests will be performed on similar cladded MMC rings. Once these test results become available, a similar finite element analysis will be conducted to verify the present fatigue damage algorithm and continuum fatigue damage model.

With regards to the micromechanics fatigue damage analysis, future work will involve predicting the transverse fatigue behavior of the same SiC/Ti-15-3 composite. Comparisons will also be made between the finite element method and the generalized method of cells in terms of accuracy and computational efficiency. Finally, an attempt will be made to repeat the macro-based MMC ring insert life analysis, but this time using a micromechanics-based approach.

References

[1] Arnold, S. M. and Kruch, S., "Differential Continuum Damage Mechanics Models for Creep and Fatigue of Unidirectional Metal Matrix Composites," *International Journal of Damage Mechanics*, Vol. 3, No. 2, 1994, pp. 170–191.

[2] Lemaitre, J. and Chaboche, J. L., *Mechanics of Solid Materials*, Cambridge University Press, Cambridge, UK, 1990.

[3] Chaboche, J. L., "Continuum Damage Mechanics: Part I–General Concepts," *Journal of Applied Mechanics*, Vol. 55, 1988, pp. 59–64.

[4] Chaboche, J. L., "Continuum Damage Mechanics: Part II–Damage Growth, Crack Initiation and Crack Growth, *Journal of Applied Mechanics*, Vol. 55, 1988, pp. 65–72.

[5] *PATRAN User Manual*, The MacNeal-Schoendler Corp., Los Angeles, CA, 1995.
[6] *MARC, Revision K.5, Volume D: User Subroutines*, MARC Analysis Research Corporation, Palo Alto, CA, 1995.
[7] Arnold, S. M. and Wilt, T. E., "A Deformation and Life Prediction of a Circumferentially Reinforced SiC/Ti 15-3 Ring," *Reliability, Stress Analysis and Failure Prevention*, DE-Vol. 55, R. J. Schaller, Ed., 1993, pp. 231–238.
[8] Wilt, T. E. and Arnold, S. M., "A Computationally-Coupled Deformation and Damage Finite Element Methodology," *HITEMP Review 1993*, Vol II, NASA CP19117, NASA, Cleveland, OH, pp. 35:1–15.
[9] Paley, M. and Aboudi, J., "Micromechanical Analysis of Composites by the Generalized Cells Model," *Mechanics of Materials*, Vol. 14, 1992, pp. 127–139.
[10] Wilt, T. E. and Arnold, S. M., *Micromechanics Analysis Code (MAC) User Guide: Version 2.0*, NASA TM-107290, NASA, Cleveland, OH, 1996.
[11] Wilt, T. E., "On the Finite Element Implementation of the Generalized Method of Cells Micromechanics Constitutive Model," NASA CR-195451, NASA, Cleveland, OH, 1995.

Alain Burr,[1] *François Hild,*[1] *and Frederick A. Leckie*[2]

Damage, Fatigue, and Failure of Ceramic-Matrix Composites

REFERENCE: Burr, A., Hild, F., and Leckie, F. A., **"Damage, Fatigue, and Failure of Ceramic-Matrix Composites,"** *Applications of Continuum Damage Mechanics to Fatigue and Fracture, ASTM STP 1315*, D. L. McDowell, Ed., American Society for Testing and Materials, 1997, pp. 83–96.

ABSTRACT: Matrix cracking, interfacial debonding and sliding, fiber breakage and fiber pullout induced loss of stiffness, inelastic strains, hysteresis loops, and crack closure. These mechanisms are analyzed within the framework of continuum mechanics through the introduction of internal variables. Two models that are faithful to the micromechanical analysis are studied. They provide guidance on the choice of the relevant internal variables to describe the mechanical behavior of unidirectional fiber-reinforced composites. Ultimate strength properties of fiber-reinforced composites are derived and compared with results related to localization. Extensions to cyclic load histories are discussed in terms of ultimate strength reached after cycling.

KEYWORDS: matrix cracking, debonding, fiber breakage, interfacial shear strength, interfacial wear, ultimate strength, continuum damage mechanics, state potential, internal variables, fatigue failure maps, fatigue (materials), fracture (materials)

The basic mechanisms related to the degradation of ceramic-matrix composites submitted to monotonic and cyclic load histories are matrix cracking, interfacial debonding and sliding, interfacial wear, and eventually fiber breakage and fiber pullout. These mechanisms are studied within the framework of continuum mechanics by using results of micromechanical analyses. An explicit expression of the Helmholtz free energy density is derived in the case of monotonic and cyclic load conditions. In particular, internal variables are carefully chosen to describe the degradation mechanisms (for example, a damage parameter characterizing matrix cracking, another one modeling fiber breakage) and written in a more appropriate format to allow the derivation of constitutive equations applicable to structural calculations [*1,2*].

In the case of cyclic load histories, the gradual degradation of the interface is modeled by an interfacial wear law. The evolution laws of some state variables have to be rewritten to account for interfacial wear.

In the case of monotonic and cyclic load histories, the failure conditions are written in terms of macrocrack initiation conditions (that is, localization conditions). Failure conditions are compared with ultimate tensile strength predictions. Under cyclic load, failure conditions are

[1] Post-graduate researcher and research associate professor, respectively, Laboratoire de Mécanique et Technologie, ENS de Cachan/CNRS/Université Paris 6, 61 avenue du Président Wilson, F-94235 Cachan Cedex, France.

[2] Professor, Department of Mechanical and Environmental Engineering, College of Engineering, University of California, Santa Barbara, CA 93106-5070.

summarized by the introduction of a shear stress map in which three different regimes appear depending on the stress amplitude and the number of cycles.

Matrix Cracking Mechanism

A continuum mechanics formulation applied to fiber-reinforced ceramic matrix composites (CMCs) is written within the framework of the thermodynamics of irreversible processes [*3,4*]. The first step in establishing such a model is to identify the internal variables that define the state of the material. The second step is to determine the expression of the state potential in terms of the state variables, and the third one is to define the evolution laws of the internal variables. The state potential, $\bar{\psi}$, is made up of the sum of two terms, namely, the elastic energy density, $\bar{\psi}_e$, and the stored energy density, $\bar{\psi}_s$. The elastic part is directly related to the applied load. The stored energy density is the result of residual stress fields that give rise to macroscopic strains with no applied load. By considering two elastic steps, the total free energy density can be evaluated following a so-called "cut and paste" technique introduced by Volterra [*5*]. This approach will be used to study the degradation of fiber-reinforced composites.

General Expression of the Free Energy Density

Loading a composite consisting of a brittle matrix supported by stronger fibers, usually causes multiple matrix cracking that is accompanied by interfacial debonding and sliding. In the following, we assume that the whole matrix cracking process occurs at load levels lower than the fiber breakage mechanism, and therefore the former mechanism will first be analyzed. The matrix cracks, which are assumed to be perpendicular to the fiber directions, cause a stiffness

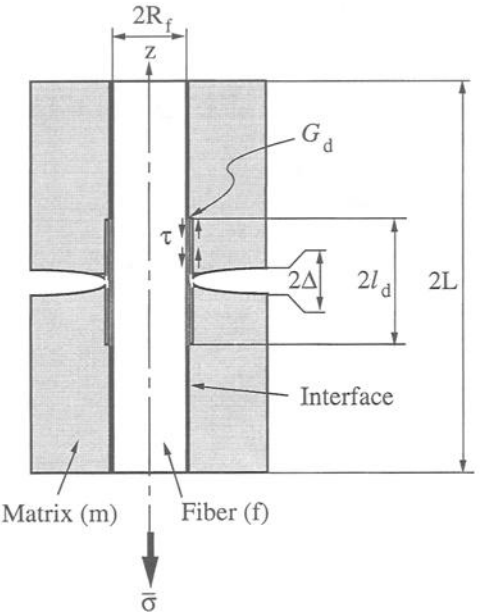

FIG. 1—*Elementary cell.*

reduction when the applied stress, $\bar{\sigma}$, is tensile. Furthermore, it is the closure of the cracks that indicates the onset of increased stiffness when the specimen is subsequently loaded in compression. We will use elementary cells of length, $2L$, characterizing the average crack spacing, and consisting of two different materials (m and f) as shown in Fig. 1, where E is the Young's modulus of the unbroken composite, E_m that of the matrix (m), and E_f that of the fiber (f). In the absence of residual stresses due to processing, the presence of matrix cracks implies a potential energy density change $\Delta\bar{\varphi}_c$ written as

$$\Delta\bar{\varphi}_c = \frac{\bar{\sigma}^2}{E}\,\bar{\omega}_c(L) \tag{1}$$

where $\bar{\omega}_c(L)$ = quantity depending on the average crack spacing, L [6].
The cracking mechanism is dissipative and does not store energy. It only influences $\bar{\psi}_e$.

Debonding followed by sliding gives rise to inelastic strains and hysteresis loops. To describe these phenomena, different models have been proposed [7,8]. They all consider a friction length, $2l_F$, here assumed to be equal to the debond length, $2l_d$ (Fig. 1). Similarly to cracking, which is a Mode I mechanism, debonding per se is purely dissipative. When debonding and slip occur simultaneously, a self-balanced microscopic stress field is introduced. The corresponding strains in the matrix and in the fiber are denoted by $\Delta\varepsilon_m(z)$ and $\Delta\varepsilon_f(z)$, respectively, where z is the current coordinate. By application of the principle of virtual work, an overall inelastic strain, $\bar{\varepsilon}_i$, can be derived [2]

$$\bar{\varepsilon}_i = \frac{1}{2L}\int_{-L}^{L} \Delta\varepsilon_f(z)\,dz \tag{2}$$

Since the additional stress field is self-balanced, the debonding and sliding processes are able to store energy. This result shows that to fully characterize both mechanisms the knowledge of the stored energy density, $\bar{\psi}_s$, is crucial. It is expressed as the total elastic energy density associated with the residual stress field due to debonding and sliding

$$\bar{\psi}_s = \frac{1}{2L}\int_{-L}^{L} \frac{1}{2}\left[fE_f\Delta\varepsilon_f^2(z) + (1-f)E_m\Delta\varepsilon_m^2(z)\right]dz \tag{3}$$

where f = fiber volume fraction.

The matrix cracking process described by an internal damage variable complies with the requirement of a fully dissipative mechanism. In a continuum damage mechanics framework, the presence of a crack results in a stiffness reduction defined by an internal damage variable, D, [9] and the potential energy change can be written as follows

$$\Delta\bar{\varphi}_c = \frac{\bar{\sigma}^2}{2E}\,\frac{D}{1-D} \tag{4}$$

so that the corresponding Gibbs' elastic energy density of a damaged material is written as $\bar{\varphi}_e = \bar{\sigma}^2/2E(1-D)$.

To characterize fully the debonding and sliding mechanisms, two variables are needed. The

first one is the inelastic strain, $\bar{\varepsilon}_i$, and the second, denoted by d, which is usually proportional to the debond length, l_d, is introduced to define the stored energy (Eq 3)

$$\bar{\psi}_s = \frac{E}{2}\frac{\bar{\varepsilon}_i^2}{d} \text{ with } d = \frac{(1-f)E_m}{fE_f}\frac{\left[\frac{1}{2L}\int_{-L}^{L}\Delta\varepsilon_f(z)\,dz\right]^2}{\frac{1}{2L}\int_{-L}^{L}\Delta\varepsilon_f^2(z)\,dz} \tag{5}$$

In addition to the total strain, $\bar{\varepsilon}$, the total free energy density, $\bar{\psi}$, is therefore dependent on three internal variables: one damage variable, D, modeling matrix cracking and related to the average crack spacing, and two variables, $\bar{\varepsilon}_i$ and d, describing debonding and sliding, and related to the debond length and the crack opening displacement due to sliding

$$\bar{\psi} = \frac{E(1-D)}{2}(\bar{\varepsilon} - \bar{\varepsilon}_i)^2 + \frac{E}{2}\frac{\bar{\varepsilon}_i^2}{d} \tag{6}$$

The associated forces are defined as follows

$$\bar{\sigma} = \frac{\partial\bar{\psi}}{\partial\bar{\varepsilon}},\ Y = -\frac{\partial\bar{\psi}}{\partial D},\ y = -\frac{\partial\bar{\psi}}{\partial d},\ \bar{X} = -\frac{\partial\bar{\psi}}{\partial\bar{\varepsilon}_i} \tag{7a,b,c,d}$$

Equation 7*a* defines the macroscopic stress, $\bar{\sigma}$. Equation 7*b* defines the energy release rate density, Y, playing a similar role as the energy release rate, G, in linear elastic fracture mechanics. Combining Eqs 7*a* and *b*, one shows that the energy release rate density, Y, is proportional to the square of the effective stress, $\bar{\sigma}/(1-D)$. Similarly, Eq 7*c* defines the stored energy density, y, released during debonding and sliding. Since the variable, d, depends upon the details of the interfacial behavior, the definition of its associated force is also dependent upon the interfacial behavior. Finally, Eq 7*d* defines the back stress, $\bar{X}$, related to debonding and sliding. Again, its exact value depends upon the interfacial behavior.

To determine the evolution laws of the internal variables, two ways can be followed. The first one is using simulations of the complete micromechanical model along the lines developed, for instance, by Feillard et al. [*10*] to get the evolution of crack spacing, L, and debond length, l_d, and then the state potential. The second one is by performing experiments. The damage variable, D, is obtained by measuring the initial unloading modulus (Fig. 2), and the corre-

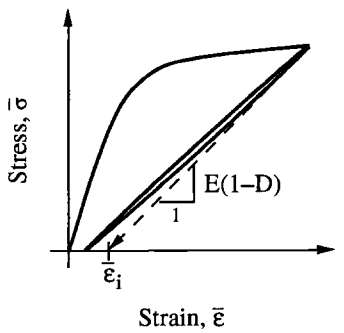

FIG. 2—*Schematic stress/strain curve.*

sponding inelastic strain is $\bar{\varepsilon}_i$. Applications of this kind of identification procedure can be found in Ref *11*. To measure the damage variable, d, the stored energy density, $\bar{\psi}_s$, has to be evaluated, for instance, by using methods developed by Chrysochoos et al. [*12*] or Cho et al. [*13*].

Relationship Between Internal Variables and Microscopic Quantities

In this subsection, expressions of the three internal variables, D, $\bar{\varepsilon}_i$ and d, are derived from some simple micromechanical models. By using a shear lag analysis [*14*] and Eqs 1 and 4, the damage variable, D, is linked to the average crack spacing, L, by the relationship

$$\frac{D}{1-D} = 2\bar{\omega}_c(L) = \frac{(1-f)E_m}{fE_f}\frac{\tanh \beta L}{\beta L} \tag{8}$$

where the constant, β, is a function of the elastic and geometric properties of the fiber and the matrix and is on the order of $1/R_f$ for many CMCs. The strain distribution, $\Delta\varepsilon_f(z)$, in the friction zone in the fiber is assumed to be linear and characterized by a constant interfacial shear strength, τ_0 [*15,16*]. It is also assumed that the debond energy release rate, G_d, is negligible so that the inelastic strain, $\bar{\varepsilon}_i$, is then given by [*8*]

$$\bar{\varepsilon}_i = \frac{\tau_0 l_d^2}{E_f R_f L} \tag{9}$$

where

R_f = fiber radius, m; and
l_d = debond length (inversely proportional to τ_0), m.

Equations 2 and 9 show that the inelastic strain is a function of the average crack spacing as well as the debond length. It is worth noting that other interfacial models can be used: they will yield other expressions in Eq 9, even though Eq 2 remains valid. The definition of the variable, d, is directly obtained from its definition in the expression of the stored energy density, $\bar{\psi}_s$, given in Eq 3

$$d = \frac{3}{4}\frac{(1-f)E_m}{fE_f}\frac{l_d}{L} \tag{10}$$

The damage variable, d, defines the size of the slip zone related to the crack spacing length, l_d/L.

Effect of Stress Redistribution Due to Matrix Cracking

To study the ability of CMCs to redistribute stresses, a two-bar structure is analyzed (see Fig. 3*a*) that describes the effect of a strain concentration. This example is representative of more complex configurations (for example, plates with holes, notched specimens, pin-loaded structures) for which strain concentrations occur. The length and cross-sectional area of Bar (1) are Λ and $(1-F)S$, and of Bar (2) are $k\Lambda$ and FS. The model allows variation of the load distribution in the bars and consequently the stress concentration. To simplify the analysis, only matrix cracking is modeled by the introduction of the damage variable, D (that is, no inelastic strain). The damage variable evolves provided any local stress is greater than the matrix cracking stress, σ_{mc}, up to the ultimate strength, σ_u. When a constant load, $S\Sigma$, is applied, three

different regimes can be defined. First, when the stress level is low (that is, $\Sigma/\sigma_{mc} < 1 - F + F/k$), there is no cracking ($\sigma_1 < \sigma_{mc}$, $\sigma_2 < \sigma_{mc}$) and the two bars behave elastically thereby defining an "elastic" regime. Second, for higher stress levels ($1 - F + F/k \leq \Sigma/\sigma_{mc} < k(1 - D_1)(1 - F) + F$), the shortest bar (that is, Bar (1)) experiences cracking ($\sigma_1 \geq \sigma_{mc}$) whereas the longest one is still elastic. This condition is defined as "confined cracking." The upper bound of this regime shows that the effect of confined cracking is a reduction of the stress concentration from an initial value of k to $k(1 - D_1)$ assumed to be greater than 1. Third, for very high stress levels (that is, $\Sigma/\sigma_{mc} \geq k(1 - D_1)(1 - F) + F$), the two bars experience matrix cracking and that defines a regime of "extensive cracking." The third regime exists provided the ultimate strength, σ_u, is not exceeded. When $\sigma_u/\sigma_{mc} < k(1 - D_u)$, where D_u is the damage parameter at the ultimate, the extensive cracking regime is excluded. On the other hand, when $\sigma_u/\sigma_{mc} \geq k(1 - D_u)$, the extensive cracking regime exists. When the strain concentration is low (that is, $\sigma_u/\sigma_{mc} \geq k$), the latter regime will always occur.

Wear Mechanism During Cyclic Loading

Under cyclic loading, wear may take place at the fiber/matrix interface because of stress reversals [*17*]. An estimate of the effect of cyclic loading on the mechanical behavior is possible when the influence of interfacial wear is included in the model. The effect of wear is a change of the residual stress field induced by debonding and sliding. Therefore, as the number of cycles, N, increases, there is a variation of the associated additional strains $\Delta\varepsilon_m(z,N)$ and $\Delta\varepsilon_f(z,N)$. By inspection of Eqs 2 and 3, there is a direct influence of wear on the inelastic strain as well as the damage variable, d. Thus, to write the evolution laws during fatigue, one needs to model the evolution of wear as a function of the number of cycles.

When a constant stress amplitude is applied and if the interfacial behavior is modeled by a constant interfacial shear strength, the evolution, $\tau(N)$, as a function, N, can be written as $\tau(N) = \tau_0\Phi(N)$, where Φ is a decreasing function with the number of cycles ($\Phi(0) = 1$) [*18*]. The evolution of the variables, $\bar{\varepsilon}_i(N)$ and $d(N)$, can be related to the initial values, $\bar{\varepsilon}_{i0}$ an l d_0, reached during the first cycle by

$$\bar{\varepsilon}_i(N) = \frac{\bar{\varepsilon}_{i0}}{\Phi(N)}, \; d(N) = \frac{d_0}{\Phi(N)} \tag{11}$$

Effect of Stress Redistribution Due to Debonding During Fatigue

The model is now used to assess the stress redistribution during fatigue of the two-bar structure depicted in Fig. 3*a*. This application is valid as long as the stress amplitude is slowly varying so that Eq 11 can be used. The key mechanisms to consider are matrix cracking modelled by D and debonding and sliding described by $\bar{\varepsilon}_i$. When the local stress is greater than the matrix cracking stress, σ_{mc}, the damage variable and the inelastic strain grow until the total strain reaches a critical value, ε_u. For the case when the cyclic load has a constant maximum value, $S\Sigma$, three different regimes can again be identified. The elastic regime is the same as for a constant load condition when the behavior is everywhere elastic (when $\Sigma/\sigma_{mc} < 1 - F + F/k$). The confined cracking regime is defined by $1 - F + F/k \leq \Sigma/\sigma_{mc} < k(1 - D_1)(1 - F) + F - (1 - D_1)(1 - F)E\varepsilon_{i1}/\Phi(N)\sigma_{mc}$, when the shortest Bar (1) experiences cracking so that debonding and wear occur. In this regime, the most loaded Bar (1) experiences a decrease of the maximum stress level, $\sigma_1(N) = (\Sigma - FE\varepsilon_{i1}/\Phi(N)k)/(1 - F + F/k(1 - D_1))$ as the number

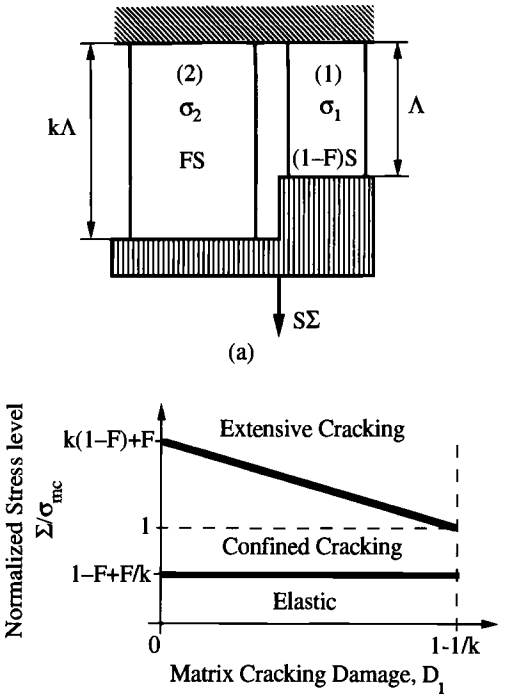

FIG. 3—(a): *Two-bar structure, and* (b): *stress redistribution map exhibited by matrix cracking.*

of cycles, N, increases, therefore the damage variable, D_1, remains constant. The effect of confined cracking is to reduce the stress concentration. Third, for very high stress levels (when $\Sigma/\sigma_{mc} \geq k(1 - D_1)(1 - F) + F - (1 - D_1)(1 - F)E\varepsilon_{i1}/\Phi(N)\sigma_{mc}$), the two bars experience cracking, debonding, and wear: it is an extensive cracking regime. The boundary between the two regimes is defined by the following condition schematically depicted in Figs. 4*a* and *b*

$$\frac{\Sigma}{\sigma_{mc}} = k(1 - F)(1 - D_1) + F - \frac{(1 - F)(1 - D_1)E\varepsilon_{i1}}{\Phi(N)\sigma_{mc}} \tag{12}$$

The third regime exists provided the maximum accumulated strain, ε_u, is not reached. The failure condition is represented by the condition, $\varepsilon_1 = \varepsilon_u$, that can be expressed as $\Sigma/\sigma_{mc} = E\varepsilon_u/k\sigma_{mc}\,[k(1 - D_1)(1 - F) + F] - (1 - F)(1 - D_1)E\varepsilon_{i1}/\Phi(N)\sigma_{mc}$. In many composites, ε_u is very well approximated by the ultimate tensile strain under monotonic load conditions and the dimensionless parameter, $E\varepsilon_u/\sigma_{mc}$, varies between 4 and 8 for many composite materials [*19*]. When $E\varepsilon_u/\sigma_{mc}k \leq 1$, the extensive cracking regime will never be reached because failure occurs prior to reaching the confined/extensive regime boundary. Conversely, when $E\varepsilon_u/\sigma_{mc}k > 1$, the extensive cracking regime will occur. If $\Phi(N \to +\infty) > (1 - F)(1 - D_1)E\varepsilon_{i1}/[\{k(1 - D_1) - 1\}(1 - F) + F - F/k]\sigma_{mc}$, fatigue life is infinite in the confined cracking regime (Fig. 4*a*). On the other hand, when $\Phi(N \to +\infty) \leq (1 - F)(1 - D_1)E\varepsilon_{i1}/[\{k(1 - D_1) - 1\}(1 - F) + F - F/k]\sigma_{mc}$, there is no fatigue endurance in the confined cracking regime (Fig.

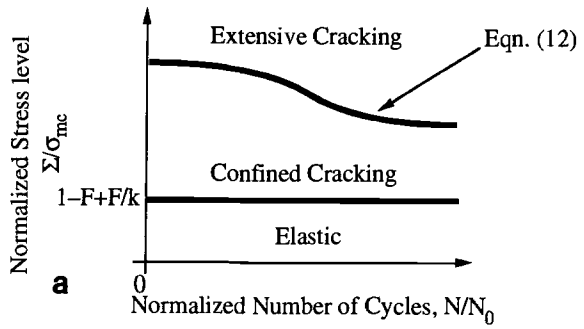

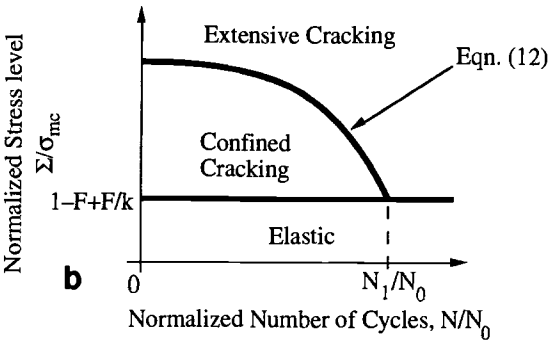

$$(a)\ \Phi(N \to +\infty) > \frac{(1-F)(1-D_1)E\varepsilon_{i1}}{\left[\{k(1-D_1)-1\}(1-F)+F-\dfrac{F}{k}\right]\sigma_{mc}}$$

$$(b)\ \Phi(N \to \pm\infty) \leq \frac{(1-F)(1-D_1)E\varepsilon_{i1}}{\left[\{k(1-D_1)-1\}(1-F)+F-\dfrac{F}{k}\right]\sigma_{mc}}$$

FIG. 4—*Stress redistribution map exhibited by debonding and sliding.*

4*b*) and one number of cycles can be defined: N_1 so that $\Phi(N_1) = (1-F)(1-D_1)E\varepsilon_{i1}/[\{k(1-D_1)-1\}(1-F)+F-F/k]\sigma_{mc}$. In Fig. 4, all the results are written in terms of a reference number of cycles, N_0, modeling the shear stress decay. In many CMCs, N_0 is on the order of 10 to 100 and can be smaller for SiC/CAS composites [*19*]. This study will be complete if fiber breakage is modeled, since for many composites, it is the key mechanism leading to final failure.

Fiber Breakage Mechanism

A unit cell of length, L_R, is considered where the matrix crack spacing is $2L$. The length, L_R, is the "recovery" length and refers to twice the longest fiber that can be pulled out and cause a reduction in the load carrying capacity. For the sake of simplicity, it is assumed that matrix cracking has saturated and the stress contribution due to the matrix is negligible when compared

to that due to the fibers. The initial Young's modulus of the composite is thus assumed to be equal to fE_f. Away from a fiber break, as in the case of matrix cracking, the fiber stress builds up through the stress transfer across the sliding fiber-matrix interface. If the interfacial shear stress, τ_0, is assumed to be constant, the recovery length is related to the maximum stress in the fiber by [*20*]

$$L_R = \frac{R_f T}{\tau_0} \tag{13}$$

where T = reference stress (that is, fiber stress in the plane of the matrix crack), Pa.

The model now discussed takes account of three features induced by fiber breakage and fiber pullout, namely, the reduction in stiffness due to fiber breakage, the inelastic strains due to fiber pullout, and the hysteresis loops. The details of the unloading and reloading process are complex and to avoid this difficulty it is useful to introduce the crack opening displacement, δ, that characterizes the material state related to the reverse friction. The crack opening displacement, δ, is also useful in determining the conditions when closure occurs. To characterize the state of the composite, four quantities are required. These are the overall strain, $\bar{\varepsilon}$, the friction length, L_F, the percentage, P_F, of broken fibers within the recovery length, $L_R = 2L_F$, and the crack opening displacement, δ. To derive the free energy density associated to a loading sequence, we consider two different elastic steps to reach the same state. The first step consists of moving the unbroken fibers with respect to the broken fibers with no external load by an amount, δ, over a length, L_F. The elastic density associated with this process is given by [*21*]

$$\bar{\psi}_s = \frac{fE_F}{2}\left(\frac{\delta}{L_F}\right)^2 P_F \frac{4 - 3P_F}{3} \tag{14}$$

and the opening displacement, δ, induces an overall inelastic strain, $\bar{\varepsilon}_i$

$$\bar{\varepsilon}_i = \frac{\delta}{L_F} P_F \tag{15}$$

The second step, during which no friction occurs, consists of adding an elastic loading from the previous state. It involves an additional elastic energy density given by

$$\bar{\psi}^e = \frac{fE_F}{2}(\bar{\varepsilon} - \bar{\varepsilon}_i)^2 \tag{16}$$

The total free energy density is then the sum of the two energies. A more convenient expression for the free energy density is obtained by using state variables in a modified form. The state variables are the total strain, $\bar{\varepsilon}$, the damage variable modeling the percentage of broken fibers within L_R, $D_f = P_F$, and the inelastic strains, $\bar{\varepsilon}_i$, due to the crack opening displacement, δ, modeling fiber pullout. The free energy density, $\bar{\psi}$, can then be written in terms of the new internal variables

$$\bar{\psi} = \frac{fE_F}{2}(\bar{\varepsilon} - \bar{\varepsilon}_i)^2 + \frac{fE_F}{2}\frac{4 - 3D_f}{3D_f}\bar{\varepsilon}_i^2 \tag{17}$$

The thermodynamic forces associated with the new state variables are respectively given by

$$\bar{\sigma} = \frac{\partial \bar{\psi}}{\partial \bar{\varepsilon}} = fE_F(\bar{\varepsilon} - \bar{\varepsilon}_i),\ Y_f = -\frac{\partial \bar{\psi}}{\partial D_f} = \frac{2fE_F}{3}\left(\frac{\bar{\varepsilon}_i}{D_f}\right)^2,$$

$$\bar{X} = -\frac{\partial \bar{\psi}}{\partial \bar{\varepsilon}_i} = fE_F\left(\frac{4\bar{\varepsilon}_i}{3D_f} - \bar{\varepsilon}\right) \quad (18a,b,c)$$

where

Y_f = energy release rate density associated with fiber breakage, Jm^{-3}; and
$\bar{X}$ = back stress, Pa.

When the fibers are assumed to exhibit a statistical variation of strength that obeys a two-parameter Weibull law, the evolution laws of the damage variable and the inelastic strain are given by [*21*]

$$D_f = 1 - \exp\left[-\left(\frac{E_f\bar{\varepsilon}_M}{S_c}\right)^{m+1}\right],\ \bar{\varepsilon}_i = \frac{1}{2}\bar{\varepsilon}_M D_f \quad (19)$$

$$S_c^{m+1} = \frac{L_0 S_0^m \tau}{R_f} \quad (20)$$

where

$\bar{\varepsilon}$ = current strain;
$\bar{\varepsilon}_M$ = maximum strain;
S_c = characteristic strength, Pa;
m = shape parameter;
S_0 = stress scale parameter, Pa;
L_0 = gage length, m; and
τ = interfacial shear strength, Pa.

Provided the fibers are subject to global load sharing, that is, the load transmitted from each failed fiber is shared equally among the intact fibers, the ultimate tensile strength, $\bar{\sigma}_{\mathrm{UTS}}$, is then scaled by the characteristic strength [*22*], S_c, according to

$$\bar{\sigma}_{\mathrm{UTS}} = fS_cF(m) \quad (21)$$

The function, F, depends upon the shape parameter, m, and whether localization happens or not before the peak stress [*20,23,24*]. To assess the ultimate tensile strength, the function, F, is given by [*20*]

$$F(m) = \left(\frac{2}{m+2}\right)^{1/(m+1)}\frac{m+1}{m+2} \quad (22)$$

and to calculate the localization tensile strength, the function, F, can be written as [*24*]

$$F(m) = \frac{1}{2}\left(\frac{1}{m+1}\right)^{1/(m+1)}\left\{1 + \exp\left(-\frac{1}{m+1}\right)\right\} \quad (23)$$

Equations 20 and 21 show that the interfacial shear resistance, τ, is a key parameter. If wear is involved, it is expected that the interfacial shear strength, τ, decreases as the number of

cycles, N, increases as discussed earlier. The simple model of interfacial wear introduced previously can be used directly to evaluate the residual ultimate strength of fatigued CMCs [*18*]. The drawback of this simple wear model is that the influence of the load ratio is not modeled. In the following, we will introduce another wear mechanism accounting for the load ratio, R.

Fatigue Failure Maps

When cyclic stress experiments are performed on CMCs, it is known that the first cycle is often the most damaging in reducing of shear strength [*17*]. Therefore, following the first reversal of sliding, the frictional shear stress is assumed to decrease from τ_0 to τ_∞. Upon first loading to a maximum stress, $\overline{\sigma}$, a friction length, $2l_{d0}$, is reached ($l_{d0} \leq L$) over which the shear strength is equal to τ_0 (Figs. 5*a* and *b*). Upon unloading to $\overline{\sigma} - \Delta\overline{\sigma} = R\overline{\sigma}$ a shear stress reversal occurs over a length, $2l_{u1}$, for which the interfacial shear strength is equal to τ_∞. Upon reloading to $\overline{\sigma}$, there is shear stress reversal over the length, $2l_{u1}$, for which the interfacial shear strength is still τ_∞; together with $\overline{\sigma}$, debonding and sliding evolve from $2l_{d0}$ to $2l_{d1}$, for which the interfacial shear stress is τ_0. As the number of cycles, N, increases, there is an increase of $l_{d(N+1)}$ and $l_{u(N+1)}$ [*25*]. A key parameter is involved: $\gamma = (\tau_0 - \tau_\infty)/(\tau_0 + \tau_\infty)$, $0 < \gamma < 1$. It measures the amount of wear. Provided subcritical crack propagation does not exist, there is no further matrix cracking under cyclic loading conditions. However, fiber breakage may occur since the longitudinal stress in the fibers increases as a result of wear. In the following, we will

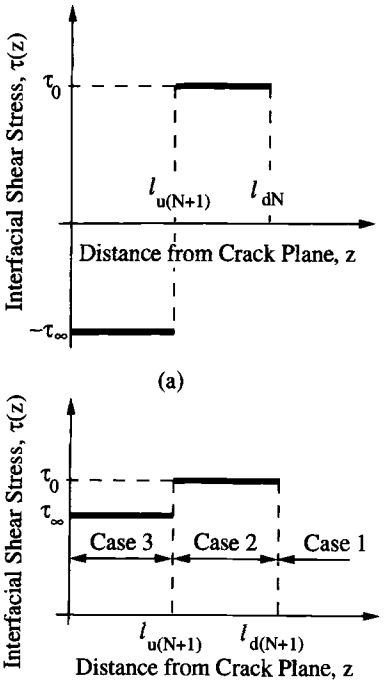

FIG. 5—*Shear stress profile along the fiber direction during one unloading* (a) *-reloading* (b) *sequence.*

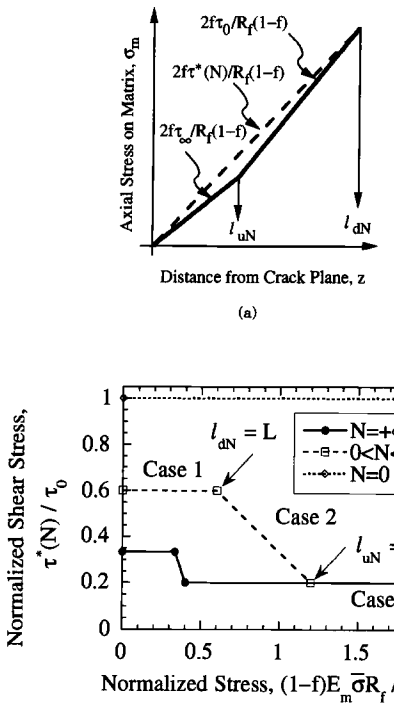

FIG. 6—(a) *Depiction of the equivalent shear stress* $\tau^*(N)$ *where the symbol* ⟶ *denotes the slope of a pointed straight line, and* (b) *shear stress map when* $\tau_\infty/\tau_0 = 0.2$, R = 0.

neglect this phenomenon. Furthermore, crack closure effects may occur upon unloading. We assume that the stress amplitude is small enough to avoid that phenomenon.

There are three cases to be considered. In case 1, $L > l_{dN}$, the condition for matrix cracking saturation is not reached. For Case 2, $l_{uN} \leq L \leq l_{dN}$, matrix cracking saturation occurs and the friction characteristics involve τ_0 and τ_∞. For Case 3, $l_{uN} > L$, matrix cracking saturation takes place but the friction characteristics only involve τ_∞ (Fig. 5*b*). An equivalent shear stress is defined to determine fatigue properties (Fig. 6*a*). The evolution of the latter is given by

$$\frac{\tau^*(N)}{\tau_0} = \begin{cases} \dfrac{1-\gamma}{1-\gamma R-(1-R)\gamma^{N+1}} & L \geq l_{dN} \\ 1-\dfrac{\gamma}{1-\gamma}\dfrac{(1-R)(1-f)E_m\bar{\sigma}R_f}{2fE\tau_0 L}(1-\gamma^N) & l_{uN} \leq L < l_{dN} \\ \dfrac{1-\gamma}{1+\gamma} = \dfrac{\tau_\infty}{\tau_0} & L < l_{uN} \end{cases} \tag{24}$$

from which the shear stress map shown in Fig. 6*b* can be obtained. When $N = 0$, $\tau^*(0) = \tau_0$ since no reversal occurred. On the other hand, when $N \to +\infty$, since $\gamma < 1$, the maximum value of $\tau^*(\infty) = \tau_0(1-\gamma)/(1-\gamma R)$ and the minimum value of $\tau^*(\infty) = \tau_\infty$. This last result

shows that τ_∞ can only be reached if saturation takes place during cycling ($L < l_{d\infty}$) and complete reversal occurs at least one cycle over a length, L ($L < l_{u\infty}$). This map is useful for deriving the ultimate fatigue strength according to Eqs 21 and 24. Under monotonic loading conditions, the value of τ in Eq 21 is taken equal to τ_0, whereas under cyclic loading conditions, it is taken equal to $\tau^*(N)$. It is worth noting that these results directly include the amplitude effect by the presence of the load ratio, R.

Conclusions

The basic mechanisms related to the degradation of CMCs submitted to monotonic and cyclic load histories were studied within the framework of continuum mechanics by using results of micromechanical analyses. An explicit expression of the Helmholtz free energy density was derived in the case of monotonic load conditions. In particular, internal variables are carefully chosen to describe the degradation mechanisms (namely, matrix cracking, fiber breakage). In the case of cyclic load histories, the gradual degradation of the interface was modeled by the introduction of the effect of interfacial wear. The effect of stress redistribution is analyzed on two-bar structures. Generalizations of these results to two-dimensional configurations can be found in Refs *2* and *26* in which the tensorial nature of each internal variable introduced herein is discussed.

In the case of monotonic and cyclic load histories, the failure conditions are written in terms of macrocrack initiation conditions (that is, localization conditions). Failure conditions are close to the ultimate tensile strength predictions. In fatigue, failure conditions are summarized by the introduction of a shear stress map in which three different regimes appear depending on the stress amplitude. These maps are useful to derive the ultimate tensile strength after cycling.

Finally, the only practical application of CMCs are under high temperature exposure. In addition to the mechanisms discussed in this paper, the effects of high temperature are a change of the residual stresses due to the temperature rise and the mismatch of coefficients of thermal expansion of the matrix and the fibers, and to creep of the fibers or the matrix or both. These changes can be introduced in the present framework with minimal change of the formulation discussed herein [*27*]. Furthermore, microscopic properties (for example, interfacial shear strength) may be affected by temperature variations and induced change of chemical composition at the interface. These phenomena can be accounted for by the relationships between microscopic and macroscopic quantities derived in this paper.

References

[*1*] Talreja, R., "Continuum Modeling of Damage in Ceramic Matrix Composites," *Mechanics of Materials*, Vol. 12, 1991, pp. 165–180.

[*2*] Burr, A., Hild, F., and Leckie, F. A., "Micro-Mechanics and Continuum Damage Mechanics," *Archive of Applied Mechanics*, Vol. 65, No. 7, 1995, pp. 437–456.

[*3*] Coleman, D. B. and Gurtin, M. E., "Thermodynamics with Internal State Variables," *Journal of Chemical Physics*, Vol. 47, No. 2, 1967, pp. 597–613.

[*4*] Germain, P., Nguyen, Q. S., and Suquet, P., "Continuum Thermodynamics," *Journal of Applied Mechanics*, Vol. 50, 1983, pp. 1010–1020.

[*5*] Volterra, V., "Sur l'équilibre des corps élastiques multiplement connexes," *Annales Scientifiques de l'Ecole Normale Supérieure, Paris*, Vol. 24, No. 3, 1907, pp. 401–518.

[*6*] Budiansky, B. and O'Connell, R. J., "Elastic Moduli of a Cracked System," *International Journal of Solids and Structures*, Vol. 12, 1976, pp. 81–97.

[*7*] Aveston, J., Cooper, G. A., and Kelly, A., "Single and Multiple Fracture," *National Physical Laboratory: Properties of Fiber Composites*, IPC Science and Technology Press, Surrey, UK, 1971, pp. 15–26.

[*8*] Hutchinson, J. W. and Jensen, H. M., "Models for Fiber Debonding and Fiber Pull-Out in Brittle Composites with Friction," *Mechanics of Materials*, Vol. 9, 1990, pp. 139–163.

[9] Lemaitre, J. and Dufailly, J., "Modélisation et identification de l'endommagement plastique des métaux," *3e congrès français de mécanique*, Grenoble, France, 1977.
[10] Feillard, P., Désarmot, G., and Favre, J. P., "Theoretical Aspects of the Fragmentation Test," *Composite Science and Technology*, Vol. 50, 1994, pp. 265–279.
[11] Hild, F., Burr, A., and Leckie, F. A., "Matrix Cracking and Debonding in Ceramic-Matrix Composites," *International Journal of Solids and Structures*, Vol. 33, No. 8, 1996, pp. 1209–1220.
[12] Chrysochoos, A., Maisonneuve, O., Martin, G., and Caumon, H., "Plastic and Dissipated Work and Stored Energy," *Nuclear Engineering and Design*, Vol. 114, 1989, pp. 323–333.
[13] Cho, C., Holmes, J. W., and Barber, J. R., "Estimation of Interfacial Shear in Ceramic Composites from Frictional Heating Measurements," *Journal of the American Ceramic Society*, Vol. 74, No. 11, 1991, pp. 2802–2808.
[14] Cox, H. L., "The Elasticity and the Strength of Paper and other Fibrous Materials," *British Journal of Applied Physics*, Vol. 3, 1952, pp. 72–79.
[15] Kelly, A. and Tyson, W. R., "Tensile Properties of Fibre-Reinforced Metals: Copper/Tungsen and Copper/Molybdenum," *Journal of the Mechanics and Physics of Solids*, Vol. 13, 1965, pp. 329–350.
[16] Evans, A. G., Domergue, J.-M., and Vagaggini, E., "Methodology for Relating the Tensile Constitutive Behavior of Ceramic Matrix Composites to Constituent Properties," *Journal of the American Ceramics Society*, Vol. 77, No. 6, 1994, pp. 1425–1435.
[17] Rouby, D. and Reynaud, P., "Fatigue Behaviour Related to Interface Modification During Load Cycling in Ceramic-Matrix Fibre Composites," *Composite Science and Technology*, Vol. 48, 1993, pp. 109–118.
[18] Evans, A. G., Zok, F. W., and McMeeking, R. M., "Fatigue of Ceramic Matrix Composites," *Acta Metallurgica et Materialia*, Vol. 43, No. 3, 1995, pp. 859–875.
[19] Heredia, F. E., "UCSB CMCs Survey," Materials Department, University of California, Santa Barbara, 1995.
[20] Curtin, W. A., "Theory of Mechanical Properties of Ceramic Matrix Composites," *Journal of the American Ceramics Society*, Vol. 74, No. 11, 1991, pp. 2837–2845.
[21] Hild, F., Burr, A., and Leckie, F. A., "Fiber Breakage and Fiber Pull-Out of Fiber-Reinforced Ceramic-Matrix Composites," *European Journal of Mechanics A/Solids*, Vol. 13, No. 6, 1994, pp. 731–749.
[22] Henstenburg, R. B. and Phoenix, S. L., "Interfacial Shear Strength Studies Using the Single-Filament-Composite Test. Part II: A Probability Model and Monte Carlo Simulations," *Polymer Composites*, Vol. 10, No. 5, 1989, pp. 389–406.
[23] Curtin, W. A., "Fiber Pull-Out and Strain Localization in Ceramic Matrix Composites," *Journal of the Mechanics and Physics of Solids*, Vol. 41, No. 1, 1993, pp. 35–53.
[24] Hild, F. and Burr, A., "Localization and Ultimate Strength of Fiber-Reinforced Ceramic-Matrix Composites," *Mechanics Research Communications*, Vol. 21, No. 4, 1994, pp. 297–302.
[25] Burr, A. and Hild, F., "Ultimate Tensile Strength during Fatigue of Fiber-Reinforced Ceramic-Matrix Composites," *Mechanics Research Communications*, Vol. 22, No. 4, 1995, pp. 401–406.
[26] Burr, A., Hild, F., and Leckie, F. A., "Continuum Description of Damage in Ceramic-Matrix Composites," *European Journal of Mechanics A/Solids*, Vol. 16, No. 1, 1997, pp. 53–78.
[27] Burr, A., Hild, F., and Leckie, F. A., "Comportement sous chargement thermomécanique cyclique de composites à matrice céramique," *10es Journées Nationales des Composites*, D. Baptiste and A. Vautrin, Eds., AMAC Paris, 1996, pp. 1275–1284.

George Z. Voyiadjis[1] *and Rainer Echle*[1]

A Micromechanical Fatigue Damage Model for Unidirectional Metal-Matrix Composites

REFERENCE: Voyiadjis, G. Z. and Echle, R., **"A Micromechanical Fatigue Damage Model for Unidirectional Metal-Matrix Composites,"** *Applications of Continuum Damage Mechanics to Fatigue and Fracture, ASTM STP 1315*, D. L. McDowell, Ed., American Society for Testing and Materials, 1997, pp. 97–115.

ABSTRACT: Improvements in design and the enhancement in performance of aerospace vehicles calls for the development of advanced materials capable of sustaining the increasing loading conditions while maintaining their structural integrity. Special consideration must be given to the behavior of such materials under fatigue loading conditions that dominate the flight regime loads. A micromechanical fatigue damage model for unidirectional metal-matrix composites is proposed. Damage evolution is considered at the constituent level through the application of the Mori-Tanaka averaging scheme. Individual damage criteria for the constituents are proposed and employed to define damage evolution equations for each of the consultants. The numerical results for high cycle fatigue loading are presented for variations in the material and model parameters.

KEYWORDS: continuum damage mechanics, cracking, fatigue (materials), fracture (materials), damage, damage evolution, micromechanical fatigue damage, metal-matrix composites

With the increased performance of aerospace vehicles, design factors such as weight and material strength play an increased role in their design philosophies. Along with such drastic performance enhancements, appropriate light-weight materials need to be developed that are capable of performing under such conditions as those occurring during flight while retaining their structural integrity. Such candidate materials have been identified among the composite materials, especially in the area of metal-matrix composites (MMCs). Special consideration has been given to titanium-matrix composites (TMC) because these materials maintain their excellent strength-to-density ratio even at elevated temperatures. This intrinsic material property has drawn attention from the turbine engine manufacturing industry for potential use in advanced aircraft turbine engines. This success can be attributed to the tremendous reduction in the weight of key engine components leading to a possible increase in engine performance or reduced fuel consumption or both. Titanium-matrix composites offer higher mechanical properties, better dimensional stability, and strength retention at elevated temperatures, such as those occurring in turbine engines, as compared to their monolithic counterparts. Nevertheless, the employment of MMCs and TMCs still has major drawbacks. First, the production and manufacturing costs for such materials are still high due to the special manufacturing processes involved. Second, the employment of such materials in vital components of an aircraft or space vehicle, such as a turbine engine, requires a thorough understanding and control of the material behavior under extreme loading conditions that occur during regular service life. This calls for the development of material models that are capable of predicting the real-life behavior of such

[1] Boyd professor and doctoral student, respectively, Department of Civil and Environmental Engineering, Louisiana State University, Baton Rouge, LA 70803.

materials with a deterministic margin of risk. As of today, the behavior of MMCs and TMCs is not yet fully understood, and appropriate material models still lack reliability and applicability as compared to those of their monolithic counterparts. A considerable experimental as well as theoretical research effort is put forward to better understand and analytically model metal-matrix composites in order to provide a more efficient use of the tremendous potential contained in these new materials. In particular, the literature lacks a consistent and systematic approach to the analysis of cyclic damage (low-cycle/high-cycle fatigue) in high-temperature metal-matrix composites. This area is addressed in this paper, especially the consistent development of a fatigue damage model for unidirectional MMCs.

Cyclic/Fatigue Damage Models in the Literature

Reviewing the literature on the subject of fatigue in engineering materials reveals that the explanation of fatigue phenomena and the prediction of fatigue life have been the focus of immense research efforts for the last 50 years. The two major analytical approaches used are the phenomenological approach and the crack propagation approach. The former is concerned with lifetime predictions of complex loading histories using existing lifetime test data, mostly *S-N* data, for constant amplitude cyclic loading. The second approach is concerned with predicting the growth of a dominant crack due to cyclic load that is not the case for metal-matrix composites.

Almost all of the known fatigue damage models for composite materials are based on the models developed for their isotropic counterparts [*1–9*]. Lack of theoretical knowledge and sufficient experimental tests on composite materials led to the application of known fatigue damage models to predict the fatigue lifetime of such materials, despite the fact that the fatigue behavior of composite materials is quite different from that of isotropic materials, such as metals. With improvements in the theoretical knowledge of composite materials and experimental equipment, numerous studies have been conducted involving fatigue life and residual strength degradation, modulus degradation, and residual life theories. However, it was soon recognized from these models that the material structure of such composites has to be included in the development of fatigue damage models in order to arrive at more feasible and reliable models. Until now, there is no universal fatigue damage model based on the microstructure of the composite material that is capable of predicting the fatigue lifetime for general fatigue loading with reasonable reliability.

Arnold and Kruch [*10,11*] presented a phenomenological, isothermal transversely-isotropic differential continuum damage mechanics (CDM) model for fatigue of unidirectional composites. The model is based on the CDM fatigue models for isotropic materials developed at ONERA [*12–17*]. They considered the MMC as a pseudohomogeneous material with locally definable characteristics. Such local characteristics have been considered in the form of a directional tensor representing the fiber direction. Furthermore, the concept of anisotropic failure surfaces has been introduced into the model based on deformation theories for the high-temperature MMCs of Robinson et al. [*18*] and Robinson and Duffy [*19*]. Despite rigorous development, the proposed model has two major drawbacks: (1) the expensive experimental setup and exhaustive experiments needed to obtain the material parameters used in the model equations, and (2) the employed scalar measure for the damage variable. Recently, Wilt and Arnold [*20*] presented a fatigue damage algorithm that employs the fatigue damage model developed by Arnold and Kruch [*10,11*]. They implemented their algorithm into the commercial finite element code MARC and used it to analyze a cladded MMC ring. Results were presented on a qualitative basis, since no experimental results are available.

Nicholas [*21*] recently reviewed fatigue lifetime prediction models for TMCs that use fundamentally different approaches. His investigation showed that various models are based on a

single parameter and have limited applicability. Two other models, a dominant damage model [*22*] and a life fraction model, show applicability to various loading ranges, frequencies, and temperature profiles. Neu [*22*] pointed out that despite the fact that several damage mechanisms exist, it is possible to consider the most dominant ones for modeling and include the influence of others, since their behavior might be similar. His model was able to match experimental data for isothermal and thermomechanical fatigue for low-cycle fatigue experiments. The life fraction models, which are based on the fact that fatigue damage accumulates simultaneously due to independent mechanisms, are able to model only specific composite layups for which their parameters have been calibrated. Various other fatigue investigations have been performed, but their focus is on specific ply-stacking sequences of interest at the time of the investigations. In general, it is found that even though micromechanical effects or mechanisms are considered and incorporated into the models there does not yet exist a true micromechanical fatigue damage model that considers the material behavior and damage evolution in the constituents individually. The following proposed micromechanical fatigue damage model is intended to exactly fill in this gap. It is considered a first step along a consistent route to develop a universal micromechanical fatigue damage model capable of modeling various loading conditions including thermomechanical as well as environmental effects that occur during the service life of dynamically loaded composite structures.

Damage Mechanics Applied to Composite Materials

Kachanov [*23*] pioneered the idea of damage in the framework of continuum mechanics. For the case of isotropic damage and using the concept of effective stress, the damage variable is defined as a scalar in the following manner

$$\varphi = \frac{A - \bar{A}}{A} \tag{1}$$

where $\bar{A}$ is the effect (net) resisting area corresponding to the damaged area, A. Using the hypothesis of elastic energy equivalence [*24*], the effective stress, $\bar{\sigma}$, can be obtained from Eq 1 by equating the force acting on the hypothetical undamaged area with the force acting on the actual damaged area.

In a general state of deformation and damage, the scalar damage variable, φ, is replaced by a fourth-order damage effect tensor, $\boldsymbol{M}$, that depends on a second-order damage tensor, ϕ. In general, the effective stress tensor, $\bar{\boldsymbol{\sigma}}$, is obtained using the following relationship

$$\bar{\boldsymbol{\sigma}} = \boldsymbol{M} : \boldsymbol{\sigma} \tag{2}$$

where (:) indicates tensor contraction over two indices. The nature of the damage effect tensor, $\boldsymbol{M}$, is discussed in the literature by Voyiadjis and Kattan [*25,26*].

In general, the analysis of composite materials falls into two categories. The first category consists of all approaches that employ the continuum concept [*27,28*], where the composite system is treated as one continuum and the equations of anisotropic elasticity are used in the analysis. The second category encompasses all approaches that use micromechanical models together with averaging procedures and homogenization techniques [*29–33*] to describe the material behavior. In these models, the composite is considered to be composed of a number of individual phases for which local equations are formulated. Employing a suitable homogenization procedure then allows one to analyze the material behavior of the entire composite system based on the local analysis.

Dvorak and Bahei-El-Din [*30,31*] employed an averaging technique to analyze the elastoplastic behavior of fiber-reinforced composites. They considered elastic fibers with an elastoplastic matrix. However, no attempt was made to introduce damage in the constitutive equations. Voyiadjis and Kattan [*34*], Voyiadjis et al. [*35*], and Voyiadjis and Kattan [*36*] introduced a consistent and systematic damage theory for MMCs utilizing the micromechanical composite model of Dvorak and Bahei-El-Din [*31*]. The introduced two approaches, referred to in the literature as the overall and the local approaches, which allow for a consistent incorporation of the damage phenomenon in a composite material system.

The overall approach [*37*] to damage in composite materials employs one single damage tensor to reflect all types of damage mechanisms that the composite undergoes like initiation, growth, and coalescence of microvoids and microcracks. Voyiadjis and Park [*38*] improved the overall approach by including and adopting a general damage criteria for orthotropic materials by extending the formulation of Stumvoll and Swoboda [*39*] to MMCs. In this improved model, all damage types are considered but the model lacks the consideration of local (constituent) as well as interfacial damage effects. In contrast to the overall approach, the local approach [*40*] introduces two independent damage tensors, ϕ^m and ϕ^f, and hence two independent damage effect tensors, $\boldsymbol{M}^m$ and $\boldsymbol{M}^f$, to reflect the appropriate damage mechanisms in the matrix and fibers, respectively. It is this latter approach which is employed in the proposed micromechanical fatigue damage model.

Micromechanical Fatigue Damage Model

Stress and Strain Concentration Tensors—In the derivation of the model, the concept of effective stress [*24,41*] is used. The effective stress is defined as the stress in a hypothetical state of deformation that is free of damage and is mechanically equivalent to the current state of deformation and damage. In a general state of deformation and damage, the effective Cauchy stress tensor, $\overline{\boldsymbol{\sigma}}$, is related to the current Cauchy stress tensor by the linear relationship given as in Eq 2. In the case of composite materials, similar constituent (local) stress relationships hold for the matrix and fiber stress tensors, $\boldsymbol{\sigma}^m$ and $\boldsymbol{\sigma}^f$, respectively

$$\overline{\boldsymbol{\sigma}}^m = \boldsymbol{M}^m : \boldsymbol{\sigma}^m \tag{3a}$$

$$\overline{\boldsymbol{\sigma}}^f = \boldsymbol{M}^f : \boldsymbol{\sigma}^f \tag{3b}$$

where $\boldsymbol{M}^m$ and $\boldsymbol{M}^f$ are fourth-order local damage effect tensors for the matrix and fiber materials, respectively. The damage effect tensors, $\boldsymbol{M}^m$ and $\boldsymbol{M}^f$ are dependent on second-order damage variables, ϕ^m and ϕ^f, respectively. These second-order tensors quantify the crack density in the matrix and fibers, respectively [*42*]. The crack density tensors incorporate both cracks in the fiber, matrix, as well as those due to fiber debonding. A complete discussion on these tensors is given in the work of Voyiadjis and Venson [*42*].

In the proposed model, the matrix is assumed to be elastoplastic and the fibers are assumed to be elastic, continuous, and aligned. Consequently, the undamaged (effective) incremental local (constituent) constitutive relationships are given by

$$d\overline{\boldsymbol{\sigma}}^m = \overline{\boldsymbol{D}}^m : d\boldsymbol{\varepsilon}^m \tag{4a}$$

$$d\overline{\boldsymbol{\sigma}}^f = \overline{\boldsymbol{E}}^f : d\boldsymbol{\varepsilon}^f \tag{4b}$$

The fourth-rank tensors, $\overline{\boldsymbol{D}}^m$ and $\overline{\boldsymbol{E}}^f$, are the undamaged (effective) matrix elastoplastic stiffness tensor and fiber elastic stiffness tensor, respectively. The incremental composite constitutive relationship in the damaged state is expressed as follows

$$d\boldsymbol{\sigma} = \boldsymbol{D} : d\boldsymbol{\varepsilon} \tag{5}$$

where $d\boldsymbol{\varepsilon}$ is the incremental composite strain tensor.

In order to arrive at the local (constituent) relationships, given by Eq 4*a* and *b*, a homogenization technique in the form of the Mori-Tanaka averaging scheme [*43*] is employed. Through the use of the so-called stress and strain concentration tensors, a relationship between the global applied effective composite stress, $\overline{\boldsymbol{\sigma}}$, and the local effective stress in the constituents, $\overline{\boldsymbol{\sigma}}^{(m,f)}$, is obtained as follows

$$\overline{\boldsymbol{\sigma}}^m = \overline{\boldsymbol{B}}^m : \overline{\boldsymbol{\sigma}} \tag{6a}$$

$$\overline{\boldsymbol{\sigma}}^f = \overline{\boldsymbol{B}}^f : \boldsymbol{\sigma} \tag{6b}$$

where $\overline{\boldsymbol{B}}^f$ and $\overline{\boldsymbol{B}}^m$ represent the effective stress concentration tensors connecting the local effective stresses with the global effective stresses. In the damaged configuration, the following relationships are obtained

$$\boldsymbol{\sigma}^m = \boldsymbol{B}^m : \boldsymbol{\sigma} \tag{7a}$$

$$\boldsymbol{\sigma}^f = \boldsymbol{B}^f : \boldsymbol{\sigma} \tag{7b}$$

Combining Eq 2, 3, 6, and 7, one obtains the relationship between the local stress concentration tensor and the local effective stress concentration tensor as follows

$$\boldsymbol{B}^f = \boldsymbol{M}^{-f} : \overline{\boldsymbol{B}}^f : \boldsymbol{M} \tag{8a}$$

$$\boldsymbol{B}^m = \boldsymbol{M}^{-m} : \overline{\boldsymbol{B}}^m : \boldsymbol{M} \tag{8b}$$

Similar relationships may be obtained for the deformations in the effective (undamaged) configuration as follows

$$\overline{\boldsymbol{\varepsilon}}^m = \overline{\boldsymbol{A}}^m : \overline{\boldsymbol{\varepsilon}} \tag{9a}$$

$$\overline{\boldsymbol{\varepsilon}}^f = \overline{\boldsymbol{A}}^f : \overline{\boldsymbol{\varepsilon}} \tag{9b}$$

where $\overline{\boldsymbol{A}}^f$ and $\overline{\boldsymbol{A}}^m$ represent the effective strain concentration tensors connecting the local effective strains with the global effective strains. In the damaged configuration, the relationships are given by

$$\boldsymbol{\varepsilon}^m = \boldsymbol{A}^m : \boldsymbol{\varepsilon} \tag{10a}$$

$$\boldsymbol{\varepsilon}^f = \boldsymbol{A}^f : \boldsymbol{\varepsilon} \tag{10b}$$

and furthermore

$$A^f = M^f : \bar{A}^f : M^{-1} \tag{11a}$$

$$A^m = M^m : \bar{A}^m : M^{-1} \tag{11b}$$

Effective Volume Fractions—During the process of damage evolution in the material, another phenomenon has to be considered. As damage progresses within each constituent, the effective load resisting area/volume changes while the gross area/volume remains the same. Since the distribution of forces/stresses to the constituents depends directly on the area/volume intact to resist an applied force/stress, there is a change in the allocation of the external applied force/stress to the constituents. This redistribution of force/stress due to progressing damage can be accounted for by defining the so-called effective volume fractions that are based on the updated damage variable during each load/stress increment. Expressions for the effective volume fractions are given as

$$\bar{c}^m = \frac{1 - \phi^m_{eq}}{(1 - \phi^m_{eq}) + (1 - \phi^f_{eq}) \dfrac{c^f_0}{c^m_0}} \tag{12}$$

and

$$\bar{c}^f = \frac{1 - \phi^f_{eq}}{(1 - \phi^f_{eq}) + (1 - \phi^m_{eq}) \dfrac{c^m_0}{c^f_0}} \tag{13}$$

where c^f_0 and c^m_0 are defined as the volume fractions for the fiber and matrix in the virgin material, respectively. The expressions for ϕ^m_{eq} and ϕ^f_{eq} are given as

$$\phi^f_{eq} = \frac{\| \phi^f \|_2}{\| \phi^f_{\text{crit}} \|_{L2}} \tag{14a}$$

$$\phi^m_{eq} = \frac{\| \phi^m \|_2}{\| \phi^m_{\text{crit}} \|_{L2}} \tag{14b}$$

with ϕ^f_{crit} and ϕ^m_{crit} defined as the critical damage tensors for the fibers and the matrix, respectively, and $\| \cdot \|_{L2}$ defined as the L_2 − norm of the quantity enclosed in the vertical bars.

Proposed Micromechanical Fatigue Damage Model—The proposed fatigue damage criterion, g, is considered a function of the applied stress, σ, the damage parameter, ϕ, the damage hardening parameter, κ, and a tensor quantity, γ, that is explained later. The equation for g is defined by

$$g = \mathcal{F}^n - 1 \tag{15}$$

where $\mathcal{F}$ is defined as

$$\mathcal{F} = w^{-1}_{ij} w^{-1}_{jk} (Y_{kl} - \gamma_{kl})(Y_{li} - \gamma_{li}) \tag{16}$$

The term $(Y_{kl} - \gamma_{kl})$ represents the translation of the damage surface and therefore accounts for damage evolution during cyclic loading. The tensor, Y, represents the thermodynamical force conjugate to the damage variable, ϕ, and is defined as

$$Y_{ij} = \frac{1}{2}\left(\sigma_{cd}C_{abpq}M_{pqkl}\sigma_{kl} + \sigma_{pq}M_{uvpq}C_{uvab}\sigma_{cd}\right)\frac{\partial M_{abcd}}{\partial \phi_{ij}} \tag{17}$$

with $C_{ijkl} = E^{-1}_{ijkl}$, while the quantity, γ, can in principle be compared to the backstress in plasticity theory, hence representing in this case the center of the damage surface in the thermodynamical conjugate force space, Y. Its evolution equation is given as follows

$$\dot{\gamma}_{ij} = \mathfrak{c}\dot{\phi}_{ij} \tag{18}$$

similarly to the evolution equation for the backstress in plasticity. The tensor quantity, w_{ij}, accounts for the anisotropic expansion of the damage surface and is given as follows

$$w_{ij} = u_{ij} + V_{ij} \tag{19}$$

where the tensor, u, is defined as

$$u_{ij} = \lambda_{(i)}\eta_{(i)}\left(\frac{\kappa}{\lambda_{(i)}}\right)^{\xi_{(i)}}\delta_{ij} \qquad \text{(no sum on } i\text{)} \tag{20}$$

The tensor, V_{ij}, can be interpreted physically as the damage threshold tensor for the constituent material considered, while κ represents the effect of damage hardening and is defined as follows

$$\kappa = \int_{\phi_1}^{\phi_2} Y : d\phi = \int_0^t Y : \dot{\phi}\, dt \tag{21}$$

Damage hardening is based on the increase in the initial damage threshold due to microhardening occurring at a very local material level [*44*]. The parameter, γ_{ij}, in Eq 16 adds to this hardening behavior due to the movement of the damage surface in the direction of the evolution, f, damage. The remaining variables, n, λ_i, η_i, ξ_i, and $\mathfrak{c}$, are material parameters to be determined for each individual constituent. The form of the variable, ξ_i, will be specifically discussed later in the numerical implementation.

Based on thermodynamical principles, a potential function for each constituent is defined as [*40*]

$$\Omega = \Pi^p + \Pi^d - \dot{\Lambda}_1 f - \dot{\Lambda}_2 g \tag{22}$$

where Π^p, Π^d, f, and g represent the dissipation energy due to plasticity, the dissipation energy due to damage, the plasticity yield surface for the constituent material considered, and the damage surface, respectively. For loading in the elastic regime (high cycle fatigue), the terms involving plastic dissipation energy are neglected. The term, Π^d, representing the dissipation energy due to damage is given as

$$\Pi^d = Y_{ij}\dot{\phi}_{ij} + \mathfrak{R}\dot{\kappa} \tag{23}$$

Applying the theory of calculus of several variables to solve for the coefficients, $\dot{\Lambda}_1$ and $\dot{\Lambda}_2$, yields

$$\frac{\partial \Omega}{\partial Y_{ij}} = 0 \tag{24}$$

from which an expression for the damage increment is obtained as follows

$$d\phi_{ij} = d\Lambda_2 \frac{\partial g}{\partial Y_{ij}} \tag{25}$$

Hence, $d\Lambda_2$ may be determined using the consistency condition

$$dg = \frac{\partial g}{\partial \sigma} : d\sigma + \frac{\partial g}{\partial \phi} : d\phi + \frac{\partial g}{\partial \kappa} d\kappa + \frac{\partial g}{\partial \gamma} : d\gamma = 0 \tag{26}$$

Substitution of the appropriate terms (Eq 18 and 21) into Eq 26 yields

$$dg = \frac{\partial g}{\partial \sigma} : d\sigma + \frac{\partial g}{\partial \phi} : d\phi + \frac{\partial g}{\partial \kappa} Y : d\phi - c \frac{\partial g}{\partial Y} : d\phi = 0 \tag{27}$$

Replacing $d\phi$ with Eq 25, an expression for $d\Lambda_2$ is obtained as follows

$$d\Lambda_2 = -\frac{\dfrac{\partial g}{\partial \sigma_{kl}} d\sigma_{kl}}{\left(\dfrac{\partial g}{\partial \phi_{ij}} + Y_{ij} \dfrac{\partial g}{\partial \kappa} - c \dfrac{\partial g}{\partial Y_{ij}}\right) \dfrac{\partial g}{\partial Y_{ij}}} \tag{28}$$

Back-substitution of Eq 28 into Eq 25 yields an expression for the damage increment for the appropriate constituent in terms of a given stress increment as

$$d\phi_{mn} = -\frac{\dfrac{\partial g}{\partial \sigma_{kl}} \dfrac{\partial g}{\partial Y_{mn}} d\sigma_{kl}}{\left(\dfrac{\partial g}{\partial \phi_{ij}} + Y_{ij} \dfrac{\partial g}{\partial \kappa} - c \dfrac{\partial g}{\partial Y_{ij}}\right) \dfrac{\partial g}{\partial Y_{ij}}} \tag{29}$$

or

$$d\phi_{ij} = \Psi_{ijkl} d\sigma_{kl} \tag{30}$$

where

$$\Psi_{ijkl} = -\frac{\dfrac{\partial g}{\partial Y_{ij}} \dfrac{\partial g}{\partial \sigma_{kl}}}{\left(\dfrac{\partial g}{\partial \phi_{rs}} + Y_{rs} \dfrac{\partial g}{\partial \kappa} - c \dfrac{\partial g}{\partial Y_{rs}}\right) \dfrac{\partial g}{\partial Y_{rs}}} \tag{31}$$

and

$$Y_{rs} = \frac{1}{2}\left[\sigma_{cd}\bar{E}^{-1}_{abpq}M_{pqkl}\sigma_{kl} + \sigma_{pq}M_{uvpq}\bar{E}^{-1}_{uvab}\sigma_{cd}\right]\frac{\partial M_{abcd}}{\partial \phi_{rs}} \tag{32, 33}$$

As stated elsewhere [*39*], a damaging state in a constituent is given if for any state the damage criterion is satisfied

$$g = 0 \tag{34}$$

for that specific constituent. In general, four different loading states are possible

$$g < 0 \qquad \text{(nondamaging loading)} \tag{35}$$

$$g = 0 \qquad \frac{\partial g}{\partial Y_{ij}}dY_{ij} < 0 \qquad \text{(elastic unloading)} \tag{36}$$

$$g = 0 \qquad \frac{\partial g}{\partial Y_{ij}}dY_{ij} = 0 \qquad \text{(neutral unloading)} \tag{37}$$

$$g = 0 \qquad \frac{\partial g}{\partial Y_{ij}}dY_{ij} > 0 \qquad \text{(loading from damaging state)} \tag{38}$$

Using Eq 29, the damage increment per fatigue cycle may be obtained by integration over one stress cycle as

$$\frac{d\phi_{ij}}{dN} = \int_{\sigma_{min}}^{\sigma_{max}} \Psi_{ijkl}d\sigma_{kl} + \int_{\sigma_{max}}^{\sigma_{min}} \Psi_{ijkl}d\sigma_{kl} \tag{39}$$

where ψ_{ijkl} is given according to Eq 31. The dependence of damage on the mean stress and the amplitude of the stress cycle is implicitly included through the integration of Eq 39.

Return to the Damage Surface

In the numerical implementation of the model, it appears that after calculating the damage increment, $d\phi$, for the current stress increment, $d\sigma$, and updating all the appropriate parameters depending on the damage variable, ϕ, the damage surface is in general not satisfied. Therefore, it is necessary to return the new image point to the damage surface by employing an appropriate return criteria.

At the beginning of the $(n + 1)^{st}$ increment, we assume that the damage surface, g, is satisfied

$$g^{(n)}(\sigma^{(n)},\phi^{(n)},\kappa^{(n)}\gamma^{(n)}) = 0 \tag{40}$$

Applying the stress increment, $d\sigma$ (assuming a damage loading), will result in a damage increment, $d\phi$, that will be used to update the values for κ and γ. Checking the damage surface (Eq 15) with the updated values for σ, ϕ, κ, and γ will in general yield

$$g^{(n+1)}(\sigma^{(n+1)},\phi^{(n+1)},\gamma^{(n+1)},\gamma^{(n+1)}) > 0 \tag{41}$$

where

$$\sigma^{(n+1)} = \sigma^{(n)} + d\sigma^{(n+1)} \tag{42}$$

$$\phi^{(n+1)} = \phi^{(n)} + d\phi^{(n+1)} \tag{43}$$

$$\kappa^{(n+1)} = \kappa^{(n)} + d\kappa^{(n+1)} \tag{44}$$

$$\gamma^{(n+1)} = \gamma^{(n)} + d\gamma^{(n+1)} \tag{45}$$

Using a "Taylor series" expansion of order, one expands the left-hand side of Eq 41 to yield

$$\begin{aligned} & g^{(n+1)}(\sigma^{(n)} + d\sigma^{(n+1)}, \phi^{(n)} + d\phi^{(n+1)}, \kappa^{(n)} + d\kappa^{(n+1)}, \gamma^{(n)} + d\gamma^{(n+1)}) \\ & = g^{(n)}(\sigma^{(n)}, \phi^{(n)}, \kappa^{(n)}\gamma^{(n)}) + \left.\frac{\partial g}{\partial \sigma}\right|^{(n)} d\sigma^{(n+1)} + \left.\frac{\partial g}{\partial \phi}\right|^{(n)} d\phi^{(n+1)} \\ & \quad + \left.\frac{\partial g}{\partial \kappa}\right|^{(n)} d\kappa^{(n+1)} + \left.\frac{\partial g}{\partial \gamma}\right|^{(n)} d\gamma^{(n+1)} > 0 \end{aligned} \tag{46}$$

Recalling the relationships in Eqs 18 and 21, Eq 46 can be written as

$$g^{(n+1)}(\sigma^{(n)} + d\sigma^{(n+1)}, \phi^{(n)} + d\phi^{(n+1)}, \kappa^{(n)} + Y^{(n)} : d\phi^{(n+1)}, \gamma^{(n)} + cd\phi^{(n+1)}) > 0 \tag{47}$$

The return to the damage surface, that is, $g^{(n+1)} = 0$, is now achieved by adjusting the damage increment, $d\phi$, using a linear coefficient, α, such that

$$g^{(n+1)}(\sigma^{(n)} + d\sigma^{(n+1)}, \phi^{(n)} + \alpha d\phi^{(n+1)}, \kappa^{(n)} + \alpha Y^{(n)} : d\phi^{(n+1)}, \gamma^{(n)} + \alpha c d\phi^{(n+1)}) = 0 \tag{48}$$

Substitution of the appropriate expressions for the derivatives in Eq 48 as well as Eqs 21 and 18 and setting the left-hand side equal to zero allows one to solve for the unknown coefficient, α, such that

$$\alpha = -\frac{\left(g^{(n)} + \left.\frac{\partial g}{\partial \sigma}\right|^{(n)} d\sigma^{(n+1)}\right)}{\left(\left.\frac{\partial g}{\partial \phi}\right|^{(n)} + \left.\frac{\partial g}{\partial \kappa}\right|^{(n)} Y^{(n)} + c\left.\frac{\partial g}{\partial \gamma}\right|^{(n)}\right) d\phi^{(n+1)}} \tag{49}$$

Numerical Analysis

The preceding model is implemented into a numerical algorithm and used to investigate the fatigue damage evolution in the individual constituents of a unidirectionally fiber-reinforced metal-matrix composite. No assumption, except those implicitly included in the stress and strain concentration tensors based on the Mori-Tanaka averaging scheme [*43*] are made. The implementation is performed using full three-dimensional modeling hence avoiding any assumptions to be made upon simplification of fourth-order tensors to two-dimensional matrix representation. The Mori-Tanaka averaging scheme is implemented using the numerical algorithm ac-

TABLE 1—*Material properties used in the analysis.*

	E, GPa	ν	σ_u, MPa	σ_y, MPa	c, %
Matrix (Ti–15–3)	92.4	0.35	933.6	689.5	67.5
Fiber (SCS–6)	400.0	0.25	N/A[a]	N/A	32.5

[a] N/A = not available.

cording to Lagoudas et al. [*45*]. Only an elastic analysis is performed at this time. Since no experimental data are yet available, a parametric study is conducted in order to demonstrate the influence of various parameters on the damage evolution in the constituents. The constituents are assumed to consist of an isotropic material. The materials used in the analysis are given in Johnson et al. [*46*] and are shown in Table 1. The fatigue loading is applied in the form of a sinusoidal uniaxial loading given as

$$\sigma_{ij} = \sigma_{ij,\text{mean}} + \sigma_{ij,A} \sin\left(\frac{\theta}{2\pi}\right) \tag{50}$$

where

$$\sigma_{11,\text{mean}} = 550 \text{ MPa} \quad \text{and } \sigma_{ij,\text{mean}} = 0 \quad (\text{for } i, j \neq 1)$$

$$\sigma_{11,A} = 450 \text{ MPa} \quad \text{and } \sigma_{ij,A} = 0 \quad (\text{for } i, j \neq 1)$$

For the numerical integration scheme, an adaptive algorithm was implemented such that the stress increments were taken as

$$\Delta\sigma_{ij} = \frac{\sigma_{ij,\text{mean}}}{25} \quad \text{if } \sigma_{ij} < \sigma_{\text{mean},ij} \quad \text{(nondamage state)}$$

$$\Delta\sigma_{ij} = 1 \text{ MPa} \quad \text{if } \sigma_{ij} < \sigma_{\text{mean},ij} \quad \text{(damage state)}$$

during the loading phase to the mean stress and

$$\Delta\sigma_{ij} = \left[\sin\left(\frac{\theta + \Delta\theta}{2\pi}\right) - \sin\left(\frac{\theta}{2\pi}\right)\right] * \sigma_{ij,A} \quad \text{(during cyclic loading)}$$

with

$$\Delta\theta = \frac{\pi}{50} \quad \text{(during a nondamaging state)}$$

$$\Delta\theta = \frac{\pi}{900} \quad \text{(during a damaging state)}$$

for the cyclic loading phase. Here, θ represents simply the phase angle during the cyclic loading. The preceding limit values were adopted based on a numerical investigation that yielded satisfactory behavior of the model using these values.

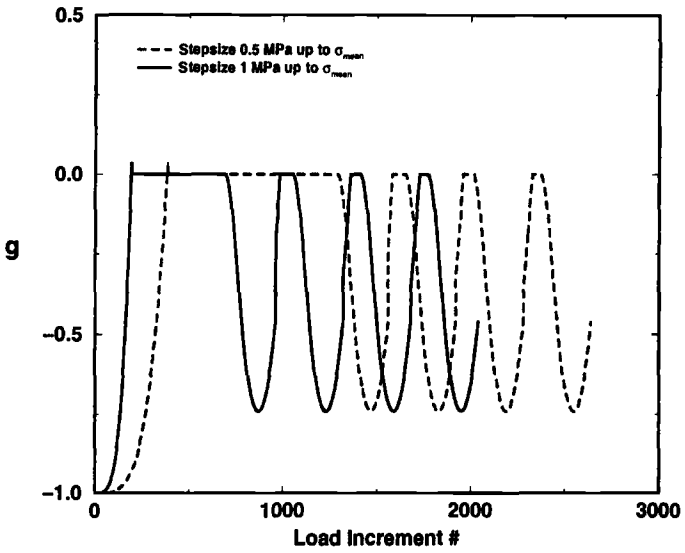

FIG. 1—*Validation of employed return criteria.*

The damage criterion is evaluated within each increment and a return criterion as described in Eqs 48 and 49 is applied if $|g^{(n+1)}| \geqq 10^{-3}$. Except at the very first incident of damage, this criterion shows satisfactory performance during the application of the return criterion (Eqs 41 to 49). The numerical noise at the initiation of damage has been investigated and it was found that a reduction in the step size for the stress increment reduces the numerical error appropriately to fall within the specified bounds. This phenomenon is not observed at any other time during the analysis (Fig. 1). It is attributed to the point of discontinuity in the damage criterion at the

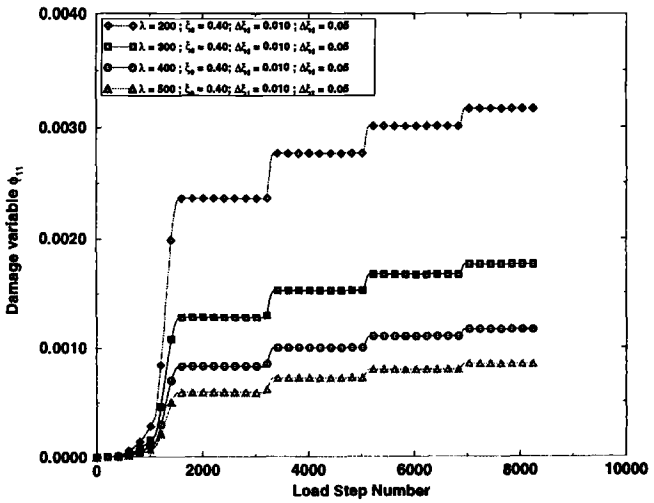

FIG. 2—*Variation in damage evolution for various values of* λ.

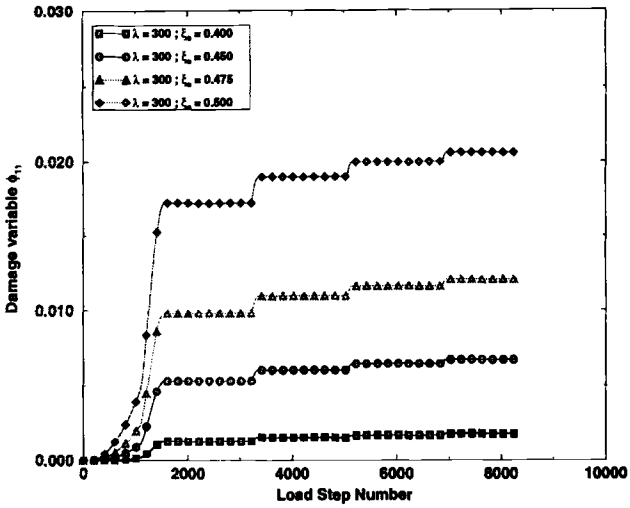

FIG. 3—*Variation in damage evolution for various values of* ξ_0.

wake of damage. The flexibility of the model is demonstrated through a parametric study based on variations in Parameters λ and ξ (see Figs. 2 and 3). For the parametric study, the values of all the parameters except for one are kept constant in order to study the effect of a single parameter on the model as shown in Table 2. The parameters, ξ^f and ξ^m, account for the variation in the damage evolution with respect to the number of cycles, especially the increase in the damage rate during the fatigue life of a material. The specific forms of Parameters ξ^f and ξ^m are obtained from experimental curves, such as those shown in Figs. 4 and 5, where the fatigue damage in the material is plotted versus the number of applied cycles. Since fatigue damage evolution for a specific stress ratio, R, is dependent on the applied mean stress as well as the stress amplitude, such experimental curves have to be obtained for different applied mean stresses and stress amplitudes. The damage, ϕ, in the material during the fatigue life may be obtained by using the stiffness degradation or an equivalent method, such as sectioning and subsequent scanning electron microscopic (SEM) evaluation of the specimens for damage quantification. Upon inspection of the obtained experimental curves, it is observed that basically three different regions can be distinguished during the fatigue life of the material (Figs. 4 and

TABLE 2—*Model parameters used in the analysis.*

	V, MPa	λ, MPa	η	ξ	c, MPa	n	Figure
Matrix (Ti–15–3)	0.1	80 000	1.0	refer to Eqs 51 to 57	1.0	1.0	6
Fiber (SCS–6)	3	160 000	1.0	refer to Eqs 51 to 57	1.0	1.0	6
	N_1	N_2	ξ_0	ξ_1	ξ_2	Figure	
Matrix (Ti–15–3)	10	110 000	0.55	0.02	0.03	6	
Fiber (SCS–6)	N/A[a]	110 000	0.56	N/A	0.03	6	

[a] N/A = not applicable.

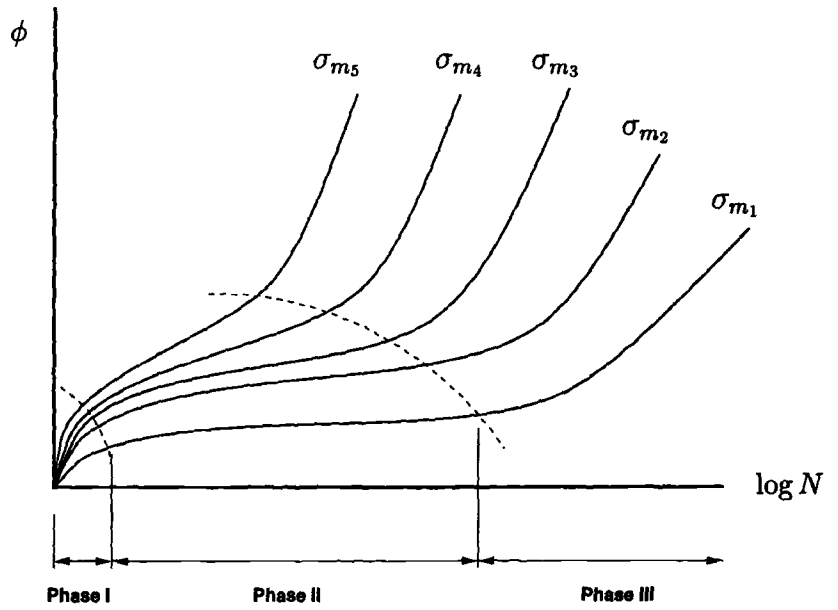

FIG. 4—ϕ − N *diagrams for determination of* ξ *for constant* R ($\sigma_{m_1} < \sigma_{m_2} < \sigma_{m_3} < \sigma_{m_4} < \sigma_{m_5}$).

5). These different regions pertain to the damage initiation phase (Phase I), the damage propagation phase (Phase II), and the failure phase (Phase III). A distinction for these regions can be made by specifying bounds in the form of the number of cycles such as N_1 and N_2, as indicated in Fig. 4. This is generally done by visual inspection using engineering judgment and physical intuition. Using these curves, an evolution equation for ξ with respect to the number of cycles, N, the applied mean stress, σ_{mean}, and the stress ratio, R, may be established. For the current analysis, since no such experimental data are available, the following forms for Parameters ξ^f and ξ^m in terms of N_1 and N_2 have been used and are given as

$$\xi_N^m = \frac{N_1^m - N}{N_1^m - 1} a^m + \left(1 - \frac{N_1^m - N}{N_1^m - 1}\right) b^m \quad (1 \le N \le N_1^m) \tag{51}$$

$$\xi_N^m = \xi_0^m + \Delta\xi_1^m + \left(\frac{N - N_1^m}{N_2^m - N_1^m}\right) \Delta\xi_2^m \quad (N_1^m < N \le N_2^m) \tag{52}$$

$$\xi_N^m = \xi_0^m + \Delta\xi_1^m + \left(\frac{N - N_1^m}{N_2^m - N_1^m}\right)^2 \Delta\xi_2^m \quad (N > N_2^m) \tag{53}$$

$$\xi_N^f = \xi_0^f + \left(\frac{N - 1}{N_2^f - 1}\right) \Delta\xi_2^f \quad (1 < N \le N_2^f) \tag{54}$$

$$\xi_N^f = \xi_0^f + \left(\frac{N - 1}{N_2^f - 1}\right)^2 \Delta\xi_2^f \quad (N > N_2^f) \tag{55}$$

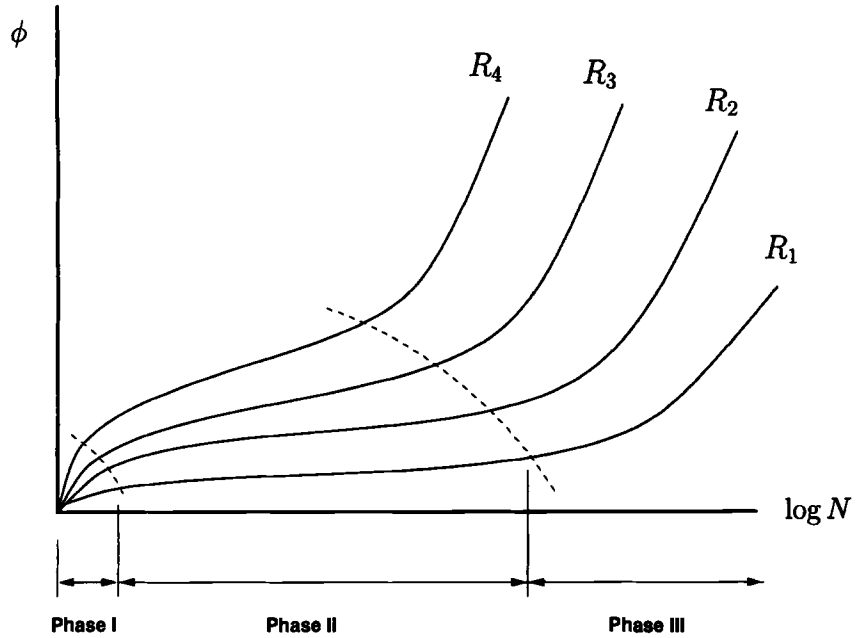

FIG. 5—ϕ − N *diagrams for determination of* ξ *for constant* σ_{mean} ($R_1 > R_2 > R_3 > R_4$).

where

$$a^m = \xi_0^m + \sqrt[4]{\frac{N_1^m}{N}} \log\left(\frac{N}{N_1^m}\right) \Delta\xi_1^m \tag{56}$$

$$b^m = \xi_0^m + \Delta\xi_1^m + \left(\frac{N - N_1^m}{N_2^m - N_1^m}\right) \Delta\xi_2^m \tag{57}$$

The results for the parametric study in order to investigate the influence of the model parameter, ξ_0, on the damage evolution in the matrix are shown in Fig. 3 with all other parameters kept constant. Varying the value of Parameter λ and keeping ξ_0 constant will result in the curves shown in Fig. 2. Only the damage variable, ϕ_{11}, is shown since the other components of ϕ are equal to zero or their value is smaller by a magnitude of 100. The reference frames of the damage tensor and the material system are identical, hence "1" representing the fiber direction while "2" and "3" indicate the transverse directions. For clarification, it should be emphasized that the plateaus exhibited in Figs. 2 and 3 represent the unloading phase in the cyclic loading where no further damage occurs.

Two sample analyses of complete fatigue simulations have been conducted to show the capabilities of the developed model. The results of such an analysis for the damage evolution in the matrix, in the fiber, and the overall composite are shown in Fig. 6. Failure of the entire composite occurs due to fiber failure at about 116 000 cycles for the case of $\sigma_{11,\max}$ = 1000 MPa and a stress ratio of R = 0.1. In a second complete fatigue simulation, failure occurs at about 217 000 fatigue cycles for $\sigma_{11,\max}$ = 940 MPa and a stress ratio of R = 0.1. The obtained fatigue life in the two cases is compared with experimental results for a unidirectional composite

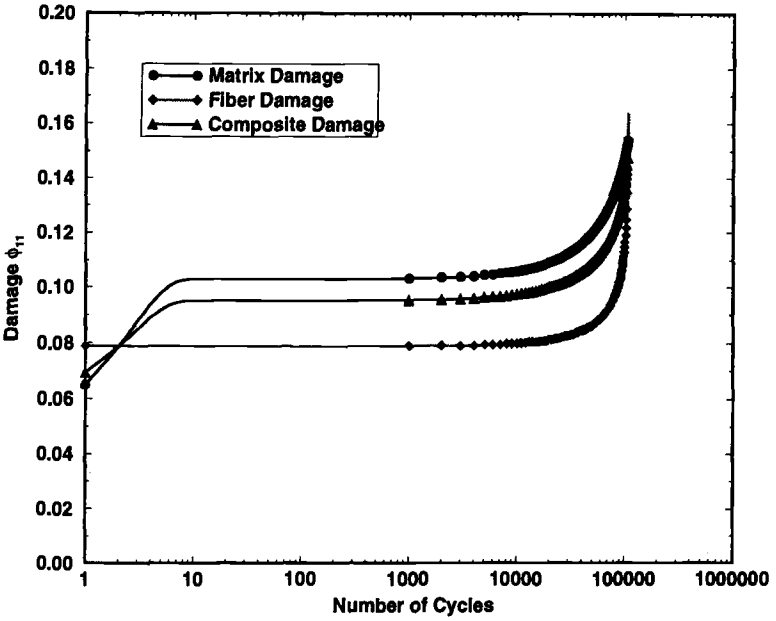

FIG. 6—*Fatigue damage evolution during a complete simulation.*

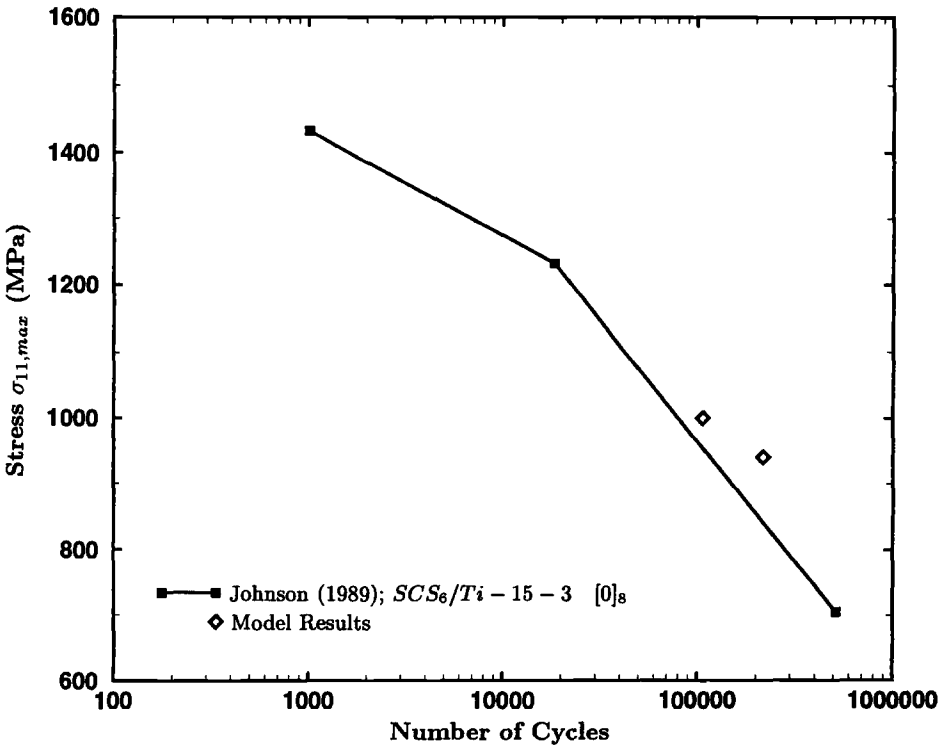

FIG. 7—*Comparison with experimental results* [47]*; Wöhler diagram for* R = *0.1.*

[47] as shown in Fig. 7. The results show satisfactory agreement that establishes the potential of the proposed model.

Conclusions

A micromechanical damage model for fatigue loading based on thermodynamic principles is proposed. The model is applied to unidirectionally reinforced MMCs. Only elastic loading in the form of a uniaxial fatigue loading (in the fiber direction) is considered thereby reflecting high cycle fatigue loading. Numerical results from the parametric study show the influence of various model parameters on the damage evolution in the constituents. A sample analysis of a complete fatigue simulation with final failure is shown.

References

[1] Owen, M. J. and Howe, R. J., "The Accumulation of Damage in a Glass-reinforced Plastic Under Tensile and Fatigue Loading," *Journal of Physics*, Vol. D:5, 1972, pp. 1637–1649.

[2] Subramanyan, S., "A Cumulative Damage Rule Based on the Knee Point of the *S-N*-Curve," *Journal of Engineering Mechanics and Technology*, 1976, pp. 316–321.

[3] Srivatsavan, P. and Subramanyan, S., "A Cumulative Damage Rule Based on Successive Reduction in Fatigue Limit, *Journal of Engineering Mechanics and Technology*, Vol. 100, 1978, pp. 212–214.

[4] Lemaitre, J. and Plumtree, A., "Application of Damage Concepts to Predict Creep-Fatigue Failures," *Journal of Engineering Mechanics and Technology*, Vol. 101, 1979, pp. 284–292.

[5] Fong, J. T., "What is Fatigue Damage?" *Damage in Composite Materials*, K. L. Reifsnider, Ed., American Society for Testing and Materials, Philadelphia, 1982, pp. 243–266.

[6] Hashin, Z., "Cumulative Damage Theory for Composite Materials, Residual Life and Residual Strength Methods," *Composite Science and Technology*, Vol. 23, 1985, pp. 1–19.

[7] Hwang, W. and Han, K. S., "Cumulative Fatigue Damage Models and Multi-Stress Fatigue Life Prediction," *Journal of Composite Materials*, Vol. 20, 1986, pp. 125–153.

[8] Hwang, W. and Han, K. S., "Fatigue of Composites—Fatigue Modulus Concept and Life Prediction," *Journal of Composite Materials*, Vol. 20, 1986, pp. 154–165.

[9] Whitworth, H. A., "Cumulative Damage in Composites," *Transactions*, ASME, Vol. 112, 1990, pp. 358–361.

[10] Arnold, S. M. and Kruch, S., "Differential Continuum Damage Mechanics Models for Creep and Fatigue of Unidirectional Metal Matrix Composites," Technical Memorandum 105213, NASA-Lewis Research Center, Cleveland, OH, Nov. 1991.

[11] Arnold, S. M. and Kruch, S., "A Differential CDM Model for Fatigue of Unidirectional Metal Matrix Composites," Technical Memorandum 105726, NASA-Lewis Research Center, Cleveland, OH, Nov. 1991.

[12] Chaboche, J. L. and Lesne, P. M., "A Non-Linear Continuous Fatigue Damage Model," *Fatigue and Fracture of Engineering Materials and Structures*, Vol. 11, No. 1, 1988, pp. 1–17.

[13] Chaboche, J.-L., "Continuum Damage Mechanics: Part I—General Concepts," *Journal of Applied Mechanics*, Vol. 55, 1988, pp. 59–64.

[14] Chaboche, J. L., "Continuum Damage Mechanics: Part II—Damage Growth, Crack Initiation and Crack Growth," *Journal of Applied Mechanics*, Vol. 55, 1988, pp. 65–72.

[15] Chaboche, J. L., "Fracture Mechanics and Damage Mechanics: Complementarity of Approaches," *Proceedings*, Fourth International Conference on Numerical Methods in Fracture Mechanics, 1987, pp. 309–324.

[16] Lesne, P. M. and Savalle, S., "A Differential Damage Rule with Microinitiation and Micropropagation," *La Recherche Aérospatiale*, Vol. 2, 1987, pp. 33–47.

[17] Lesne, P. M. and Cailletaud, G., "Creep-Fatigue Interaction Under High Frequency Loading," *Proceedings*, International Conference on Mechanical Behavior of Materials, Beijing, China, 1987.

[18] Robinson, D. N., Duffy, S. F., and Ellis, J. R., "A Viscoplastic Constitutive Theory for Metal Matrix Composites at High Temperature," *Thermal Stresses, Material Deformation, and Thermomechanical Fatigue*, H. Sehatoglu and S. Y. Zamrik, Eds., 1987, pp. 49–56.

[19] Robinson, D. N. and Duffy, S. F., "Continuum Deformation Theory for High-Temperature Metallic Composites," *Journal of Engineering Mechanics*, Vol. 116, No. 4, 1990, pp. 832–844.

[20] Wilt, T. E. and Arnold, S. M., "A Coupled/Uncoupled Deformation and Fatigue Damage Algorithm Utilizing the Finite Element Method," NASA TM 106526, NASA, Lewis Research Center, Cleveland, OH, 1994.

[21] Nicholas, T., "Fatigue Life Prediction in Titanium Matrix Composites," *Journal of Engineering Materials and Technology*, Vol. 117, 1995, pp. 440–447.

[22] Neu, R. W., "A Mechanistic-Based Thermomechanical Fatigue Life Prediction Model for Metal Matrix Composites," *Fatigue and Fracture of Engineering Materials and Structures*, Vol. 16, *Izvestiva Akademii Nauk SSSR Odtelinie Tekhnicheskikh Nauk No. 8*, 1993, pp. 811–828.

[23] Kachanov, L. M., "On the Creep Fracture Time," *Izvestiva Akademii Nauk SSSR Odtelinie Tekhnicheskikh Nauk No. 8*, 1958, pp. 26–31.

[24] Sidoroff, F., "Description of Anisotropic Damage Application to Elasticity," *Physical Non-Linearities in Structural Analysis*, J. Hult and J. Lemaitre, Eds., IUTAM Series, Springer-Verlag, New York, 1980, pp. 237–244.

[25] Voyiadjis, G. Z. and Kattan, P. I., "A Plasticity-Damage Theory for Large Deformation of Solids—I. Theoretical Formulation," *International Journal of Engineering Science*, Vol. 30, No. 9, 1992, pp. 1089–1108.

[26] Voyiadjis, G. Z. and Kattan, P. I., "A Plasticity-Damage Theory for Large Deformation of Solids—II. Applications to Finite Simple Shear," *International Journal of Engineering Science*, Vol. 31, No. 1, 1993, pp. 183–199.

[27] Talreja, R., *Fatigue of Composite Materials*, Technomic Publishing Co., Lancaster, PA, 1987.

[28] Christensen, R. M., "Tensor Transformations and Failure Criteria for the Analysis of Fiber Composite Materials. Part II: Necessary and Sufficient Conditions for Laminate Failure," *Journal of Composite Materials*, Vol. 24, 1990, pp. 796–800.

[29] Poursatip, A., Ashby, M. F., and Beaumont, P. W. R., "Damage Accumulation During Fatigue of Composites," *Progress in Science and Engineering Composites*, T. Hayashi, K. Kawata, and S. Umekawa, Eds., ICCM-IV, Tokyo, 1982, pp. 693–700.

[30] Dvorak, G. J. and Bahei-El-Din, Y. A., "Plasticity Analysis of Fibrous Composites," *Journal of Applied Mechanics*, Vol. 49, 1982, pp. 327–335.

[31] Dvorak, G. J. and Bahei-El-Din, Y. A., "A Bimodal Plasticity Theory of Fibrous Composite Materials Theory," *ACTA Mechanica*, Vol. 69, 1987, pp. 219–241.

[32] Dvorak, G. J. and Laws, N., "Analysis of Progressive Matrix Cracking in Composite Laminates–II. First Ply Failure," *Journal of Composite Materials*, Vol. 21, 1987, pp. 309–329.

[33] Dvorak, G. J., Laws, N., and Hejazi, M., "Analysis of Progressive Matrix Cracking in Composite Laminates—I. Thermoelastic Properties of a Ply with Cracks," *Journal of Composite Materials*, Vol. 19, 1985.

[34] Voyiadjis, G. Z. and Kattan, P. I., "Damage of Fiber-Reinforced Composite Materials with Micromechanical Characterization," *International Journal of Solids and Structures*, Vol. 30, No. 20, 1993, pp. 2757–2778.

[35] Voyiadjis, G. Z., Kattan, P. I., and Venson, A. R., "Evolution of a Damage Tensor for Metal Matrix Composites," *MECAMAT 93*, International Seminar on Micromechanics of Materials, Vol. 84, Moret-sur-Loing, France, 1993, pp. 406–417.

[36] Voyiadjis, G. Z. and Kattan, P. I., "Micromechanical Characterization of Damage-Plasticity in Metal Matrix Composites," *Studies in Applied Mechanics, Vol. 34: Damage in Composite Materials*, G. Z. Voyiadjis, Ed., Elsevier, Amsterdam, New York, 1993, pp. 67–102.

[37] Kattan, P. I. and Voyiadjis, G. Z., "Overall Damage and Elasto-Plastic Deformation in Fibrous Metal Matrix Composites," *International Journal of Plasticity*, Vol. 9, 1993, pp. 931–949.

[38] Voyiadjis, G. Z. and Park, T., "Anisotropic Damage of Fiber Reinforced MMC Using an Overall Damage Analysis," *Journal of Engineering Mechanics*, Vol. 121, No. 11, 1995, pp. 1209–1217.

[39] Stumvoll, M. and Swoboda, G., "Deformation Behavior of Ductile Solids Containing Anisotropic Damage," *Journal of Engineering Mechanics*, Vol. 119, No. 7, 1993, pp. 169–192.

[40] Voyiadjis, G. Z. and Kattan, P. I., "Local Approach to Damage in Elasto-Plastic Metal Matrix Composites," *International Journal of Damage Mechanics*, Vol. 2, 1993, pp. 92–114.

[41] Rabotnov, Y. N., *Creep Problems in Structural Members*, North Holland, Amsterdam, London, 1993.

[42] Voyiadjis, G. Z. and Venson, A. R., "Experimental Damage Investigation of a SiC-Ti-Aluminide Metal Matrix Composite," *International Journal of Damage Mechanics*, Vol. 4, No. 4, 1995, pp. 338–361.

[43] Chen, T., Dvorak, G. J., and Benveniste, Y., "Mori-Tanaka Estimates of the Overall Elastic Moduli of Certain Composite Materials," *Journal of Applied Mechanics*, Vol. 59, 1992, pp. 539–546.

[44] Chow, C. L. and Lu, T. J., "On Evolution Laws of Anisotropic Damage," *Engineering Fracture Mechanics*, Vol. 34, No. 3, 1989, pp. 679–701.

[45] Lagoudas, D. C., Gavazzi, A. C., and Nigam, H., "Elastoplastic Behavior of Metal Matrix Composites Based on Incremental Plasticity and the Mori-Tanaka Averaging Scheme," *Computational Mechanics*, Vol. 8, 1991, pp. 193–203.

[46] Johnson, W. S., Lubowinski, S. J., and Highsmith, A. L., "Mechanical Characterization of Unnotched SCS_6 Ti-15-3 Metal Matrix Composites at Room Temperature," *Thermal and Mechanical Behavior of Metal Matrix and Ceramic Matrix Composites, ASTM STP 1080*, J. M. Kennedy, H. H. Moeller, and W. S. Johnson, Eds., American Society for Testing and Materials, Philadelphia, 1990, pp. 193–218.

[47] Johnson, W. S., "Fatigue Testing and Damage Development in Continuous Fiber Reinforced Metal Matrix Composites," *Metal Matrix Composites: Testing, Analysis and Failure Modes, ASTM STP 1032*, W. S. Johnson, Ed., American Society for Testing and Materials, Philadelphia, 1989, pp. 194–221.

Distribution Effects and Homogenization

Hassan Yaacoub Agha,[1] *François Hild,*[1] *and René Billardon*[1]

Microscopic and Mesoscopic Damage Localization

REFERENCE: Yaacoub Agha, H., Hild, F., and Billardon, R., "**Microscopic and Mesoscopic Damage Localization,**" *Applications of Continuum Damage Mechanics to Fatigue and Fracture, ASTM STP 1315*, D. L. McDowell, Ed., American Society for Testing and Materials, 1997, pp. 119–130.

ABSTRACT: Initial defects are the main cause of the failure of structures made of brittle or quasi-brittle materials. The aim of this paper is to model within the framework of continuum damage mechanics these defects and their influence on the mechanical behavior of the structure they lie in by using a strain localization criterion. The microscopic and mesoscopic conditions for localization are studied by utilizing isotropic or anisotropic damage variables. A representative volume element (RVE) containing one defect is defined and the failure criterion of such an RVE is derived. The initial defect is modeled by an initial damage parameter. The evolution law of this damage value depends upon the nature of induced damage. Finally, an extension of this study to the case of high-cycle fatigue is proposed.

KEYWORDS: brittle materials, quasi-brittle materials, initial defects, initial damage parameter, induced damage parameter, continuum damage mechanics, damage localization, high-cycle fatigue, cracking, fatigue (materials), fracture (materials)

Initial defects are usually the cause of failure of structures made of brittle or quasi-brittle materials such as ceramics, concrete, and cast iron under high-cycle fatigue loading conditions. Studying the failure of this kind of material requires information about the initial distribution of these defects as well as their evolution. In the case of brittle materials, failure can be studied at a mesoscopic level where the structure is divided into representative volume elements (RVEs) that contain only one defect. The defects can be modeled by penny-shaped cracks. The failure criterion may be defined by a critical size of the propagating defect. Statistical models may be employed to analyze the failure of these structures [*1*]. For quasi-brittle materials, the details of the defect geometry must be taken into consideration. In this case, studying the failure of the structure requires information at a microscopic level.

Stationary waves were studied by Hadamard [*2*] in elasticity and by Hill [*3*] and Mandel [*4*] in elastoplasticity. Rice [*5*] related the localization of plastic shear bands to jumps of the velocity gradient. Borré and Maier [*6*] gave the conditions necessary for the onset of localized modes inside the body. These conditions are a generalization of the sufficient conditions derived by Rice and Rudnicki [*5,7*]. Strain localization corresponds to the onset of a surface across which the velocity field is discontinuous. In the framework of infinitesimal strain, damage may be one of the mechanisms responsible of such a localization. Localization is due to strain softening. Hence, continuum damage mechanics is an appropriate theory to determine the local failure of an RVE, that is, to define a macrocrack initiation condition. This criterion is then a strain and

[1] Research assistant, research associate professor, and professor, respectively, Laboratoire de Mécanique et Technologie, E.N.S. Cachan/C.N.R.S./Université Paris 6, 61, avenue du Président Wilson, F-94235 Cachan Cedex, France.

damage criterion to predict localization corresponding to the transition from a homogeneous deterioration to a localized one. This approach has successfully been used for ductile materials [*8,9*].

The aim of this paper is to model, in the framework of continuum damage mechanics, the defects and their influence on the mechanical behavior of the structure they lie in. The first step consists of studying the behavior of a matrix without defects and the corresponding localization conditions by using two different damage models. The first model corresponds to an isotropic description, and the second one to an anisotropic description that describes the creation of cracks in the matrix. In a second step, we define an RVE containing an initial defect and the failure criterion for such an RVE. The defects are modeled by an initial value of a damage variable. The evolution law of this damage parameter depends upon the nature of induced damage due to the loadings. In this paper, monotonic and high-cycle fatigue loadings are considered. Two phenomenological models are introduced: the first one is called an additive model where the induced damage is of the same nature as the initial damage, and the second is a multiplicative model where the induced damage is different from the initial one. Micromechanical analyses are carried out on pre-cracked cells and on volumes containing initial defects that can be modeled as cylindrical holes, and the propagating defects as penny-shaped cracks embedded in an elastic matrix.

State Coupling: Elasticity and Damage

The behavior of the matrix containing initial defects is considered to be elastic-damageable. The degradation mechanism is characterized by one scalar variable, D. This variable can be either isotropic or anisotropic. For the sake of simplicity, we will consider the case of plane stress. In the case of an isotropic damage description, the Helmholtz free energy density, ψ, and the associated force, Y, to the damage variable (that is, the energy release rate density [*10*]) can be written as [*11*]

$$\rho\psi = \frac{1}{2}\frac{E(1-D)[\varepsilon_{11}^2 + 2\nu\varepsilon_{11}\varepsilon_{22} + \varepsilon_{22}^2]}{1-\nu^2} + 2\tilde{G}(D)\varepsilon_{12}^2$$

$$Y = -\rho\frac{\partial\psi}{\partial D} = \frac{\sigma_{11}^2 + 2\nu\sigma_{11}\sigma_{22} + \sigma_{22}^2}{2E(1-D)^2} + \frac{\sigma_{12}^2}{2\tilde{G}(D)(1-D)},\ \tilde{G}(D) = G(1-D) \tag{1}$$

where

ρ = material density, kg/m^3;
ε_{11}, ε_{22}, ε_{12} = components of the infinitesimal strain tensor;
σ_{11}, σ_{22}, σ_{12} = components of the Cauchy stress tensor, Pa; and
E, ν = Young's modulus, Pa, and Poisson's ratio of the virgin material.

In the case of cracking that is normal to the 1-direction, an anisotropic damage variable is more appropriate. The damage variable, D, then is a function of the crack density (that is, $\pi a^2/S$, where $2a$ is the crack size within a surface, S) and the Helmholtz free energy density, ψ, and the energy release rate density, Y, are the following [*12*]

$$\rho\psi = \frac{1}{2}\frac{E\{(1-D)\varepsilon_{11}^2 + 2\nu(1-D)\varepsilon_{11}\varepsilon_{22} + \varepsilon_{22}^2\}}{1-\nu^2(1-D)} + 2\tilde{G}(D)\varepsilon_{12}^2$$

$$Y = -\rho\frac{\partial\psi}{\partial D} = \frac{\sigma_{11}^2 + \sigma_{12}^2}{2E(1-D)^2},\ \tilde{G}(D) = \frac{E}{2(1+\nu) + \dfrac{D}{1-D}} \tag{2}$$

Damage Evolution Law

In the case of an isotropic or anisotropic description, it was decided to model the damage evolution by a law developed by Marigo [*13*]. In this model the elastic domain is defined as

$$f(Y,D) = Y - (Y_{th} + MD) \leq 0 \tag{3}$$

where

Y_{th} = threshold energy release rate density below which no evolution occurs, J/m^3; and
M = scaling parameter, J/m^3.

For an initially virgin material ($D(t = 0) = 0$), the damage evolution is written as

$$\mathring{D} = \frac{\partial F}{\partial Y}\mathring{\lambda} \tag{4a}$$

where the loading/unloading conditions are formulated in Kuhn-Tucker form as

$$\mathring{\lambda} \geq 0,\ f \leq 0,\ \mathring{\lambda} f = 0 \tag{4b}$$

where

$\mathring{\lambda}$ = damage multiplier derived from the consistency condition $\mathring{\lambda}\mathring{f} = 0$, and
F = damage potential written as $F(Y) = (Y - Y_{th})/M$ so that $\mathring{\lambda} = \mathring{Y}$ and $\mathring{D} = \mathring{D}(\mathring{Y})$.

Microscopic Initiation Conditions

Local failure corresponds to the strain and damage localization in one point of the structure, that is, to the onset of a surface across which the strain rate is discontinuous, in other words, to the failure of the ellipticity condition. The strain rate is related to the stress velocity by

$$\underline{\underline{\mathring{\sigma}}} = \begin{cases} \underline{\underline{\underline{\underline{E}}}} : \underline{\underline{\mathring{\varepsilon}}} \text{ if } \mathring{D} = 0 & \text{(unloading)} \\ \underline{\underline{\underline{\underline{H}}}} : \underline{\underline{\mathring{\varepsilon}}} \text{ if } \mathring{D} \neq 0 & \text{(loading)} \end{cases} \tag{5}$$

where

$\underline{\underline{\underline{\underline{E}}}}$ = fourth order elastic operator, Pa;
$\underline{\underline{\underline{\underline{H}}}}$ = fourth order tangent operator, Pa; and
$\underline{\underline{\mathring{\sigma}}}, \underline{\underline{\mathring{\varepsilon}}}$ = second order stress rate (Pa/s) and strain rate tensors (1/s).

Localization occurs inside the structure if and only if [*6,7*]

$$\det\left(\underline{n} \cdot \underline{\underline{\underline{\underline{H}}}} \cdot \underline{n}\right) = 0 \tag{6}$$

where $\underline{n}$ = vector normal to the localization surface.

In the case of an isotropic damage description, the localization conditions for a plane stress state are depicted in Fig. 1, where k denotes the ratio of the in-plane minimum principal strain,

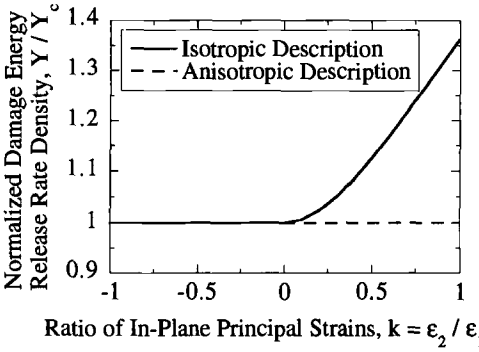

FIG. 1—*Evolution of the normalized energy release rate density at localization as a function of the ratio of in-plane principal strains.*

ε_2, upon the maximum principal strain, ε_1. The orientation of the localization surfaces are given in Figs. 2 and 3. The localization direction is unique and aligned with the maximum principal stress direction when the two principal strains are positive. On the other hand, they vary between 0° and ±45° if the minimum principal strain is negative.

When an anisotropic description is used, a closed-form solution for localization can be found provided the normal to the crack is parallel to the maximum principal strain direction, that is, the 1-direction. Localization occurs when

$$H_{1111} = \nu H_{1122} = \nu H_{2211} = 0 \text{ which leads to } Y = Y_c \tag{7}$$

where H_{1111}, H_{1122}, and H_{2211} are components of the tangent operator $\underline{\underline{\underline{H}}}$, Pa.

If $F(Y) = (Y - Y_{th})/M$, then $Y_c = (Y_{th} + M)/3$ and at localization $\sigma_{11} = (1 - F(Y_c))\sqrt{2EY_c}$. This value is the same as that obtained with the isotropic description in the case of

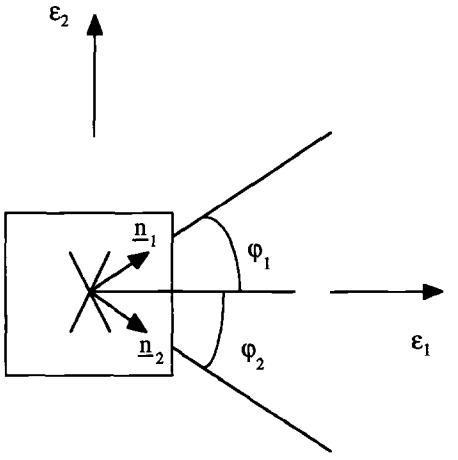

FIG. 2—*Orientation of the localization surfaces.*

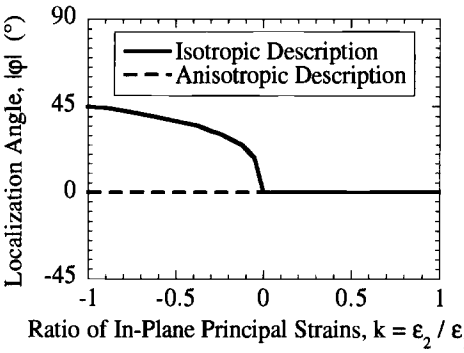

FIG. 3—*Evolution of the orientation of the localization surface as a function of the ratio of in-plane principal strains in plane stress conditions,* $|\varphi| = |\varphi_1|$ *or* $|\varphi| = |\varphi_2|$.

pure tension. In Figs. 1 and 3, the results of the present analysis are shown in dashed lines. It must be noticed that in this case, the localization direction always coincides with that of the cracking direction.

Behavior of a Predamaged RVE

The presence of defects in a considered RVE is modeled on a mesoscopic scale by damage parameters that are chosen uniform in the RVE and dependent on both the RVE size and the defect characteristics (for example, size, orientation). In the case of cylindrical holes, an initial value, D_0, of a mesoscopic isotropic damage variable, D, is assumed to be sufficient to model the influence of that kind of defect distribution. This isotropic damage variable is a function of the volume fraction of voids. In the case of a crack of size $2a$ with its normal aligned along the 1-direction in a cell of surface S, a mesoscopic anisotropic description may be used. It is characterized by a unique mesoscopic damage variable, D, of initial value, D_0, that is a function of the crack density (that is, $\pi a^2/S$).

In both isotropic and anisotropic cases, the question to address is the evolution of damage induced by the load history. When the nature of induced damage, d, is identical to that of the initial damage, D_0, a first approach assumes that

$$\mathring{D} = \frac{\partial F}{\partial Y}\mathring{\lambda} \text{ and } D(t = 0) = D_0 \tag{8}$$

In this case, induced damage, d, is defined by the following relationship

$$D = D_0 + d \tag{9}$$

This kind of approach has been used to model predamaged ductile materials [*14*].

On the other hand, if the induced damage is of a different nature from the initial damage, D_0, other assumptions may be valid. The Helmholtz free energy density must take into account D_0 so that in the case of an isotropic description, the Young's modulus of the material in its initial state (at $t = 0$) is equal to $E(1 - D_0)$. The damage evolution law for the induced damage, d, may be given by

$$\mathring{d} = \frac{\partial F}{\partial Y}\mathring{\lambda} \text{ and } d(t = 0) = 0 \tag{10}$$

In the case of an isotropic description for initial and induced damages, the final damaged elastic stiffness appears as $E(1 - D_0)(1 - d)$ that can be noted $E(1 - D)$ so that the final damage, D, is expressed by

$$D = D_0 + d(1 - D_0) \tag{11}$$

such a multiplicative coupling corresponds to the model proposed by Hayhurst and Perrin to study weldments [*15*].

Initial Damage is a Crack

Let us consider crack propagation of a pre-cracked system constituted of a plate with an initial crack of a size, $2a_0$. It can be shown that if this RVE is subjected to a load such that the maximum principal stress is normal to the initial crack, the final anisotropic damage variable, D, can be written as a function of the initial damage due to the initial crack, D_0, and the induced anisotropic damage, d

$$D = \frac{D_0 + d - 2D_0 d}{1 - D_0 d} \tag{12}$$

In this case, we have an expression corresponding to neither an additive nor a multiplicative model. In particular, the additive model, $D = D_0 + d$, is recovered only in the case of small values of $(D_0 d)$, even though the initial and induced damages are of the same nature.

Let us consider a case where there is an initial anisotropic damage, D_1, corresponding to cracking normal to the 1-direction. If the material is subsequently loaded in the perpendicular 2-direction, an induced damage variable, D_2, may develop so that the Helmholtz free energy density can be written as [*12*]

$$\rho\psi = \frac{1}{2}\frac{E\{(1 - D_1)\varepsilon_{11}^2 + 2\nu(1 - D_1)(1 - D_2)\varepsilon_{11}\varepsilon_{22} + (1 - D_2)\varepsilon_{22}^2\}}{1 - \nu^2(1 - D_1)(1 - D_2)} + 2\tilde{G}(D_1, D_2)\varepsilon_{12}^2$$

$$\tilde{G}(D_1, D_2) = \frac{E}{2(1 + \nu) + \dfrac{D_1}{1 - D_1} + \dfrac{D_2}{1 - D_2}} \tag{13}$$

In that case, the multiplicative effect only appears in the terms modeling the Poisson effect.

Initial Damage is a Hole

In this part, numerical simulations are performed on plates containing holes of different sizes. The value of the initial isotropic damage, D_0, is obtained by computing loss of stiffness due to the presence of a hole of a given diameter.

Simulations are done on six plates of size $2b$ containing holes of diameters, $2r$, so that the ratio b/r varies between 0.1 and 0.6 with a step of 0.1. Plates are subjected to a remote uniaxial displacement. For each displacement, the global reaction force is computed. The value of the mesoscopic damage variable then corresponds to the loss of stiffness. The mesoscopic damage

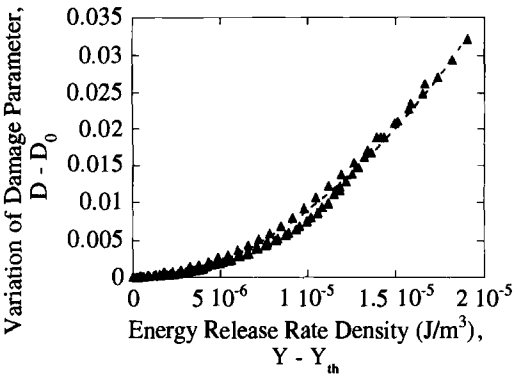

FIG. 4—*Evolution of the variation of the mesoscopic induced damage,* $D - D_0$, *as a function of the mesoscopic energy release rate density,* $Y - Y_{th}$, *for all the analyzed hole diameters with an isotropic damage description at the microscopic level.*

evolution (defined by a damage offset of 0.0001) occurs when the energy release rate density, Y, reaches a threshold value depending upon the initial damage, $Y_{th}(D_0)$. The numerical results can be fitted by the following relationship

$$Y_{th}(D_0) = Y_{th0}(1 - D_0)^2 \tag{14}$$

The mesoscopic damage evolution is plotted as a function of the evolution of the energy release rate density, $Y - Y_{th}(D_0)$, in Fig. 4. The relationship between the two variables can be fitted by

$$D - D_0 = A\left[\frac{Y - Y_{th}(D_0)}{Y_{th0}}\right]^B \tag{15}$$

where A, B = material parameters.

Equation 15 shows again that in this case the damage evolution is neither multiplicative nor additive. However, if one assumes that the evolution of induced damage, d, may be influenced by the initial damage, D_0, then Eq 15 corresponds to an additive model.

Monotonic Failure Conditions of an RVE

In this section, the failure criterion for an RVE containing an initial defect is analyzed in terms of strain and damage localization at a microscopic level. First, the localization conditions are obtained for cells containing cylindrical holes subjected to remote tension, σ_∞, in plane stress conditions. The induced microscopic damage in the surrounding matrix is assumed to be either isotropic or anisotropic.

The influence on the localization conditions of different parameters characteristic of the mesh refinement were studied. Figure 5 shows a typical mesh used for these numerical simulations. After several simulations, it appeared that the parameter that has the most important effect on the localization conditions is the size of the most loaded element, Δ. Figure 6 shows the evolution of the failure stress at localization for one initial damage value ($D_0 = 0.02$) as a function

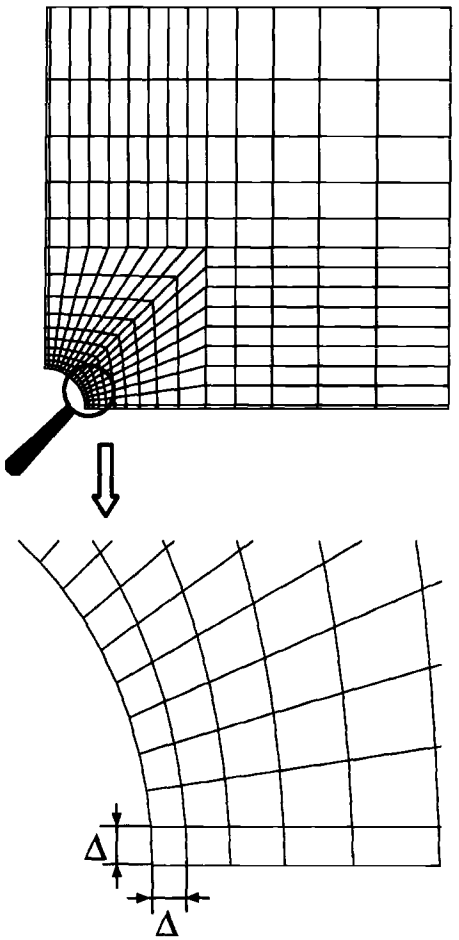

FIG. 5—*Mesh of a plate with a hole corresponding to an initial damage,* $D_0 = 0.02$.

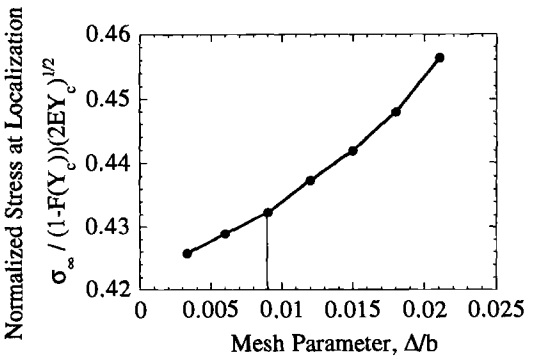

FIG. 6—*Evolution of a mesoscopic stress at localization as a function of the* Δ *mesh size* ($D_0 = 0.02$).

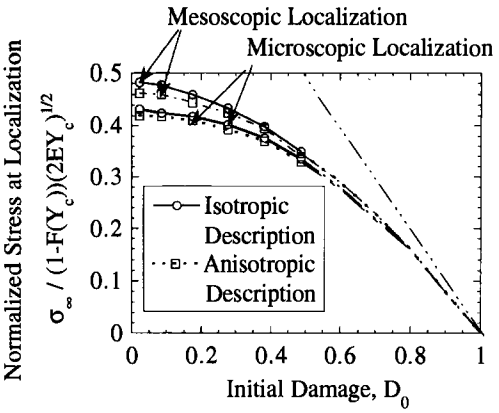

FIG. 7—*Mesoscopic stress at microscopic and mesoscopic damage localization for isotropic and anisotropic damage models at a microscopic level.*

of Δ/b. A fixed value, $\Delta/b = 0.009$, is used for all simulations. The present value is taken as a compromise between mesh sensitivity and computation cost.

Figure 7 shows the mesoscopic stress, σ_∞, at microscopic localization for different values of the initial damage variable, D_0. The difference between the stress values at localization for the two models is not very important, which can be justified by the results of Fig. 1 for which the localization conditions for values of the strain ratio, $k < 0$, are identical for both models. The same conclusion can be drawn for the stress levels at mesoscopic localization, that is, peak of the mesoscopic stress, σ_∞. Besides, it can be shown that all the curves of Fig. 7 can be approximated by the following expression

$$\Sigma = \beta(1 - D_0)^{-1/\beta} + (1 - D_0) \tag{16}$$

where

Σ = normalized stress, and
β = material parameter depending on the damage description.

It is worth noting that in this case the mesoscopic stress levels at microscopic and mesoscopic localization are very close to each other. Similar results have already been found for unidirectional fiber-reinforced composites [*16*]. It is worth remembering that the mesoscopic stress level at mesoscopic localization may be mesh-dependent. Since the latter is very close to that at microscopic localization, it is expected that the mesh-dependence is very weak.

Extension to High-Cycle Fatigue

It is assumed that the damage evolution law has the main features of a macrocrack propagation law based upon a generalized Paris' law [*17*]

$$\frac{1}{(1 - D)^2}\frac{dD}{dN} = C\left(\frac{\sqrt{Y_{\max}} - \sqrt{Y_{\text{th}}}}{\sqrt{Y_c} - \sqrt{Y_{\text{th}}}}\right)^n \tag{17}$$

where

C,n = material parameters;

$Y_{max} = \dfrac{\sigma_{max}^2}{2E(1-D)^2}$, maximum over one cycle of the energy release rate density, Jm^{-3};

Y_c = critical energy release rate corresponding to microscopic failure (localization), Jm^{-3}; and

Y_{th} = threshold energy release rate density below which no damage evolution occurs, Jm^{-3}.

If we consider that the initial damage values are bounded by a maximum damage value, D_{0M}, two threshold stresses can be defined. A monotonic threshold stress, S_c, denoting the minimum value of the applied local stress above which local failure is certain under monotonic loading (that is, when the initial damage value of the RVE is equal to D_{0M}). A cyclic threshold stress, S_{th} denoting the minimum value of the applied local stress below which local failure does not occur. These two stresses are defined by

$$S_c = (1 - D_{0M})\sqrt{2EY_c},\ S_{th} = (1 - D_{0M})\sqrt{2EY_{th}} \tag{18}$$

Integration of Eq 17 gives the relationship between the damage value, D, after N cycles of constant amplitude $Y_{max} - Y_{min} \geq Y_{max} - Y_{th}$ and the initial damage value, D_0

$$\varphi(D) - \varphi(D_0) = \frac{(1-n)C}{\left(\dfrac{1}{k} - 1\right)^n \dfrac{1}{(1 - D_{0M})^n}} \left(\frac{\sigma_{max}}{S_{th}}\right)^n N \tag{19}$$

with

$$\varphi(D) = \left(\frac{1}{1-D} - \frac{1}{1 - D_{th}}\right)^{1-n} \text{ if } D_0 \geq D_{th},\ k = \frac{S_{th}}{S_c}$$

where D_{th} = threshold damage value associated to the applied stress σ_{max}: $Y_{th} = \dfrac{\sigma_{max}^2}{2E(1 - D_{th})^2}$.

Microscopic localization occurs when the damage value reaches a critical value, D_c, corresponding to the critical energy release rate density

$$Y_c = \frac{\sigma_{max}^2}{2E(1 - D_c)^2} \tag{20}$$

so that the number of cycles to failure, N_F, is given by

$$\varphi(D_c) - \varphi(D_0) = g\left(N_F; \frac{\sigma_{max}}{S_{th}}\right) \tag{21}$$

where

$$g\left(N_F; \frac{\sigma_{max}}{S_{th}}\right) = \frac{(1-n)C}{\left(\dfrac{1}{k} - 1\right)^n \dfrac{1}{(1 - D_{0M})^n}} \left(\frac{\sigma_{max}}{S_{th}}\right)^n \text{ and } N_F \text{ represents the effect of induced damage.}$$

Equation 21 shows that in the general case, the effect of induced damage is neither additive nor multiplicative.

Conclusions

An elastic law coupled with damage is introduced to study the behavior of quasi-brittle materials. Two kinds of damage variables are introduced to model the material degradation. The first one is an isotropic damage variable and the second is an anisotropic one able to model microcracking. The local failure criterion is damage localization at one point of the structure. Under plane stress conditions, the isotropic and anisotropic descriptions are equivalent in terms of load level and angle at localization when the ratio between the principal strains is less than zero. Microscopic localization corresponding to local failure appears when the energy release rate density reaches a critical value, Y_c.

The presence of an initial defect in an RVE is modeled by an initial damage value, D_0, measuring stiffness loss due to the presence of the defect. Two models are introduced to study the damage evolution in an RVE containing an initial defect. The first one is an additive model, where the induced damage is of the same nature as the initial damage. The second one is a multiplicative law, which can model the cases where the induced damage is of a different nature from initial damage. A micromechanical study of a pre-cracked system shows that the damage law can be an additive model for small values of induced damage. In the general case, however, the damage law is more complicated as exemplified by a numerical micromechanical study of plates with holes. A mesoscopic damage law evolution can be identified by studying the evolution of the induced damage as a function of the energy release rate density.

An extension to high-cycle fatigue using a damage evolution law deduced from a generalized Paris' law for the case of macrocrack propagation is also proposed. The damage value after N cycles is given as a function of the initial damage value and the maximum applied stress. A critical damage value leading to damage localization is deduced from the critical value of the energy release rate density. This model also shows the complexity of the damage law in the general case.

References

[1] Hild, F., Béranger, A.-S., and Billardon, R., "Fatigue Failure Maps of Heterogeneous Materials," *Mechanics of Materials*, Vol. 22, 1996, pp. 11–21.

[2] Hadamard, J., "Leçon sur la propagation des ondes et les équations de l'hydrodynamique," *Libraries scientifiques A*, Hermann, Paris, 1903.

[3] Hill, R., "Acceleration Waves in Solids," *Journal of the Mechanics and Physics of Solids*, Vol. 10, 1962, pp. 1–16.

[4] Mandel, J., "Ondes plastiques dans un milieu indéfini à trois dimensions," *Journal de Mécanique*, Vol. 1, No. 1, 1962, pp. 3–30.

[5] Rice, J. R., "The Localization of Plastic Deformations," *Theoretical and Applied Mechanics*, W. T. Koiter, Ed., North-Holland, Amsterdam, London, 1976, pp. 207–220.

[6] Borré, G. and Maier, G., "On Linear versus Nonlinear Flaw Rules in Strain Localization Analysis," *Meccanica*, Vol. 24, 1989, pp. 36–41.

[7] Rudnicki, J. W. and Rice, J. R., "Conditions for Localization of Deformation in Pressure-Sensitive Dilatant Materials," *Journal of the Mechanics and Physics of Solids*, Vol. 23, 1975, pp. 371–394.

[8] Billardon, R. and Doghri, I., "Prévision de l'amorçage d'une macro-fissure par la localisation de l'endommagement," *Comptes Rendus de l'Académie des Sciences, Paris*, Vol. 308, Série II, 1989, pp. 347–352.

[9] Doghri, I. and Billardon, R., "Investigation of Localization due to Damage in Elasto-Plastic Materials," *Mechanics of Materials*, Vol. 19, 1995, pp. 129–149.

[10] Chaboche, J.-L., "Description thermodynamique et phénoménologique de la viscoplasticité cyclique avec endommagement," Thèse d'Etat, Université Paris 6, 1978.

[11] Lemaitre, J., *A Course on Damage Mechanics*, Springer-Verlag, Berlin, 1992.

[12] Burr, A., Hild, F., and Leckie, F. A., "Micro-Mechanics and Continuum Damage Mechanics," *Archive of Applied Mechanics*, Vol. 65, No. 7, 1995, pp. 437–456.

[13] Marigo, J.-J., "Formulation d'une loi d'endommagement d'un matériau élastique," *Comptes Rendus de l'Académie des Sciences, Paris*, Vol. 292, Série II, 1981, pp. 1309–1312.

[*14*] Benallal, A., Billardon, R., Doghri, I., and Moret-Bailly, L., "Crack Initiation and Propagation Analyses Taking into Account Initial Strain Hardening and Damage Fields," *Numerical Methods in Fracture Mechanics*, A. Luxmore, Ed., Pineridge Press, Swansea, UK, 1987, pp. 337–351.

[*15*] Hayhurst, D. R. and Perrin, I. J., "CDM Analysis of Creep Rupture in Weldments," *Proceedings*, 10th ASCE Engineering Mechanics Conference, S. Sture, Ed., Boulder, CO, American Society of Civil Engineers, New York, 1995, pp. 393–396.

[*16*] Hild, F. and Burr, A., "Localization and Ultimate Strength of Fiber-Reinforced Ceramic-Matrix Composites," *Mechanics Research Communications*, Vol. 21, No. 4, 1994, pp. 297–302.

[*17*] Pellas, J., Baudin, G., and Robert, M., "Mesure et calcul du seuil de fissuration après surcharge," *Recherche aérospatiale*, Vol. 3, 1977, pp. 191–201.

Thomas E. Lacy,[1] *Ramesh Talreja,*[2] *and David L. McDowell*[1]

Effects of Damage Distribution on Evolution

REFERENCE: Lacy, T. E., Talreja, R., and McDowell, D. L., **"Effects of Damage Distribution on Evolution,"** *Applications of Continuum Damage Mechanics to Fatigue and Fracture, ASTM STP 1315*, D. L. McDowell, Ed., American Society for Testing and Materials, 1997, pp. 131–149.

ABSTRACT: Recent micromechanically inspired phenomenological theories using internal state variable (ISV) representations of damage have been used to predict the thermomechanical behavior of microcracked solids. These models do not, in an explicit manner, account for distributions of microcracks in a representative volume element (RVE) and have been used successfully only to determine the effective moduli of damaged solids. It has been demonstrated that while the distribution and interaction of damage entities within an RVE generally have a minor effect on the effective moduli, it has a significant effect on the evolution of damage and failure at the macroscale. Damage evolution rates, in general, cannot be described adequately by such theories because of their inability to account for interactions between damage entities in an arbitrary distribution.

Key issues pertaining to the development of viable damage evolution equations using a continuum damage mechanics approach are addressed. In particular, limitations associated with the use of ISVs that can be expressed either in terms of macroscopically measurable quantities or through a spatial average of the geometric features of individual damage entities are discussed. Numerical simulations of evolving crack systems in two-dimensional perfectly brittle solids indicate that "effective stress" models may have difficulty in characterizing damage evolution in brittle microcracked solids when the damage consists of cracks of variable size or spatial distributions. An argument for implementing ISVs based on higher-order moments of the damage distribution within an RVE is presented.

KEYWORDS: continuum damage mechanics, damage evolution, brittle microcracked solids, internal state variable theory, damage distribution effects, cracking, fatigue (materials), fracture (materials)

Characterization of the thermomechanical response of materials with distributed damage remains one of the key problems in solid mechanics. Many such materials are capable of sustaining substantial loading-induced mesostructural damage prior to catastrophic failure. Two primary aspects of the problem involve determination of effective properties for damaged solids and formulation of damage evolution laws. The former has received the bulk of the treatment in the literature, whereas the latter is much less developed. Critical differences in the way the distribution of damage influences the effective moduli and subsequent damage evolution dictate the manner in which each aspect of the problem may be appropriately described. Numerous micromechanical and continuum damage models have been suggested in order to address the problem.

Micromechanical approaches, in general, attempt to predict the macroscale thermomechanical response of heterogeneous materials based on mesostructural models of a representative

[1] Doctoral candidate and professor, respectively, Department of Mechanical Engineering, Georgia Institute of Technology, Atlanta, GA 30332–0405.

[2] Professor, Department of Aerospace Engineering, Georgia Institute of Technology, Atlanta, GA 30332–0150.

volume element (RVE) within the material. An RVE may be defined as the minimum material volume that contains a sufficient number of damage entities to provide a "statistically homogeneous" representation of the mesostruction [*1*]. Statistical homogeneity, for general purposes, requires that all global geometrical characteristics (volume fraction of constituents, two-point statistics, etc.) are the same in any RVE, irrespective of its position. Commonly, the RVE is defined as a cube of material with dimension, l_{REV}, subject to the condition that l_{RVE}/d is "sufficiently large." Here, d is the wavelength over which the traction or displacement on the RVE boundary fluctuates about some mean value under conditions of uniform displacement or traction, respectively [*2,3*]. The RVE may include specific mesostructural details of composite phase geometry, nature and distribution of damage, and properties of constituent materials. Micromechanical models have the distinct advantage of being able to capture structural details at the microscale and mesoscale, and to allow formulation of the kinetic equations for damage evolution based on the actual physical processes involved. The models, however, can be computationally inefficient in many practical applications, and can only be applied to limited classes of materials and damage mechanisms [*4–6*]. Mural [*7*], Nemat-Nasser and Hori [*3*], Christensen [*8*], and Torquato [*9*] provide extensive overviews of micromechanics of heterogeneous materials.

Given the large-scale numerical calculations generally required for micromechanical analysis of heterogeneous materials, perhaps the most practical vehicle for the development of a general thermomechanical constitutive theory for damaged solids lies within the framework of continuum damage mechanics (CDM) using internal state variables (ISVs). Arising from the classical studies of creep rupture of metals by Kachanov [*10*] and Rabotnov [*11*], CDM is based on the thermodynamics of irreversible processes [*12–14*], internal state variable theory [*15*], and relevant physical considerations (assumption of distributed damage, homogenization concepts, definition of the damage variable, formulation of kinetic laws for damage evolution, etc. see Ref *4*). A solid that is highly heterogeneous at the mesoscale is considered an effective homogeneous continuum at the macroscale. Macroscopic damage variables are judiciously selected to reflect the effects of RVE level irreversible processes on macroscale material behavior. The fact that the theory refers to a homogeneous continuum, however, presents a serious obstacle in the development of damage evolution laws that incorporate effects of the heterogeneity of the solid at the mesoscale. Whereas effective moduli are somewhat insensitive to the distribution of damage, damage evolution is highly dependent on the local fluctuations in the damage distribution within the RVE used for stiffness calculations [*16–19*]. In the homogenization process, critical information regarding the largest flaw size, minimum distance between flaws, and distribution of damage within an RVE may be irrevocably lost. Such information is crucial to the development of viable evolution equations. Current CDM approaches have been limited generally to the case of dilute (noninteracting) damage. Lacy et al. [*20*] summarize key issues pertaining to the use of CDM to predict effective moduli and damage evolution in brittle microcracking solids.

Brief Overview of CDM

The specific Helmholtz free energy of a damaged solid can be characterized for the thermoelastic case by the constitutive relationship

$$\Psi = \Psi(\epsilon, T, \boldsymbol{D}^{(\alpha)}) \tag{1}$$

where Ψ is the Helmholtz free energy, ϵ is the small strain tensor, T is the absolute temperature, and $\boldsymbol{D}^{(\alpha)}$ are the damage internal state variables (ISVs) necessary to characterize the effect of mesostructural damage (and its distribution) on the macroscopic response ($\alpha = 1, 2, \ldots, N$).

Here, boldface characters denote tensorial quantities. The ISVs may be represented by scalar, vector, or higher-rank tensor quantities, although a tensorial representation of damage is usually preferable [*21*].

According to standard arguments, this framework leads to certain relationships for conjugate thermodynamic forces [*4,22–29*], that is

$$\boldsymbol{\sigma} = \rho \frac{\partial \Psi}{\partial \boldsymbol{\epsilon}}, \; s = -\frac{\partial \Psi}{\partial T}, \; \boldsymbol{Y}^{(\alpha)} = -\rho \frac{\partial \Psi}{\partial \boldsymbol{D}^{(\alpha)}} \tag{2a,b,c}$$

where $\boldsymbol{\sigma}$ is the Cauchy stress tensor, s is the specific entropy, $\boldsymbol{Y}^{(\alpha)}$ is the generalized thermodynamic force conjugate to $\boldsymbol{D}^{(\alpha)}$ (hereinafter referred to as "thermodynamic force"), and ρ is the mass density of the solid. $\boldsymbol{Y}^{(\alpha)}$ is often interpreted as the strain energy release rate (ERR) associated with an increment of damage extension (evolution). The elasticity tensor for a given state of damage, C, is given by

$$C_{ijkl} = \rho \frac{\partial^2 \Psi}{\partial \epsilon_{ij} \partial \epsilon_{kl}} \tag{3}$$

It should be noted that damage development in heterogeneous materials may result in a change in material symmetry properties [*6,30*]. The rate of change of the internal state of the solid is governed by the evolution equations

$$\dot{\boldsymbol{D}}^{(\alpha)} = \dot{\boldsymbol{D}}^{(\alpha)}(\boldsymbol{\epsilon}, T, \boldsymbol{D}^{(\gamma)}) \tag{4}$$

It is important to note that evolution of a given internal state variable, $\dot{\boldsymbol{D}}^{(\alpha)}$, depends on the instantaneous values of all other ISVs, $\boldsymbol{D}^{(\gamma)}$, where $\gamma = 1, \ldots, N$. In general, the kinetic equations describing the evolution of damage may be written as independent equations of evolution for every internal state variable (Eq 4) or as derivatives of a suitably chosen potential function, invoking the postulate of generalized normality [*14*]. Furthermore, as a consequence of the second law of thermodynamics, the evolution equations (Eq 4) are governed by the dissipation inequality

$$\sum_{\alpha=1}^{N} (\boldsymbol{Y}^{(\alpha)} \cdot \dot{\boldsymbol{D}}^{(\alpha)}) \geq 0 \tag{5}$$

where a dot $(\cdot)$ denotes the scalar product of two tensors. Thus, the purely mechanical response of a damaged solid may be determined by the formulation of the constitutive equations given by Eqs 1 and 4, and by invoking the corollary conditions (Eqs 2*a* and *c*, and Eq 5). Equivalently, the formulation may be posed in terms of the Gibbs potential

$$g = g(\boldsymbol{\sigma}, T, \boldsymbol{Y}^{*(\alpha)}) \tag{6}$$

resulting in equations analogous to Eqs 2 through 4 in terms of Variables $\boldsymbol{\sigma}$, T, and $\boldsymbol{Y}^{*(\alpha)}$ as well as the compliance tensor, $\boldsymbol{S}$. We will focus on isothermal, purely mechanical applications here.

Implementation of CDM

The previous development, Eqs 1 through 6, is general in nature and may be used to characterize the response of materials containing damage that is both arbitrary in character (cracks,

voids, other inelastic deformation) and distribution. Practical considerations, however, often dictate the type and number of damage ISVs that can be used effectively in this approach.

The selection of a macroscopic damage variable, in principle, may be somewhat arbitrary and need not directly reflect any of the underlying dissipative or energy transfer processes occurring at the mesoscale. Commonly, a damage parameter is selected that can either be expressed in terms of macroscopically measurable quantities (giving rise to so-called "effective-stress" or similar models) or that incorporates prominent aspects of damage morphology in its definition (that is, so called "micromechanically inspired" damage variables). Either choice of damage parameter has inherent limitations that affect its utility in a CDM formulation. Some of the drawbacks associated with each approach are discussed in the following subsections.

Effective Stress Models

Numerous damage models have incorporated scalar or tensorial damage variables that can be characterized at the macroscale (for example, by change in compliance). Chaboche [*31*] developed a fourth-rank tensor representation of damage for the three-dimensional case, that is

$$\boldsymbol{D} = \boldsymbol{I} - \boldsymbol{C}^* : \boldsymbol{C}_0^{-1} \tag{7}$$

where $\boldsymbol{C}^*$ and $\boldsymbol{C}_0$ are the stiffness tensors for the solid in the damaged and undamaged states, respectively, $\boldsymbol{I}$ is the fourth rank unit tensor, and a colon (:) denotes the second-order contraction of tensor indices. The components of the damage tensor in this case can be determined from elastic compliance changes. With such a representation of damage, it is possible to define a fictitious "effective stress," $\boldsymbol{\sigma}^*$, that produces the same elastic deformation in the undamaged solid as does the actual stress $\boldsymbol{\sigma}$, in the damaged configuration. The two stress states are related by the relationship [*31*]

$$\boldsymbol{\sigma}^* = (\boldsymbol{I} - \boldsymbol{D})^{-1} : \boldsymbol{\sigma} \tag{8}$$

Such approaches have been used extensively to describe damage development in initially isotropic homogeneous ductile materials under creep and fatigue [*28,31–38*]. Damage variables inferred on the basis of the effective stress concept or similar notions (for example, effective area, section, volume, etc.) do not contain information regarding the nature and distribution of damage.

In order to assess the viability of such macroscopic damage variables in a CDM formulation, parametric studies were performed to examine the effect of initial crack patterning on self-similar damage evolution for a number of periodic distributions of parallel cracks in two-dimensional, idealized, brittle solids under plane-strain conditions. Following the methodology outlined by Lacy et al. [*20*], numerical simulations of evolving crack systems were conducted, and the effective moduli and the RVE averaged ERR were calculated at each increment of damage evolution, for a given measure of damage. A macroscopically measurable damage parameter was selected in order to evaluate its utility in assessing damage evolution in periodic arrays of flaws of various sizes and spatial distribution. Such an idealized problem is used here to clearly demonstrate the issues, although we assert that these issues pertain to much broader classes of damage in nonlinear, history-dependent materials.

Figure 1 shows a schematic of a representative model used in the numerical study. A periodic distribution of cracks parallel to the x_1-axis was assumed in an RVE consisting of a linearly elastic, isotropic, homogeneous solid under isothermal conditions. Periodic boundary conditions were applied to simulate a repeating mesostructure. A displacement, u_2, was applied in the x_2-direction to the upper RVE boundary. The magnitude of u_2 was chosen such that Mode I

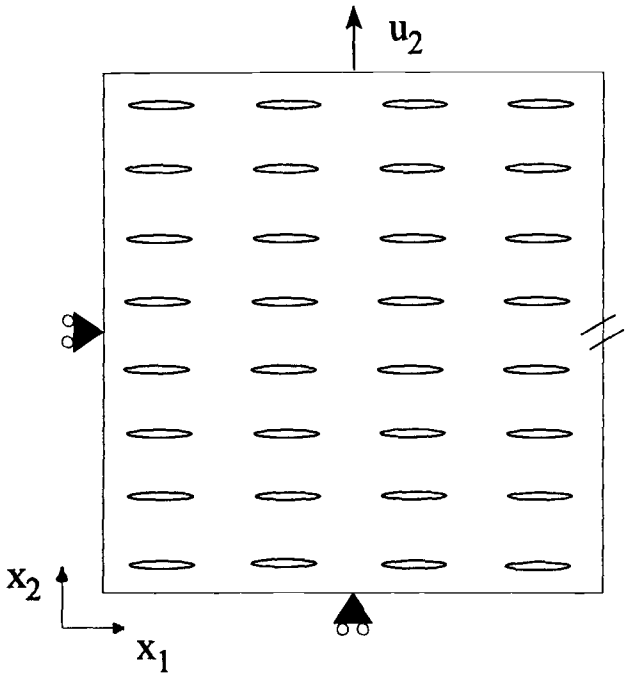

FIG. 1—*Schematic of typical RVE and associated boundary conditions used in numerical simulations of damage evolution.*

crack extension of the worst-case crack tip in the RVE was imminent. Individual crack tips were incremented in self-similar fashion whenever K equaled K_{1C}, where K is the Mode I stress intensity factor (SIF) and K_{1C} is the plane-strain fracture toughness of the material; the material was assumed to have no intrinsic toughening capability (that is, perfectly brittle). Accordingly, the applied displacement, u_2, was adjusted at every increment of crack growth to ensure stable damage evolution. The RVE-averaged stiffness and ERR, as well as the local driving forces, were evaluated for each stable damage configuration. For illustration purposes, a macroscopically measurable damage variable analogous to Eq 8 was used to characterize the damage distribution, that is

$$D = \frac{E_0 - E_2}{E_0} = \frac{\Delta E}{E_0} \tag{9}$$

where E_2 and E_0 are Young's moduli in the x_2-direction for the damaged and virgin isotropic materials, respectively. For an RVE with some initial distribution of cracks, continuous damage evolution may be numerically simulated by a sequence of $M - 1$ increments of damage associated with M stable damage states, $D^{(i)}$, where $i = 1, \ldots, M$. Each stable damage state, $D^{(i)}$, has an associated threshold RVE-averaged strain energy density value, $W^{(i)}$, necessary for additional damage evolution to occur (that is, such that $K = K_{1C}$ for any given crack tip contained in the RVE). Following Lacy et al. [*20*], Eq 2*c* may be approximated for the *i*th stable damage state using the three-point formula [*39*]

$$Y^{(i)} = -\rho \frac{W^{(i+1)} - W^{(i-1)}}{D^{(i+1)} - D^{(i-1)}} \qquad i = 2, \ldots, M - 1 \tag{10}$$

where $Y^{(i)}$ is the value of the RVE-averaged thermodynamic force conjugate to damage, $D^{(i)}$, at the ith stable damage state. Two-point formulas analogous to Eq 10 may be used to evaluate $Y^{(i)}$ for the cases of $i = 1$ and $i = M$ [*39*]. Thus, Eqs 9 and 10 may be used to evaluate the RVE-averaged scalar damage ISV (in this case, effective modulus) and thermodynamic force conjugate to damage at every increment of damage evolution.

Figure 2 shows three uniform crack distributions over the RVE consisting of one, four, and sixteen cracks, respectively. Each distribution had the same normalized vertical and horizontal spacing between neighboring cracks ($h/w = 1$); however, the initial crack lengths, a/w_{RVE}, of the second and third configurations were approximately one-half and one-fourth, respectively,

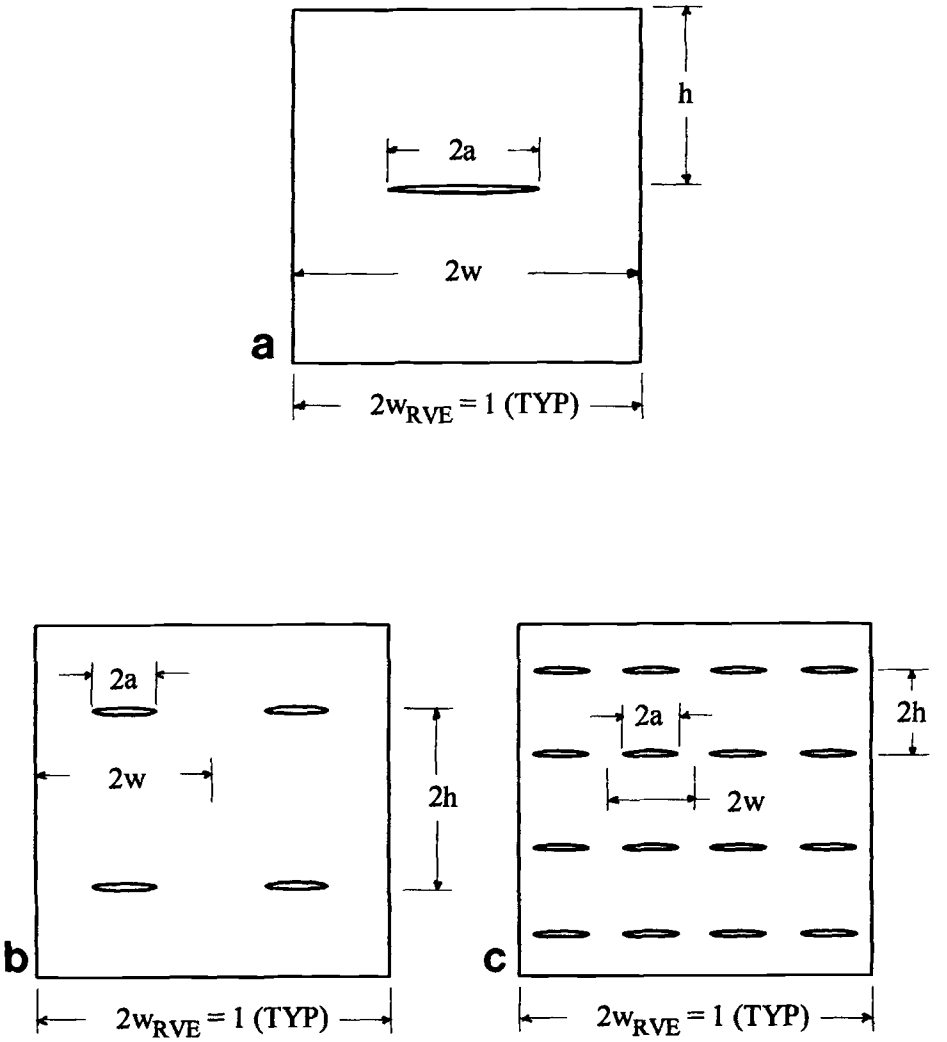

FIG. 2—*Uniform crack distributions used in numerical simulations of damage evolution:* (a) *uniform crack distribution No. 1* (h/w = *1, 0.3* ≤ a/w_{RVE} ≤ *0.95*), (b) *uniform crack distribution No. 2* (h/w = *1, 0.14* ≤ a/w_{RVE} ≤ *0.46*), *and* (c) *uniform crack distribution No. 3* (h/w = *1, 0.07* ≤ a/w_{RVE} ≤ *0.23*).

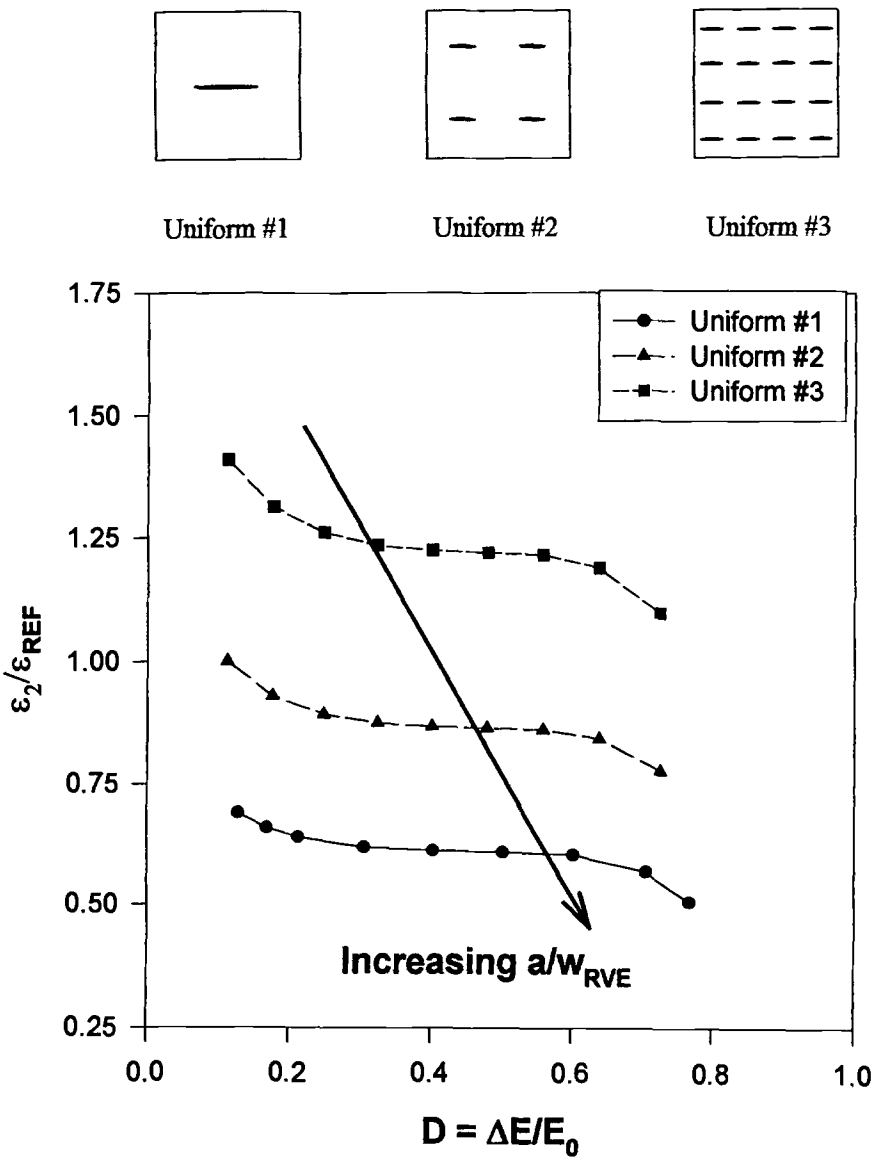

FIG. 3—*Normalized strain necessary to initiate damage evolution.*

of that of the first configuration. These configurations were used to demonstrate the effect of the relative distribution of crack lengths on macroscopic stiffness and ERR. Figure 3 shows a plot of the normalized critical threshold strain, $\epsilon_2/\epsilon_{REF}$, necessary to initiate damage evolution for each configuration, where ϵ_2 is the RVE-averaged strain in the x_2-direction and ϵ_{REF} is the critical threshold strain associated with the initial damage state of the crack distribution shown in Fig. 2*b*. As expected, the uniform distributions with the largest characteristic crack sizes had the lowest threshold strain values throughout the entire range of damage evolution. The results suggest that for periodic arrays of cracks in brittle solids, knowledge of the reduction in moduli

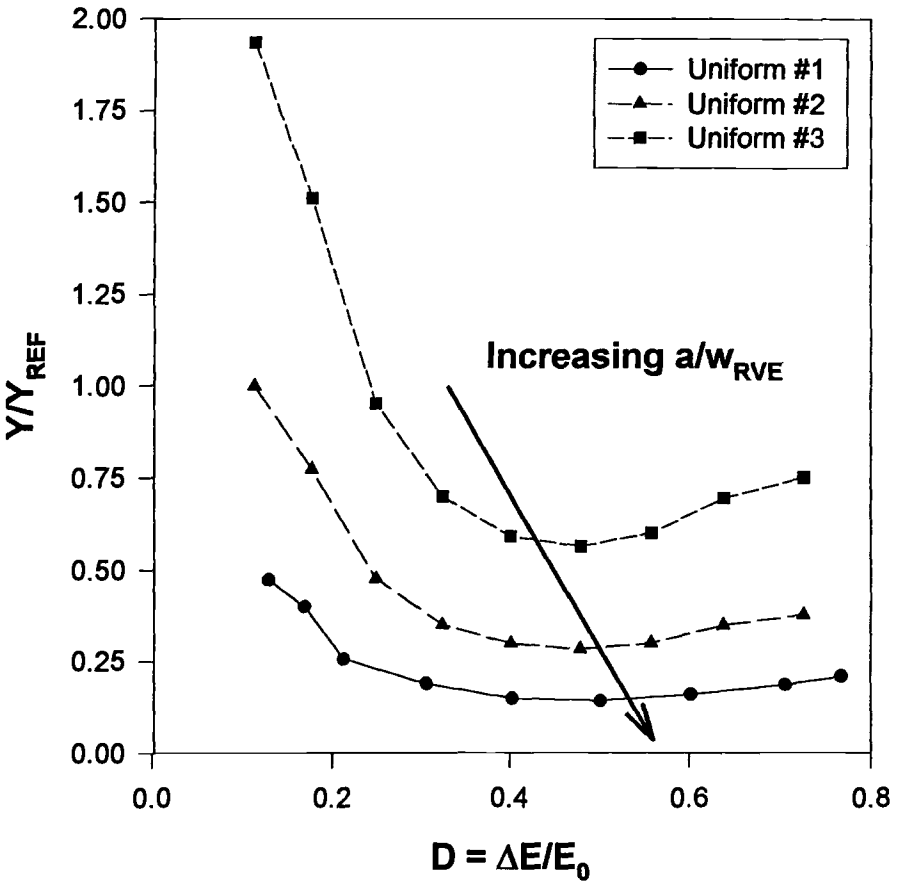

FIG. 4—*Normalized thermodynamic force obtained from numerical simulations of damage evolution in uniform crack distributions.*

due to the presence of defects is insufficient to assess the likelihood of damage evolution or failure or both; the characteristic size of defects relative to the RVE size also has a significant effect on the critical strain necessary to initiate damage evolution. Similarly, the RVE averaged ERR was markedly different for each distribution. Figure 4 shows that, for a given reduction in stiffness, the normalized thermodynamic force, Y/Y_{REF}, necessary for damage evolution decreased as the characteristic crack size of the distribution increased, where Y is the thermodynamic force and Y_{REF} is a reference (constant) thermodynamic force associated with the onset of crack extension for the initial damage state of the crack distribution shown in Fig. 2*b*. For each of the three uniform distributions, the thermodynamic force initially decreased rapidly with increasing stiffness reduction, and then approached a nearly asymptotic value that depended on the characteristic crack size. This reflects, perhaps, the effect of increasing shielding as the parallel cracks evolve from relatively dilute to strongly interactive configurations. These results indicate that distributions consisting of larger cracks will reach criticality and evolve at lower load levels and lower RVE strain energy release rates than distributions consisting of smaller cracks having the same degraded elastic modulus.

In addition to the distribution of crack lengths, the spatial distribution of flaws also plays a

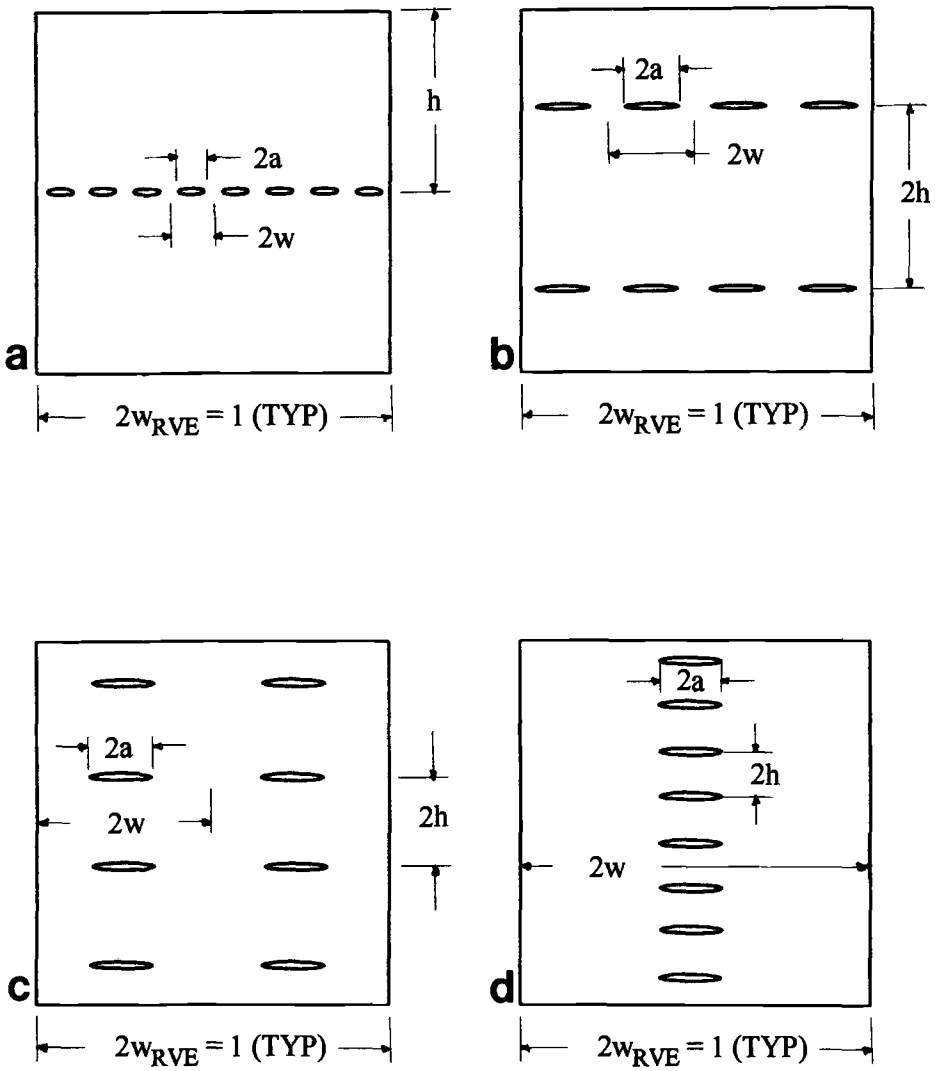

FIG. 5—*Nonuniform crack distributions used in numerical simulations of damage evolution:* (a) *strong enhancement* (h/w = *8, 0.05* ≤ a/w_{RVE} ≤ *0.11*), (b) *moderate enhancement* (h/w = *2, 0.1* ≤ a/w_{RVE} ≤ *0.23*), (c) *moderate shielding* (h/w = *1/2, 0.1* ≤ a/w_{RVE} ≤ *0.45*), *and* (d) *strong shielding* (h/w = *1/8, 0.08* ≤ a/w_{RVE} ≤ *0.52*).

critical role in damage evolution. Crack distributions that are biased toward either crack-tip shielding or enhancement configurations may exhibit markedly different RVE behavior. Figure 5 shows four periodic crack distributions that are initially biased toward strong enhancement (h/w = 8), moderate enhancement (h/w = 2), moderate shielding (h/w = 1/2), and strong shielding (h/w = 1/8) configurations. These distributions were used to illustrate the effect of the relative spatial distribution of cracks on macroscopic stiffness and thermodynamic forces. Figure 6 shows that the normalized critical strain, $\epsilon_2/\epsilon_{REF}$, necessary to initiate damage evolution, similar to the uniformly distributed case, is a strong function of the initial patterning of

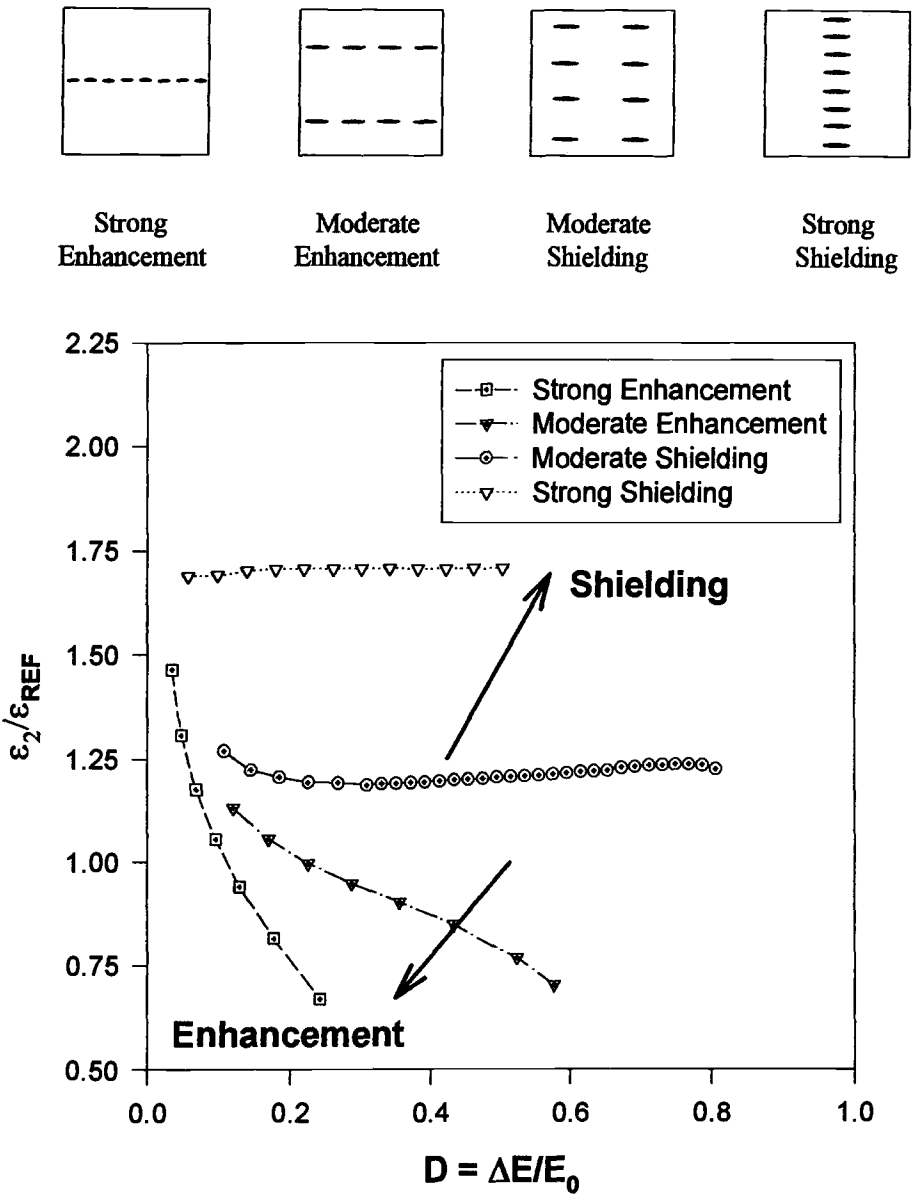

FIG. 6—*Normalized strain necessary to initiate damage evolution.*

damage. Those distributions biased toward enhancing configurations had significantly lower threshold strain levels. Furthermore, the critical strain decreased rapidly with increasing damage for the enhancing configurations. The threshold strain levels associated with shielding configurations, however, remained relatively constant with increasing damage. This implies that in the presence of crack shielding, stable crack growth is possible in perfectly brittle materials. The differences in the trajectory of critical threshold strain for enhancement and shielding

configurations are understandable when considering that crack enhancement results in increased crack opening displacements and, correspondingly, higher SIFs, while in the case of crack shielding the opposite is true. For a given stiffness reduction, as the relative vertical spacing between cracks, a/h, decreased, the critical threshold strain, $\epsilon_2/\epsilon_{REF}$, increased accordingly.

Figure 7 shows the normalized thermodynamic force (ERR), Y/Y_{REF}, associated with progressive crack extension for each damage configuration. Unlike the uniformly distributed cases, the results are not as straightforward to interpret. For a given damage state, the ERR for the strong enhancement configuration was significantly larger than the other three cases, which is consistent with the previous observation suggesting that evolution of distributions of smaller cracks will require a larger thermodynamic force. It is also noted that the change of Y with $\Delta E/E_0$ is greatest for the strongest enhancement, that is, crack extension releases the most strain energy for a finite change of D in this case. The thermodynamic force for the strong enhancement case remained a decreasing function of damage throughout the entire range of damage evolution. The thermodynamic force for the moderate enhancement and shielding cases initially decreased with damage evolution at low damage levels before approaching a nearly asymptotic value at higher damage values; the ERRs for both of these cases were comparable throughout

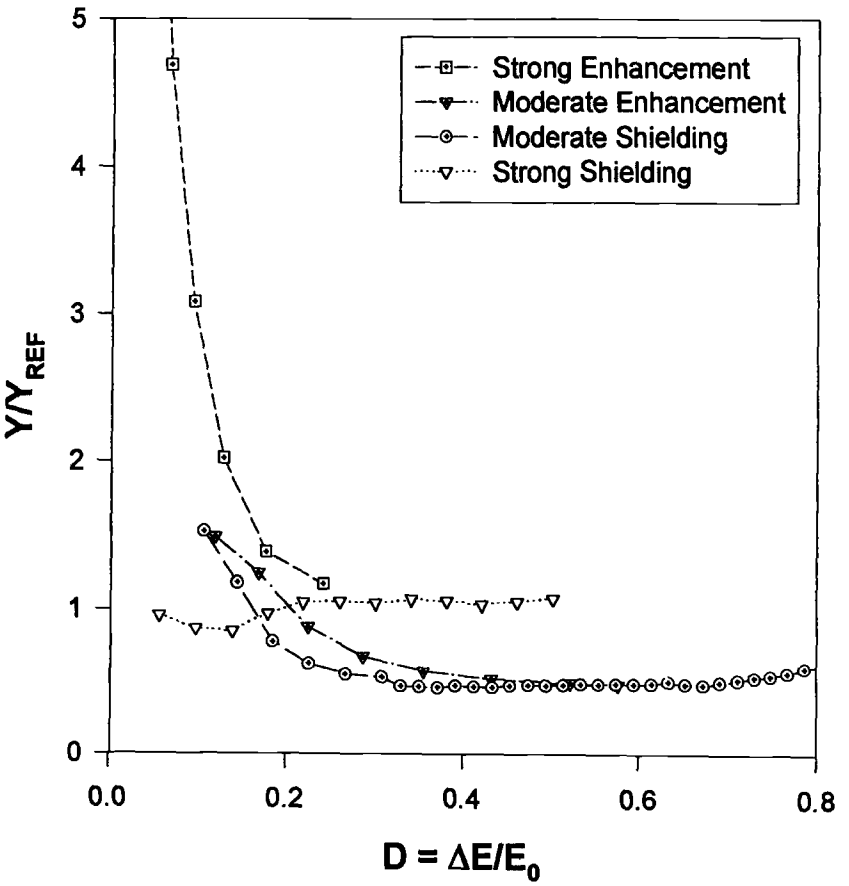

FIG. 7—*Normalized thermodynamic force obtained from numerical simulations of damage evolution in nonuniform crack distributions.*

the entire range of damage evolution, in spite of the difference in the nature of crack interactions associated with each distribution. Finally, the thermodynamic force associated with the strong shielding configuration, after a slight initial decline, increased with damage evolution before approaching an asymptotic value at higher damage values.

The preceding numerical results confirm that certain macroscopically defined damage descriptors such as Eq 9 are incapable of distinguishing between various crack distributions that produce markedly different global responses. The "nonuniqueness" of results obtained in the numerical evaluation of threshold strain and thermodynamic forces for the given crack configurations with common D values calls into question the viability of such a damage descriptor in addressing damage evolution of highly interactive crack systems in a CDM approach. Damage variables inferred on the basis of the effective stress concept or similar notions (for example, effective area, section, volume, etc.) do not contain information regarding the nature and distribution of damage. Talreja [*40*] noted that in such an approach, two sets of damage entities of different characteristic sizes and concentrations leading to the same elastic compliance changes will be represented by the same damage variable. Damage evolution laws in such a formulation cannot be expressed in terms of the actual dissipative processes and energy release occurring at the mesoscale, and frequently result in estimation of damage evolution laws based on curve fitting experimental data. Even if stiffness change is correlated, internal dissipation may be quite inaccurately described, and extrapolation to other geometries and damage configurations is suspect. Consequently, ultimate failure or damage mode bifurcations or both cannot be accurately described, particularly those that might result from thermomechanical coupling or localization of damage within the RVE or both.

As an alternative to using a macroscopically measurable damage parameter, implementing a damage variable that retains key information regarding the mesostructural damage distribution may better model the actual dissipative processes and energy release during damage extension. Use of such a parameter, however, is not without potentially serious shortcomings, particularly if it is based solely on the spatial average of key geometric features of the damage distribution in the RVE [*20*].

Micromechanically Inspired Damage Models

In order to better model underlying dissipative or energy transfer processes occurring at the mesoscale, it is advantageous to choose a set of damage ISVs that incorporate salient aspects of damage morphology in their definition (that is, so-called "micromechanically-inspired" damage parameters). Damage evolution laws in such a formulation potentially may be expressed in terms of the actual dissipative processes and energy release occurring at the mesoscale. Examples of micromechanically-inspired damage models have been introduced in the study of initially isotropic homogeneous brittle materials [*4,16,17,24–27,41–43*]. A second-rank tensorial characterization of cracks was first proposed by Vakulenko and Kachanov [*44*], and was further clarified by Kachanov [*41*], that is

$$D_{ij} = \frac{1}{V}\int_S \boldsymbol{u}_i \boldsymbol{n}_j dS \tag{11}$$

where $\boldsymbol{n}$ is a unit normal vector to the crack surface, $\boldsymbol{u}$ is the displacement jump across the crack surface, V is the volume of the RVE, and the integral is evaluated over all crack surfaces, S. Analogous to the damage descriptor given by Eq 11 is the crack density tensor [*41,44*], that is

$$D_{ij} = \frac{1}{V}\sum_{k=1}^{N} r_k^3 \, \boldsymbol{n}_i^k \boldsymbol{n}_j^k \tag{12}$$

for a three-dimensional solid with penny-shaped cracks and

$$D_{ij} = \frac{1}{A} \sum_{k=1}^{N} a_k^2 \, n_i^k n_j^k \tag{13}$$

for a two-dimensional solid with slit cracks where r_k and a_k are crack radii and half-lengths of the kth crack, respectively; V and A are the volume and area of averaging, respectively; $\boldsymbol{n}^k$ is the unit normal vector to the kth crack, and N is the total number of cracks. Allen et al. [*45,46*], Weitsman [*47*], and Talreja [*6,48,49*] used dyads similar to that of Eq 11 to construct volume-averaged macroscopic damage variables to represent the effect of various crack-like surface discontinuities in composites (matrix cracks, fiber/matrix debonds, slipped surfaces, ply delaminations, etc.). It is essential to note that macroscopic damage variables obtained through a spatial average of the geometric features of individual damage entities, such as Eqs 11 through 13, do not account for nonuniformity of the distribution of damage in the RVE and specifically neglect damage interactions. Such parameters are inappropriate to characterize the damage evolution of solids except for the case of dilute and noninteractive damage, such damage growth depends strongly on interactions.

A set of micromechanically inspired damage ISVs necessary to adequately characterize the thermomechanical response of damaged solids may be represented as

$$\{\boldsymbol{D}^{(\alpha)}\} = \{\{\boldsymbol{D}_0^{(\beta)}\}, \{\boldsymbol{D}_1^{(\zeta)}\}, \{\boldsymbol{D}_2^{(\xi)}\}, \ldots, \{\boldsymbol{D}_n^{(\chi)}\}\} \tag{14}$$

where

$$\begin{aligned}
&\alpha = 1, \ldots, N \\
&\beta = 1, \ldots, M \\
&\zeta = 1, \ldots, P \\
&\xi = 1, \ldots, Q \\
&\chi = 1, \ldots, V \\
&N = M + P + Q + \cdots + V
\end{aligned}$$

Here, $\{\boldsymbol{D}_0^{(\beta)}\}$ represents the set of ISVs associated with the weighted zeroth-order moment (spatial average) of the geometric features of the RVE damage distribution. Equations 11 through 13 are specific examples of ISVs of this type. $\{\boldsymbol{D}_1^{(\zeta)}\}$ represents the set of ISVs associated with the weighted first-order moment of the RVE damage distribution, and characterizes nearest-neighbor interaction effects. $\boldsymbol{D}_1^{(\zeta)}$ can be estimated using mark correlation functions [*50,51*] or other two-point statistics. These parameters would capture the effects of the gradients of geometric features of the damage distribution on the macroscopic response. $\{\boldsymbol{D}_2^{(\xi)}\}, \ldots, \{\boldsymbol{D}_n^{(\chi)}\}$ are the sets of ISVs that reflect increasingly higher-order moments of the weighted damage distribution and, generally, could be quantified using n-point statistics ($n = 3, \ldots, N - 1$). Each of the sets of ISVs will have associated sets of thermodynamic forces, $\{\boldsymbol{Y}_0^{(\beta)}\}, \{\boldsymbol{Y}_1^{(\zeta)}\}, \ldots, \{\boldsymbol{Y}_n^{(\chi)}\}$, that may be evaluated using Eq 2*c*. The dissipation inequality (Eq 5) for this case may be expressed as

$$\sum_{\beta=1}^{N} (\boldsymbol{Y}_0^{(\beta)} \cdot \dot{\boldsymbol{D}}_0^{(\beta)}) + \sum_{\zeta=1}^{P} (\boldsymbol{Y}_1^{(\zeta)} \cdot \dot{\boldsymbol{D}}_1^{(\zeta)}) + \cdots + \sum_{\chi=1}^{V} (\boldsymbol{Y}_n^{(\chi)} \cdot \dot{\boldsymbol{D}}_n^{(\chi)}) \geq 0 \tag{15}$$

Clearly, the inclusion of ISVs characterizing the higher-order moments of the damage distribution greatly complicate the formulation, particularly considering that the higher-order terms must be reevaluated at every increment of damage evolution. This is especially troublesome for the case where individual damage entities are of arbitrary shape and damage evolution is

not self-similar. Current micromechanically inspired CDM models typically utilize ISVs of Type $\boldsymbol{D}_0^{(\beta)}$, and in practical applications it may only prove feasible to include ISVs of Types $\boldsymbol{D}_0^{(\beta)}$ and $\boldsymbol{D}_1^{(\zeta)}$. Note that inclusion of ISVs of Type $\boldsymbol{D}_1^{(\beta)}, \ldots, \boldsymbol{D}_n^{(\xi)}$ in the Helmholtz free energy (Eq 1) or Gibbs free energy (Eq 6) explicitly introduce gradients of the damage distribution into the formulation, providing an inherently nonlocal description of the mesostructure.

The number and type of ISVs that must be retained in order to minimally characterize the macroscopic response of damaged solids largely depends on the problem to be solved. If the primary interest is determination of effective elastic moduli, then the number of ISVs necessary to characterize the problem is somewhat reduced. The effective moduli of a damaged solid primarily depend on the "average" size, orientation, and spatial position of defects within an RVE; use of a spatially averaged damage variable, $\boldsymbol{D}_0^{(\beta)}$, is generally suitable for this purpose. Kachanov [*16,18*] summarized the effect of crack systems on the effective moduli of linearly elastic isotropic solids. He observed that the effective moduli of solids containing randomly distributed, strongly interacting cracks are relatively insensitive to the distribution of cracks within a given material sample, provided the crack systems are not biased toward either crack shielding or enhancement configurations. Kachanov [*16*] noted that the assumption of noninteracting cracks was a reasonably good approximation when evaluating the stiffness properties of two-dimensional linearly elastic isotropic solids containing randomly distributed cracks, particularly at low crack densities. Kachanov [*16–18*] pointed out that this result is to be expected since effective moduli are "volume averaged" quantities that should remain somewhat insensitive to the distribution of mesostructural constituents. When the crack distribution is "periodic" (nonrandom), however, significant differences in elastic moduli are possible for different crack distributions with the same crack density [*52,53*]. This suggests the need to incorporate additional sets of ISVs, $\{\{\boldsymbol{D}_1^{(\zeta)}\}, \ldots, \{\boldsymbol{D}_n^{(\xi)}\}\}$, to evaluate the effective moduli for this case.

When considering damage evolution for the case of nondilute interacting damage, however, it is essential to include ISVs that retain information regarding the distribution of damage within the RVE (for example, $\boldsymbol{D}_1^{(\zeta)}, \ldots, \boldsymbol{D}_n^{(\xi)}$). Damage evolution is highly dependent on the local fluctuations in the damage array geometry (see Refs *16*, *17*, and *19*) as well as on the "extreme values" of the defect distribution (that is, largest defect size, minimum nearest neighbor distance between flaws, etc.). Such information is crucial to the development of viable damage evolution laws. Lacy et al. [*20*] performed numerical simulations of self-similar damage evolution in two-dimensional, perfectly brittle, microcracked solids. They illustrated that the use of the ISVs of Type $\boldsymbol{D}_0^{(\beta)}$ (specifically Eq 12) to characterize damage evolution can result in nonunique values of the thermodynamic force conjugate to damage (Eq 2*c*) for different distributions of cracks that have the same crack density (Eq 12). The study underscored the need to include higher-order ISVs to better account for damage distribution effects on stiffness and evolution. One key obstacle in a CDM formulation, however, is determination of the minimal set of ISVs that can be used to adequately quantify the RVE energy release rate during damage evolution yet provide for a tractable solution. It is clear that the energy dissipated during damage evolution is not uniformly distributed throughout the RVE, but depends on the distribution of heterogeneities and damage entities in the RVE as well as the applied loading. The minimal set of ISVs necessary to characterize the evolution problem is that which adequately accounts for the distribution of Helmholtz free energy (Eq 1) or Gibbs potential (Eq 6) and energy release rate within an RVE.

RVE Subvolumes and Length Scales

In the preceding sections, the thermomechanical response of damaged solids in a CDM formulation was cast in terms of sets of ISVs that characterize the weighted damage distribution

within an RVE. Equivalently, the problem may be expressed in terms of the distribution of Helmholtz free energy within an RVE. For a damaged heterogeneous solid under a given thermomechanical loading, the local Helmholtz free energy, Ψ_{LOC}, will assume a characteristic pointwise distribution within an RVE, that is

$$\Psi_{\text{LOC}} = \Psi_{\text{LOC}}(\boldsymbol{x}, \boldsymbol{\epsilon}_{\text{LOC}}, T_{\text{LOC}}) \tag{16}$$

where $\boldsymbol{x} = (x_1, x_2, x_3)$ denotes local RVE coordinates, and $\boldsymbol{\epsilon}_{\text{LOC}}$ and T_{LOC} are the local RVE strain and temperature, respectively. Implicit in this relationship is the dependence of the local free energy on the distribution of heterogeneities and damage entities within the RVE. The volume averaged free energy for the RVE, in the sense of Hill [2], is given by

$$\Psi_{\text{AVE}}(\boldsymbol{\epsilon}, T, \boldsymbol{D}_0^{(\beta)}) = \frac{1}{V}\int_V \Psi_{\text{LOC}}(\boldsymbol{x}, \boldsymbol{\epsilon}_{\text{LOC}}, T_{\text{LOC}})\, d\boldsymbol{x} \tag{17}$$

Assuming a sufficient number of damage ISVs (Eq 14) have been retained in order to provide a statistically homogeneous representation of the RVE damage distribution, mapping functions, $\mathcal{L}^{(\alpha)}$, may be defined, in principle, that relate the RVE distribution of free energy to the damage ISVs, that is

$$\Psi_{\text{LOC}}(\boldsymbol{x}, \boldsymbol{\epsilon}, T) = \mathcal{L}^{(\alpha)}(\boldsymbol{x}, \boldsymbol{\epsilon}, T, \boldsymbol{D}^{(\alpha)}) : \boldsymbol{D}^{(\alpha)} \tag{18}$$

where summation over $\alpha = 1, \ldots, N$ is implied. In practice, however, the exact form of the mapping functions would be very difficult to determine. Nonetheless, if the RVE distribution of free energy is known, the effective moduli of the damaged solid may be estimated from Eqs 3 and 17, that is

$$C_{ijkl} = \rho \frac{\partial^2 \Psi_{\text{AVE}}}{\partial \epsilon_{ij} \partial \epsilon_{kl}} \tag{19}$$

Note that Eqs 17 and 19 implicitly neglect the distribution of free energy and damage in the RVE. As a consequence of the spatial variation of the free energy within an RVE, the energy dissipated during damage evolution, in general, will not be uniformly distributed throughout the RVE. Furthermore, we may assert that the microstructure will evolve along those trajectories that maximize the local energy dissipated (released) with a given increment of damage extension. Dissipation in regions of the RVE characterized by peaks in the distribution of free energy release may be much higher than the RVE averaged dissipation. It would be inappropriate to characterize the evolution of damage in the RVE by using a spatial average of dissipation.

The preceding discussion illustrates that the commonly accepted RVE definition (that is, l_{RVE}/d is "sufficiently large") is best suited for determination of effective elastic moduli. Damage evolution, in general, involves length scales well below the characteristic RVE dimension, that is

$$l_{SV}/d \approx 1 \qquad \text{(to first-order)} \tag{20}$$

and

$$l_{SV} \ll l_{RVE} \tag{21}$$

where l_{SV} is the characteristic dimension of an RVE "subvolume." Note that volume averaging over individual subvolumes is insufficient to determine effective moduli, whereas volume av-

eraging over an RVE is insufficient to address damage evolution. The operative length scales over which these two critical aspects of the CDM problem must be characterized are markedly different. Furthermore, damage evolution occurs only in those subvolumes that reach criticality earlier due to preferred arrangement of microstructure (that is, "active" subvolumes). Any robust micromechanically inspired CDM model must distinguish between active and stationary RVE subvolumes in order to accurately characterize the energy dissipated during damage evolution. Incorporating a similar philosophy, Costanzo et al. [*54*] used micromechanics and homogenization theory to derive exact macroscopic constitutive laws and evolution equations for inelastic heterogeneous materials with growing cracks. An approximate solution technique was suggested whereby an RVE can be discretized into a finite number of subvolumes; the distribution of ISVs within each subvolume was approximated using the products of finite dimensional variable functions of time and appropriately chosen shape functions. In general, however, optimum RVE subvolume averaging procedures for damage evolution remain undeveloped.

While the focus of this paper has been directed toward perfectly brittle microcracked solids, the notion that distributed damage evolution (and associated energy release) occurs only within active RVE-subvolumes is completely general and may be applied to wide classes of materials sustaining various types of damage. Arguably, the problem of self-similar microcrack evolution in initially isotropic brittle solids may best be addressed using micromechanics. When other types of damage are considered in heterogeneous materials, however, micromechanical solutions become less tractable. In contrast, the higher-order CDM approach outlined here, in principle, is suitable for characterizing the thermomechanical response of multiphase materials with a wide array of damage mechanisms (for example, nucleation and nonself-similar growth of microcracks and voids in ductile materials, distributed matrix cracking and delamination in brittle composite laminates, etc.). The key challenge lies in defining appropriate damage ISVs (Eq 14) that adequately account for the distribution of energy released throughout the RVE during damage evolution.

Conclusions

Key issues pertaining to the development of viable damage evolution equations using a CDM approach have been addressed. In particular, limitations associated with the use of ISVs that can be expressed either in terms of macroscopically measurable quantities or through a spatial average of the geometric features of individual damage entities have been discussed. Implementation of either type of ISV effectively "smears out" the effect of variations in the mesostructure within the RVE; such variations play a crucial role in damage evolution and, in general, cannot be ignored. Numerical simulations of evolving crack systems in two-dimensional perfectly brittle solids indicate that "effective stress" models may have difficulty in characterizing damage evolution in brittle microcracked solids when the damage consists of cracks of variable size or spatial distributions. In such cases, effective stress models cannot accurately predict the strain to initiate damage extension nor the energy released during damage evolution for a given state of damage. Use of micromechanically inspired ISVs derived from quantities that are spatially averaged over the RVE, however, have similar shortcomings. An argument for implementing ISVs based on higher-order moments of the damage distribution within an RVE has been presented. Inherent in such a formulation is the assumption that the RVE, by definition, is somewhat better suited to characterize effective elastic moduli than damage evolution. Damage evolution involves length scales well below that of the characteristic RVE dimension; evolution occurs in a number of "active" subvolumes, the sum total of which may only represent a small fraction of the overall RVE volume. Further investigation of appropriate damage descriptors and RVE subvolume averaging procedures as well as numerical

simulations involving irregularly distributed damage systems are warranted to develop the higher-order CDM approach outlined here.

Acknowledgment

This work was made possible by the award of NASA Fellowship NGT-51178 to T. E. Lacy. In addition, use of Cornell University's special-purpose finite element code, FRANC 2-D, in our numerical calculations was greatly appreciated.

References

[1] Hashin, Z., "Analysis of Composite Materials—A Survey," *Journal of Applied Mechanics*, Vol. 50, 1983, pp. 481–505.
[2] Hill, R., "The Essential Structure of Constitutive Laws for Metal Composites and Polycrystals," *Journal of the Mechanics and Physics of Solids*, Vol. 15, 1967, pp. 79–95.
[3] Nemat-Nasser, S. and Hori, M., *Micromechanics: Overall Properties of Heterogeneous Materials*, North-Holland, Amsterdam, 1993.
[4] Krajcinovic, D., "Damage Mechanics," *Mechanics of Materials*, Vol. 8, 1989, pp. 117–197.
[5] Krajcinovic, D., Basista, M., and Sumarac, D., "Basic Principles," *Damage Mechanics of Composite Materials, Composite Materials Series, 9*, R. Talreja, Ed., Elsevier, Amsterdam, 1994, pp. 1–51.
[6] Talreja, R., "Internal Variable Damage Mechanics of Composite Materials," *Yielding, Damage, and Failure of Anisotropic Solids*, J. P. Boehler, Ed., Mechanical Engineering Publications, London, 1990, pp. 509–533.
[7] Mura, T., *Micromechanics of Defects in Solids*, 2nd ed., M. Nijhoff Publishers, The Hague, 1991.
[8] Christensen, R. M., "A Critical Evaluation for a Class of Micromechanics Models," *Journal of the Mechanics and Physics of Solids*, Vol. 38, 1990, pp. 379–404.
[9] Torquato, S., "Random Heterogeneous Media: Microstructure and Improved Bounds on Effective Properties," *Applied Mechanics Reviews*, Vol. 44, 1991, pp. 37–76.
[10] Kachanov, L. M., "On the Creep Rupture Time," *Izvestiva Akademii Nauk SSSR Odtelenie Tekhnicheskikh Nauk*, No. 8, 1958, pp. 26–31.
[11] Rabotnov, Y. N., "On the Equations of State for Creep," *Progress in Applied Mechanics, the Prager Anniversary Volume*, Macmillan, New York, 1963, p. 307.
[12] Kestin, J., "On the Application of the Principles of Thermodynamics to Strained Solid Materials," *Irreversible Aspects of Continuum Mechanics, and Transfer of Physical Characteristics in Moving Fluids*, H. Parkus and L. I. Sedov, Eds., Springer, New York, 1966, pp. 177–212.
[13] Kestin, J. and Rice, J. R., "Paradoxes in Application of Thermodynamics to Strained Solids," *A Critical Review of Thermodynamics*, E. B. Sutart, A. J. Brainard, and B. Gal-Or, Eds., Mono Book, Baltimore, 1970, pp. 275–298.
[14] Rice, J. R., "Inelastic Constitutive Relations for Solids: An Internal-Variable Theory and its Application to Metal Plasticity," *Journal of the Mechanics and Physics of Solids*, Vol. 19, 1971, pp. 433–455.
[15] Coleman, B. C. and Gurtin, M., "Thermodynamics with Internal State Variables," *Journal of Chemical Physics*, Vol. 47, 1967, pp. 597–613.
[16] Kachanov, M., "Effective Elastic Properties of Cracked Solids: Critical Review of Some Basic Concepts," *Applied Mechanics Reviews*, Vol. 45, 1992, pp. 304–335.
[17] Kachanov, M., "On Continuum Characterization of Crack Arrays and its Limits," *Recent Advances in Damage Mechanics and Plasticity*, J. W. Ju, Ed., AMD-Vol. 132, MD-Vol. 30, American Society of Mechanical Engineers, pp. 103–113.
[18] Kachanov, M., "Elastic Solids with Many Cracks and Related Problems," *Advances in Applied Mechanics*, Vol. 30, Academic Press, New York, 1994, pp. 259–445.
[19] Mauge, C. and Kachanov, M., "On Interactions of Cracks in Anisotropic Matrix and Related Problems," *Microcracking Induced Damage in Composites*, G. J. Dvorak and D. C. Lagoudas, Eds., AMD-Vol. 111, MD-22, American Society of Mechanical Engineers, 1990, pp. 95–99.
[20] Lacy, T. E., McDowell, D. L., Willice, P. A., and Talreja, R., "On Representation of Damage Evolution in Continuum Damage Mechanics," *International Journal of Damage Mechanics*, Vol. 6, 1997, pp. 62–95.

[21] Ju, J. W., "Isotropic and Anisotropic Damage Variables in Continuum Damage Mechanics," *Journal of Engineering Mechanics*, Vol. 116, 1990, pp. 2764–2770.
[22] Chaboche, J.-L., "Description Thermodynamique et Phenomenologique de la Viscoplasticite Cyclique avec Endommagement," These d'Etat, Universite Paris et M. Curie (Paris VI), 1978.
[23] Germain, P. Nguyen, Q. S., and Suquet, P., "Continuum Thermodynamics," *Journal of Applied Mechanics*, Vol. 50, 1983, pp. 1010–1020.
[24] Krajcinovic, D., "Constitutive Equations for Damaging Materials," *Journal of Applied Mechanics*, Vol. 50, 1983, pp. 355–360.
[25] Krajcinovic, D., "Continuous Damage Mechanics," *Applied Mechanics Reviews*, Vol. 37, 1984, pp. 1–6.
[26] Krajcinovic, D., "Continuous Damage Mechanics Revisited: Basic Concepts and Definitions," *Journal of Applied Mechanics*, Vol. 52, 1985, pp. 829–834.
[27] Krajcinovic, D., "Constitutive Theories for Solids with Defective Microstructure," *Damage Mechanics and Continuum Modeling*, N. Stubbs and D. Krajcinovic, Eds., American Society of Civil Engineers, New York, 1985, pp. 39–56.
[28] Lemaitre, J. and Chaboche, J.-L., *Mechanics of Solid Materials*, Cambridge University Press, Cambridge, 1990.
[29] Allen, D. H., "Thermomechanical Coupling in Elastic Solids," *Applied Mechanics Reviews*, Vol. 44, 1991, pp. 361–373.
[30] Talreja, R., "A Continuum Mechanics Characterization of Damage in Composite Materials," *Proceedings*, Royal Society of London: A, Vol. 399, 1985, pp. 195–216.
[31] Chaboche, J.-L., "Anisotropic Creep Damage in the Framework of Continuum Damage Mechanics," *Nuclear Engineering and Design*, Vol. 79, 1984, pp. 309–319.
[32] Chaboche, J.-L., "Continuum Damage Mechanics, Part I–General Concepts," *Journal of Applied Mechanics*, Vol. 55, 1988, pp. 59–64.
[33] Chaboche, J.-L., "Continuum Damage Mechanics, Part II–Damage Growth, Crack Initiation, and Crack Growth," *Journal of Applied Mechanics*, Vol. 55, 1988, pp. 65–72.
[34] Lemaitre, J., "Coupled Elasto-Plasticity and Damage Constitutive Equations," *Computer Methods in Applied Mechanics and Engineering*, Vol. 51, 1985, pp. 31–49.
[35] Lemaitre, J., "A Continuous Damage Mechanics Model for Ductile Fracture," *Journal of Engineering Materials and Technology*, Vol. 107, 1985, pp. 83–89.
[36] Lemaitre, J., "Formulation and Identification of Damage Kinetic Constitutive Equations," *Continuum Damage Mechanics: Theory and Application*, D. Krajcinovic and J. Lemaitre, Eds., Springer-Verlag, Wien, 1987, pp. 37–89.
[37] Lemaitre, J., *A Course on Damage Mechanics*, Springer-Verlag, Berlin, 1992.
[38] Lemaitre, J. and Chaboche, J.-L., "Aspect Phenomenologique de la Rupture par Endommagement," *Journal de Mecanique Appliquee*, Vol. 2, No. 3, 1978, pp. 317–365.
[39] Hoffman, J. D., *Numerical Methods for Engineers and Scientists*, McGraw-Hill, New York, 1992.
[40] Talreja, R., "Damage Characterization by Internal Variables," *Damage Mechanics of Composite Materials, Composite Materials Series, 9*, R. Talreja, Ed., Elsevier, Amsterdam, 1994, pp. 53–78.
[41] Kachanov, M., "A Continuum Model of Medium with Cracks," *Journal of Engineering Mechanics*, Vol. 106, 1980, pp. 1039–1051.
[42] Krajcinovic, D., "Micromechanical Basis of Phenomenological Models," *Continuum Damage Mechanics: Theory and Application*, D. Krajcinovic and J. Lemaitre, Eds., Springer-Verlag, Wien, 1987, pp. 195–206.
[43] Krajcinovic, D., Basista, M., and Sumarac, D., "Micromechanically Inspired Phenomenological Damage Model," *Journal of Applied Mechanics*, Vol. 58, 1991, pp. 305–310.
[44] Vakulenko, A. A. and Kachanov, M., "Continual Theory of a Medium with Cracks," *Mechanics of Solids*, Vol. 6, No. 4, 1971, pp. 159–166.
[45] Allen, D. H., Harris, C. E., and Groves, S. E., "A Thermomechanical Constitutive Theory for Elastic Composites with Distributed Damage,–I. Theoretical Development," *International Journal of Solids and Structures*, Vol. 23, 1987, pp. 1310–1318.
[46] Allen, D. H., Harris, C. E., and Groves, S. E., "A Thermomechanical Constitutive Theory for Elastic Composites with Distributed Damage,–II. Application to Matrix Cracking in Laminated Composites," *International Journal of Solids and Structures*, Vol. 23, 1987, pp. 1319–1338.
[47] Weitsman, Y., "Damage Coupled with Heat Conduction in Uni-Axially Reinforced Composites," *Constitutive Modeling for Nontraditional Materials*, V. Stokes and D. Krajcinovic, Eds., AMD-Vol. 85, American Society of Mechanical Engineers, 1987, pp. 161–174.
[48] Talreja, R., "Damage Development in Composites: Mechanisms and Modeling," *Journal of Strain Analysis*, Vol. 24, 1989, pp. 215–222.

[49] Talreja, R., "Continuum Modeling of Damage in Ceramic Matrix Composites," *Mechanics of Materials*, Vol. 12, 1991, pp. 165–180.
[50] Stoyan, D. and Stoyan, H., *Fractals, Random Shapes and Point Fields, Methods of Geometrical Statistics*, Wiley, New York, 1994.
[51] Pyrz, R., "Correlation Between Microstructure Variability and Local Stress Field in Two-Phase Materials," *Material Science Engineering: A*, Vol. 177, 1994, pp. 253–259.
[52] Deng, H. and Nemat-Nasser, S., "Microcrack Arrays in Isotropic Solids," *Mechanics of Materials*, Vol. 13, 1992, pp. 15–36.
[53] Nemat-Nasser, S., Yu, N., and Hori, M., "Solids with Periodically Distributed Cracks," *International Journal of Solids and Structures*, Vol. 30, 1993, pp. 2071–2095.
[54] Costanzo, F., Boyd, J. G., and Allen, D. H., "Micromechanics and Homogenization of Inelastic Composite Materials with Growing Cracks," *Journal of the Mechanics and Physics of Solids*, Vol. 44, 1996, pp. 333–370.

Yilong Bai,[1] *Wensheng Han,*[1] *and Jie Bai*[1]

A Statistical Evolution Equation of Microdamage and Its Application

REFERENCE: Bai, Y., Han, W., and Bai, J., **"A Statistical Evolution Equation of Microdamage and Its Application,"** *Applications of Continuum Damage Mechanics to Fatigue and Fracture, ASTM STP 1315*, D. L. McDowell, Ed., American Society for Testing and Materials, 1997, pp. 150–162.

ABSTRACT: A general equation governing the evolution of number density of microdamage in the phase space has been derived previously, based on the concept of ideal microdamage. The phase space consists of necessary mesoscopic variables describing the state of microdamage. In the cases of parallel penny-shaped microcracks and spherical microvoids, two independent variables, that is, their current and initial sizes, play a significant role in the evolution. This paper focuses on the two-dimensional (current and initial sizes) version of the equation and its solution. These results constitute a basis for the understanding of the underlying mechanisms governing damage evolution. Experimental techniques dealing with the statistical evolution of microcracks under impact and fatigue loadings are reported. These include specimen design, testing methods providing multifrozen stages of microdamage evolution, counting of microdamage, etc. Data processing, especially the conversion from sectional counting to volumetric distribution of microdamage, is provided. In this way, the microdamage evolution is measured. As applications to the damage evolution under impact loading, two inverse problems are discussed, that is, nucleation and growth rates are deduced from the measured data of statistical evolution of microcracks. Another application is the prediction of the evolution of continuum damage in terms of nucleation rate, n_N, and microdamage front, c_f

$$\dot{D}_j = \alpha \int_0^\infty c_f^j(t, c_0; \sigma) n_N(c_0; \sigma) dc_0$$

This expression concisely links continuum damage evolution to its underlying mesoscopic dynamics. This approach can be effective until a cascade of coalescence of microdamages leads to an evolution-induced catastrophe—a critical failure.

KEYWORDS: continuum damage mechanics, cracking, fatigue (materials), microdamage, statistical evolution, number density, fracture (materials)

Nomenclature

- A Growth rate of microcracks in Phase Space $[c]$
- c Current size of microcracks
- c_0 Initial size of microcracks
- D Continuum damage
- n Number density of microcracks in Phase Space $[c]$
- n_0 Number density of microcracks in Phase Space $[c, c_0]$
- n_A Annihilation rate of microcracks in Phase Space $[c]$

[1] Professor, associate professor, and research assistant, respectively, Laboratory for Nonlinear Mechanics of Continuous Media, Institute of Mechanics, Chinese Academy of Sciences, Beijing 100080, China.

n_N Nucleation rate of microcracks in Phase Space $[c]$
n_{0N} Nucleation rate of microcracks in Phase Space $[c, c_0]$
p_i Explicit ($P_i = \dot{p}_i \neq 0$) independent variables describing the state of microdamage
q_j Implicit ($\dot{q}_j = 0$) independent variables describing the state of microdamage
t Time, cyclic number, etc.
V Growth rate of microcracks in Phase Space $[c, c_0]$
α Geometric factor of microdamage
σ Stress

Damage mechanics has become a very helpful tool for engineers to deal with failure problems. Actually, the physical essence of damage is the population of distributed microdamage in a continuum element. Take an aluminum alloy, for example, the counting of microcracks on a sectional surface of the alloy subjected to impact loading is 10^2 to 10^4/mm^2. Then, the density of microcracks is about (10^3 to 10^6)/mm^3. That is to say, in a continuum element, approximately 1 mm^3 large, the evolution of continuum damage is the collective statistical behavior of the distributed microcracks. Despite this, continuum damage mechanics assumed a phenomenological measure of damage, D, and successfully treated a number of engineering problems, for example, see Ref *1*. However, when one intends to correlate the damage evolution to the mesoscopic dynamics of microstructure of a particular material, it becomes necessary to investigate the statistical evolution of distributed microdamage.

Microdamage can be grouped into microcracks and microvoids. This paper will be mainly concerned with microcracks in metals under impact and fatigue loadings. But the reviewed theoretical framework and relevant experimental techniques are also suitable for microvoids.

Evolution Equation

General Equation

The equation governing the evolution of microdamage has been derived according to the conservation of microdamage in the phase space. That is to say, the rate of change of number density of microdamage within a control element in the phase space plus the excess of outgoing over incoming microdamage flux is equal to the excess of nucleation rate over annihilation rate [*2*]

$$\frac{\partial n}{\partial t} \sum_{i=1}^{I} \frac{\partial (n \cdot P_i)}{\partial p_i} = n_N - n_A \tag{1}$$

Here, p_i and q_j are the independent variables describing the state of microdamage and constitute the phase space. They can be the size, orientation, position, etc., of microdamage. $P_i = \dot{p}_i$ are the dynamic rates and I denotes the total of variables p_i. Whereas the rates of q_j are equal to zero, hence, q_j becomes implicit in Eq 1. For example, in Phase Space $[c,c_0]$, $p_1 = c$, the current size of microdamage, and then $I = 1$, but $q_1 = c_0$ because of the invariable initial size at nucleation of a microcrack. Finally, n is number density of microdamage. For example, in Phase Space $[c]$, $n \cdot dc$ is the number of microdamages in the interval $(c, c + dc)$ per unit volume. Also, all mesoscopic dynamics, P_i, n_N, and n_A, are functions of corresponding variables as well as stress. Therefore, the number density of microdamage, n, should be $n = n(t, p_i, q_j; \sigma)$.

Ideal Microdamage

According to the estimation of microcrack density (10^3 to 10^6)/mm^3, there is one microcrack in a cube with edges tens of μm long. On the other hand, microcracks are only a few micrometers large. Hence, microcracks are sparsely distributed in the alloy. In this case, a useful model is the ideal microdamage [*3*]. In this model, the coalescence of microdamages is ignored, that is, $n_A \approx 0$ in Eq 1. Also, the nucleation and growth of microdamage are governed by an average stress field due to the average interaction of microdamages.

Practical Model

In out impact and fatigue testing, the specimens are subjected to homogeneous and uniaxial loading. Hence, under planar impact loading, for example, microcracks were found to be parallel and penny-shaped. So, the sizes of microcracks are the unique independent variables in the evolution. In practical measurements of microcracks, only the current sizes of microcracks can be measured, whereas their initial sizes at nucleation are unknown. Therefore, one can obtain the number density, $n = n(t, c; \sigma)$, for measurement only. But, from micromechanics, the growth rate of microcracks is usually a function of current as well as initial sizes of microcracks, $V = V(c, c_0; \sigma)$ [*4*]. So, we should consider two simplified ideal models in Spaces $[c]$ and $[c,c_0]$, respectively

$$\frac{\partial n}{\partial t} + \frac{\partial (n \cdot A)}{\partial c} = n_N \tag{2}$$

$$\frac{\partial n_0}{\partial t} + \frac{\partial (n_0 V)}{\partial c} = n_{0N} \tag{3}$$

In the equations, the initial size of microcracks is an implicit independent variable, because it stays invariant during the course of evolution. The relationships between the two equations are

$$n(t, c; \sigma) = \int_0^\infty n_0 \, dc_0 \tag{4}$$

$$A = \int_0^\infty V n_0 \, dc_0 / n \tag{5}$$

$$n_{0N} = n_N(c_0) \cdot \delta(c - c_0) \tag{6}$$

Typical Solution

From our tests of an aluminum alloy under impact loading, not only the growth rate, V, but also the nucleation rate, n_N, are time independent. Based on this fact and the assumption of constant stress, σ, a simple solution to Eq 3 has been derived

$$n_0(t, c, c_0; \sigma) = n_0(c, c_0; \sigma) = \frac{n_N(c_0,\sigma)}{V(c, c_0,\sigma)} \qquad \text{when } c_0 \leq c \leq c_f \tag{7}$$

The unsteady front of microcracks, c_f, is defined by the upper limit of the following integration

$$t = \int_{c_0}^{c_f} \frac{dc'}{V(c', c_0; \sigma)} \tag{8}$$

Apart from the unsteady front, c_f, the number density, n_0, remains steady in the region, $c_0 < c < c_f$. Figure 1 shows the steady solution, n_0, and the front, c_f, of microcracks. The front, c_f, moves forward with velocity $V(c_f, c_0; \sigma)$.

Measurement

Testing Methods

For material testing of microcrack evolution, a requirement is the homogeneity of stress in the field of observation of microcracks. So, in impact testing, we use one stage light gas gun to establish a uniaxial strain state in the specimen [5]. Moreover, a short stress pulse with 0.1 μs duration was used to investigate the nucleation, and a multistress pulse technique was used to study microcrack evolution. In the multistress pulse technique, a flyer plate was counterbored with several holes to create multistress pulses (Fig. 2) [6]. In this way, constant stresses with different durations are applied to different regions in one specimen. This test provides several frozen stages of microcrack evolution in one shot. The testing material is an aluminum alloy (Table 1). Typical parameters in the impact tests are 0.1 to 1 μs load durations and 1 to 7 GPa tensile stresses.

For fatigue testing, a triangular-shaped specimen was used, see Fig. 3 [7]. When one end of the specimen is clamped in a support and another end is connected to a vibration testing machine, the surface tensile stress within the isosceles triangular section will keep constant. The test material is a structural steel (Table 1). Typical testing parameters are as follows:

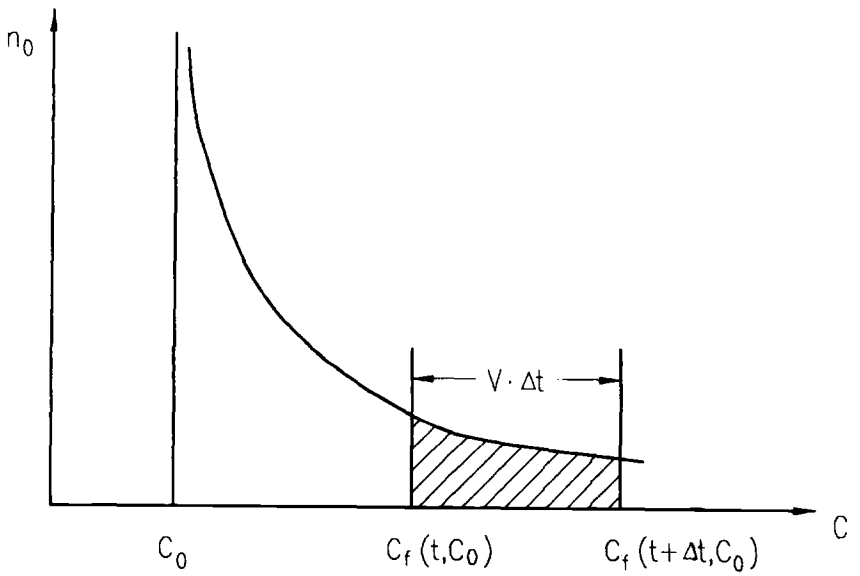

FIG. 1—*Schematic solution,* n_0, *and interpretation of continuum damage evolution.*

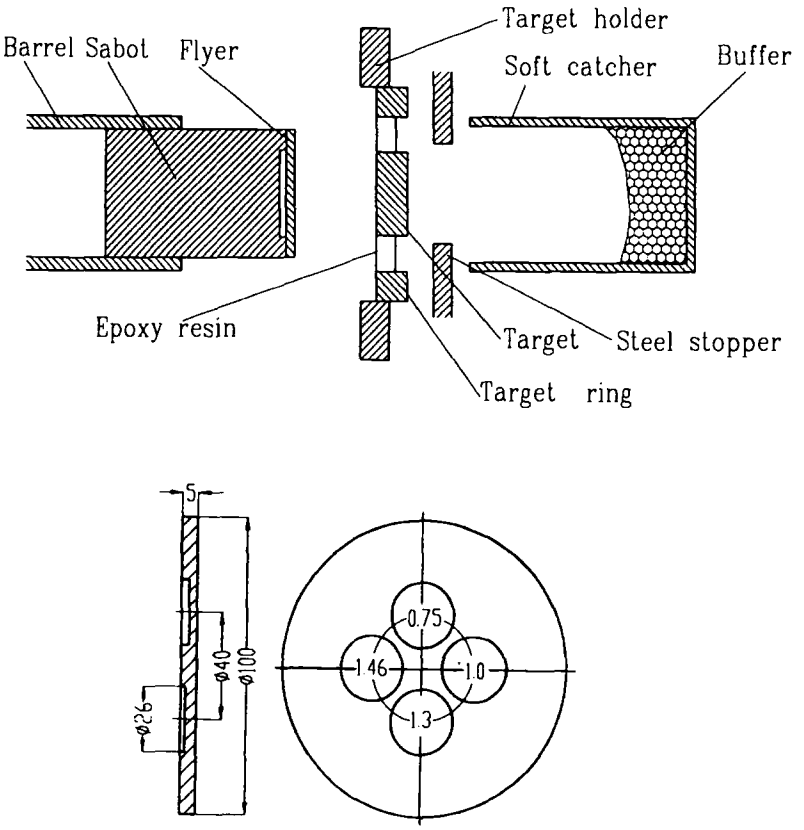

FIG. 2—*Planar plate impact test layout and multiholed flyer.*

TABLE 1—*Compositions of tested materials.*

	Constituents, % by weight					
Material	Cu	Mo	V	Zr	Ti	Al
Aluminum alloy[a]	6.3	0.3	0.2	0.18	0.06	

	Constituents, % by weight				
	C	Si	Mn	Cr	Fe
Steel[b]	0.30	1.0	0.90	0.90	

[a] First heated and rolled then quenched and aged. Average effective grain size is 32.8 μm and average size of second phase particle is 3.4 μm.

[b] Annealed from 860°C. Average ferrite grain size is 17.9 μm.

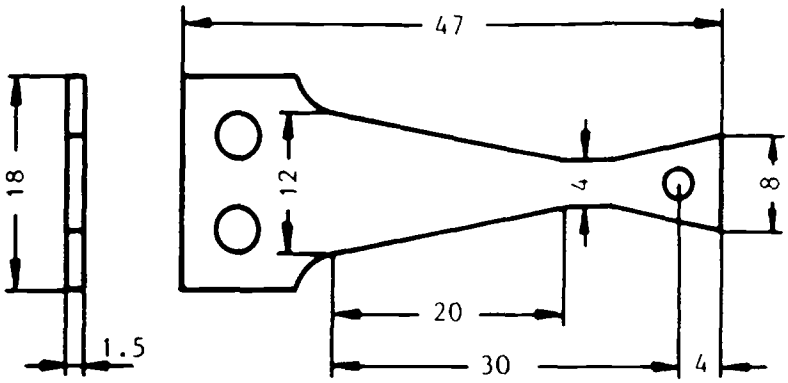

FIG. 3—*Triangular specimen in fatigue tests.*

frequency = 8 to 10 Hz, stress ratio = −1, and maximum stress = 1.0 to 1.5 times yield strength.

Observations of Microcracks

In order to investigate the evolution of microcracks, proper counting of microcracks in tested specimens is a key step.

For specimens subjected to plate impact loading, the following steps were taken. Before testing, the transverse isotropy and homogeneity of the aluminum alloy plate were examined and the size distribution of second phase particles was also measured. After testing, specimens were carefully recovered by a specially designed catcher in the gun to prevent secondary damage. Then, the tested specimens were sectioned and polished carefully. Microscopic observations and counting of microcracks were conducted with an S-570 scanning electron microscope and a *Q*-520 image analysis system with Polyvar-Met microscope. When using the image analysis system to count the number of microcracks, one should pay attention to the selection of contrast. In order to obtain reliable data, we usually perform counting on several view fields and use the two microscopes to double-check the counting. A typical processed evolution of microdamages is shown in Fig. 4.

A similar counting procedure is applied to the fatigue specimen [7]. The difference is that for a fatigue test we can trace the evolution of microcracks at a fixed field on the specimen's surface. In order to do this, some marks were made before testing on an assigned field on the surface with a hardometer. The fatigue test was periodically interrupted at pre-set intervals. Microscopic observations and counting of microcracks were conducted with microscopes during the intervals. A measured evolution of microcrack distribution is shown in Fig. 5. An interesting feature of the measurement is the double peaks. The location of the main peak is slightly less than the average ferrite grain size, see Fig. 5 and Table 1 [7].

Data Processing

The counts of microcracks should be processed for further analysis of microdamage evolution. Now, we focus on the data processing for impact tests.

First, the counting of microcracks was conducted on sectional surfaces. Clearly, the counts

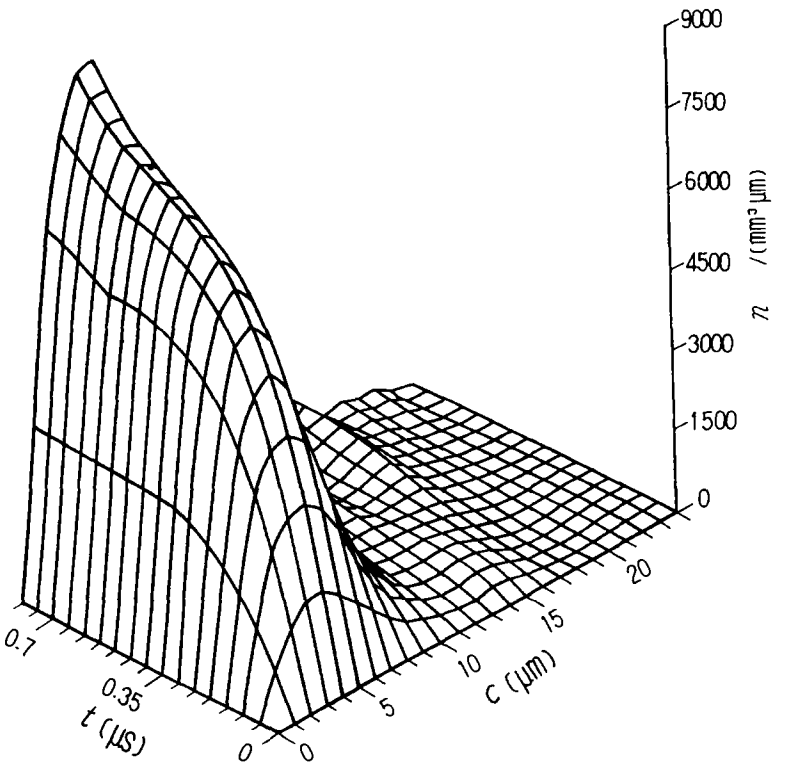

FIG. 4—*Measured number density of microcracks in impact test.*

should be converted to volumetric distribution. Seaman et al. [*8*] have developed a transformation to do this. In our impact tests of the aluminum alloy, due to the uniaxial strain state and the transverse isotropy, the microcracks are approximately parallel to each other and penny-shaped. In this case, the transformation can be simply performed by the following integral equation and its conversion

$$m(c') = c' \int_{c'}^{\infty} n(c) \frac{dc}{\sqrt{(c^2 - c'^2)}} \tag{9}$$

$$N(c) = \int_{c}^{\infty} n(c'')\, dc'' = \frac{2}{\pi} \int_{c}^{\infty} \frac{m(c')}{\sqrt{c'^2 - c^2)}}\, dc' \tag{10}$$

where m is the number density of microdamages with Size c' on the sectional surface. In fact, both spherical voids and parallel penny-shaped cracks follow the same Eqs 9 and 10 [*9*]. The accuracy of the transformation from sectional to volumetric distributions has been checked by a critical numerical simulation. For the case of equal spheres that are 10 μm in diameter and randomly distributed in a volume, Fig. 6 shows the calculated volumetric distribution converted from sectional counting, $m(c')$. The converted volumetric distribution does show a sharp step at 10 μm.

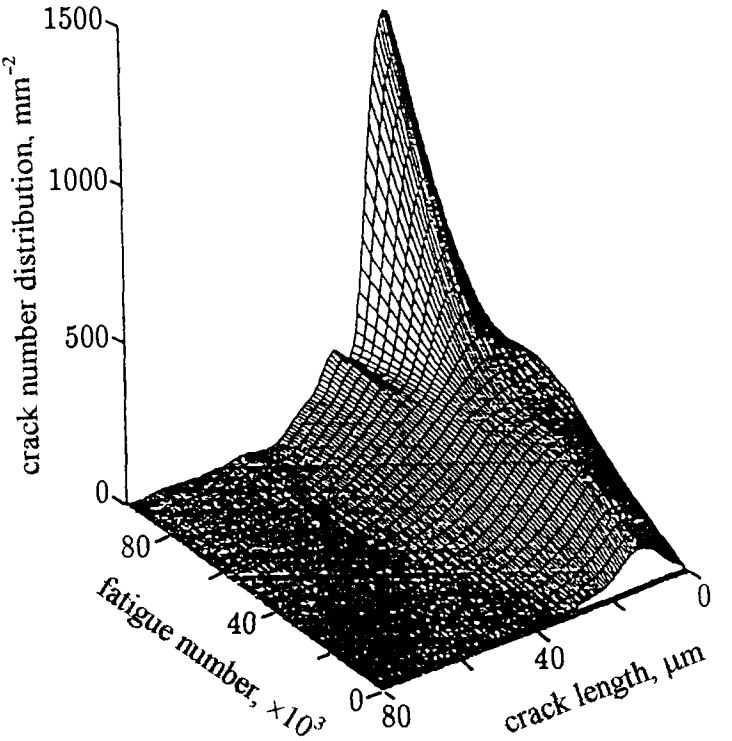

FIG. 5—*Measured microcrack number on sectional surface of a fatigue specimen.*

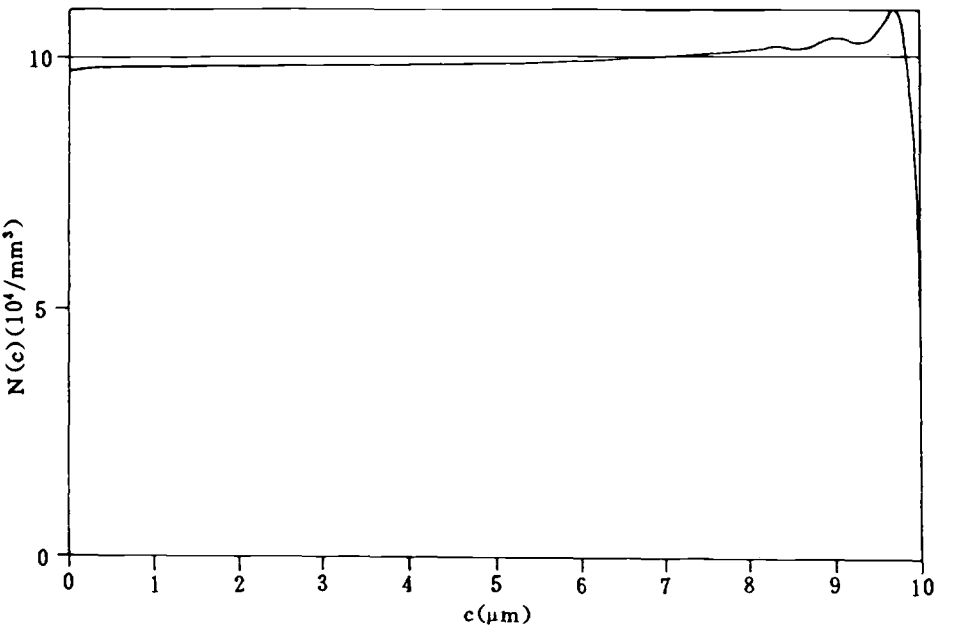

FIG. 6—*Cumulative volumetric distribution of equal spheres (10 μm in diameter and total 10 000 in a 1 mm^3 cube) calculated from sectional counting.*

Other data processing includes commonly used Fourier smoothing, Lagrange interpolation, etc. Then, a set of data of evolution of microcracks, $n = n(t, c; \sigma)$, is obtained, see Fig. 4.

Applications

Now, we have had two foundations for the study of damage evolution in materials. Theoretically, we have the equations governing the evolution of microcracks. Experimentally, we have a set of data for the evolution. The following discussion shows some examples of their applications. The first two examples are inverse problems, that is, from the measured data of microcracks to inversely deduce the mesoscopic dynamics of microcracks aided by the evolution equation. The third one is a direct application of the evolution equation and the mesoscopic dynamics of microcracks to predict damage evolution.

Nucleation

The key to reveal the nucleation law is to separate nucleation from the growth of microcracks. From Eq 2, one can deduce the following approximation [*5*]

$$n_N = n(t, c; \sigma)/t, \qquad \text{when } c \gg At \tag{11}$$

In our impact tests, the measurements demonstrate that the typical values of crack size, c, and growth rate, A, in the aluminum alloy are about 4 μm and 10 m/s, respectively. So, when the load duration is chosen to be 10^{-7}, Eq 11 can be satisfied. We applied a short stress pulse (about 100 ns load duration) to investigate the nucleation law. It was found that the normalized distribution of microcracks at nucleation is in agreement with that of second phase particles

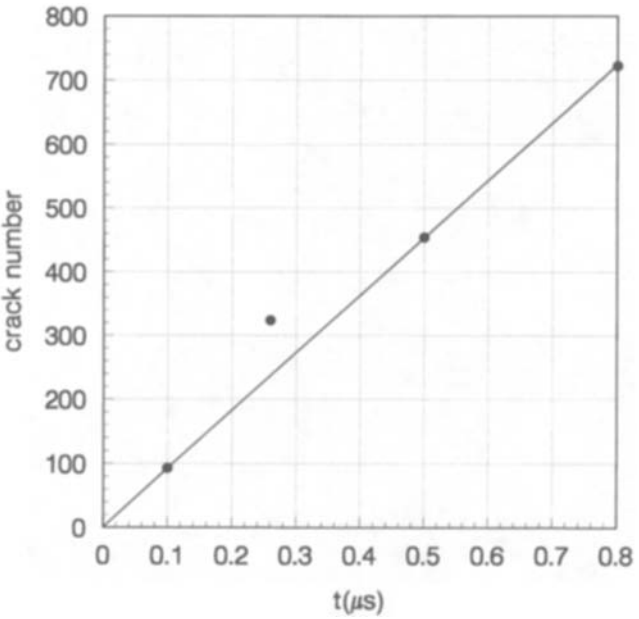

FIG. 7—*Time-independent nucleation rate of microcracks in impact tests of an aluminum alloy.*

[5] and the nucleation rate is independent of time. Further tests with longer durations, approaching to fracture, confirms the time-independence, Fig. 7.

Growth Rate

From Eq 2, the determined nucleation rate, n_N, and the measured evolution of number density, $n(t,c;\ \sigma)$, one can deduce the nominal growth rate, A

$$A = A(t,\ c;\ \sigma) = \int_0^c \left(n_N - \frac{\partial n}{\partial t}\right) dc'/n \tag{12}$$

However, the deduced growth rate, A, demonstrates obvious time-dependence. This is an indication of the existence of implicit variables governing the growth. As mentioned earlier, the growth rate of microcracks should be dependent on current as well as initial sizes of microcracks. When looking back to the definition (Eq 5) and the solution (Eq 7), one can find that the movement of the front, $c_f = c_f(t,\ c_0;\ \sigma)$, can be calculated as the upper limit of the integral

$$A(t,\ c_f;\ \sigma) = \int_{c_0}^{c_f} n_N(c_0';\ \sigma)\ dc_0'/n(t,\ c_f;\ \sigma) \tag{13}$$

according to the measured number density of microcracks, $n(t,c;\ \sigma)$; the determined nucleation rate, $n_N(c_0;\ \sigma)$; and the deduced nominal growth rate, $A(t,c;\ \sigma)$. Then differentiation of the unsteady front, c_f, with respect to time gives the growth rate, V,

$$V = V(c_f,\ c_0;\ \sigma) = \left(\frac{\partial c_f}{\partial t}\right) \tag{14}$$

When we plot the growth rate, V, against the extension $(c - c_0)$, rather than the ratio, c/c_0 [4], all data approximately collapse on a linear line, see Fig. 8.

Evolution Law of Continuum Damage

One can define the following damage moments as continuum damage

$$D_j = \alpha \int_0^\infty c^j \cdot n(t,c;\ \sigma)\ dc \tag{15}$$

where α is a geometric factor and j is the index of the damage moments. When $j = 3$, D_3 represents the volumetric fraction of damage and $\alpha = \pi/6$ for spherical voids. When substituting the solution (Eq 7) and the expression (Eq 4) into the damage moments (Eq 15), one can obtain

$$D_j = \alpha \int_0^\infty dc_0 \int_{c_0}^{c_f} \frac{c^j n_N(c_0;\ \sigma)}{V(c,\ c_0;\ \sigma)}\ dc \tag{16}$$

Differentiation of Eq 16 with respect to time leads to the evolution law of continuum damage

$$\dot{D}_j = \alpha \int_0^\infty c_f^j(t,\ c_0) n_N(c_0;\sigma)\ dc_0 \tag{17}$$

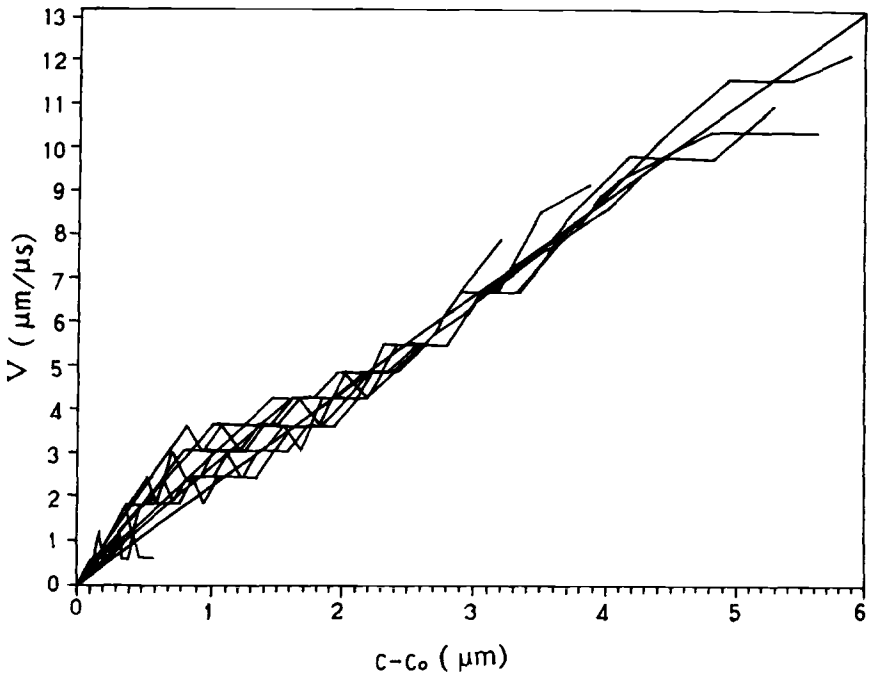

FIG. 8—*Collapse of data of growth rate,* V, *of microcracks in impact tests of an aluminum alloy.*

This evolution law concisely correlates the evolution of continuum damage to its two mesoscopic dynamics: nucleation rate, n_N, and growth rate, V, via the microdamage front, c_f, defined by Eq 8. The implication of Eq 17 is shown in Fig. 1. The product of the shaded area, $n_0 \cdot V \cdot dt = n_N \cdot dt$, and a weight function, c_f^j, is the integrand and the core of the evolution law (Eq 17). To confirm this interpretaion, Fig. 9 provides two numerical results of number density of microcracks at different times, based on Eq 3. This figure clearly demonstrates the steady profile, n_0, and its unsteady front, c_f. The following example illustrates the application of Eq 17 more concretely.

Suppose $j = 1$, which demonstrates the effect of linear size of microdamage, and

$$V = V^*(c - c_0)/c^* \tag{18}$$

$$n_N = n_N^* f(c_0/c^*) \tag{19}$$

where V^* and n_N^* are functions of stress, σ, and c^* is a characteristic size. After calculating c_f according to Eq 8, one can obtain the evolution law of damage from Eq 17, $\dot{D}_0$ and $\dot{D}_1$. Then

$$\dot{D}_1 = c^* F_1 \dot{D}_0/F_0 + V^*\{D_1 - c^* F_1 D_0/F_0\}/c^* \tag{20}$$

where

$$F_j = \int_0^\infty f(x)\, x^j\, dx$$

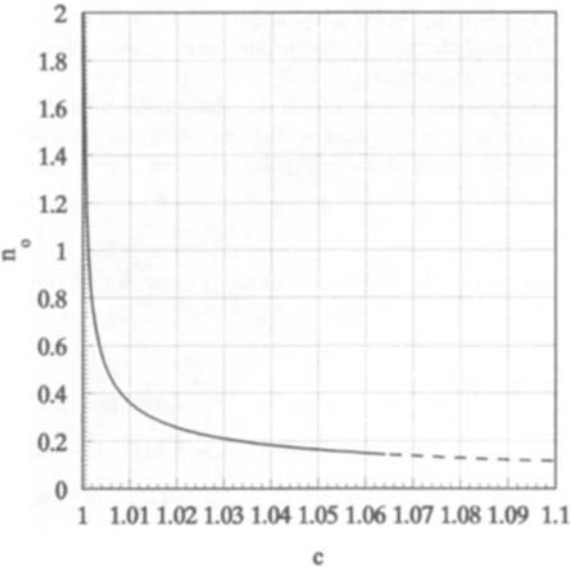

FIG. 9—*Calculated dimensionless profiles of number density of microcracks,* n_0, *for impact tests, showing steady profile and unsteady front,* c_f, *(dimensionless variables,* $c_0 = 1$, —— $t = 2$ *and* -------- $t = 2.5$*).*

Generally, one can define compound damage moments [*10*]

$$D_{i,j} = \alpha \int_0^\infty dc_0 \int_{c_0}^\infty dc\ c_0^i c^j n_0(t,c,c_0;\ \sigma) \tag{21}$$

Integration of Eq 3 with respect to c and c_0 and substitution of the linear growth rate (Eq 18) into the obtained integration can lead to

$$D_{ij} = D_{N,i+j} + jV^* \cdot (D_{ij} - D_{i+1,j-1})/c^* \tag{22}$$

where

$$D_{N,j} = \alpha \int_0^\infty n_N \cdot c^j\, dc$$

Details of the manipulation can be found in Ref *10*. Equation 22 is macroscopically closed recurrently. Actually, the Eq 20 is the special case of Eq 22, when $i = 0$ and $j = 1$. So, in terms of damage moments, it is demonstrated that the evolution law of damage, $\dot{D}$, can always be closely expressed for the cases with linear growth rate of microdamage.

Summary

An equation governing the statistical evolution of microdamage has been proposed. Relevant experimental techniques used in impact and fatigue tests and data processing of evolving microcracks were developed. After considering the equation and the measured data of micro-

cracks, the mesoscopic laws of nucleation and growth of microcracks were determined. A concise formula of continuum damage evolution correlating mesoscopic dynamics of nucleation and growth of microcracks was obtained.

The approach can accommodate nonuniform distributions of microcracks, etc., by introducing new independent variables in the phase space. For example, damage localization has been recently examined with Eq 1 by introducing spatial variable.

Acknowledgment

This work was supported by the National Natural Science Foundation of China.

References

[1] Chaboche, J. L., "Continuum Damage Mechanics," *Journal of Applied Mechanics*, Vol. 55, 1988, pp. 59–72.

[2] Bai, Y. L., Ke, F. J., and Xia, M. F., "Formulation of Statistical Evolution of Microcracks in Solids," *Acta Mechania Sinica*, Vol. 7, 1991, pp. 59–66.

[3] Ke, F. J., Bai, Y. L., and Xia, M. F., "Evolution of Ideal Microcrack System," *Science in China A*, Vol. 33, 1990, pp. 1447–1459.

[4] Curran, D. R., Seaman, L., and Shockey, D. A., "Dynamic Failure of Solids," *Physics Reports*, Vol. 147, 1987, pp. 253–388.

[5] Bai, Y. L., Ling, Z., Luo, L. M., and Ke, F. J., "Initial Development of Microdamage under Impact Loading," *Journal of Applied Mechanics*, Vol. 59, 1992, pp. 622–627.

[6] Zhao, S. D., Long, Z., Shen, L. T., Chen, S. X., and Bai, Y. L., "An Experimental Approach to Evolution of Spallation," *Shock Compression in Condensed Matter*, S. C. Schmidt, R. D. Dick, J. W. Forbes, and D. G. Tasker, Eds., Elsevier Science Publishers, B. V., Amsterdam, North Holland, 1992, pp. 523–526.

[7] Fang, B., Hong, Y. S., and Bai, Y. L., "Experimental and Theoretical Study on Number Density Evolution of Short Fatigue Cracks," *Acta Mechanica Sinica*, Vol. 11, No. 2, 1995, pp. 143–152.

[8] Seaman, L., Curran, D. R., and Crewdson, R. C., "Transformation of Observed Crack Traces on a Section to True Crack Density for Fracture Calculation," *Journal of Applied Physics*, Vol. 49, 1978, pp. 5221–5229.

[9] Bai, Y. L., Xia, M. F., Ke, F. J., Guo, W. H., and Ling, Z., "Statistical Interpretation on the Relationship between the Volumetric and Sectional Size Distributions of Disordered Meso-Structures," *Acta Physica Sinica*, Vol. 42, 1993, pp. 351–359.

[10] Xia, M. F., Han, W. S., Ke, F. J., and Bai, Y. L., "Statistical Meso-scopic Damage Mechanics and Damage Evolution Induced Catastrophe," (I) and (II), *Advances in Mechanics*, Vol. 25, 1995, pp. 1–40 and 145–173.

Local Approaches to Fatigue and Fracture

C. L. Chow[1] *and L. G. Yu*[2]

A Unified Approach to Metal Fatigue Based on the Theory of Damage Mechanics

REFERENCE: Chow, C. L. and Yu, L. G., **"A Unified Approach to Metal Fatigue Based on the Theory of Damage Mechanics,"** *Applications of Continuum Damage Mechanics to Fatigue and Fracture, ASTM STP 1315*, D. L. McDowell, Ed., American Society for Testing and Materials, 1997, pp. 165–185.

ABSTRACT: This paper presents a unified approach to fatigue damage in metals based on the theory of damage mechanics. The theory that takes into account the gradual material degradation or deterioration under load is ideally suited for characterizing material behaviors progressively damaged under fatigue loading. This is because fatigue damage is caused by material degradation resulting from the initiation, growth, and coalescence of microcracks/voids in real-life materials under repeated/cyclic loading. In addition, a unified fracture criterion based on the damage mechanics theory has been developed to predict the threshold conditions of macrocrack initiation and propagation as well as damage evolution in a material element with or without the presence of a macrocrack. This type of unified approach would not otherwise be possible using the conventional fatigue design methodology based on either the *S-N* diagram or the concept of fracture mechanics.

The proposed fatigue damage model is based on the thermodynamic theory of irreversible processes with internal state variables. With the introduction of a new damage effect tensor, the necessary constitutive equations of elasticity and plasticity coupled with damage are developed. The constitutive equations derived enable the formulation of a fatigue damage dissipative potential function and a fatigue damage criterion. The criterion is designed to subdivide the overall damage into two domains, namely, "fatigue damage" and "plastic damage." The fatigue damage evolution equation is subsequently developed based on the hypothesis that the overall damage is induced by the summation of "fatigue" and "plastic" damages. The model has been applied to predict successfully the fatigue life of smooth, notched, and center-cracked specimens under a wide range of loading cycles.

KEYWORDS: damage mechanics, fatigue (materials), crack initiation, crack propagation, aluminum alloys, finite element analysis, continuum damage mechanics, cracking, fracture (materials)

Rupture of materials under varying loads, of which the magnitude and the direction are changing periodically or irregularly with time, is called fatigue failure. There are fundamental distinctions between the fatigue failure and the failure due to static loads.

Characteristics of Fatigue Failure

In the practical engineering environment, fatigue is a very important problem, since for the majority of engineering components of machines, equipment, vehicles, and structures, few external loads are static, but varying with time. Some researchers have argued that 50 to 90%

[1] Professor and chair, Department of Mechanical Engineering, University of Michigan-Dearborn, Dearborn, MI 48128-1491.
[2] Principal mechanical engineer, ZEI Inc., 1159 East Michigan Ave., Ypsilanti, MI 48197.

material failures are due to fatigue. In recent years, with the improvement of static design, and the applications of high-strength materials under high operation speed, the fatigue problems are becoming more and more important.

Various theories and methods have been developed to study the fatigue process, including fatigue life estimation with macroscopic approaches, and a fatigue mechanism study with microscopic schemes. There a great number of papers discussing fatigue problems published by researchers every year. However, accidents caused by fatigue are still occurring. This indicates that many problems of fatigue mechanism and fatigue phenomenon remain unsolved. The main shortcomings of the current theories and methods of fatigue study can be summarized as follows:

(1) Most models to predict fatigue crack propagation are empirical formulae based on linear elastic fracture mechanics (LEFM). These models do not even perfectly mirror constant amplitude fatigue crack behavior. Kanninen and Popelar [*1*] have indicated that conventional fatigue crack growth models work because, being empirical, experimental results can be predicted when similitude exists. This is true despite the fact that the basic assumptions of LEFM are violated for fatigue. In fact, K-dominance exists only when the inelastic region can be contained within an annular region surrounding the crack tip. Obviously, for a growing crack that leaves a wake of residual plasticity behind it, this condition cannot be satisfied. When similitude does not exist, nonlinear methods are required.

(2) Another major inconsistency in the LEFM is the use of ΔK that is defined as $K_{max} - K_{min}$. Since unlike K_{1C}, which is an intrinsic material property, both K_{max} and K_{min} are dependent on specimen geometry and loading condition, the conventional fatigue growth rate in terms of ΔK, like the S-N curve, is based on a one-dimensional curve-fitting technique.

(3) The conventional studies of the fatigue crack initiation and propagation are separated. The parameters used for crack initiation and propagation are different. So far, there are few models available for both processes.

(4) In most studies of fatigue, only the variables related to the current state are taken into account, while the effects of load history are generally ignored. However, experimental data have shown that the effects of load history, such as the load sequence and the overload, affect the fatigue life greatly.

(5) So far, some important factors, such as stress gradient, have not been taken into account in the fatigue calculation satisfactorily yet.

The difficulty of fatigue study is not only that there are many influencing factors that can be classified as material properties; load characters; geometry, dimension, and surface conditions of components; and circumstances, but also that a very small variation of some factor, which is usually ignored for static loads, can cause great influence to the fatigue process. The effects of these factors, including their interactions, are very complicated.

General Survey of Damage Mechanics

In recent years, a new theory known as "damage mechanics" has been developed to study the engineering problems of strength, such as ductile fracture, creep rupture, and fatigue failure. Some successful progress has been made in theoretical studies and engineering applications.

It is well known that macroscopic fracture has been studied for a long time. Around 1500, Leonardo da Vinci was already preoccupied with the characterization of fracture by means of

mechanical variables. And then, a number of failure criteria, that is, functions of components of stress or strain, characterizing the fracture of the volume element were proposed (for example, by Coulomb, Rankine, Tresca, von Mises, Mohr, and Caquot). However, it is only quite recently that concern has been directed towards modeling the progressive deterioration of materials preceding the macroscopic fracture.

The development of damage mechanics began in 1958. In that year, Kachanov published the first paper devoted to a continuous damage variable, conceived within the framework, limited indeed, of creep failure of metals under uniaxial loads. This concept was taken up again in the 1970s, mainly in France (Lemaitre and Chaboche), United States (Krajcinovic), Sweden (Hult), England (Leckie), and Japan (Murakami) and extended to ductile fracture and fatigue failure.

Spectacular progress has been achieved by damage mechanics during the past decade, making it into a scientific discipline and one of the most active research frontiers in the failure theories of materials. The scope of the present damage mechanics theory encompasses research originated from macroscopic, mesoscopic, and microscopic levels. The development of damage theory opens a new dimension to solve engineering problems.

According to damage mechanics, "damage" refers to microcracks or microvoids, or both, in a damaged material element with certain geometric configuration. The geometry and material background of such an element will evolve with respect to the loading environment. The theory of damage mechanics studies the laws governing the formation and evolution of the microdefects, and appropriate criteria by which material or structural failure under a prescribed loading environment can be predicted.

The damage mechanics can be developed in the form of internal variable theory with the following assumptions [2]:

(1) The response of the material depends only on the current state of the microstructural arrangement, and
(2) The current state of the microstructural arrangement can be described by a finite set of internal variables.

The damage theory comes as a product of the interdisciplinary studies of solid mechanics and material science. On one hand, the damage theory neglects the numerous details during the physical process of damage so that lengthy calculations in statistical mechanics are avoided. On the other hand, the incorporation of actual geometric images and physical procedures featured in the damage provide a realistic background for damage variables and damage evolution. Consequently, damage is substantiated beyond abstract mathematical variables and equations. The damage theory enhances our understanding towards the essential aspects of damage and clarifies the ad hoc phenomenological assumptions. The damage model deals with, from geometry as well as the thermal-mechanical deformation process, the configurations and distributions of various damage structures and predicts their nucleation, growth, and coalescence leading to macroscopic defects. In essence, the damage theory links structures of different length scales. As long as the constitutive equations and damage evolution laws for the material element are obtained, they can be directly invoked to assess the macroscopic damage behavior of specimens and structure components.

Though the basic concept of damage was proposed for the study of creep, as it develops, the damage theory is being applied in many fields, such as metal forming, ductile fracture, fatigue, creep-fatigue, and creep with plastic deformation. In addition, its application is not only to metallic materials, but also to nonmetallic materials such as composites, concrete, and ceramics.

Objective

As stated earlier, it is necessary and possible to develop new models to study fatigue problems, to improve the predicted results, and to give better explanations to the fatigue mechanisms. The models can be established with the theory of damage mechanics with the following features:

(1) Damage is defined as an accumulated variable related to the load history, and the history effects can thus be taken into account. Also some factors mentioned earlier can be considered. Thus, the studies of fatigue procedure would be more comprehensive.
(2) From the point of view of damage mechanics, there is actually no difference between crack initiation and propagation, both of which resulted from the failure of an element with a characteristic dimension. Thus, fatigue crack initiation and propagation can be studied with one model as a unified approach.
(3) Under monotonic or cyclic loading, or both, most metallic material would become anisotropic, which can be described by anisotropic damage.
(4) One advantage of damage mechanics is that it provides a natural means of predicting the effects of interaction among damages of different physical natures.

In this work, an orthotropic damage model of fatigue and plastic deformation is established to estimate fatigue life, including fatigue crack initiation and fatigue crack propagation. The model takes into account the effect of load history and the interaction of plastic damage and fatigue damage. With a modified general-purpose finite element program, the stresses and the total damage (including fatigue damage and plastic damage) near a notch root or crack tip can be calculated, and the life of crack initiation and the rate of crack propagation can therefore be predicted.

Basic Concepts

The basic concepts of the anisotropic damage theory, for which the elastic energy equivalence hypothesis is shown to be valid [*3*], has been described by Chow and Wang [*4–11*], and interested readers may refer to these references for details. However, some salient points of the theory are briefly illustrated in this section as they are required for the development of the proposed fatigue damage model.

$$\tilde{\boldsymbol{S}} = \boldsymbol{M}(\boldsymbol{D}):\boldsymbol{S} \tag{1}$$

$$\tilde{\boldsymbol{E}}^e = \boldsymbol{M}(\boldsymbol{D})^{\mathrm{T},-1}:\boldsymbol{E}^e \tag{2}$$

$$W^e(\boldsymbol{S},\boldsymbol{D}) = \frac{1}{2}\tilde{\boldsymbol{S}}:\boldsymbol{C}^{-1}:\tilde{\boldsymbol{S}} = \frac{1}{2}\boldsymbol{S}:\tilde{\boldsymbol{C}}^{-1}:\boldsymbol{S} \tag{3}$$

$$\tilde{\boldsymbol{C}} = \boldsymbol{M}(\boldsymbol{D})^{-1}:\boldsymbol{C}:\boldsymbol{M}(\boldsymbol{D})^{\mathrm{T},-1} \tag{4}$$

where $\boldsymbol{S}$ is the stress tensor, $\tilde{\boldsymbol{S}}$ is the effective stress tensor, $\boldsymbol{E}^e$ is the elastic strain tensor, $\tilde{\boldsymbol{E}}^e$ is the effective elastic strain tensor, $W^e(\boldsymbol{S},\boldsymbol{D})$ is the elastic complementary energy, $\boldsymbol{C}$ is the elastic

stiffness tensor, and $\boldsymbol{M}(\boldsymbol{D})$ is the damage effect tensor. In the principal system of damage, $\boldsymbol{M}(\boldsymbol{D})$ is assumed as

$$\boldsymbol{M}(\boldsymbol{D}) = \begin{bmatrix} \frac{1}{1-D_1} & & & & & \\ & \frac{1}{1-D_2} & & & & \\ & & \frac{1}{1-D_3} & & & \\ & & & \frac{1}{1-\frac{1}{2}(D_2+D_3)} & & \\ & & & & \frac{1}{1-\frac{1}{2}(D_3+D_1)} & \\ & & & & & \frac{1}{1-\frac{1}{2}(D_1+D_2)} \end{bmatrix} \tag{5}$$

where D_1, D_2, and D_3 are the principal values of damage, $\boldsymbol{D}$, which is a symmetric tensor of second order. In this paper, the damage variable, $\boldsymbol{D}$ is defined as the overall damage tensor, including the fatigue damage and plastic damage

$$d\boldsymbol{D} = d\boldsymbol{D}_f + d\boldsymbol{D}_p \tag{6}$$

where $\boldsymbol{D}_f$ and $\boldsymbol{D}_p$ are the fatigue damage tensor and the plastic damage tensor, respectively.

Plastic Damage

Plastic deformation, due to which plastic damage results, is a phenomenon of global slip. It is well known that fatigue cracks always appear along the persistent slip bands due to localized plastic deformation in smooth specimens [*12*]. Therefore, there is a close interaction between plastic damage and fatigue damage. Accordingly, it is necessary to take into account the effect of plastic damage on the evolution of fatigue damage.

The evolution equations of plastic damage may be established by the damage energy release rate, Y_p, defined as

$$\boldsymbol{Y}_p = -\frac{\partial W^e(\boldsymbol{S},\boldsymbol{D})}{\partial \boldsymbol{D}_p} = -\boldsymbol{S}:\left(\tilde{\boldsymbol{C}}^{-1}:\boldsymbol{M}^{-1}:\frac{\partial \boldsymbol{M}}{\partial \boldsymbol{D}_p}\right)^s:\boldsymbol{S} \tag{7}$$

in which the superscript, s, means that the symmetric part only should be taken. The plastic damage criterion is assumed as

$$F_{pd} = Y_{peq}^{1/2} - [C_{p0} + C_p(Z)] = 0 \tag{8}$$

where C_{p0} is the initial strengthening threshold, $C_p(Z)$ is the increment of the threshold, Z is the equivalent overall damage, and Y_{peq} is defined as

$$Y_{peq} = \frac{1}{2} \boldsymbol{Y}_p : \boldsymbol{L}_p : \boldsymbol{Y}_p \tag{9}$$

$\boldsymbol{L}_p$ is the characteristic tensor of plastic damage that may be expressed as

$$\boldsymbol{L}_p = \begin{bmatrix} 1 & \eta_p & \eta_p & 0 & 0 & 0 \\ \eta_p & 1 & \eta_p & 0 & 0 & 0 \\ \eta_p & \eta_p & 1 & 0 & 0 & 0 \\ 0 & 0 & 0 & 2(1-\eta_p) & 0 & 0 \\ 0 & 0 & 0 & 0 & 2(1-\eta_p) & 0 \\ 0 & 0 & 0 & 0 & 0 & 2(1-\eta_p) \end{bmatrix} \tag{10}$$

where η_p is assumed to be a material constant.

If the plastic damage criterion of Eq 8 is taken as the potential function, the plastic damage evolution equations can be accordingly deduced as

$$\dot{Z}_p = \dot{Z} = \lambda_{pd} \frac{\partial F_{pd}}{\partial(-C_p)} = \lambda_{pd} \tag{11}$$

$$\dot{\boldsymbol{D}}_p = \dot{\boldsymbol{D}} = \lambda_{pd} \frac{\partial F_{pd}}{\partial(-\boldsymbol{Y}_p)} = \frac{-\lambda_{pd}}{2Y_{peq}^{1/2}} \boldsymbol{L}_p : \boldsymbol{Y}_p \tag{12}$$

where Z_p is the equivalent plastic damage.

Fatigue Damage

It is well accepted that the elastic strain energy conventionally defined for static loading is unable to describe the fatigue damage without suitable modifications. Its evolution equations may be derived from the cyclic elastic complementary energy, $W_c^e(\boldsymbol{S}_c, \boldsymbol{D})$, defined as

$$W_c^e(\boldsymbol{S}_c, \boldsymbol{D}) = \frac{1}{2} \tilde{\boldsymbol{S}}_c : \boldsymbol{C}^{-1} : \tilde{\boldsymbol{S}}_c = \frac{1}{2} \boldsymbol{S}_c : \tilde{\boldsymbol{C}}^{-1} : \boldsymbol{S}_c \tag{13}$$

where $\tilde{\boldsymbol{S}}_c$ is the effective cyclic stress range tensor expressed as

$$\tilde{\boldsymbol{S}}_c = \boldsymbol{M}(\boldsymbol{D}) : \boldsymbol{S}_c = \boldsymbol{M}(\boldsymbol{D}) : (\boldsymbol{S} - \boldsymbol{S}_{me}) = \tilde{\boldsymbol{S}} - \tilde{\boldsymbol{S}}_{me} \tag{14}$$

where $\boldsymbol{S}$ is the stress tensor and $\boldsymbol{S}_{me}$ is the mean stress tensor. $\boldsymbol{S}_{me}$ is given by

$$\boldsymbol{S}_{me} = \frac{1}{2} (\boldsymbol{S}_{\max} + \boldsymbol{S}_{\min}) \tag{15}$$

where $\boldsymbol{S}_{\max}$ and $\boldsymbol{S}_{\min}$ are the maximum stress tensor and the minimum stress tensor, respectively. For multiaxial stress state, the terms "maximum" and "minimum" become ambiguous, but they may be regarded as two reverse points of a particular cyclic load range.

The damage energy release rate, $\boldsymbol{Y}_f$, corresponding to the fatigue damage can be obtained from

$$\boldsymbol{Y}_f = -\frac{\partial W_c^e(\boldsymbol{S}_c,\boldsymbol{D})}{\partial \boldsymbol{D}_f} = -\boldsymbol{S}_c:\left(\tilde{\boldsymbol{C}}^{-1}:\boldsymbol{M}^{-1}:\frac{\partial \boldsymbol{M}}{\partial \boldsymbol{D}_f}\right)^s:\boldsymbol{S}_c \tag{16}$$

where $\boldsymbol{Y}_f$ describes the variation of cyclic elastic strain energy due to cyclic loading and is used to derive the evolution equations of fatigue damage. During the nth cycle, the fatigue damage criterion is assumed as

$$F_{fd} = Y_{feq}^{1/2} - [C_{f0}(\boldsymbol{S}_{me}) + C_f(Z_{fn},Z)] = 0 \tag{17}$$

where $C_{f0}(\boldsymbol{S}_{me})$ is the initial strengthening threshold, $C_f(Z_{fn},Z)$ is the increment of the threshold, and Z_{fn} is the equivalent fatigue damage yielded at the nth cycle. Y_{feq} is defined as follows

$$Y_{feq} = \frac{1}{2}\boldsymbol{Y}_f:\boldsymbol{L}_f:\boldsymbol{Y}_f \tag{18}$$

where $\boldsymbol{L}_f$ is the characteristic tensor of fatigue damage, which may be expressed as

$$\boldsymbol{L}_f = \begin{bmatrix} 1 & \eta_f & \eta_f & & & \\ \eta_f & 1 & \eta_f & 0 & 0 & 0 \\ \eta_f & \eta_f & 1 & 0 & 0 & 0 \\ 0 & 0 & 0 & 2(1-\eta_f) & 0 & 0 \\ 0 & 0 & 0 & 0 & 2(1-\eta_f) & 0 \\ 0 & 0 & 0 & 0 & 0 & 2(1-\eta_f) \end{bmatrix} \tag{19}$$

where η_f is assumed to be a material constant.

If the fatigue damage criterion of Eq 17 is taken to be the energy dissipation function, the evolution equations of fatigue damage may be accordingly deduced as

$$\dot{Z}_{fn} = \lambda_{fd}\frac{\partial F_{fd}}{\partial(-C_f)} = \lambda_{fd} \tag{20}$$

$$\dot{\boldsymbol{D}}_{fn} = \lambda_{fd}\frac{\partial F_{fd}}{\partial(-\boldsymbol{Y}_f)} = \frac{-\lambda_{fd}}{2Y_{feq}^{1/2}}\boldsymbol{L}_f:\boldsymbol{Y}_f \tag{21}$$

where the Subscript, n, indicates the nth cycle.

The increments of fatigue damage and equivalent fatigue damage yielded in one cycle are

$$dZ = \frac{dZ_f}{dN} = dZ_f = \int dZ_{fn} \tag{22}$$

$$d\boldsymbol{D} = \frac{d\boldsymbol{D}_f}{d\boldsymbol{N}} = d\boldsymbol{D}_f = \int d\boldsymbol{D}_{fn} \tag{23}$$

The integrals are conducted over one cycle. Similar to Eq 6, it is assumed that

$$dZ = dZ_f + dZ_p \tag{24}$$

The fatigue failure criterion governing the threshold of a macrocrack initiation is

$$Z = Z_{cr} \tag{25}$$

where Z_{cr} is the critical value of the overall equivalent damage, Z, measured from experiments.

Determination of Parameters in the Damage Model

In order to conduct a validation analysis for the proposed fatigue damage model described in the preceding sections, a series of experiments was conducted. The material chosen for fatigue tests was aluminum alloy 2024-T3, whose composition and mechanical properties are as follows: Fe 0.5%; Cu 3.8–4.9%; Mn 0.3–0.9%; Mg 1.2–1.8%; Zn 0.25%; Ti 0.15%; modulus of elasticity, E = 74 343 MPa; Poisson's ratio = 0.33, yield stress, σ_y = 330.0 MPa; ultimate strength, σ_u = 482.2 MPa; and fatigue strength, σ_f = 138.2 MPa (5×10^8 cycles). The parameters of plastic damage were determined by Wang [*11*]. Under uniaxial load, the element, η_p, in the characteristic tensor of plastic damage, $\boldsymbol{L}_p$, is 0.5526, and the critical value of equivalent damage, Z_{cr} = 0.161.

The incremental fatigue damage is a localized phenomenon and is therefore impractical to be measured effectively cycle by cycle. The increment of strengthening threshold of fatigue damage, $C_f(Z_{fn},Z)$, to be evaluated may be assumed as

$$C_f(Z_{fn},Z) = Z_{fn}C_{f1}Z^{Cf2} \tag{26}$$

In order to determine Parameters C_{f1} and C_{f2}, eight groups of uniaxial fatigue test under the single block loading were conducted. The range of maximum stress was varied from 252 to

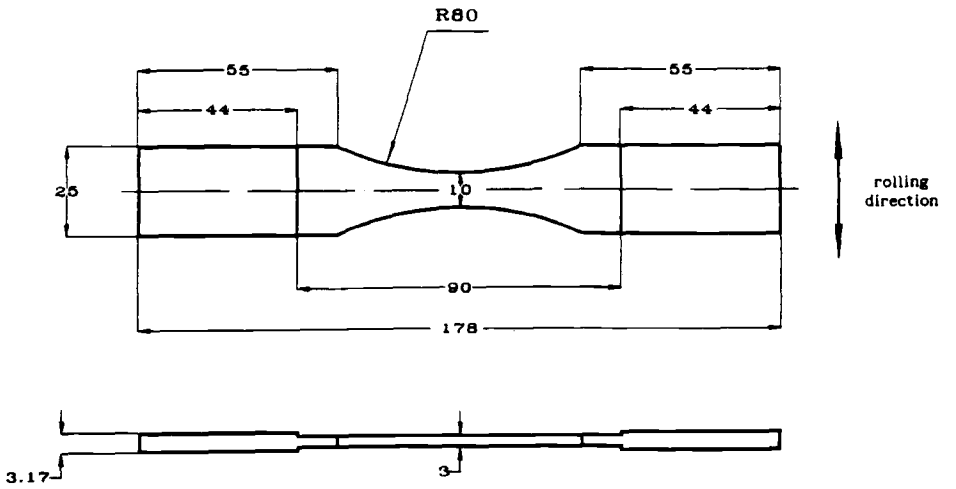

FIG. 1—*Smooth fatigue specimen.*

TABLE 1—*Fatigue data for determination of parameters of the fatigue damage model.*

Stress, MPa	N_{exp}[a]	$\bar{N}_{exp}$	N_{cal}	E_r, %	S_m
420 to 60	21.7, 23.9, 27.5, 27.5, 33.0	26.7	24.3	−8.9	3
420 to 170	57.6, 61.2, 63.4, 66.3	62.1	52.6	−15.3	3
400 to 50	30.3, 32.2, 33.0, 37.2	33.2	30.7	−7.6	3
400 to 150	78.3, 78.7, 82.1, 84.5	80.9	63.8	−20.7	3
350 to 50	50.8, 57.8, 63.2, 72.8	61.2	70.1	14.8	3
350 to 150	154.9, 170.3, 211.2, 215.8	188.1	200.9	6.8	3
300 to 50	161.7, 198.0, 207.6, 223.1	197.6	196.5	−0.6	3
252 to 2	119.0, 178.3, 267.9, 293.1, 315.2, 423.8	266.2	292.3	9.8	5

[a] $N \times 10^3$.

420 MPa with each load increment of either 50 or 20 MPa, while the range of stress amplitude was from 100 to 180 MPa.

The geometry of smooth fatigue specimens is shown in Fig. 1. The severely scratched protective coating from as-received aluminum alloy, whose strength is about 33% lower than the aluminum alloy, was milled off. After machining, all specimens were polished with fine emery papers from No. 240 to No. 800.

The test machine used was an electrohydraulic servocontrolled MTS machine of ±100 kN load range. Tests were performed at room temperature. The frequencies of the tests were varied from 5 to 20 Hz. The experiments were carried out under load control. All of the specimens were measured before each test with the precision of 0.02 mm.

A least-squares method was used to determine the C_{f1} and C_{f2} parameters in Eq 26 with the experimental data. The fitted parameters are: $C_{f1} = 16877$ and $C_{f2} = -0.5474562$. $C_{f2} < 0$ means that the development of fatigue damage is accelerated with the overall equivalent damage, Z. The element, η_f, is the characteristic tensor of fatigue damage, $\boldsymbol{L}_f$, is assumed to be equal to η_p.

The experimental and calculated results are shown in Table 1, where N_{exp} is the experimental fatigue life; $\bar{N}_{exp}$ is the mean value of N_{exp}; N_{cal} is the calculated fatigue life; E_r is the relative error $= (N_{cal} - \bar{N}_{exp})/\bar{N}_{exp}$, and S_m is the minimum number of specimens recommended for fatigue studies [*13*], with the confidence level $\gamma = 95\%$, and the relative error limit $\delta = 5\%$. The prediction confirms the validity and accuracy of the fatigue damage parameters, C_{f1} and C_{f2}, to be employed for the subsequent fatigue analysis.

Predications of Fatigue Damage

In order to verify the proposed damage model, fatigue damage predictions for different specimen geometries and loading conditions are conducted, including smooth specimens with overload (Fig. 1), smooth specimens under two-block loads (Fig. 1), notched specimens (Fig. 2) and center-cracked specimens (Fig. 3). The specimens are chosen to test validity of the proposed damage model as a unified approach to predict crack initiation from smooth and notched specimens and then cracked specimens. The conventional methods would employ two fundamentally different approaches to achieve similar predictions.

Smooth Specimen

Single Overload—In the practical engineering environment, structures and components undergo not only cyclic loads, but also some abrupt load changes, such as collision and impact,

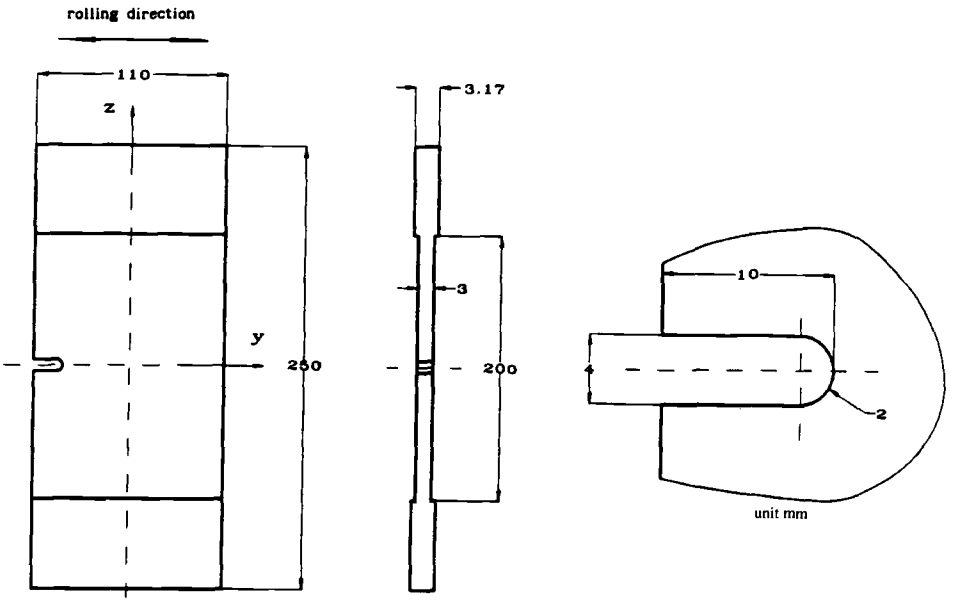

FIG. 2—*Notched specimen for fatigue crack initiation.*

which are usually much higher than the maximum loads imposed in normal cycles. On one hand, the abrupt load change would yield work hardening and residual stresses, which can retard the fatigue crack initiation and propagation. On the other hand, the abrupt load change may cause plastic deformation and therefore plastic damage.

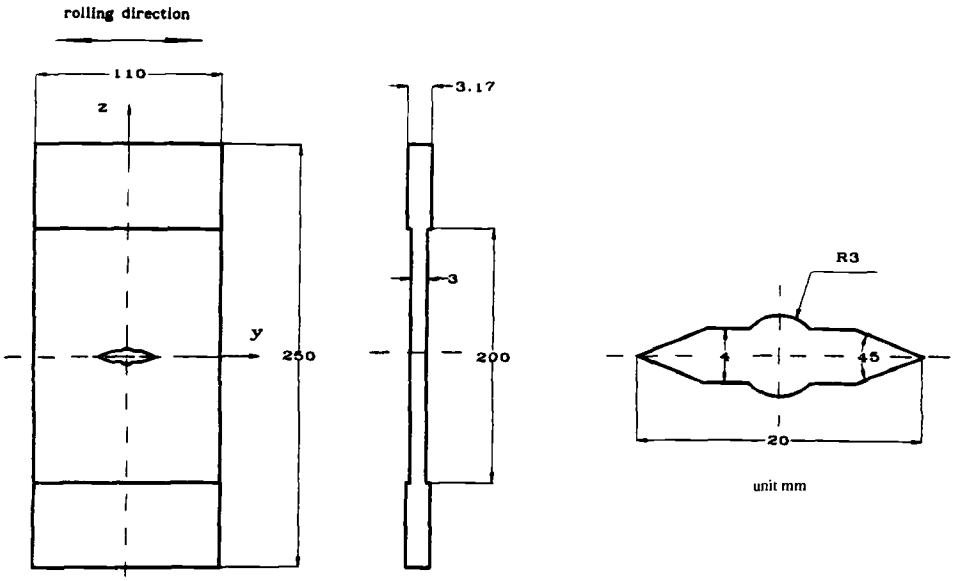

FIG. 3—*Center-cracked specimen for fatigue crack propagation.*

Four groups of loading conditions with overload are considered. The geometry of the specimens is the same as that for the determination of the fatigue damage as shown in Fig. 1.

The stress chosen for overload for each group is 400 MPa. The load conditions are listed as

Group	σ_{max}	to	σ_{min}	N_{pri}
1	252.0	to	2.0	0
2	300.0	to	50.0	0
3	300.0	to	50.0	60 000
4	300.0	to	50.0	120 000

where N_{pri} is the cyclic number prior to the overload. After a given cyclic load for N_{pri} cycles, the overload is introduced (if $N_{pri} = 0$, the overload is applied before the cyclic load), then the specimen is cyclically loaded again until final rupture.

When N_{pri} is 0, the plastic damage due to the overload is calculated before the prediction of the fatigue damage. If N_{pri} is greater than 0, and the maximum stress of the cyclic load is higher than the yield stress, the plastic damage is calculated in the first cycle. The total equivalent damage is Z_0. The plastic damage due to the overload is calculated next. After overload, the cyclic number of fatigue to final rupture is calculated where the integral is taken from Z_0 to Z_{cr}.

The calculated results, N_{cal}, are given in Table 2, where E_r is the relative error = $(N_{cal} - \bar{N}_{exp})/\bar{N}_{exp}$.

Two-Block Loads—In order to investigate the effect of load sequence on the fatigue damage accumulation, two-block load fatigue is considered. Four groups of loading conditions are considered here:

Group	σ_{1max}	to	σ_{1min}	N_{exp1}	σ_{2max}	to	σ_{2min}
1	400.0	to	50.0	15 000	300.0	to	50.0
2	300.0	to	50.0	100 000	400.0	to	50.0
3	350.0	to	150.0	94 000	350.0	to	50.0
4	350.0	to	50.0	30 600	350.0	to	150.0

where N_{exp1} is the cyclic number for Block 1.

Group 1 is high-low fatigue, and Group 2 is low-high fatigue, while Group 3 and Group 4 have the same σ_{max} and alternative σ_{min}. For each load of Block 1, the cyclic number is about half of the fatigue life under the corresponding cyclic load.

For Group 1, the plastic damage is calcualted in the first cycle of the first block with the maximum stress of 400 MPa, and then fatigue damage is calculated under the stress range of

TABLE 2—*Fatigue with overload.*

Stress, MPa	Overload, MPa	N_{pri}[a]	$\bar{N}_{exp}$	N_{cal}	E_r, %
252 to 2	400	0	136.8	152.1	11.1
300 to 50	400	0	108.7	101.6	−6.5
300 to 50	400	60	84.9	83.3	1.9
300 to 50	400	120	54.2	45.1	16.7

[a] $N \times 10^3$.

TABLE 3—*Fatigue with two-block load.*

Step 1		Step 2					
Stress, MPa	N_{exp}[a]	Stress, MPa	$\bar{N}_{exp2}$	N_{cal2}	E_r, %	N_{m2}	E_{rm}, %
400 to 50	15	300 to 50	49.8	53.4	7.3	108.3	117.5
300 to 50	100	400 to 50	22.4	18.7	−16.5	16.4	−26.8
350 to 150	94	350 to 50	35.6	38.6	8.3	30.6	−14.0
350 to 50	30.6	350 to 150	96.5	116.9	21.1	94.0	−2.6

[a] $N \times 10^3$.

400 to 50 MPa for 15 000 cycles. Finally, the cyclic number of fatigue under the stress range of 300 to 50 MPa to final rupture is calculated.

For Group 2, no plastic damage is expected under Block 1. The fatigue damage is calculated under the applied stress range of 300 to 50 MPa for 100 000 cycles. The plastic damage is calculated in the first cycle of Block 2 with the maximum stress of 400 MPa, and then the cyclic number of fatigue under the stress range of 400 to 50 MPa to final rupture is assessed.

For Group 3, the plastic damage is calculated in the first cycle of Block 1 with the maximum stress of 350 MPa, then fatigue damage is calculated under the stress range of 350 to 150 MPa for 94 000 cycles. Finally, the cyclic number of fatigue under the stress range of 350 to 50 MPa to final rupture is calculated.

For Group 4, the plastic damage is calculated in the first cycle of Block 1 with the maximum stress of 350 MPa, then fatigue damage is calculated under the stress range of 350 to 50 MPa for 30 600 cycles. Finally, the cyclic number of fatigue under the stress range of 350 to 150 MPa to final rupture is calculated.

The predicted results are summarized in Table 3, where N_{cal2} is the calculated fatigue life under the load of the second block, and E_r is the relative error = $(N_{cal2} - \bar{N}_{exp2})/\bar{N}_{exp2}$.

Miner's Rule—Since the Miner's rule is often adopted for the calculation of fatigue life under multiblock load, the calculated results (N_{m2}) by the Miner's rule are also given in Table 3 for comparison, where E_{rm} is the relative error = $(N_{m2} - \bar{N}_{exp2})/\bar{N}_{exp2}$.

The advantage of the Miner's rule is its simplicity, but there are persistent errors in the predicted results. Many experimental data have shown that for high-low fatigue the value of accumulated damage at failure is less than 1, while for low-high fatigue it is greater than 1. In Table 3, Group 1, the fatigue life calculated by the Miner's rule is 108.3×10^3 cycles, but the experimental result to be discussed later is 49.8×10^3 cycles, and the corresponding accumulated damage is 0.704.

In addition, for the fatigue with overload, if we introduce the overload as one fatigue cycle under high maximum stress, the errors of the predicted results by the Miner's rule would be very large, about 49, 45, 27, and 12% for Group 1, Group 2, Group 3, and Group 4, respectively.

Fatigue Crack Initiation at Notch Root

For the fatigue life prediction of notched components, several methods have been proposed to calculate the stress or strain, or both, at the notch root, and to determine the fatigue life based on the fatigue data obtained from smooth specimens. As elucidated before, the method is based on the one-dimensional *S-N* curve that should not be used indiscriminately to predict fatigue life of the three-dimensional state of stresses in notched specimen. Therefore, using the theory of damage mechanics, the characteristics of stresses and strains near the notch root are different from those obtained with the conventional methods.

The geometry of notched specimens is shown in Fig. 2. Six groups of loading conditions are introduced as follows:

Group	σ_{max}	to	σ_{min}
1	85.0	to	5.0
2	80.0	to	30.0
3	110.0	to	30.0
4	110.0	to	60.0
5	140.0	to	60.0
6	140.0	to	90.0

For the finite element calculation, the eight-node isoparametric element is used, as shown in Fig. 4. Two types of element mesh are adopted, for which the dimensions of the finest elements near the notch root are 0.1×0.1 mm^2.

Upon loading, the plastic damage at each Gaussian integral point, if any, is calculated first. At the steps where the remote load reaches the maximum value, the maximum stress at each Gaussian integral point is stored for the subsequent calculation of fatigue damage. In the steps where the remote load is reduced to the minimum value, the minimum stress at each Gaussian integral point is saved and the fatigue damage is calculated and accumulated.

When the overall equivalent damage, Z, at the Gaussian integral point, 9, in the notch root element (Fig. 4) reaches the critical value Z_{cr}, it is assumed that a fatigue crack initiates from the node, 1, at the notch root to the point, 9′ (for 0.1×0.1 mm^2 element, 1-9′ = 0.0113 mm), and the corresponding cyclic number is N_{cal1}. Then the crack propagation was calculated by the damage field mobility (DFM) method [*14*]. The cyclic number for the fatigue crack to propagate from the point, 9′, to reach the 1-mm length is N_{cal2}. The total cyclic number, N_{calt}, for the initiation of fatigue crack with a length of 1 mm at notch root is

$$N_{calt} = N_{cal1} + N_{cal2} \tag{27}$$

After crack initiation at the notch root under the load ranges of 85 to 5 MPa, 110 to 30 MPa, and 140 to 60 MPa, there is slight crack closure occurring at minimum load steps. The order

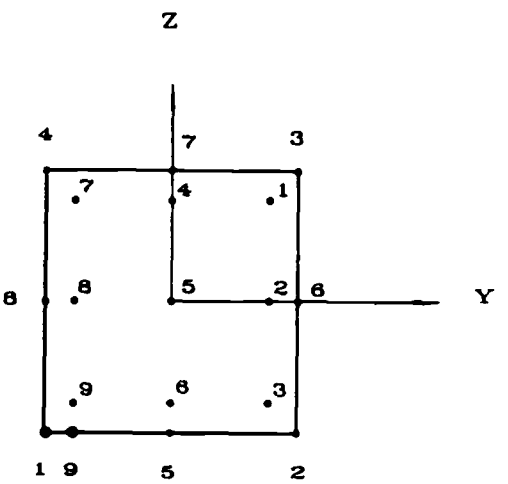

FIG. 4—*Eight-node isoparametric element.*

TABLE 4—*Fatigue lives at notch root.*

Load, MPa	$\bar{N}_{exp}$ [a]	N_{eq}	N_{cal1}	N_{cal2}	N_{calt}	E_r, %
85 to 5	28.1	250	24.3	2.1	26.4	−6.0
80 to 30	115.6	750	78.0	4.6	82.6	−28.5
110 to 30	20.4	200	20.0	2.1	22.1	8.3
110 to 60	86.7	500	54.5	7.6	62.1	−28.4
140 to 60	13.1	150	17.1	3.4	20.5	56.4
140 to 90	69.4	500	50.5	3.3	53.8	22.4

[a] $N \times 10^3$.

of magnitude of negative displacement is 10^{-5} to 10^{-4} mm, since the dominant part of the cyclic number for crack initiation is N_{cal1}. On the other hand, for N_{cal2} the cyclic number for crack initiation at notch root is considerable, but it is not affected by the crack closure. In the present investigation, the crack closure effect is not considered. For other steps and other loading conditions, no crack closure has been observed.

For the finite element calculation, to calculate fatigue damage cycle by cycle would be an extremely time-consuming task. Therefore, one calculation cycle is equivalent to N_{eq} real cycles ($N_{eq} \approx N_{cal2}/100$), which is determined after a numerical investigation for each load range. The calculated results are described in Table 4, where E_r is the relative error ($= [N_{calt} - \bar{N}_{exp}]/\bar{N}_{exp}$).

Fatigue Crack Propagation in Center-Cracked Specimens

The geometry of center-cracked specimens is given in Fig. 3. Three groups of loading conditions are introduced as listed here:

Group	σ_{max}	to	σ_{min}
1	60.0	to	20.0
2	60.0	to	40.0
3	80.0	to	60.0

For the finite element calculation, the element configuration is the same as that for the notched specimen, Fig. 4. Two types of element mesh are adopted, for which the dimensions of the finest elements along the crack propagation line are 0.25×0.25 mm^2.

Upon loading, plastic damage at each Gaussian integral point, if any, is calculated first. At the load steps where the remote load reaches the maximum value, the maximum stress at each Gaussian integral point is stored for the subsequent calculation of fatigue damage. In those loads where the remote load is reduced to the minimum value, the minimum stress at each Gaussian integral point is stored. There is no crack closure found for any load given previously. Also, at the minimum load steps, the crack propagation rate is calculated by the DFM method in the tip element. It is assumed that the crack propagation rate, da/dN, is constant for the crack-tip element (different constants for different tip elements). The cyclic number, N_p, which is needed for the crack to propagate the length of the tip element, can be obtained.

$$N_p = \frac{a_e}{da/dN} \tag{28}$$

where a_e is the length of the element at the crack tip, and da/dN is the crack propagation rate of the tip element. During the crack propagation, N_p decreases as da/dN increases.

If fatigue damage at the Gaussian integral points in other elements occurs, the fatigue damage increments, dZ and $d\boldsymbol{D}$, for one cycle are calculated, and the fatigue damage increments, ΔZ and $\Delta \boldsymbol{D}_p$ for N cycles are calculated as

$$\Delta Z_f = N_p dZ_f \tag{29}$$

$$\Delta \boldsymbol{D}_f = N_p d\boldsymbol{D}_f \tag{30}$$

where ΔZ_f and $\Delta \boldsymbol{D}_f$ are accumulated to the total damage, Z and $\boldsymbol{D}$.

The calculated results and curves of crack propagation rate versus crack length are shown in Table 5.

Experiment and Discussion

Smooth Specimen

Single Overload—Four groups of experiments of fatigue with overload were conducted. The stress chosen for overload for each group is 400 MPa. The loading conditions are identical to those described earlier for the fatigue life prediction.

The experimental data are summarized in Table 2, where $\bar{N}_{\text{exp}}$ is the mean value of experimental fatigue life over overload.

For smooth specimens, it is assumed that there is no residual stress occurring due to overload. The experimental data, Table 2, shows that there is a considerable effect of the plastic damage on fatigue lives. The less the cyclic number of fatigue prior to the overload (N_{pri}), the longer the fatigue life after overload ($\bar{N}_{\text{exp}}$), but the more the total fatigue life ($N_{\text{pri}} + \bar{N}_{\text{exp}}$) was reduced. If the cyclic number of fatigue prior to overload is 0, the fatigue life was reduced by about 45%.

Two-Block Loading—The smooth specimens used are the same as those for the determination of the parameters of the fatigue damage model, Fig. 1. Four groups of experiments were conducted with the loading conditions identical to those used for fatigue life prediction described in an earlier section.

Group 1 is high-low fatigue, and Group 2 is low-high fatigue, while Group 3 and Group 4 have a constant $\sigma_{\max}$ but varying $\sigma_{\min}$. For each load of Block 1, the cyclic number is about half of the fatigue life under the corresponding cyclic load. After Block 1 loading, the dimensions of each specimen were remeasured.

The experimental data are listed in Table 3, where $\bar{N}_{\text{exp2}}$ is the mean value of experimental fatigue life under the load of Block 2.

From the experimental results of two-block fatigue and fatigue with overload, it can be seen that the higher the maximum stress and the earlier it is applied, the larger the error is yielded due to the Miner's rule. The reason is not only the load sequence, but also the effect of plastic damage. Although the effect of load sequence can be taken into account in some nonlinear accumulation models, the effect of overload cannot be effectively considered in such a model.

According to the Miner's rule, if the fatigue life is N under a certain cyclic stress, the contribution of fatigue damage in each cycle is a constant $1/N$, which is very small. But this assumption is not true for some materials, to which the plastic damage would greatly reduce the fatigue life. In the first cycle of a block load, or in the case of overload, if the maximum stress is the highest stress in the load history and exceeds the yield stress, plastic damage would be yielded, which is much greater than the fatigue damage accumulated in each cycle. With the consideration of plastic damage, the damage accumulation rule is neither the form shown in Fig. 5 (*left*) for linear accumulation nor Fig. 5 (*right*) for nonlinear accumulation, but the form shown in Fig. 6 (*left*) for linear accumulation or in Fig. 6 (*right*) for nonlinear accumulation, provided the plastic damage identical to the fatigue damage defined by the cyclic number can be determined.

TABLE 5—*Fatigue crack propagation rate.*

	Crack Length, mm														
	16			20			24			28			32		
Load, MPa	*da/dN*,[a] exp	*da/dN*,[a] cal	E_r, %	*da/dN*,[a] exp	*da/dN*,[a] cal	E_r, %	*da/dN*,[a] exp	*da/dN*,[a] cal	E_r, %	*da/dN*,[a] exp	*da/dN*,[a] cal	E_r, %	*da/dN*,[a] exp	*da/dN*,[a] cal	E_r, %
60 to 20	11.78	7.80	−34	17.19	13.10	−24	30.10	21.40	−29	47.78	36.56	−23	67.49	69.19	3
60 to 40	2.03	2.50	23	3.52	3.64	3	5.24	4.94	6	8.37	6.66	−20	14.10	9.01	−36
80 to 60	2.16	4.02	86	4.45	5.42	22	6.41	6.54	2	10.03	8.46	816	17.26	10.71	−38

[a] $da/dN \times 10^{-5}$.

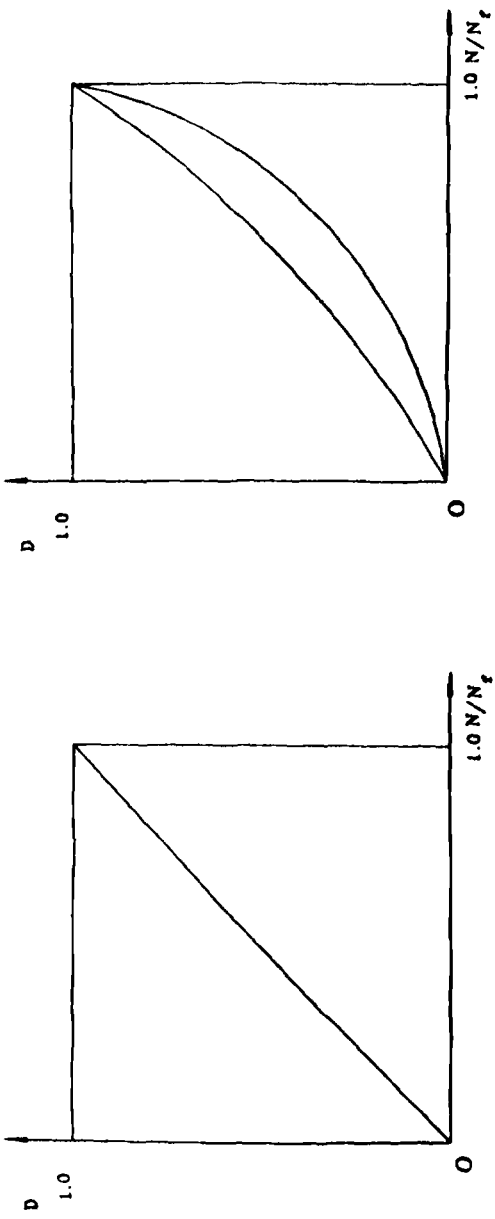

FIG. 5—*Fatigue damage accumulation without plastic damage:* (left) *linear accumulation and* (right) *nonlinear accumulation.*

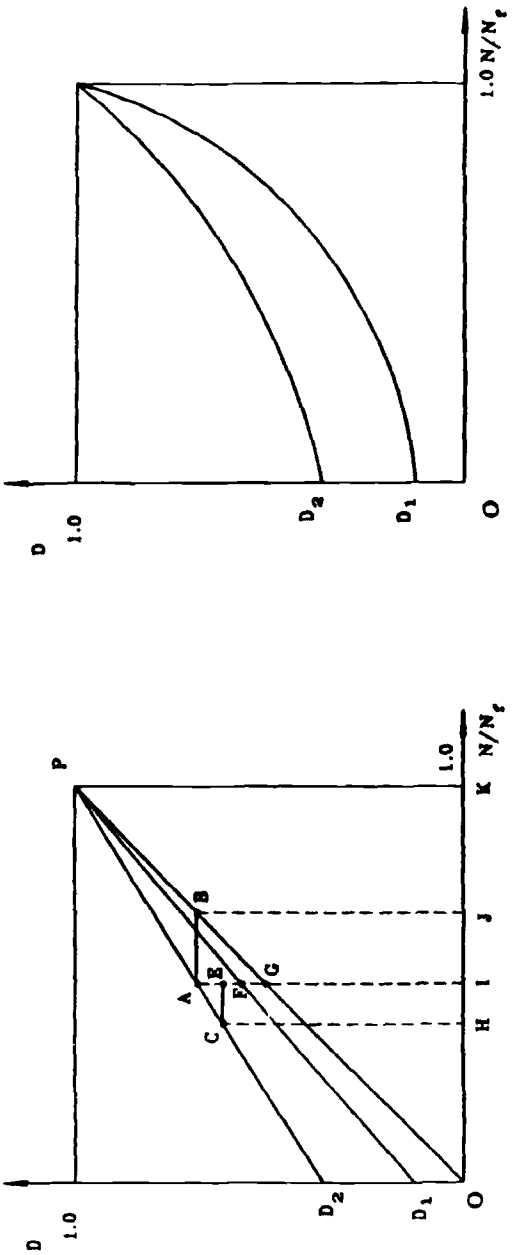

FIG. 6—*Fatigue damage accumulation with plastic damage:* (left) *linear accumulation and* (right) *nonlinear accumulation.*

Now, take a qualitative study of a linear fatigue damage accumulation accompanied by plastic damage, Fig. 6 (*left*). For Group 1 and Group 2, the fatigue damage accumulation line under the stress of 300 to 50 MPa is $\overline{OP}$, and that under the stress of 400 to 50 MPa is $\overline{OD_2P}$, where $\overline{OD_2}$ is the plastic damage due to the maximum stress of 400 MPa. For Group 1, the path of damage accumulation during the first block is $\overline{OD_2A}$, and the path of damage accumulation during the second block is $\overline{BP}$. The total accumulated damage is then

$$\overline{OI} + \overline{JK} < 1 \tag{31}$$

where $\overline{OK} = 1$. For Group 2, the path of damage accumulation during the first block is $\overline{OG}$, the plastic damage yielded in the first cycle of the second block is $\overline{GE}$, and the path of damage accumulation during the second block is $\overline{CP}$. The total accumulated damage is

$$\overline{OI} + \overline{HK} > 1 \tag{32}$$

If the maximum stresses of the first block and the second block are the same, such as those in Group 3 and Group 4, the damage accumulation paths are also the same, that is, $\overline{OD_1P}$ in Fig. 6 (*left*). Thus for both Group 3 and Group 4, the damage accumulation path of Block 1 is $\overline{OD_1F}$, the damage accumulation path of Block 2 is $\overline{FP}$, and the total accumulated damage is

$$\overline{OI} + \overline{IK} = 1 \tag{33}$$

In Table 3, it can be seen that the errors of the Miner's rule of Group 3 and Group 4 are less than those in Group 1 and Group 2. In Group 4, the error of the Miner's rule is very small, even much less than the error of the damage model proposed.

Therefore for some materials, the effect of plastic damage should be taken into account. If so, the results obtained by the Miner's rule can even be improved.

Fatigue Crack Initiation at Notch Root

The geometry of notched specimens is shown in Fig. 2. The specimens were prepared in accordance with Ref *15*. The severely scratched protective coating was milled off. After machining, the area around the notch root is polished with fine emery papers from No. 240 to No. 800. The dimensions of the specimens were measured with precision up to 0.02 mm.

The crack initiation was defined as the appearance of a macrocrack with the length of 1 mm, and monitored with a traveling microscope of 10 times magnification, which enabled the recording of the crack extension up to 0.01 mm.

Six groups of experiments were conducted with the identical loading conditions used for the finite element analysis. For each group, six specimens were used. The experimental data are given in Table 4, where $\overline{N}_{exp}$ is the mean value of the fatigue life at notch root.

In the fatigue experiments, it was observed that for a notched specimen, the rate of crack propagation from about 0.1 to 1 mm is rapid. Most fatigue life was spent in initiating a tiny crack (<0.1 mm) at notch root, which corresponds to the calculated results N_{cal1}. In Table 4, it can be seen that most calculated results are acceptable, except those under the load of 140 to 60 MPa, which are considered greater than $\overline{N}_{exp}$.

Fatigue Crack Propagation of Center-Cracked Specimens

The geometry of center-cracked specimens is given in Fig. 3. The preparation of the specimens is made in accordance with Ref *15*. The severely scratched protective coating was milled

off. After machining, the crack propagation area is polished with fine emery papers from No. 240 to No. 800. The dimensions of the specimens were measured with precision up to 0.02 mm.

The pre-cracking of the specimens, the measurement of fatigue crack propagation, and the data treatment complied with the procedures specified in ASTM Test Method for Tensile Strain-Hardening Exponents (n-Values) of Rates (E 646–93). For pre-cracking, the mean stress was the same as the mean stress of the test, while the stress amplitude was from 50 to 70% of the stress amplitude of the test cited later.

After pre-cracking, the initial crack length measured was $2a_0 \approx 28$ mm. Then the crack propagated until the crack length was $2a \geq 68$ mm, after which the crack propagated very fast in an unstable manner. The crack propagation was monitored with a traveling microscope of $\times 10$ magnification, which enabled the reading of the crack extension up to 0.01 mm. The crack increment, Δa, is about 0.5 to 1.5 mm.

Three groups of experiments were conducted, with the loading conditions described in the section on center-cracked specimens. For each group, six specimens were tested. The crack propagation rate, da/dN, of each specimen was calculated by secant method, that is, ASTM Test Method for Measurements of Fatigue Crack Growth Rates (E 647–93), and then fitted by a polynomial. The mean value of da/dN against crack length of each group was taken as the experimental result, shown in Table 5.

One of the shortcomings of finite element analysis is its accuracy in stress calculation, which in turn affects damage. This would induce considerable errors in the calculation of the gradient of the total equivalent damage, Z, since the damage gradient is related to the values of Z at three Gaussian integral points, that is, Points 3, 6, and 9 (Fig. 4). In order to reduce the errors after each complete calculation, the calculated values of Z at Gaussian integral Points 3, 6, and 9 of all crack elements were fitted respectively as straight lines by the least squares method. The gradient of Z for each crack-tip element was calculated by the modified values of Z.

Because large scatter in fatigue test results is often observed, the predicted results shown in Table 5 are considered acceptable.

Conclusions

1. A damage model based on the damage mechanics theory and related to the elastic energy release rate has been established, in which the effect of maximum stress for plastic damage, and the stress amplitude and mean stress for fatigue damage are taken into account. This model can be used to calculate the fatigue lives for both low-cycle and high-cycle fatigue, under multiple-block loads, or with overloads, or a combination thereof, and also can be used to calculate the fatigue crack propagation rate.

2. A general-purpose finite element program has been modified to conduct the damage-coupled calculation of stresses, strains, and damage, and also to simulate the fatigue crack propagation. The fatigue lives of crack initiation and fatigue crack propagation rates of different specimens with complex geometry have been satisfactorily predicted.

3. For the fatigue under two-block loads and the fatigue with overload using smooth specimens, the calculated results show good agreement with the experimental data. The important influence of plastic damage on the fatigue damage is discussed. A qualitative analysis indicates that if plastic damage can be taken into account in the Miner's rule, an improvement in its prediction can be achieved.

4. For fatigue in notched specimens, there is a phenomenon of stress reduction at notch root due to damage, which can increase the fatigue lives. For the fatigue crack propagation using center-cracked specimens, the calculated results are considered satisfactory.

References

[1] Kanninen, M. F. and Popelar, C. H., *Advanced Fracture Mechanics*, Oxford University Press, New York, 1985.

[2] Krajcinovic, D., "Continuum Damage Mechanics," *Applied Mechanics Reviews*, Vol. 37, 1984, pp. 1–6.

[3] Cordebois, J. P. and Sidoroff, F., "Damage Induced Elastic Anisotropy," *Euromech Colloquium 115*, Comportement M, canique des solides anisotropes, Grenoble, 1979, pp. 761–774.

[4] Chow, C. L. and Wang, J., "An Anisotropic Theory of Elasticity for Continuum Damage Mechanics," *International Journal of Fracture*, Vol. 33, 1987, pp. 3–16.

[5] Chow, C. L. and Wang, J., "An Anistropic Theory of Continuum Damage Mechanics for Ductile Fracture," *Engineering Fracture Mechanics*, Vol. 27, No. 5, 1987, pp. 547–558.

[6] Chow, C. L. and Wang, J., "An Anistropic Continuum Damage Theory and Its Application to Ductile Crack Initiation," *Damage Mechanics in Composites*, ASME AD-Vol.12, 1987, pp. 1–10.

[7] Chow, C. L. and Wang, J., "Ductile Fracture Characterization with an Anisotropic Continuum Damage Theory," *Engineering Fracture Mechanics*, Vol. 30, No. 5, 1988, pp. 547–563.

[8] Chow, C. L. and Wang, J., "A Finite Element Analysis of Continuum Damage Mechanics for Ductile Fracture," *International Journal of Fracture*, Vol. 38, 1988, pp. 83–102.

[9] Wang, J. and Chow, C. L., "Mixed Mode Ductile Fracture Studies with Nonproportional Loading Based on Continuum Damage Mechanics," *Journal of Engineering Materials and Technology*, Vol. 111, 1989, pp. 204–209.

[10] Chaboche, J. L. and Lesne, P. M., "A Non-Linear Continuous Fatigue Damage Model, *Fatigue Fracture Engineering Materials and Structures* Vol. 11, No. 1, 1981, pp. 1–17.

[11] Wang, J., "Development of an Anisotropic Damage Mechanics Model in Ductile Fracture," Ph.D. thesis, University of Hong Kong, 1987.

[12] Frost, N. E., Marsh, K. J., and Pook, L. P., *Metal Fatigue*, Clarendon Press, Oxford, 1974.

[13] Gao, Z. T., *Applied Statistics of Fatigue* (in Chinese), National Defense Industry Press, Beijing, China, 1986.

[14] Yu, L. G., Chow, C. L., and Duggan, B. J., "An Orthotropic Damage Model with Damage Field Mobility (DFM) Method for Fatigue Crack Propagation," *Proceedings*, Asia-Pacific Symposium on Advances in Engineering Plasticity and Its Applications—AEPA '92, Hong Kong, 15–17 Dec. 1992, pp. 363–370.

[15] Swanson, S. R., Ed., *Handbook of Fatigue Testing, ASTM STP 566*, American Society for Testing and Materials, Philadelphia, 1974.

Peter J. Woytowitz[1] *and Roger H. Richman*[2]

Solid Mechanics Modeling of Erosion Damage

REFERENCE: Woytowitz, P. J. and Richman, R. H., **"Solid Mechanics Modeling of Erosion Damage,"** *Applications of Continuum Damage Mechanics to Fatigue and Fracture, ASTM STP 1315*, D. L. McDowell, Ed., American Society for Testing and Materials, 1997, pp. 186–199.

ABSTRACT: The erosion process is studied from a solid mechanics perspective. This paper describes the analysis of multiple coincident particle impacts of an elastic steel sphere on an elastic-plastic copper target material. The analysis is performed using the DYNA2D nonlinear dynamic finite element code. The results of the DYNA2D analysis are compared against experimental results for the single impact case. Next, three methods of computing the damage induced by the impact process are studied; a strain-life approach using rainflow counting, the technique of cyclic plastic work, and a continuum damage mechanics based fatigue criterion. The damage predicted by each technique is presented and reviewed. Extensions of the procedures are discussed.

KEYWORDS: continuum damage mechanics, cracking, fatigue (materials), fracture (materials), erosion, solid particle, impact, strain life, cyclic plastic work, nonlinear finite element analysis, modeling analysis

It is well known that erosive wear, which ensues when solid particles entrained in fluid streams impinge on surfaces, is a serious problem for engineering systems such as catalytic cracking, combustion turbines, helicopter rotors, coal-fired steam generators, and many others. The importance of erosion is reflected in numerous detailed investigations of all its aspects (see, for example, the reviews in Ref *1–4*). On the basis of those studies, reasonable consensus has been reached about the influences of particle (hardness, size, shape, and density) and particle-flow (velocity, impact angle, and flux rate) parameters on erosion behavior.

In contrast, the role played by properties of the eroding material, particularly ductile metals and alloys, is not well understood. This situation stems, in large part, from uncertainty about how damage accumulates with successive impacts on a surface. Thus, although erosion losses can, in principle, be lessened by materials improvements and surface treatments, the choices for such improvements are unclear because the materials properties that will ensure better erosion resistance cannot be specified. In consequence, resistant alloys and coatings are still selected on the basis of previous experience or by trial and error. A main motivation of the work reported here is to advance beyond the current reliance on empiricism; it seems much more promising to develop a mechanistic model that could lead to rational methods for designing resistant materials or coatings.

Although there has not been a consensus about damage mechanisms in erosion, there is agreement that material removal in multiple-impact situations (cavitation-erosion, liquid-droplet erosion, and most instances of solid-particle erosion) is not a result of single impacts. Damage can accumulate for thousands of impacts before a fragment of material is dislodged, and several investigations have treated solid-particle erosion as a manifestation of fatigue [5–

[1] Vice president and principal engineer, Engineering Mechanics Technology Inc., San Jose, CA 95129.
[2] President, Daedalus Associates, Inc., Mountain View, CA 94043.

7]. More recently, good correlation was obtained between cyclic deformation parameters and material removal rates from six unalloyed metals that were eroded by glass spheres (about 14 μm in diameter) at 90° incidence and 30 m/s velocity [*8*]. Thus, damage by cyclic deformation seems a reasonable starting point for a model of solid-particle erosion.

Early attempts at finite element modeling of erosion usually simulated a single load cycle (that is, one particle impact) with isotropic hardening of the indented material [*9,10*]. The few studies of repeated elastic-plastic contacts [*11,12*] were hampered by limited variability of material responses and by sparse information about cyclic constitutive relations. More realistic simulation was achieved with a model that incorporated kinematic hardening and up to 50 randomly located indentations [*13*]. Stress-strain responses characteristic of cyclic deformation were reproduced: stress and strain reversals, hysteresis loops, and strong history effects. However, the assumptions of plane strain, quasi-static loading rates, and a damage algorithm derived for predominantly tensile load configurations, made it difficult, if not impossible, to relate quantitatively the model predictions to experimental observations of solid-particle erosion.

The current study builds on previous work and attempts to remove some of the earlier modeling assumptions and limitations. In addition, since computation of the damage plays a major role in assessing erosion mechanisms, a comparison of three major techniques has been performed within the context of particle impact damage. The present study attempts to quantify the damage induced by multiple coincident impacts of a steel sphere on a copper target material. The results of this study form a basis for future predictions of erosion damage.

Finite Element Analysis

Modeling of Single Particle Impact

In order to extend understanding of the erosion process, a solid mechanics model of a single particle impacting a surface was developed. Past studies have included elastic and plastic effects. However, previous work in this area considered the process as quasi-static and often did not directly treat the contact surface effect. In the current study, a full dynamic analysis of the impact process is considered. The impacting particle is assumed to be a hardened steel sphere and the target material is copper. This system was selected for several reasons. First, experimental data were available from Sundararajan [*14*]. These experimental data included the effects of particle size and impact speed on the resulting target material's crater dimensions. The steel sphere was considered to be much stronger than the copper material so that the plastic deformations and associated mechanical properties such as yield strength and the elastic-plastic stress-strain response for the steel were not needed. A copper target material was selected so as to minimize the strain rate effects. It is well known that copper generally has small strain rate effects compared to materials such as stainless steel. Thus, the mechanical model for the steel was taken to be elastic. The copper target material was modeled as a kinematically hardening elastic-plastic material with a constant tangent modulus. The mechanical properties for the two materials are summarized in Table 1. The steel properties of Table 1 are typical for

TABLE 1—*Mechanical properties.*

Property	Steel Sphere (particle)	Copper Target
Young's modulus, E	203×10^3 MPa	138×10^3 MPa
Poisson's ratio, ν	0.30	0.30
Density, ρ	7850 kg/m^3	8990 kg/m^3
Yield strength, S_y	N/A (elastic)	279 MPa
Tangent modulus, E_t	N/A (elastic)	125.2 MPa

steel, while the copper properties were obtained by processing the static elastic-plastic stress-strain response from Sundararajan [*14*]. In order to model the copper material as a linearly hardening material, the total plastic work (area under the stress-strain curve) for the actual stress-strain curve was equated to the total area under the stress-strain curve assuming linear hardening. Using this approach, the yield strength and hardening modulus of Table 1 were obtained.

The axisymmetric finite element model used in shown in Fig. 1. The DYNA2D [*15*] finite element code was used for the analysis, which allowed accurate modeling of dynamic effects. Slide lines (contact surfaces) were included in the analysis between the impacting sphere and target material. Since the model is axisymmetric, the results are applicable for normal impact situations. The first task was to test the accuracy of the finite element solution procedure against

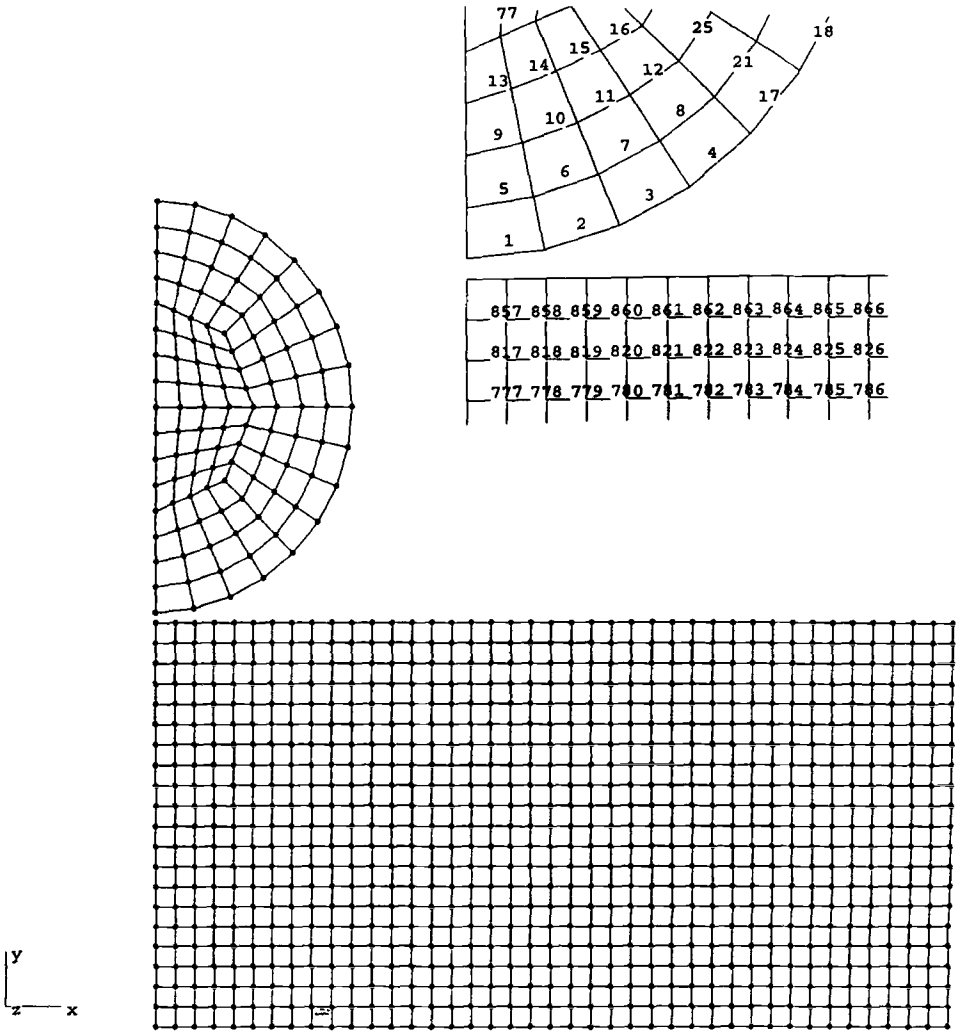

FIG. 1—*Finite element model of sphere and target material.*

TABLE 2—*Comparison of finite element and experimental results for single impact.*

Impact Velocity, m/s	Crater Depth, *FE*, d_{FE} (mm)	Crater Depth [*14*], *d* (mm)	Percent Error, $100 \times d_{FE}/d$	Crater Width, *FE*, w_{FE} (mm)	Crater Width [*14*], *w* (mm)	Percent Error, $100 \times w_{FE}/w$
54.5	0.2820	0.248	13.7	2.233	2.20	1.0
127.5	0.7019	0.626	12.1	3.369	3.20	5.3
198.7	1.192	1.058	12.7	4.265	3.87	10.2
253.1	1.529	1.412	8.3	4.539	4.30	5.5

the test results of Sundararajan [*14*]. For this comparison, a steel sphere diameter of 4.76 mm was used and the analysis was performed for several different impact velocities. Comparisons against the measured test data of Sundararajan [*14*] are shown in Table 2. The crater depth, *d*, and width, *w*, are shown in Fig. 2 along with the deformed plot of a typical simulation. The displacements shown in Fig. 2 are to scale and have not been magnified relative to the other geometry. The sphere shown in Fig. 2 is in its rebound position from the surface.

As can be seen, reasonable correlation has been obtained. The finite element results always overpredict both the crater depth and crater width. Perhaps this is a consequence of neglecting the rate effect on the stress-strain response. The 253.1 m/s simulation was tested using stress-strain data from Sundararajan [*14*] for a strain rate of 1×10^4 s^{-1} and improved correlation

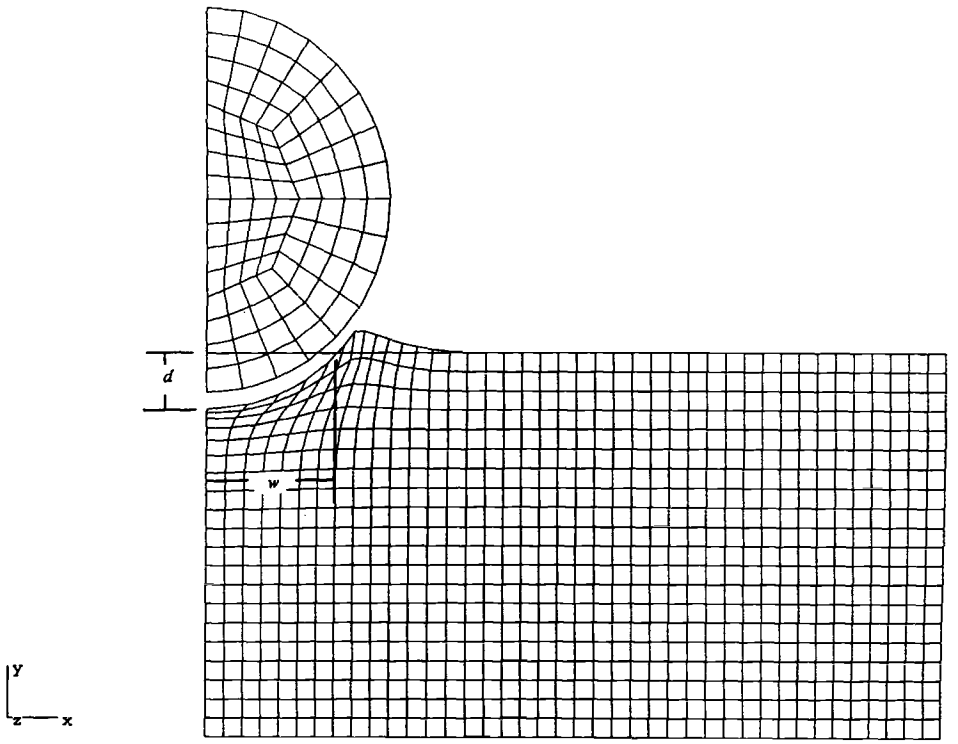

FIG. 2—*Deformed plot for impact velocity of 127.5 m/s (analysis time = 25 μs).*

was obtained. However, since the strain rates are different throughout the model, there is no justification for using this constant strain rate data. For purposes of this investigation, the correlation with test data of Table 2 is considered adequate and no further refinement of the finite element modeling procedure was investigated.

Modeling of Multiple Coincident Particle Impacts

The finite element procedure just discussed was extended to allow for modeling of multiple coincident particle impacts. Up to four coincident particle impacts were investigated. This is considered to be the first step in eventually analyzing multiple noncoincident impacts that would be more representative of an actual erosion process. However, the modeling of noncoincident impacts precludes the use of an axisymmetric analysis and requires a three-dimensional dynamic analysis. Understanding of the multiple coincident impact analysis was considered an important step toward this future goal.

The finite element model used is essentially identical to that used for the single impact study with the exception that three additional steel spheres were introduced into the analysis. Slide lines (contact interfaces) were not introduced between the impacting spheres in order that they would pass through one another without any interaction. This is the natural behavior of most finite element codes unless special care is taken to introduce contact surfaces between objects. Therefore the analysis is set up such that at $t = 0$ there were four spheres located at different distances from the target surface. The spheres were spaced relative to one another so that each sphere had sufficient time to rebound from the surface before the next sphere impacted it. For this study, each of the spheres was given an initial velocity of 54.5 m/s.

Selected results of this analysis are as follows. The y component of stress, σ_{yy}, typically displayed large peaks of compressive stress followed by periods of essentially zero stress in between impacts, as expected. The shear stress response for an element located five elements in from the symmetry centerline and on the surface of the target material is shown in Fig. 3. (This element displayed a particularly high response.) Examination of the deformed shapes physically verifies that large shear stress responses would be expected at this location. A somewhat unexpected result is the plot of infinitesimal shear strain for the same element that is also shown in Fig. 3. The shape shown in Fig. 3 is caused by the very high levels of plastic deformation; the elastic unloading is completely "swamped out" by the plastic deformation. This same basic behavior has been verified by performing identical analyses with the NIKE2D [*16*] code. When the levels of plastic strain are reduced by considering much lower impact velocities, then responses very similar to those obtained by McNaughton et al. [*13*] were obtained.

Computation of Damage for Single and Multiple Coincident Impacts

The main goal of the solid mechanics modeling procedure is to predict damage accumulation associated with particle impacts that can in turn be related to the erosion process. There are a number of approaches available for predicting damage. In order to gain confidence in the predicted damage levels, three prominent techniques for computing damage are investigated here. These techniques have been implemented in such a way that the damage does not feed back into the finite element analysis, except to the extent that the plasticity represents damage.

Strain Life Approach

The strain life approach to calculating impact damage has been investigated previously by McNaughton et al. [*13*] and was based upon the shear strain form described by Kandil et al.

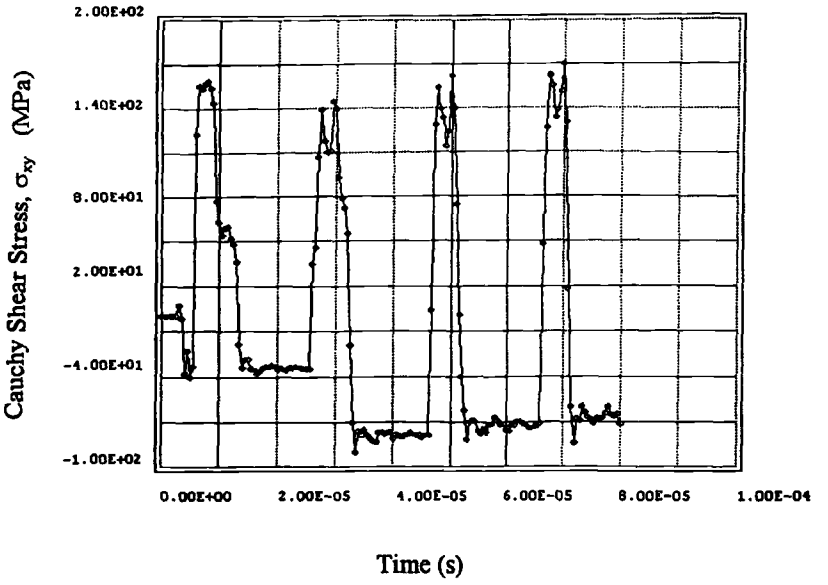

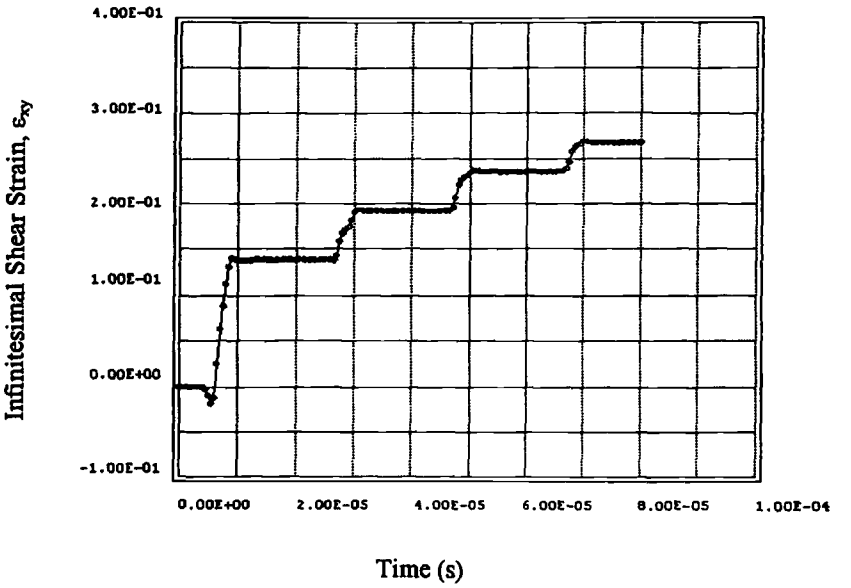

FIG. 3—*Shear stress and strain versus time for multiple coincident impacts (initial velocity = 54.5 m/s).*

[17] as later modified by Socie et al. [18] to include mean stress effects. In this form, the strain life equation is written as

$$\frac{\Delta\gamma_{\max}}{2} + \frac{\sigma_{n0}}{E} = \frac{\tau_f'}{G}(2N_f)^b + \gamma_f'(2N_f)^c \tag{1}$$

where $\Delta\gamma_{\max}$ is the change in the maximum shear strain, σ_{n0} is the mean normal stress, E is Young's modulus, G is the shear modulus, $\tau_f' = \sigma_f'/\sqrt{3}$ is the shear strength coefficient, $\gamma_f' = \sqrt{3}\varepsilon_f'$ is the shear ductility coefficient, b is the fatigue strength exponent, c is the fatigue ductility exponent, and N_f is the number of cycles. The damage associated with a predicted $\Delta\gamma_{\max}$ and a corresponding N_f cycles to failure was taken to be $D = 1/N_f$.

The fatigue properties in Eq 1 are summarized in Table 3 for the copper target material. While Eq 1 appears to be a reasonable generalization of the uniaxial form of the strain life equation, there are some physically unappealing difficulties associated with using it. First, in the case where the axis of stress and strain are changing, the maximum shear difference ($\Delta\gamma_{\max}$) in general will refer to different physical planes of the material. This is particularly problematic for the case of large plastic deformation (large strains). Additionally, if one wishes to count the cycles to be used in Eq 1 using a procedure such as rainflow counting [19], the problem associated with changing planes of maximum shear strain is accentuated because the planes are even more likely to change owing to the rainflow counting procedure's rearrangement of the strain sequences. To circumvent these problems, Eq 1 is used in the following manner. First, instead of using the infinitesimal definition of shear strain, we use the Green-Lagrange measure of shear strain in such a way that it reduces to Eq 1 for small deformation. Next, with reference to Fig. 1 of the axisymmetric finite element model, we first assume that the worst plane (the one that is associated with the maximum damage) occurs such that it is aligned with the x-y coordinate system of Fig. 1. The shear stress (τ_{xy}) in the x-y coordinate system is first rainflow counted over the time history of interest and the entire strain and stress tensor at each sample in time is sorted according to the rainflow counting procedure. Now assuming that the worst damage occurs on this plane, the change in shear strain, $\Delta\gamma_{xy}$ is used in Eq 1 to compute the predicted life and associated damage, D. This calculation is repeated over all the elements of the finite element model and the computed damage, D, for each element is saved. Next, it is assumed that the worst damage occurs on a plane that is rotated relative to the x-y coordinate system by some small angle, $\Delta\theta$. Call this new coordinate system x'-y'. The same procedure of rainflow counting the transformed shear stress, $\tau_{x'y'}$, and computing the damage for all elements is now performed using $\Delta\gamma_{x'y'}$ (the transformed $\Delta\gamma_{xy}$) in Eq 1. By repeating this procedure such that we cover the entire right-hand plane ($\theta \in [0, \pi/2]$) and always saving the largest damage for any given element, the distribution of damage over the entire model is obtained. This has a physically appealing characteristic that shear strains occurring on different planes are not combined and one can also predict the angular orientation associated with the maximum damage. This orientation will in general be different for each element of the model.

TABLE 3—*Fatigue properties for copper target material.*

Property	Value
Fatigue strength coefficient, σ_f'	564 MPa
Fatigue strength exponent, b	−0.0857
Fatigue ductility coefficient, ε_f'	0.483
Fatigue ductility exponent, c	−0.5714
Cyclic strain hardening exponent, n'	0.15

TABLE 4—*Damage versus number of impacts, strain life approach.*

Impact Number	D_{max}	Angle, θ	Element
1	0.674	45°	858
2	1.150	45°	858
3	1.480	45°	858
4	1.790	45°	858

This technique has been applied to the impact process characterized by the shear stress and shear strain responses, τ_{xy} and γ_{xy}, shown in Fig. 3. The resulting maximum damage, the angle associated with maximum damage and element number, is shown in Table 4 after 1, 2, 3, and 4 coincident impacts. (The element numbers are shown in Fig. 1.) The same calculations done for the infinitesimal definition of shear strain produces damages approximately 5 to 14% greater and worst case angles similar to those of Table 4. Additionally, it was found that for these very high levels of plastic strain, the normal stress correction of Eq 1, (σ_{n0}/E) has negligible effect, as would be expected, since this normal stress correction will always have values on the order of elastic strains, which are very small compared to the plastic strains observed in this simulation.

Cyclic Plastic Work Approach

The technique of using the cyclic plastic work for characterizing damage has been studied for some time. Early studies by Morrow [*20*] discuss the use of this technique in the context of fully reversed, uniaxial loading. Later work, for example by Garud [*21*], generalized the approach to include multiaxial and effects of changing the principal axes of stress and strain over a cycle. The basic idea states that the cyclic plastic work, W_p, given at any point in a body can be used to characterize the accumulated damage at that point. The cyclic plastic work, W_p, generalized to the case of large deformations can be written as

$$W_p = \int \sigma_{ij} d_{ij}^p \, dt \tag{2}$$

where σ_{ij} is the Cauchy stress and d_{ij}^p is the plastic part of the rate of deformation tensor as discussed, for example, in Malvern [*22*]. Owing to the fact that for the present work the plastic strains are so much larger than the elastic strains, the plastic part of the rate of deformation tensor is simply approximated as the total rate of deformation in Eq 2. In order to convert the plastic work computed by Eq 2 to some measure of damage, a result due to Morrow [*20*] is used. According to Morrow's analysis, the plastic work associated with a single cycle of a symmetric power-hardening material with cyclic strain hardening exponent, n', cycled over a total plastic strain range of $\Delta\varepsilon_p$ and with fully reversed stress amplitude, σ_a, is given by

$$\Delta W_p = 2\sigma_a \Delta\varepsilon_p \left(\frac{1 - n'}{1 + n'}\right) \tag{3}$$

where

$$\sigma_a = \sigma_f' \left(\frac{\Delta\varepsilon_p}{2\varepsilon_f'}\right)^{n'} \tag{4}$$

TABLE 5—*Number of cycles, damage, and plastic work per cycle for target copper material predicted by Eq 5.*

N_f	D	$\Delta\varepsilon_p$	ΔW_p, Power Hardening	ΔW_p, Linear Hardening
1	1	0.6578	510.7 MPa	365 MPa
5	0.20	0.2739	177.4	151
10	0.10	0.1807	112.5	98.6
100	0.010	0.0520	39.6	26.8
1000	0.001	0.0168	8.6	7.1
10^6	10^{-6}	0.0026	0.1	0.2

Substituting Eq 4 into Eq 3 and using the uniaxial (tension/compression) form of Eq 1 for $\Delta\varepsilon_p$, we arrive at the following relationship between the plastic work per cycle, ΔW_p, and the number of cycles to failure, N_f

$$N_f = \frac{1}{2}\left[\frac{(1 + n')}{(1 - n')}\frac{\Delta W_p}{4\sigma_f'\varepsilon_f'}\right]^{\frac{1}{(n'+1)c}} \tag{5}$$

Applying Eq 5 to the copper target material, the results of Table 5 can be obtained showing the predicted number of cycles to failure associated with a specified amount of plastic work. Taking the damage, $D = 1/N_f$, we arrive at the tabulated damage associated with the specified amounts of plastic work also shown in Table 5. Table 5 also indicates the associated plastic work per cycle assuming a linear-hardening material (constant tangent modulus, E_t) that is used in the actual finite element modeling procedure. Thus, similar results will be obtained from the power-hardening material model and a linear-hardening material model as long as the relative levels of plastic strain are such that more than a few cycles are predicted before failure.

Using the finite element model to calculate the accumulated plastic work from Eq 2 and the correlation between plastic work and damage just discussed, the results of Table 6 are obtained. The first column of damages displayed in Table 6 uses Eq 2 to compute W_p then substitutes this result directly into Eq 5, which then results in a damage from the relationship, $D = 1/N_f$. The second column of damages displayed in Table 6 uses the same approach but first doubles the W_p computed using Eq 2. Note that this second column of damages correlates well with the damages predicted using the strain-life approach. The reason for this can be seen by reference to Fig. 4. Since the strain-life equation has been used to correlate the cyclic plastic work to damage, we see that given a $\Delta\varepsilon_p$ the strain-life equation assumes this is associated with a completely reversed cycle. The plastic work associated with a completely reversed cycle is approximately double that associated with a half cycle or one reversal. Hence, doubling the computed W_p is equivalent to assuming complete reversal for each impact; the doubled W_p

TABLE 6—*Damage versus number of impacts, cyclic plastic work approach.*

Impact Number	D, W_p, Eq 2	D, Double W_p	Element
1	0.235	0.674	857
2	0.369	1.060	857
3	0.479	1.376	857
4	0.585	1.680	857

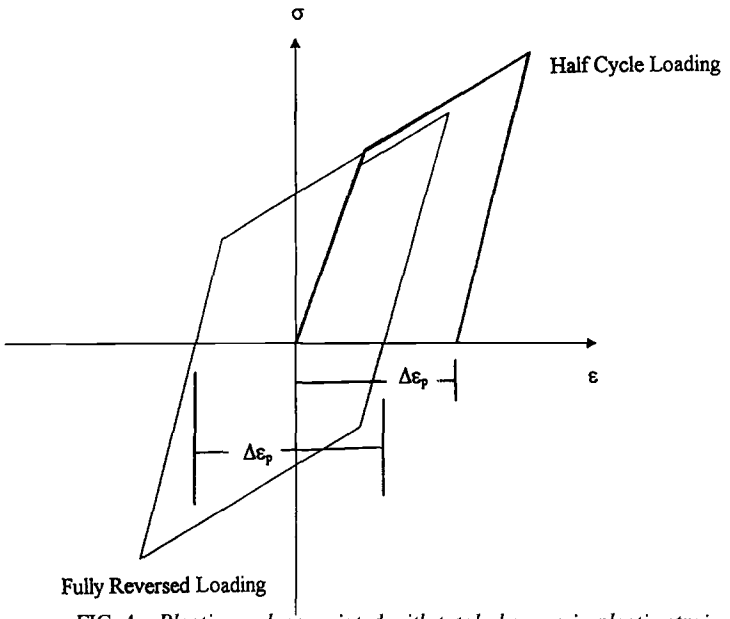

FIG. 4—*Plastic work associated with total changes in plastic strain.*

values in Table 6 are included mainly for the purposes of comparison to the damages computed by the strain-life approach in Table 4. We believe that the impact processes modeled here are better represented by the half-cycle type of loading shown in Fig. 4 and computed by Eq 2.

Continuum Damage Mechanics Approach

The last technique studied for computation of damage for the impact process is based upon continuum damage mechanics. Although this is still an active field of research and a number of approaches can be used, we selected an approach presented by Lemaitre [*23*] for computation of fatigue damage. With this approach, one develops a kinetics relationship that is used to predict damage. For the present formulation, the kinetics equation is given by Lemaitre [*23*] as

$$\frac{dD}{dt} = \frac{R_v(\bar{\varepsilon}_p - \bar{\varepsilon}_0)^\gamma \dot{\bar{\varepsilon}}_p}{\Gamma(1 - D)^\alpha} \tag{6}$$

where

$$R_v = \left(\frac{\sigma^*}{\bar{\sigma}}\right)^2 \qquad \bar{\sigma} = \left(\frac{3}{2}\,\boldsymbol{\sigma}':\boldsymbol{\sigma}'\right)^{\frac{1}{2}} \qquad \dot{\bar{\varepsilon}}_p = \left(\frac{2}{3}\,\boldsymbol{d}:\boldsymbol{d}\right)^{\frac{1}{2}} \tag{7}$$

and Γ, α, and γ are material constants that can be determined from the strain-life relations as

$$\gamma = -\left(\frac{1}{c} + 1\right) \quad \text{and} \quad \Gamma = \frac{\alpha + 1}{\gamma + 1}\,(2^{c+1}\varepsilon_f')^{(\gamma+1)} \tag{8}$$

In Eq 7, $\boldsymbol{\sigma}'$ denotes the Cauchy stress deviator tensor, $\boldsymbol{d}$ is the rate of deformation tensor, and σ^* is an equivalent damage stress given by Lemaitre [*23*] as

$$(\sigma^*)^2 = (1 + \nu)\langle\boldsymbol{\sigma}\rangle:\langle\boldsymbol{\sigma}\rangle - \nu\langle tr\langle\boldsymbol{\sigma}\rangle\rangle^2 + h\left(\frac{1 - D}{1 - Dh}\right)^2 [(1 + \nu)\langle-\boldsymbol{\sigma}\rangle:\langle-\boldsymbol{\sigma}\rangle - \nu\langle tr\langle-\boldsymbol{\sigma}\rangle\rangle^2] \tag{9}$$

where the symbol ":" denotes the inner product

$$\boldsymbol{a}:\boldsymbol{a} = a_{ij}a_{ij}$$

where summation is performed over the repeated subscripts. The constant, α, affects the linearity or nonlinearity of the damage versus time response. For the present study, α was taken to be zero. Also in Eq 9, the stresses inside the Macaulay brackets $\langle\ \rangle$ are principal stresses and any term inside the Macaulay brackets that is less than zero is taken as zero. Equation 9 represents a decomposition of the stress tensor into compressive (negative) and tensile (positive) parts. The compressive stresses are contained in the terms that are multiplied by h while the tensile stresses are contained in the first two terms. The variable, h, is termed the closure coefficient and Lemaitre [*23*] indicates that the value, $h = 0.20$, has been determined for a number of materials. From Eq 9, one can see that the closure coefficient is related to the amount of damage introduced by compressive stress fields. The $h = 0$ value indicates that compressive stress fields do not affect the damage, while $h = 1$ indicates that compressive stress fields and tensile stress fields introduce the same amount of damage. Strictly speaking, the rate of deformation tensor used in Eq 7 should be decomposed into an elastic and plastic part, using only the plastic part in Eq 7. However, for the present study, the plastic strains are much larger than the elastic strains and, therefore, the total $\boldsymbol{d}$ is used in Eq 7 for convenience.

Using the kinetics relationship of Eq 6, we computed the damage for the present simulation. Table 7 presents the results using a closure coefficient, $h = 0.20$, and also using a closure coefficient, $h = 0.10$. For closure coefficient, $h = 0.0$, very small values for damage are predicted. This is ascribable to the fact that for the impact process a highly compressive stress field is obtained. Damage values greater than 1.0 are not physically consistent with the form of Eq 6, therefore, it is not possible to compare such damages against previous predictions. As can be seen, the predicted damage values are quite consistent with those obtained using the strain-life and the cyclic plastic work approach. It is also of interest that the continuum damage mechanics approach predicts the most highly damaged element to be Element 817 that is directly below Element 857. Element 857 is predicted to be the most highly damaged element using the strain-life and cyclic plastic work methods.

The strain-life and cyclic plastic work approaches to computing damage define the damage as being $D = 1/N_f$. Therefore, in doing numerical calculations, it is possible to compute a damage, D, greater than 1.0. Computing a damage greater 1.0 has sometimes been physically

TABLE 7—*Damage versus number of impacts, continuum damage mechanics approach.*

Impact Number	D, $h = 0.20$	D, $h = 0.10$	Element
1	0.689	0.452	817
2	1.0	0.899	817
3	1.0	1.0	817
4	1.0	1.0	817

explained by stating that failure is predicted to occur in less than one fully reversed cycle. This is probably pushing the experimental data and basis for computing the strain life parameters beyond their predictive capability. However, it is at least some measure of how "over damaged" the material is. For this reason, damage values greater than 1.0 have been left in Tables 4 and 6. On the other hand, continuum damage mechanics does not allow damage values greater than 1.0 and such values are considered undefined. It is assumed that the material completely fails when $D = 1.0$. For this reason, the computations of damage using the continuum damage mechanics approach must stop when $D = 1.0$, and Table 7 reflects this.

Discussion

As expected, using different techniques to compute damage for such a complex process produces different predictions of damage. The fact that the cyclic plastic work predictions can be brought into line with the strain-life predictions by doubling the plastic work computed in the finite element analysis, and then using this doubled W_p in Eq 5 is physically understood. The reason for this behavior stems from the fact that the cyclic plastic work associated with an increment in plastic strain, as computed from Eq 3 assumes the increment in plastic strain was fully reversed. Such a fully reversed increment in plastic strain yields approximately double the plastic work compared to the case where the increment in plastic strain is not reversed, that is, substituting values of W_p computed from Eq 2 directly into Eq 5.

Thinking of this in terms of using the strain life equation to predict damage, such as was done in producing Table 4, it seems that the damage computed in this manner is probably overstated. This is caused by the nature of the loading associated with the present study. The loading is indeed not fully reversed, but rather, approximately half of a fully reversed cycle. Thus, it seems likely that the cyclic plastic work computed from Eq 2 is the more realistic approach to assessing damage induced by repeated impacts of spherical particles on a metal target.

Lemaitre's continuum damage mechanics approach to fatigue using a closure coefficient, $h = 0.20$, produces results that agree well with the strain-life approach and the cyclic plastic work approach when the computed W_p is doubled. This agreement indicates that damage prediction can be reliably reproduced using any of the preceding techniques, providing that one treats the cyclic plastic work in the manner discussed here (doubling W_p), even though from the previous discussion this may lead to overstating the damage. If treating the increment in plastic strain as fully reversed is founded in experimental fact, then the preceding approaches to computing the damage associated with the complex impact process studied here are all in agreement.

Conclusions

The analyses presented here indicate that use of a nonlinear, dynamic, finite element procedure can accurately predict the response of a target material subjected to single normal impacts. Comparisons of crater dimensions from the finite element results and the experimental results of Sundararajan [*14*] are considered very good.

It is also concluded that equivalent measures of damage can be predicted with three different approaches based upon strain life, cyclic plastic work, and continuum damage mechanics. This is important in providing confidence in computed results. It is worth noting, however, that computing cyclic plastic work by a procedure that does not assume fully-reversed loading is probably the most realistic approach to damage calculation. From a practical perspective, the cyclic plastic work and continuum damage mechanics approaches will be much easier to apply than the strain life approach in three-dimensional analyses. The strain life approach discussed

here turns out to be very computationally intensive because of the repetitive transformations needed to compute damage in every conceivable plane for each element.

As briefly mentioned earlier, future work associated with studying the damage caused by erosion will eventually involve three-dimensional modeling of impacts that are noncoincident and spatially located based upon stochastic considerations. The techniques developed herein provide a framework within which one can predict damage for such processes. It is hoped that this ability to predict the temporal and spatial growth of the damage field will eventually allow analytical predictions of material removal rates under erosive conditions.

Acknowledgments

This research was performed for the Electric Power Research Institute (EPRI) under Contract No. WO8042-02. We are grateful for that support and for numerous discussions about erosion with Dr. J. Stringer, the EPRI project manager. Thanks are also due to Dr. D. O. Harris of Engineering Mechanics Technology for critical suggestions and valuable guidance.

References

[1] Ruff, A. W. and Wiederhorn, S. M., "Erosion by Solid Particle Impact," *Treatise on Materials Science and Technology, Vol. 16, Erosion*, C. M. Preece, Ed., Academic Press, New York, 1979, pp. 69–126.

[2] Shewmon, P. and Sundararajan, G., "The Erosion of Metals," *Annual Review of Materials Science*, Vol. 13, 1983, pp. 301–318.

[3] Field, J. E. and Hutchings, I. M., "Surface Response to Impact," *Materials at High Strain Rates*, T. Z. Blazynski, Ed., Elsevier Applied Science, New York, 1987, pp. 243–293.

[4] Finnie, I., "Some Reflections on the Past and Future of Erosion," *Wear*, Vols. 186–187, 1995, pp. 1–10.

[5] Rickerby, D. G. and Macmillan, N. H., "The Erosion of Aluminum by Solid Particle Impingement at Normal Incidence," *Wear*, Vol. 60, 1980, pp. 369–382.

[6] Follansbee, P. S., Sinclair, G. B., and Williams, J. C., "Modelling of Low Velocity Particulate Erosion in Ductile Materials by Spherical Particles," *Wear*, Vol. 74, 1981–1982, pp. 107–122.

[7] Mamoun, M. M., "Analytical Models for the Erosive-Corrosive Wear Process," Materials Science Division, *Coal Technology Quarterly Reports*, ANL Technical Report XX-2 through XX-5, Appendix I, Argonne National Laboratory, 1975.

[8] Richman, R. H. and McNaughton, W. P., "Fatigue Damage in Erosive Wear," *Proceedings*, Morris E. Fine Symposium, P. L. Liaw et al., Eds., The Minerals, Metals & Materials Society, Warrendale, PA 1991, pp. 383–397.

[9] Follansbee, P. S. and Sinclair, G. B., "Quasi-Static Normal Indentation of an Elasto-Plastic Half-Space by a Rigid Sphere–I. Analysis," *International Journal of Solids Structures*, Vol. 20, 1984, pp. 81–91.

[10] Sinclair, G. B., Follansbee, P. S., and Johnson, K. L., "Quasi-Static Normal Indentation of an Elasto-Plastic Half-Space by a Rigid Sphere–II. Results," *International Journal of Solids Structures*, Vol. 21, 1985, pp. 865–888.

[11] Bhargava, V., Hahn, G. T., and Rubin, C. A., "An Elastic-Plastic Finite Element Model of Rolling Contact, Part 2: Analyses of Repeated Contacts, *Journal of Applied Mechanics*, Vol. 52, 1985, p. 75.

[12] Hahn, G. T., Bhargava, V., Yoshimura, H., and Rubin, C., "Analysis of Rolling Contact Fatigue and Fracture," *Advances in Fracture Research*, S. R. Valluri et al., Eds., Pergamon Press, Oxford, 1985, pp. 295–316.

[13] McNaughton, W. P., Richman, R. H., and Beaupre, G. S., "Strain History and Hysteresis Effects for Elastic-Plastic Materials Subject to Cyclic Contacts," *Philosophical Magazine A*, Vol. 65, 1992, pp. 531–549.

[14] Sundararajan, G., "The Nature of Plastic Deformation During Single Impact and its Relevance to Solid Particle Erosion," Ph.D. thesis, The Ohio State University, Columbus, OH, 1981.

[15] Hallquist, J. O., "User's Manual for DYNA2D—An Explicit Two-Dimensional Hydrodynamic Finite Element Code," UCID-18756, Rev. 3, Lawrence Livermore National Laboratory, Livermore, CA, 1988.

[16] Engelmann, B., "NIKE2D—A Nonlinear, Implicit, Two-Dimensional Finite Element Code for Solid Mechanics," UCRL-MA-105413, Lawrence Livermore National Laboratory, Livermore, CA, 1991.
[17] Kandil, F. A., Brown, M. W., Miller, K. J., "Biaxial Low-Cycle Fatigue of 316 Stainless Steel at Elevated Temperatures," *Mechanical Behavior and Nuclear Applications of Stainless Steel at Elevated Temperatures*, Metals Society, London, 1982, pp. 203–210.
[18] Socie, D. F., Kurath, P., and Koch, J., *Proceedings*, Second International Symposium on Multiaxial Fatigue, Sheffield, UK, 1985.
[19] Fuchs, H. O. and Stephens, R. I., *Metal Fatigue in Engineering*, Wiley, New York, 1980.
[20] Morrow, J., "Cyclic Plastic Strain Energy and Fatigue of Metals," *ASTM STP 378*, American Society for Testing and Materials, Philadelphia, 1965.
[21] Garud, Y. S., "A New Approach to the Evaluation of Fatigue Under Multiaxial Loadings," *Journal of Engineering Materials and Technology*, Vol. 103, April 1981.
[22] Malvern, L. E., *Introduction to the Mechanics of a Continuous Medium*, Prentice-Hall Inc., New York, 1969.
[23] Lemaitre, J., "Formulation and Identification of Damage Kinetic Equations," *Continuum Damage Mechanics Theory and Applications*, D. Krajcinovic and J. Lemaitre, Eds., Springer-Verlag, Berlin, 1987.

Dong-Zhi Sun[1] *and Winfried Schmitt*[1]

Assessment of a Semielliptical Crack in the Interface Between Ferritic and Austenitic Material on the Basis of the Gurson Model

REFERENCE: Sun, D.-Z. and Schmitt, W., **"Assessment of a Semielliptical Crack in the Interface Between Ferritic and Austenitic Material on the Basis of the Gurson Model,"** *Applications of Continuum Damage Mechanics to Fatigue and Fracture, ASTM STP 1315*, D. L. McDowell, Ed., American Society for Testing and Materials, 1997, pp. 200–215.

ABSTRACT: In safety analyses of nuclear reactor pressure vessels, hypothetical cracks are often postulated in the ferritic base material beneath the austenitic cladding that is used to protect against corrosion. The criticality of the hypothetical cracks is strongly influenced by the integrity of the cladding. If the cladding is intact, the crack tip loading is significantly reduced compared with the case where the cladding is assumed to be broken. The assessment of the load-carrying capacity of such a cladding cannot be done on the basis of the *J*-integral concept since its application is problematic at the interface of two materials and steep gradients in the material properties in the heat-affected zone cannot be characterized by fracture mechanics tests meaningfully. Moreover, the shape of cracks is usually assumed as semielliptical and the conventional *J*-concept has to be modified to take into account the effect of the constraint, changing along the crack front, on the crack resistance behavior. To avoid these problems, the behavior of a flaw in the interface between ferritic and austenitic material has been analyzed by a micromechanical material model based on the Gurson flow function.

A three-point-bend specimen consisting of a ferritic block with an austenitic cladding and a semielliptical crack in the ferritic base material beneath the cladding was tested and evaluated. The global (that is, load versus displacement curve) and local (that is, ductile crack extension in ferrite and austenite) behaviors of this specimen were predicted by means of two- and three-dimensional finite element analyses with the Gurson parameters determined for different material zones. The material characterization was done by utilizing subsized tension tests with improved evaluation and fracture mechanics tests with precracked Charpy-type specimens.

KEYWORDS: micromechanical modeling, ductile fracture, Gurson model, finite element method, austenitic cladding, semielliptical crack, subsized specimens, continuum damage mechanics, cracking, fracture (materials)

Nuclear reactor pressure vessels made from ferritic steel usually of the type ASTM A 508 Cl 2 or Cl 3 have an austenitic cladding layer on the inner surface for corrosion protection. Beneath this cladding, there is a small region where the capability of nondestructive examination to detect cracks might be reduced. Therefore, in safety analyses, hypothetical cracks are postulated for just that small region. The prediction of the initiation and propagation behavior of those cracks into the ferritic vessel wall depends on whether the cladding remains intact. The assessment of the integrity of the cladding under these circumstances, however, is complicated, because at the boundary of two materials the *J*-integral concept is not applicable without further modifications, and because steep gradients in the material properties have to be taken into account.

[1] Senior scientist and department head, respectively, Fraunhofer-Institute für Werkstoffmechanik, D-79108 Freiburg, Germany.

In contrast to the *J*-integral concepts, micromechanical material models can be employed to assess the initiation and propagation behavior of a crack at the interface of two different materials, like ferrite and austenite, with different properties melted together. Micromechanical models are based on the physical understanding of microscopic processes of ductile fracture that are characterized by three phases: void nucleation, growth, and coalescence [*1*]. Gurson [*2*] derived a plastic potential for porous materials in which a scalar internal variable, the void volume fraction, f, was used to quantify an averaged effect of voids on the yielding behavior. Needleman and Tvergaard [*3*] introduced an empirical modification of Gurson's yield function to model the final stage of void growth, void coalescence, and developed evolution equations for the internal variable to take void nucleation into account. The modified Gurson model has been applied successfully to predict fracture behavior of notched tensile specimens [*3,4*] and cracked specimens [*5,6*]. Sun et al. [*6–8*] found that both global and local behavior of different specimens under various loading conditions can be properly simulated with one set of Gurson parameters that may be determined by testing and modeling simple specimens. Similar results were also found by Xia et al. [*9*] and Klingbeil et al. [*10*]. Rousselier [*11*] established another material model for ductile fracture as an alternative to the Gurson model. Since the difference between the Rousselier model and the Gurson model in description of the influence of stress triaxiality on void growth is negligible, the Rousselier model could be also successful applied to predict the geometry dependence of crack resistance curves of materials [*12*].

Due to the transferability of micromechanical parameters between different geometries and loading situations, the modified Gurson model has been used to extend the fracture mechanics database of an irradiated weld material [*13*]. This model can also be applied to calculate ductile crack extension preceding cleavage rupture in the brittle-to-ductile transition regime and to estimate the probability of cleavage fracture based on the Weibull concept [*14*]. The aim of this work is to demonstrate that it is possible to assess the behavior of a subclad crack located in a regime with steep property gradients based on the modified Gurson model.

Micromechanical Model and It's Verification

The Modified Gurson Model

To take the interaction of voids into account and to model void coalescence, Tvergaard [*15*] modified the Gurson's plastic potential by introducing the values, q_1 and f^*. The modified Gurson's plastic potential is given by

$$\Phi = \frac{3\sigma'_{ij}\sigma'_{ij}}{2\sigma_m^2} + 2q_1 f^* \cosh\left(\frac{\sigma_{kk}}{2\sigma_m}\right) - 1 - (q_1 f^*)^2 = 0 \tag{1}$$

with

$$f^* = \begin{cases} f & \text{for } f \le f_c \\ f_c + \dfrac{f_u^* - f_c}{f_f - f_c} \cdot (f - f_c) & \text{for } f > f_c \end{cases} \tag{2}$$

where σ_{ij} and σ'_{ij} are the macroscopic Cauchy stress and its deviator, respectively; and σ_m is the actual flow stress of the matrix material. The parameter, q_1, holds for an earlier loss of the stress carrying capability of the material as in the Gurson original yield function. The modified void volume fraction, f^*, is introduced to describe the coalescence of voids that occurs after a critical void volume fraction, f_c, is reached. The material fully loses the stress carrying capa-

bility when f reaches the final value of f_f. The variable, f^*, is equal to $f_u^* = 1/q_1$ at $f = f_f$. The evolution equation for f consists of two terms describing void nucleation and growth

$$\dot{f} = \dot{f}_{\text{nucl}} + \dot{f}_{\text{growth}} \tag{3}$$

The process of void nucleation is usually described by a formula based on a normal distribution [*3,5*].

Three-Dimensional Unit Cell Calculations

Micromechanical models derived analytically, for example, the modified Gurson model, can be verified by cell model calculations if no void nucleation is considered. The cell model calculations start from the assumption that the solid consists of a periodic assemblage of unit cells. Every cell contains a spherical hole in its center. Due to the periodic array of the cells, it is sufficient to simulate a representative unit cell by using appropriate boundary conditions. Koplic and Needleman [*16*] investigated the influence of stress triaxiality on the rate of void growth by means of axisymmetric computations of cylindrical unit cells and compared the results of the cell calculations with the predictions of the modified Gurson model. Since an assemblage of cylindrical cells cannot fill the space continuously and the stress ratios applied to these cells cannot be arbitrarily changed in all three directions, some three-dimensional cell calculations have been performed [*17–19*]. However, in all works mentioned earlier, a cubic periodical array of initially spherical voids is assumed for the cell calculations and it represents only one possibility of idealized spatial arrangements of voids. Of course, in real structural materials, voids or void-nucleating sites are located rather irregularly.

Recently, Kuna and Sun [*20*] have analyzed the influence of the spatial arrangement of voids on the mesoscopic deformation response and the void growth of the unit cells for various stress triaxialities. Three different void arrangements, cubic primitive array, body-centered cubic array, and hexagonal array, were considered in three-dimensional unit cell calculations (Fig. 1). Due to symmetry, only ⅛ of the unit cell had to be discretized for cubic primitive array and body-centered array. To change the stress ratios in all three axial directions, higher symmetry properties were not utilized. Since all symmetry conditions were used for the hexagonal void arrangement, only 1/24 of the cell had to be generated. Each calculation of the cell models was carried out by keeping a prescribed stress triaxiality constant throughout the loading history.

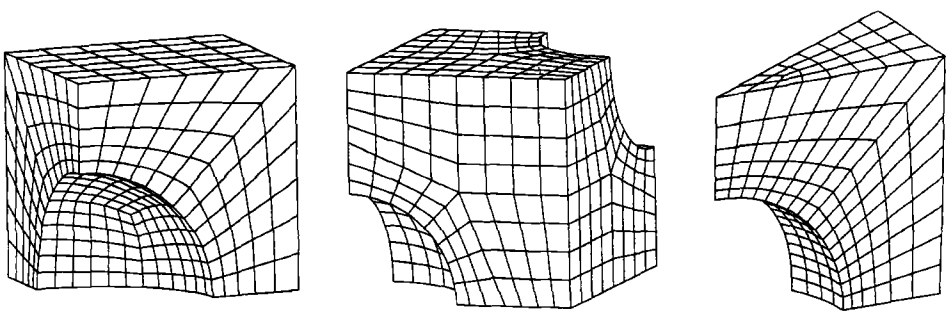

FIG. 1—*Finite element meshes for three different unit cells models:* (a) *⅛ cubic primitive cell,* (b) *⅛ cubic body centered cell, and* (c) *1/24 hexagonal cell.*

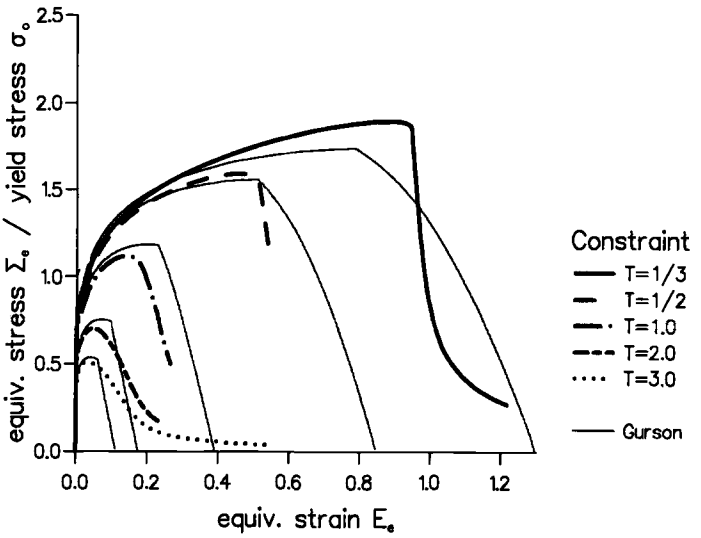

FIG. 2—*Mesoscopic response of the cubic primitive cell model for various values of triaxiality compared with approximations by the modified Gurson model.*

Comparing the results of the cell model calculations, it was found that the type of void arrangement affects only weakly the deformation behavior, whereas the maximum load and mechanism of plastic collapse are strongly influenced. Consequently, different sets of the Gurson parameters (f_c, f_f, and q_1) were obtained by fitting the cell-model results for different void distributions [*20*]. An interesting result is that for each void arrangement one may find one set of Gurson parameters with which the modified Gurson can predict the deformation and the collapse behavior of the corresponding cell for different values of triaxiality. For the cubic primitive arrangement, Fig. 2 shows the computed mesoscopic effective stress versus the effective strain curves for a variation of stress triaxiality from $T = \frac{1}{3}$ up to $T = 3.0$. The semianalytical Gurson solutions added in Fig. 2 as thin lines were achieved by using the parameters that were fitted to the results of finite element cell models [*20*]. Considering the large variation of stress triaxiality and the high initial void volume fraction ($f_0 = 0.114$), the agreement between the unit cell calculations and the Gurson predictions is relatively good. This implies that the modified Gurson model describes the constraint effect of the void growth very reasonably, and its parameters can be transferred between specimens with different constraints.

Characterizaton of Materials in Different Regions

The test component was made from a block of a ferritic steel, German Designation 20 MnMoNi 5 5. At the surface of the block, an initial slit was produced by spark eroding and subsequently propagated by fatigue loading. The surface of the block was then removed up to the depth of the originally eroded slit, and the crack was closed by a thin Manna Metal Arc (MMA) welding layer. After grinding smooth, a two-layer band cladding with a total thickness of 7 mm was applied. The dimensions of the test piece were 900 by 120 by (60 + 7) mm^3. The semielliptical subclad crack was 5 mm deep and 30 mm long. Figure 3 shows a schematic view of the cross section of the test piece. A second similar cladded block was available for material characterization.

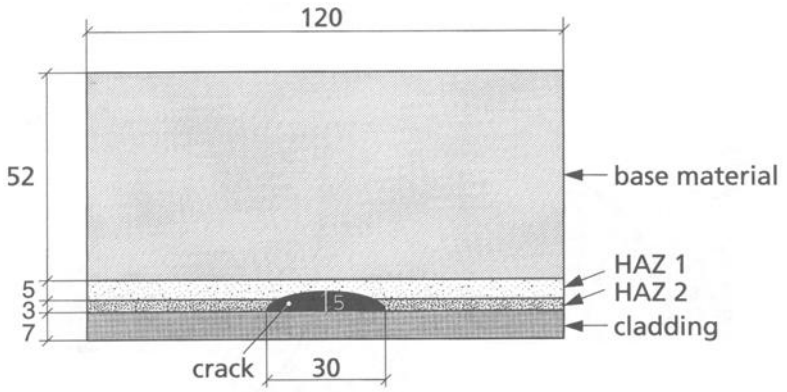

FIG. 3—*Schematic view of cross section of the test piece.*

In order to determine mechanical and micromechanical parameters for the base material, the heat-affected zones, and the cladding two actions were taken:

1. determination of stress-strain curves and the modified Gurson model parameters from subsized smooth round tension specimens with diameter of 2 mm, and
2. verification of these parameters and determination of the characteristic material length, l_c, by testing and simulating SENB-(10 × 10)-type fracture mechanics specimens in which the front of the fatigue crack was located in the material zone to be characterized.

Evaluation of Tension Tests

To quantify the large gradients in the material properties in the region where the crack is located, the tensile specimens must be as small as possible. Therefore, in a preliminary study with ferritic base material, round and quadratic specimens with 2 mm and 10 mm diameter or width and rectangular specimens with dimensions 1 by 6 mm^2 were tested and analyzed in order to find suitable specimen shapes and sizes. Within the unavoidable material scatter, all curves fall nicely together and no size effect is found [*21*]. For the determination of true stress versus true strain curves, not only the actual area of the necking cross section but also the curvature radius of the necking part must be known to take account for effects of triaxiality in the necking region (Bridgman correction). The experimental determination of these quantities is much more difficult for specimens with quadratic or rectangular cross sections than for round bars. Therefore, only round specimens with 2-mm diameter were used to determine the parameters of the cladded test block.

The experiments were conducted at room temperature, and the necking profile was measured optically from photographs taken during the tests. Figure 4 shows the variation of yield stress, σ_y, and reduction of area, Z, over the thickness of the block. As expected, the yield stresses obtained for the austenitic cladding lie below those of the heat-affected zone and also below the base material. It is remarkable that the ductility of the material in a narrow zone at the fusion line is much lower than those of the ferritic base material and the austenitic cladding.

A total of seven tests representing different material zones were analyzed numerically in order to optimize the stress-strain curves and to determine the Gurson parameters. Based on earlier results, it was assumed that no initial voids were present ($f_0 = 0$). The parameters for strain-controlled void formation were chosen according to Needleman and Tvergaard [*3*]: $\varepsilon_n = 0.3$, $s_n = 0.1$. The volume fraction of void-forming particles, f_n, was fixed such that the resulting critical void volume fraction, f_c, was around 3 to 6%, which lay in the range of the

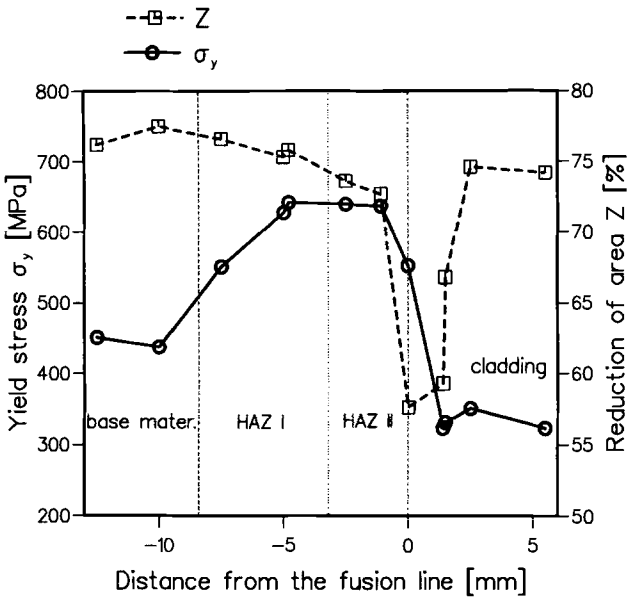

FIG. 4—*Yield stress and reduction of area over the thickness of the test piece.*

measured values for this class of materials. Finally, the f_c-value for each material zone was determined by fitting the sharp kink in the calculated load versus deformation curve to the experimental data at this point. The sudden drop of the load at the kink point is caused by the onset of macroscopic fracture in the specimen center. Figure 5 shows as an example the

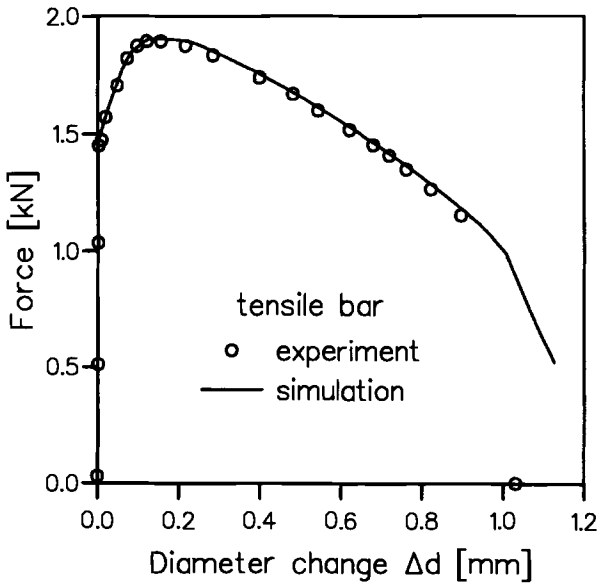

FIG. 5—*Measured and calculated force versus diameter-change curves for a tensile bar of the base material.*

TABLE 1—*Micromechanical material parameters of different material zones.*

Material Zone	Specimen Number (Fig. 5)	Gurson Parameters		
		f_n	f_c	f_f
Base material	AY 519	0.002	0.06	0.212
Base material	AY 518	0.002	0.06	0.212
HAZ 1	AY 517	0.002	0.06	0.212
HAZ 1	AY 516	0.002	0.06	0.212
HAZ 2	AY 515	0.002	0.04	0.197
HAZ 2	AY 502	0.002	0.04	0.197
Cladding	AY 507	0.012	0.03	0.189

measured and calculated force versus diameter change curves for specimen AY519 (base material). Table 1 compiles the micromechanical material parameters for the different zones. The values of f_f were calculated from f_c (Eq 2) by keeping the factor for the description of void coalescence constant, $(f_u^* - f_c)/(f_f - f_c) = 4$; and $q_1 = 1.5$ and $f_u^* = 0.99/q_1 = 0.66$ were used for all material zones.

Simulation of Fracture Mechanics Tests

An additional material parameter, the characteristic distance, l_c, is required for the application of micromechanical models to cracked specimens or structures, as it is not sufficient for crack initiation to reach a criterion at one material point but that a minimum volume of material should be involved. The characteristic length, l_c, is related to the microstructure (inclusion spacing). Since there is no size-scale in the Gurson model, many attempts have been made to introduce the length parameter, l_c, into the Gurson model [*7,9,11,22*]. Here, we used a simple but practical concept to solve this problem. The mesh size at the crack tip was varied so that the measured load versus displacement curve of a fracture mechanics specimen was well reproduced by the Gurson model with the parameters obtained from tension tests. This implied that the l_c-value was identified with the element length at the crack tip. Generally, the f_c and l_c pair can be considered material constants that allow the transfer from tensile specimens to fracture mechanics specimens [*7,8,22*].

Four three-point-bend SENB (10 × 10) specimens taken from different material zones were tested and simulated in order to determine the l_c-values and to verify the transferability of the Gurson material parameters obtained from tension tests. The specimens were side-grooved (10% each side) and have an initial crack length of 5 mm ($a/W = 0.5$). Each specimen was so fabricated that the crack propagated in the direction of the base material and the front of the fatigue crack was located as exactly as possible in the material zone to be characterized. As an example, the SENB specimen for the Heat-Affected Zone II (HAZ 2) is schematically presented in Fig. 6. During the $J_R(\Delta a)$-tests, the potential drop method was used to determine the actual crack lengths. In addition to the investigations with SENB (10 × 10) specimens, a compact specimen, CT25, from base material was tested and simulated.

According to previous experience with the 22 NiMoCr 3 7 material, the crack tip region of SENB and CT specimens was modeled with element sizes of 0.1 by 0.06 mm^2. The material properties for the Gurson model were identical with those obtained from the numerical simulations of the tensile specimens. The different material zones of the small SENB-specimens were represented by different material properties in different mesh zones. All fracture mechanics specimens were side-grooved (20%), thus plane-strain models with isoparametric eight-noded elements and (2 × 2) integration scheme were used for the numerical simulations.

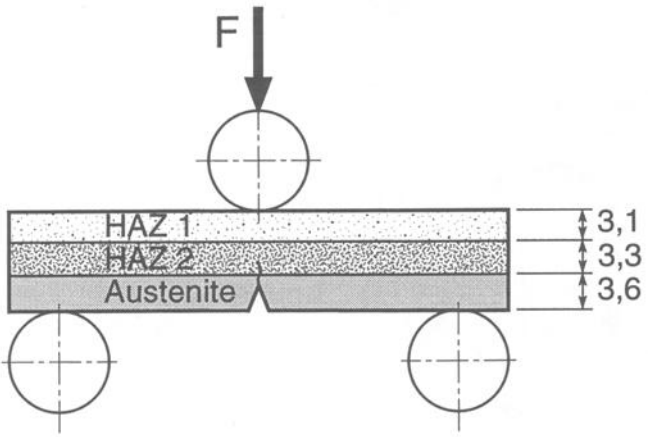

FIG. 6—*Width of different material zones in the SENB-specimen for HAZ II.*

Figure 7 compares the measured and calculated force-displacement curves of the compact specimen of the base material. Figure 8 shows the corresponding J_R-curves. In the numerical models, the crack propagation is identified with the extension of the damage zone along the ligament where the void volume fraction exceeds f_f and where the stresses approach zero. The good agreement with the experimentally determined crack propagation confirms the choice of the element length (0.1 mm) and the transferability of the Gurson parameters from tensile to fracture mechanics specimens. For the austenitic cladding material, an element length of 0.05 mm was determined by modeling the SENB specimen.

In order to minimize the influence of friction, the tests with SENB (10 × 10)-type specimens were performed using supporting rolls that were not fixed and free to rotate. This setup caused

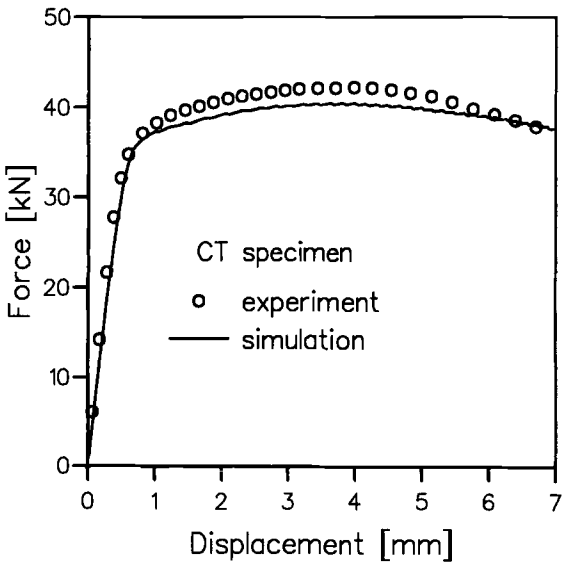

FIG. 7—*Measured and calculated force versus displacement curves for a CT specimen of the base material.*

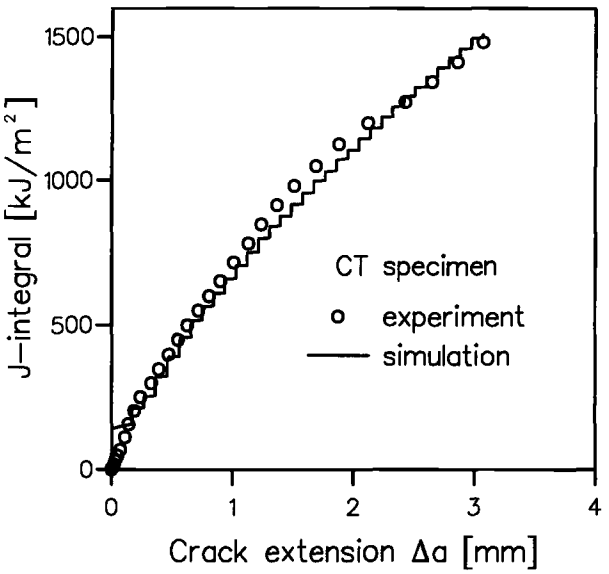

FIG. 8—*Measured and calculated* J *resistance curves for a CT specimen of the base material.*

unexpected difficulties for the numerical simulations. Figure 9 shows the deformed mesh for such a specimen and setup. While the support was modeled as a rigid surface, the rolls were modeled with volume elements with contact surfaces between rolls and specimen. The loading hammer was introduced with truss elements having gaps of different size according to the shape of the hammer. During the experiments, small plates of hardened steel were put between specimen and supporting rolls to avoid plastic indentation on the specimen surfaces. The influence of the hardened steel plates was modeled by increasing the yield strength of the respective elements in the specimen.

Assuming a realistic friction coefficient, $\mu = 0.2$, between rolls, support, and specimen, this model gave convergent results only up to about maximum load, see Fig. 10, where the measured and calculated force versus displacement curves are compared. Beyond that point (arrow), convergence could be regained by increasing the friction coefficient to $\mu = 0.3$. It is understandable that a higher friction force stabilizes the numerical model as it makes the supporting rolls more difficult to slip away from the system in an unstable manner. However, now the calculated force deviates significantly from the measured one. Therefore, measured and calculated *J*-resistance curves can only be compared for small amounts of crack extension, Fig. 11. The reasonable agreement confirms the choice of the material parameters. Keeping in mind that for the simulation of the component test three-dimensional modeling would be required, it was decided to change the test setup of the component test and to fix the rolls.

Prediction of the Crack Behavior in the Component

Experiment and Evaluation

The cladded specimen was tested at room temperature in a three-point-bend setup (Fig. 12) with fixed supports in a servohydraulic test machine with a load capacity of 1.6 MN. The bending displacement was measured with an inductive displacement gage. Strain gages were applied to the specimen surface directly and was monitored with a direct-current potential drop

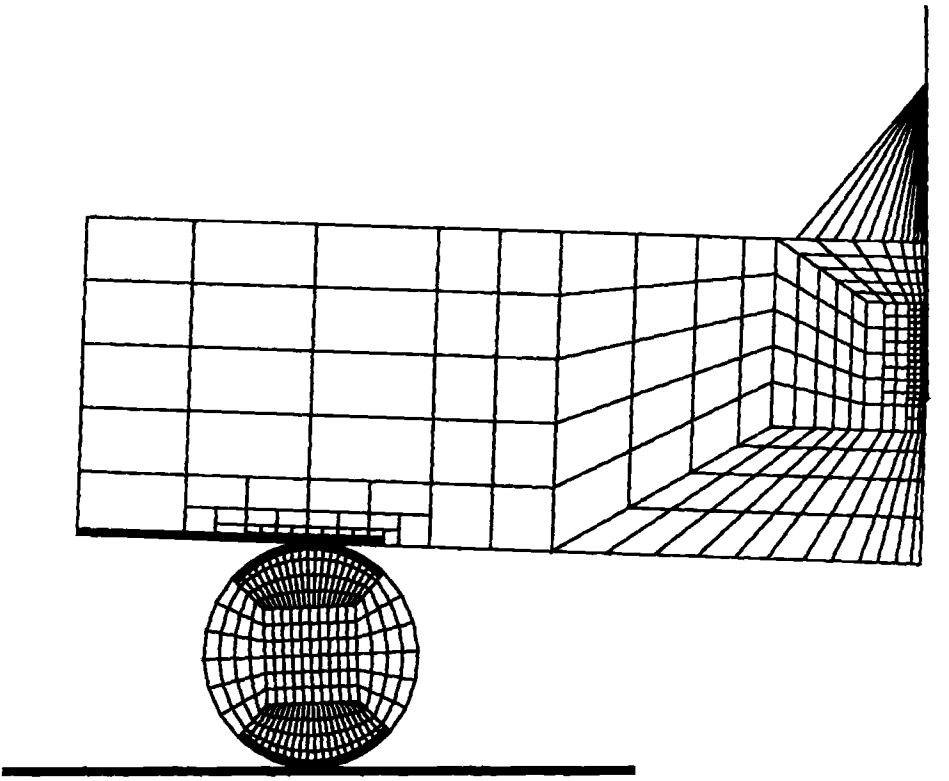

FIG. 9—*Deformed finite element mesh for a SENB (10 × 10) specimen.*

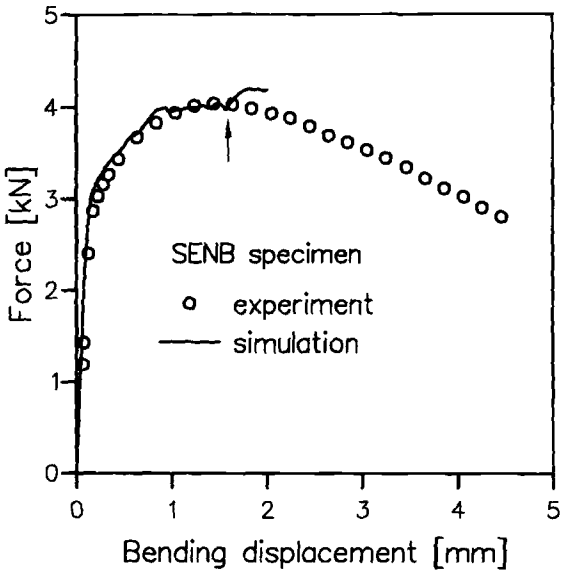

FIG. 10—*Measured and calculated force versus bending displacement curves for a SENB (10 × 10) specimen of the base material.*

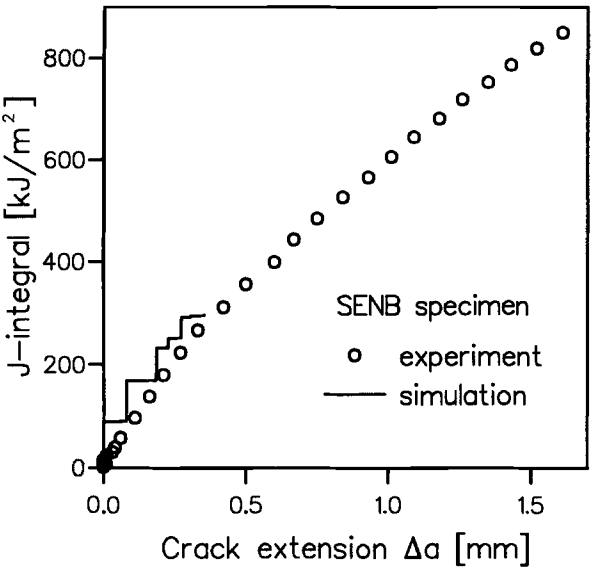

FIG. 11—*Measured and calculated J-resistance curves for a SENB (10 × 10) specimen of the base material.*

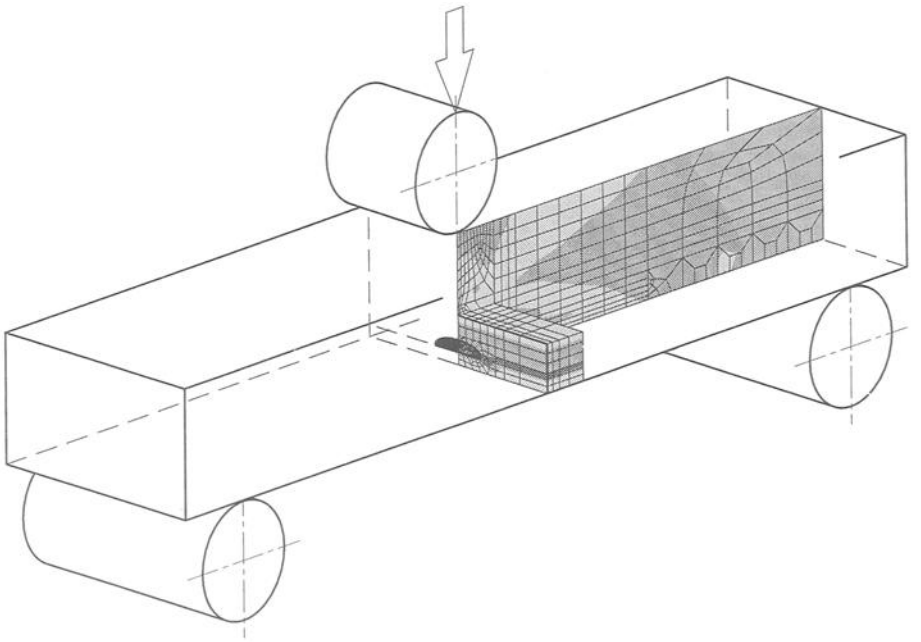

FIG. 12—*Setup of component test, geometry of cladded specimen and, two-dimensional/three-dimensional combined finite element model.*

(DCPD) arrangement at a constant current of 60 A. The potential drop was measured on the cladded specimen surface above the crack with a probe distance of 40 mm, catching predominantly crack extension in the cladding. For a better resolution of crack extension towards the base material, two additional probes were placed on the specimen sides directly beneath the cladding [*21*]. Before and after the test, the crack was sized by ultrasound.

Figure 13 shows the measured force versus bending displacement curve as a solid line. Small load drops can be seen at displacements of about 3, 8, and 13 mm that were accompanied by audible signals probably caused by the specimen sliding over the supports. At a bending displacement of about 25 mm, the test was terminated and the specimen unloaded. Figure 14 shows the fracture surface after severing the specimen by fatigue. Starting from the initial fatigue crack with dimensions of 5.4 by 31 mm^2, ductile crack propagation, predominantly into the cladding, is observed with no lateral extension. On the ferritic side, the crack extended uniformly by about 1.7 mm.

The correlation of the fracture events with signals measured during the test is difficult because the changes are small with respect to the overall dimensions of the specimen. Figure 15 shows the two potential-signals versus bending displacement. Three sections with roughly constant slope are identified: between 3 mm and 6 to 8 mm, between 8 and 15 mm, and between 15 and 24 mm. Experience shows that indications for crack initiation and propagation may be drawn from changes in the slope. The change of slopes at 8 mm is more pronounced in the cladding signal while the change at 15 mm is clearly seen both in the cladding and in the base material signals. The potential signals together with those of strain gage indicate initiation events in the cladding at 3 or 8 mm, and in the ferritic base material at 15 mm bending displacement.

Two-Dimensional and Three-Dimensional Simulations of the Component Test

A schematic view of the specimen and test setup has already been given in Fig. 12. The stress-strain curves and the Gurson parameters of the materials in different zones determined earlier were used for the corresponding elements in the finite element models for the component. Before the test, a two-dimensional calculation was made in order to check different model variants and to give indications for the test results to be expected. In the two-dimensional calculation, the actual semielliptic crack had to be treated as one with two straight crack fronts (embedded crack) through the thickness of the component. Based on previous experience [*8*], a combined plane-strain/plane-stress model was established to compute both the local and the global behaviors correctly. A small region around the crack was modeled in plane strain, the other part in plane stress. The force versus displacement curve predicted by this two-dimensional model has been given in Fig. 13. The calculated damage developments at both crack tips were shown in Fig. 16. The dark areas imposed on the deformed mesh represent the damage zones where the final value of void volume fraction, f_f, is reached. Since the stresses in the damage zone are nearly zero, the length of the damage zone can be defined as the numerical ductile crack extension. According to the two-dimensional model, the crack first initiates at the side of the austenitic cladding and propagates about 1 mm into the cladding before the crack initiation takes place at the side of ferritic base material.

The post-test simulation was done with a combined three-dimensional/two-dimensional model with 1189 three-dimensional elements, 331 two-dimensional elements, and a total of 6690 nodal points as shown in Fig. 12 where the distribution of the effective stress is imposed on the mesh. The mesh refinement in propagation direction around the crack corresponded to the two-dimensional meshes of the pre-test calculations. Due to limited computer capacities, the refined zone around the crack front extended only 1 mm, thus allowing damage and crack

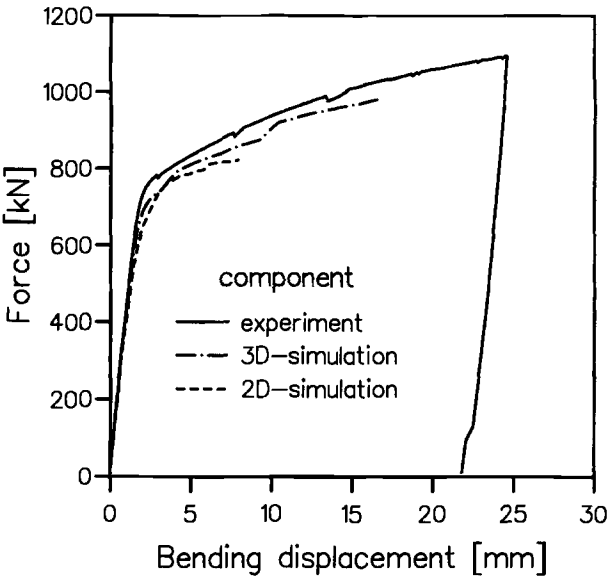

FIG. 13—*Measured and calculated force versus bending displacement curves for the component.*

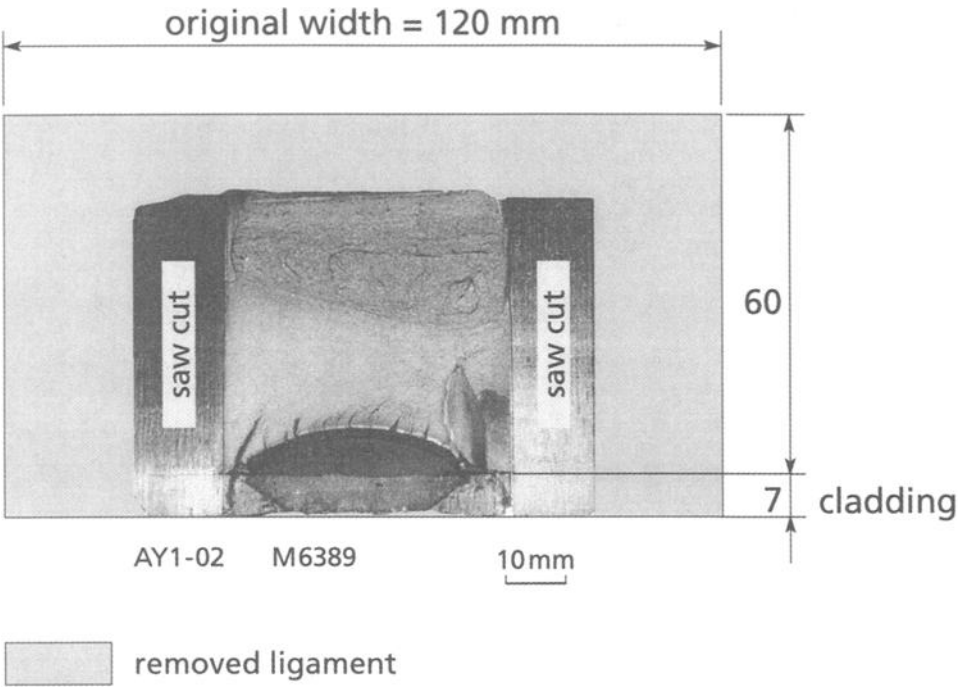

FIG. 14—*Fracture surface of the component.*

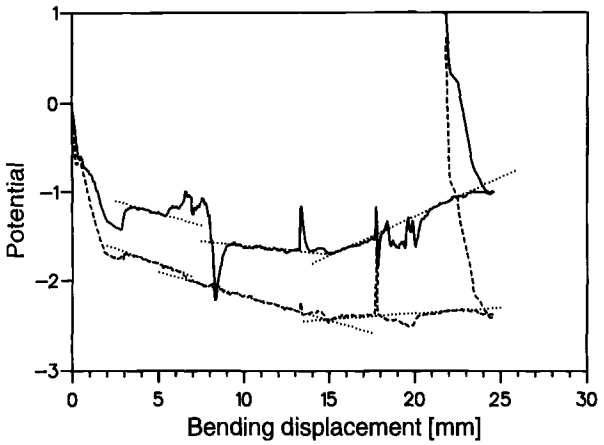

FIG. 15—*Electric potential in austenite and ferritic measured during the component test.*

propagation of only 1 mm. This is the reason why the analysis had to stop at 17-mm bending displacement when in the cladding the crack had extended by 1 mm. The calculated force versus bending displacement curves of the three-dimensional post-test calculations are included in Fig. 13 as well. The three-dimensional curve shows a very good agreement with the measured curve while the two-dimensional simulation increasingly underestimates the measured force.

The crack extensions evaluated at the center plane of the specimen, that is, at the deepest point of the semielliptical crack in the three-dimensional model, are shown in Fig. 17 for the base material and the cladding. The calculations predict crack propagation to begin in the cladding and in the base material at about 3-mm bending displacement. While the crack propagates steadily through the cladding, the crack extension in the base material remains constant at a very small level of about 0.1 mm and accelerates only at a displacement of about 14 mm. These results are in agreement with the experimental findings with indications for initiation and propagation events at 3 and 15 mm also. It should be noted here that at a bending displacement of 3 mm the specimen is already in general yield conditions.

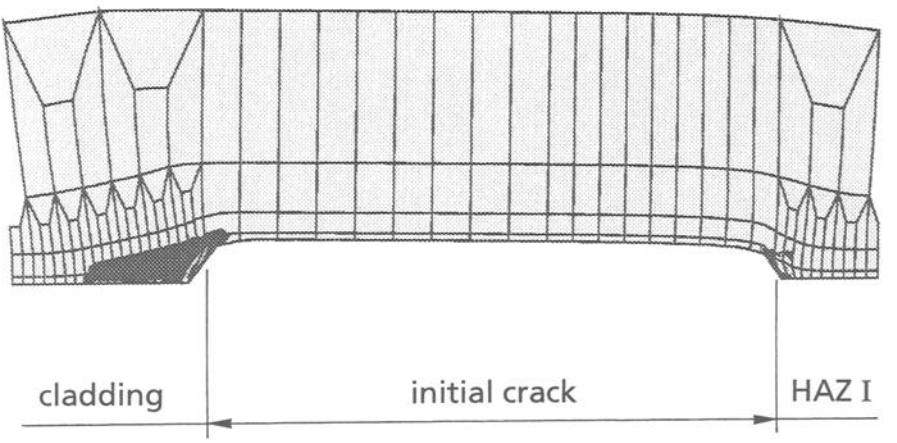

FIG. 16—*Deformed finite element mesh and calculated damage zones at two crack tips.*

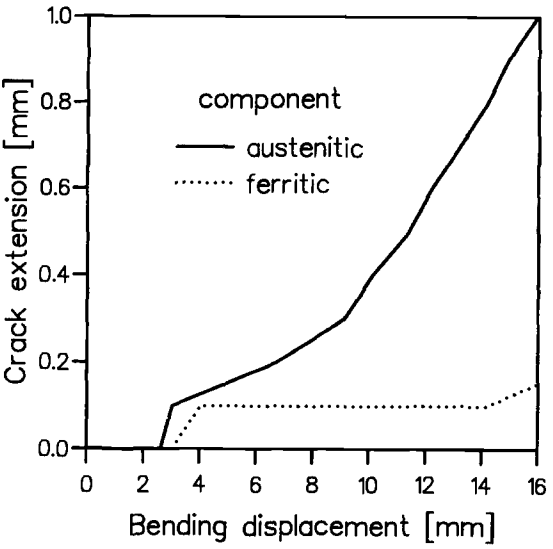

FIG. 17—*Calculated crack extension in austenite and ferrite for the component.*

Conclusions

A correct prediction of the behavior of a crack in the transition region between austenitic cladding and ferritic base material, taking into account gradients in the material properties, is possible by the application of micromechanical material models, like the Gurson model. The situation investigated here is typical for situations to be assessed in safety analyses. Three-dimensional cell calculations were used to verify the Gurson parameters. It turned out that the dependence of void growth and the corresponding deformation response in a porous material on stress triaxiality could be described by the Gurson model using one set of parameters, even for a large amount of porosity.

For the numerical analyses, the determination of the local material properties including toughness behavior was essential, considering the large gradients in the boundary layer. This was achieved through testing and analysis of small tensile specimens, with a diameter of only 2 mm, yielding micromechanical material parameters that are dependent on the distance from the fusion line. The transferability of these Gurson parameters into fracture toughness was confirmed by testing and evaluating SENB (10 × 10)–type specimens. Pre- and post-test simulations of the cladded specimen showed a very good agreement with the experiment. Ductile crack initiation and extensions could be observed only above general yield. Although with increasing load (above general yield), the crack penetrated the cladding layer, crack extension in the ferritic base material was only marginal.

References

[1] Garrison, W. M., Jr. and Moody, N. R., "Ductile Fracture," *Journal of the Physics and Chemistry of Solids*, Vol. 48, 1987, pp. 1035–1074.

[2] Gurson, A. L., "Continuum Theory of Ductile Rupture by Void Nucleation and Growth: Part 1–Yield Criteria and Flow Rules for Porous Ductile Media," *Journal of Engineering Materials and Technology*, Vol. 99, 1977, pp. 2–15.

[3] Needleman, A. and Tvergaard, V., "An Analysis of Ductile Rupture in Notched Bars," *Journal of the Mechanics and Physics of Solids*, Vol. 32, 1984, pp. 461–490.

[4] Sun, D.-Z., Siegele, D., Voss, B., and Schmitt, W., "Application of Local Damage Models to the Numerical Analysis of Ductile Rupture," *Fatigue & Fracture of Engineering for Materials & Structures*, Vol. 12, 1988, pp. 201–212.

[5] Needleman, A. and Tvergaard, V., "An Analysis of Ductile Rupture Modes at a Crack Tip," *Journal of the Mechanics and Physics of Solids*, Vol. 35, 1987, pp. 151–183.

[6] Sun, D.-Z. and Schmitt, W., "Application of Micromechanical Models to the Analysis of Ductile Fracture Resistance Behaviour," *Numerical Methods in Fracture Mechanics*, A. R. Luxmoore and D. R. J. Owen, Eds., Pineridge Press, Swansea, UK, 1990, pp. 275–286.

[7] Sun, D.-Z., Kienzler, R., Voss, B., and Schmitt, W., "Application of Micromechanical Models to the Prediction of Ductile Fracture," *Fracture Mechanics: Twenty-Second Symposium (Volume II), ASTM STP 1131*, S. N. Atluri, J. C. Newman, Jr., I. S. Raju, and J. S. Epstein, Eds., American Society for Testing and Materials, Philadelphia, 1992, pp. 368–378.

[8] Sun, D.-Z., Hönig, A., Böhme, W., and Schmitt, W., "Application of Micromechanical Models to the Analysis of Ductile Fracture Under Dynamic Loading," *Fracture Mechanics: 25th Volume, ASTM STP 1220*, F. Erdogan, Ed., American Society for Testing and Materials, Philadelphia, 1995, pp. 343–357.

[9] Xia, L., Shih, C. F., and Hutchinson, J. W., "A Computational Approach to Ductile Crack Growth Under Large Scale Yielding Conditions," *Journal of the Mechanics and Physics of Solids*, Vol. 43, 1995, pp. 389–413.

[10] Klingbeil, D., Künecke, J., and Schicker, J., "On the Application of Gurson's Model to Various Fracture Mechanics Specimens," Report BAM-1.31 93/3, Federal Institute for Material Research and Testing (BAM), Berlin, 1993.

[11] Rousselier, G., "Ductile Fracture Models and Their Potential on Local Approach of Fracture," *Nuclear Engineering and Design*, Vol. 105, 1987, pp. 97–111.

[12] Lidbury, D. P. G., Sherry, A. H., Bilby, B. A., Howard, I. C., Li, Z. H., and Eripret, C., "Prediction of the First Spinning Cylinder Test Using Continuum Damage Mechanics," *Nuclear Engineering and Design*, Vol. 152, 1994, pp. 1–10.

[13] Schmitt, W., Sun, D.-Z., Böhme, W., and Nagel, G., "Evaluation of Fracture Toughness Based on Results of Instrumented Charpy Tests," *International Journal of Pressure Vessels and Piping*, Vol. 59, 1994, pp. 21–29.

[14] Schmitt, W., Sun, D.-Z., Bernauer, G., and Nagel, G., "New Approaches to Improve the RPV Material Data Base," *Nuclear Engineering and Design*, to be published.

[15] Tvergaard,V., "On Localization in Ductile Materials Containing Spherical Voids," *International Journal of Fracture*, Vol. 18, 1982, pp. 237–252.

[16] Koplic, J. and Needleman, A., "Void Growth and Coalescence in Porous Plastic Solids," *International Journal of Solids Structures*, Vol. 24, 1988, pp. 835–853.

[17] McMeeking, R. M and Hom, C. L., "Finite Element Analysis of Void Growth in Elastic-Plastic Materials," *International Journal of Fracture*, Vol. 42, 1990, pp. 1–19.

[18] Worswick, M. J. and Pick, R. J., "Void Growth and Constitutive Softening in a Periodically Voided Solid," *Journal of the Mechanics and Physics of Solids*, Vol. 38, 1990, pp. 601–625.

[19] Richelsen, A. B. and Tvergaard, V., "Dilatant Plasticity or Upper Bound Estimates for Porous Ductile Solids," *Acta Metallurgica*, Vol. 42, 1994, pp. 2561–2577.

[20] Kuna, M. and Sun, D.-Z., "Three-Dimensional Cell Model Analyses of Void Growth in Ductile Materials," *International Journal of Fracture*, Vol. 81, 1996, pp. 235–258.

[21] Schmitt, W. and Brocks, W., "Analyse und Weiterentwicklung bruchmechanischer Versagenskonzepte," *IWM-Beiricht T 19/94*, Dec. 1994.

[22] Sun, D.-Z. and Hönig, A., "Significance of the Characteristic Length for Micromechanical Modelling of Ductile Fracture," *Localized Damage III, Computer-Aided Assessment and Control*, M. H. Aliabadi, A. Carpinteri, S. Kališky, and D. J. Cartwright, Eds., Computational Mechanics Publications, Southampton, UK, 1994, pp. 287–296.

Mark F. Horstemeyer[1] *and Vera Revelli*[1]

Stress History Dependent Localization and Failure Using Continuum Damage Mechanics Concepts

REFERENCE: Horstemeyer, M. F. and Revelli, V., **"Stress History Dependent Localization and Failure Using Continuum Damage Mechanics Concepts,"** *Applications of Continuum Damage Mechanics to Fatigue and Fracture, ASTM STP 1315*, D. L. McDowell, Ed., American Society for Testing and Materials, 1997, pp. 216–237.

ABSTRACT: Since the notion of damage was introduced by Kachanov and Rabatnov in the late 1950s and early 1960s, the paradigm to better capture the physics of the internal state of a material has been realized in developing macroscale constitutive relationships for monolithic and composite materials. For ductile metals, damage occurs mainly in the form of void nucleation, growth, and coalescence. Localization and failure occur at two different stages in the deformation history and are very much functions of the void (porosity) evolution, which can be interpreted as the damage evolution, and the stress state history. The damage evolution of a polycrystalline metal is fully coupled to the stress history. In this study, different initial material properties are varied in four different boundary value problems to reflect the stress state and deformation history effects. Special attention is paid to three internal state variable evolution equations; one represents scalar damage, and the other two represent isotropic (scalar) hardening and kinematic (tensorial) hardening. Internal state evolution equations that capture history effects are necessary when trying to solve complex boundary value problems. This constitutive framework is embedded into a finite element formulation to solve such boundary value problems. Mesoscale analyses of A356-T6 aluminum under different stress states and initial material states are used to give insight into the void nucleation, growth, and coalescence issues that arise when formulating an internal state porosity evolution rule within a macroscale framework. This work was based on previous studies related to the four boundary value problems. Numerical calculations were performed to compare to 6061-T6 aluminum notch tension tests with different notched radii. The various notch radii induce different levels of stress triaxiality and allow for correlation of different void growth rules. Numerical calculations of forming limit diagrams for 6061-T6 aluminum compared favorably to experimental results. Finally, penetration analyses were performed with 6061-T6 aluminum disks as targets.

KEYWORDS: continuum damage mechanics, internal state variable, localization, failure, finite element method, boundary value problem, cracking, fatigue (materials), fracture (materials)

The mechanical properties of an engineering material depend upon the amount and type of microdefects within its structure. Deformation changes these microstructural features. When deterioration develops, damage is said to have occurred. The terminology of continuum damage mechanics (CDM) emerged when Kachanov [*1*] first introduced a damage variable to describe the microdefect density locally in a creeping material. The notion was that damage could be measured by the volume fraction of voids under creep conditions. Rabatnov [*2*]

[1] Senior members, Technical Staff, Center for Materials and Engineering Sciences, Sandia National Laboratories, Livermore, CA 94551–0969.

furthered this notion with evolution of void density. CDM was developed for fatigue [*3,4*], creep [*5–7*], creep-fatigue interactions [*8,9*], and ductile plastic damage [*10–13*]. CDM has been applied recently to brittle materials [*14,15*] such as concrete [*16,17*] and geomaterials [*18,19*]. In this study, we employ CDM concepts in the context of void-induced damage in ductile metals.

In ductile metals, most of the damage arises from nucleation, growth, and coalescence of voids. Nucleation can occur from either fracture of second-phase particles of decohesion of particles from the matrix material. It can also occur at triple points in a material via grain boundary diffusion [*20,21*]. The voids can grow as the stress triaxiality increases around the newly formed void; void growth can also result from grain boundary diffusion, surface diffusion, slip-dominated large deformation, or a combination of these mechanisms. Many researchers have investigated different aspects of void growth and these are reviewed in Refs *20–22*, from which porosity evolution rules have been used and couched in the context of internal state variable theory.

Because porosity evolution is represented by an internal state variable evolution equation, it must be consistent with an appropriate thermodynamical framework [*23,25*]. Two classes of thermodynamically based constitutive equations have been posed that would include history effects of the microstructure within a material. The first is denoted by the concept of hereditary integrals: that the present state of the material depends on the present values and past history of observable variables. The second is based on the concept that the present state of the material depends only on the present values of observable variables and a set of internal state variables (ISVs) [*26*]. We employ the second approach in this paper. For the sake of conciseness, suffice it to say that porosity evolution must be taken into account by the free energy function or as a dissipative force that can be defined by a pseudo-potential of dissipation.

From the viewpoint of rational thermodynamics [*26*], the ISVs provide the additional information necessary for a rational description of the thermodynamic state of the material. From the viewpoint of thermodynamics of irreversible processes [*27*], the ISVs provide the information required to describe neighboring constrained equilibrium states. Davidson et al. [*28*] and more recently Fremond and Nedjar [*29*] described the details of the irreversible state caused by damage from porosity evolution.

This paper contains a summary of various features that are often included in CDM and ISV frameworks [*30–34*]. The ISV hardening equations and void growth rule are described. Four boundary value problems with different initial conditions are discussed. These problems use the local form of the Cocks-Ashby [*22*] void growth rule while neglecting void nucleation. One example includes an idealized mesoscale analysis of two pre-existing voids and a particle that nucleates a void by fracture or decohesion depending on the stress state. Another example includes analysis of different notch radii experiments. A third example involves analysis of the localization and failure involved with the forming limit diagrams (FLDs). A final example is presented in which a penetrator strikes an aluminum disk. Different initial material properties were examined in the context of porosity evolution. The initial porosity levels and the initial hardening variables were changed to simulate prestrain effects.

Hardening Internal State Variables

The deviatoric inelastic flow rule is that of Bammann [*32,33,35*],

$$\tilde{D}^p = \sqrt{\frac{3}{2}}\, f(T) \sinh\left[\frac{\sqrt{3J_2'} - \{R + Y(T)\}\{1 - \phi_{\text{growth}}\}}{V(T)\{1 - \phi_{\text{growth}}\}}\right] \frac{\tilde{\sigma}' - \frac{2}{3}\tilde{\alpha}'}{\| \tilde{\sigma}' - \frac{2}{3}\tilde{\alpha}' \|} \tag{1}$$

where

J_2' = second invariant of deviatoric overstress,
$\tilde{\sigma}'$ = deviatoric part of the Cauchy stress,
$\tilde{\alpha}'$ = deviatoric part of the kinematic hardening internal state variable,
R = isotropic hardening internal state variable, and
$f(T)$, $V(T)$, and $Y(T)$ = temperature dependent functions related to yielding [*33,35*].

Each of the two hardening internal state evolution equations represent effects of populations of dislocations in a hardening-recovery format. The kinematic hardening captures some of the directional hardening effects during inelastic deformation by shifting the yield surface center. The kinematic hardening evolution is given by

$$\dot{\tilde{\alpha}} = h(T)\tilde{D}^p - \left[\sqrt{\frac{2}{3}}\, r_d(T) \parallel \tilde{D}^p \parallel + r_s(T)\right] \parallel \tilde{\alpha} \parallel \tilde{\alpha} \tag{2}$$

The evolution of the isotropic hardening variable, R, reflecting the effect of the gross dislocation density on hardening, is given by

$$\dot{R} = H(T) \parallel \tilde{D}^p \parallel - \left[\sqrt{\frac{2}{3}}\, R_d(T) \parallel \tilde{D}^p \parallel + R_s(T)\right] R^2 \tag{3}$$

where

$h(T)$ and $H(T)$ = direct hardening moduli,
$r_s(T)$ and $R_s(T)$ = scalar functions describing the diffusion-controlled static or thermal recovery, and
$r_d(T)$ and $R_d(T)$ = functions describing dynamic recovery.

Void (Porosity) Relationships

Void growth rules have been studied by many researchers, but few have been used in solving boundary value problems with finite element codes. With finite element models, an initial porosity level is assumed in order to initialize the void growth rule. The Cocks-Ashby void growth rule has been used successfully in macroscale boundary value problems [*35–38*]. This void growth rule was based on experimental creep data in which void growth was controlled by boundary diffusion and power law creep. At low stresses, voids are generally confined to grain boundaries in wrought materials or in dendritic arms in cast metals, where the boundary controls the growth mechanism. As voids become larger, the growth mechanism changes to power law creep. This rule is employed in our finite deformation plasticity problems because the mechanism for void growth is the same. The Cocks-Ashby rule is given by

$$\dot{\phi}_{\text{growth}} = \sqrt{\frac{2}{3}} \sinh\left[\frac{2(2n-1)I_1}{3(2n+1)\sqrt{3J_2}}\right]\left[\frac{1}{(1-\phi_{\text{growth}})^n} - (1-\phi_{\text{growth}})\right] \parallel \tilde{D}^p \parallel \tag{4}$$

where n is determined by notch tensile experiments, and I_1 is the first invariant of stress. We note that other functions for the void growth rule can be implemented into this framework but have not been exercised, for example, Cocks [*39*].

Numerical Calculations

Four problems are discussed in this section that illustrate the applicability of the CDM method at several length scales. Mesoscale analyses under different stress states were performed to give insight into the void nucleation, growth, and coalescence issues that arise when developing internal state porosity evolution functions within a macroscale framework. Numerical calculations were performed to compare to 6061-T6 aluminum notch tension tests with different notched radii. Numerically calculated FLDs of 6061-T6 were validated experimentally. Finally, macroscale analyses are compared to test in which high-speed steel rods penetrated aluminum disks.

Mesoscale Analysis

Initially Isotropic Material

The following analyses are at the mesoscale where an idealized single second-phase elastic material with a failure criterion is embedded in a pure ductile matrix material. Included in the quarter-plane analysis are two holes within the matrix material representing idealized voids. Continuum principles are used and no intrinsic length scale parameter is employed. Our goal in these idealized mesoscale studies is to give insight into the interaction of the nucleation, growth, and coalescence of voids to help motivate macroscale functions. Various researchers have performed mesomechanical calculations on a representative volume element (RVE) to understand various features of the damage. To date, many of these mesoscale calculations did not directly incorporate multiple voids within an RVE with potential nucleation from a second-phase material. Our analysis represents a material such as A356-T6 cast aluminum in which the second-phase material content (mainly silicon) is 7% by volume. The silicon, which is stiffer and harder than the aluminum matrix, if a void nucleation site. The discontinuity gives rise to local stress concentrations leading to decoherance with the aluminum or fracture. The failure mechanism can also be influenced by porosity that develops from hydrogen shrinkage during the casting process. For A356 cast aluminum, this porosity level can reach a maximum of 1% void volume fraction. The schematic in Fig. 1 was used as an idealized case to represent the volume fraction of silicon and initial porosity in a mesomechanical context to understand the nucleation and growth of voids. In Fig. 1, L is the length of the side of the RVE with a value of unity so the geometry can be characterized in a normalized unitless state. R_s is the radius of the silicon particle with a value of 0.1781 to make 7% of the area fraction, l is the distance between the two holes with a value of 0.07978, and D_h is the diameter of each hole with a value of 0.07978. For future studies, these parameters will be varied to determine their interactions and effects on macroscale RVE quantities. Several calculations were performed to understand the response under different stress states and initial material conditions. For the first set of calculations, the material's initial state was assumed to be isotropic. In wrought and cast conditions, some materials can exhibit different length scales of porosity from hydrogen shrinking. As a consequence, an initial small-scale "microporosity" level was introduced ($\phi_o = 10^{-5}$) with an even distribution in the aluminum matrix.

In ductile metals, a smooth and continuously varying deformation pattern can give rise to a highly localized deformation pattern that forms into a so-called shear band. Localization into shear bands can be associated with three phenomena. The first is from local thermal softening. A thermomechanical instability arises locally in a narrow band of material that causes higher strain rates than in the adjacent region. This leads to softening in the narrow band. Also affecting localization is geometric softening that relates to the other two phenomena. Geometric softening is associated with evolving texture and dislocation substructures. Within a narrow band, one

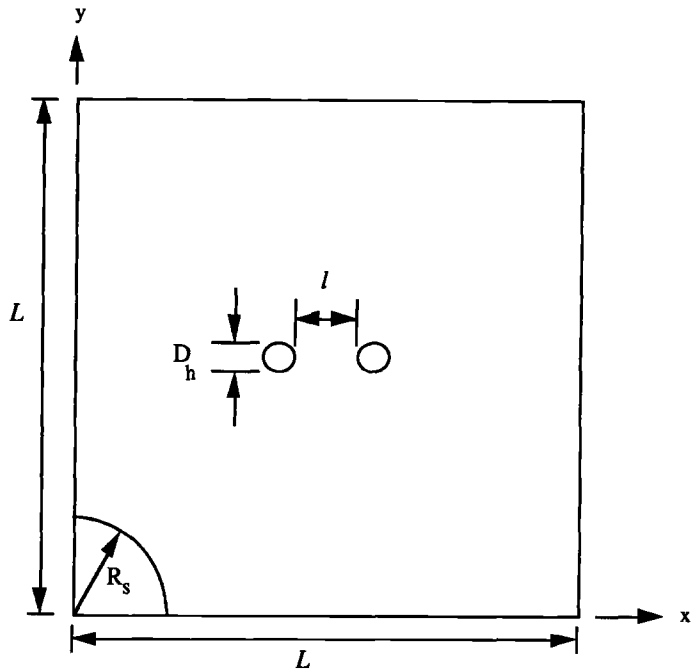

FIG. 1—*Schematic of RVE with two holes and a silicon particle in a plate analysis with symmetric boundaries existing along the* x *and* y *axes.*

slip system would be more favorably oriented for crystallographic texture than those of the adjacent material, causing localization. The final form of localization comes from dislocation substructures that form in localized regions from evolving microbands at finite strains.

Most of the constitutive developments related to these kinds of calculations have been associated with rate-independent inelastic behavior. For rate-dependent inelasticity, the equilibrium equations never lose ellipticity, so localization develops from global instabilities in the solution rather than by bifurcations. Clearly, the rate- and temperature-dependent model presented in this paper experiences the global instabilities that induce the localization.

The volume-averaged peak stress from the elements near the traction boundary was used to approximate the localization strain. These boundary elements all gave uniform stress-strain curves, but elements near the localized region gave an increase in hardening rate. We appreciate that localization can indeed occur before this strain, but our approximation is close to first order.

When loaded in uniaxial tension and biaxial tension, similar RVE responses arose. When the RVE was loaded in the y-direction, the normal component of strain in the y-direction incurred intense strain gradients at the boundary edges of the RVE at $x = 0$ and $y = 0.5$. When the RVE was loaded in the y-direction, the intense strain gradients were also observed at $x = 0.5$ and $y = 0$ for the normal component of strain in the x-direction. Figure 2 shows the effective plastic strain, porosity level, hydrostatic tensile pressure, and von Mises stress contours at localization within the RVE. Localization occurred in these banded regions as demonstrated in Fig. 2*b* that shows the porosity levels under biaxial loading conditions. It is interesting that localization did not occur near the two larger holes. Although the stresses were higher between the holes and at the particle-matrix interface as shown by the von Mises stress contour in Fig.

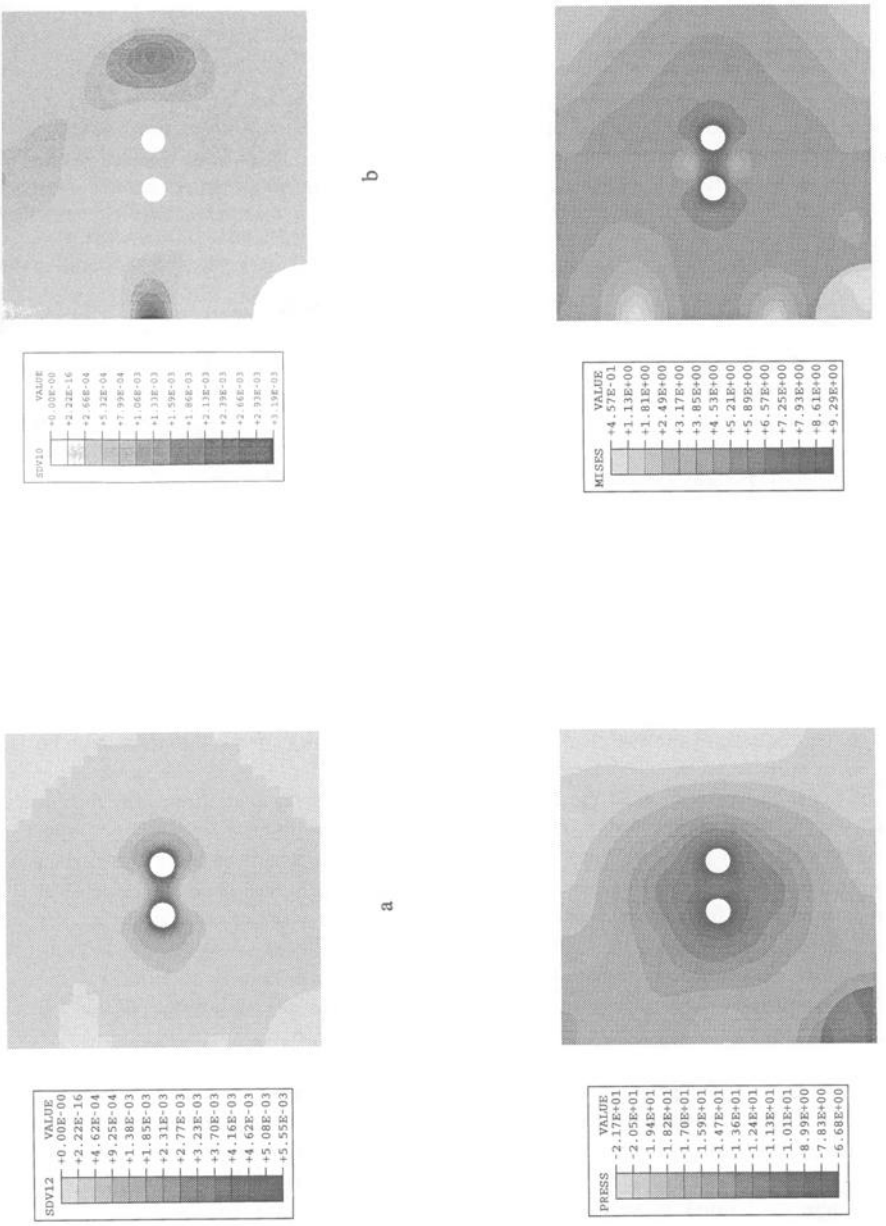

FIG. 2—*For the case with an initial porosity level distributed evenly within the aluminum matrix under biaxial loading conditions at localization:* (a) *effective plastic strain (SDV12),* (b) *porosity level (SDV10),* (c) *hydrostatic pressure, and* (d) *von Mises stress.*

$2d$, the localization did not occur in those regions. The porosity rate is highest in these banded regions because the tensile pressure (I_1) is very high compared to the von Mises (J_2) stress. The porosity rate is a function of the stress triaxiality as Eq 4 illustrates, where the stress triaxiality is defined as the ratio of the tensile pressure over the von Mises stress. Although the tensile pressure and von Mises stresses are highest near the larger holes, the ratio of the two is smaller compared to their ratio at the edges. Figure 2 also demonstrates that although the stress triaxiality is highest at the plate edges, the highest levels of hardening and effective plastic strain are near the two larger holes and near the particle-matrix interface.

These calculations assume a perfect interface between the silicon and aluminum interface. This assumption would allow for silicon fracture but no decohesion. Under these tensile loading conditions, the aluminum would tend to pull away from the silicon-inducing decohesion. As it turns out, the two holes were so close together that the influence on coalescence was not affected by decohesion nor fracture.

When the initial microporosity distribution was neglected with the aluminum matrix ($\phi_o = 0$), the intense band of porosity was not observed at the boundaries. The triaxiality did not develop as quickly near the edges compared to the center of the RVE. As a result, localization occurred between the two larger holes in the middle of the RVE as the holes grew and coalesced. The distance between the two larger holes was too close for void nucleation to occur from the silicon particle either fracturing or decohering from the aluminum. Figure 3 shows contours of the tensile pressure, von Mises stress, and effective plastic strain at the localization when no initial microporosity level was assumed within the aluminum matrix. When the loaded elements are volume averaged to determine the localization and coalescence strains, they are much lower than for the case when an initial porosity level was introduced ($\phi_o = 10^{-5}$). For the case of no initial microporosity ($\phi_o = 0$), the peak stress occurred at around 1.4% strain, but when $\phi_o = 10^{-5}$, the peak stress occurred at a strain of about 0.56%. When comparing the pressure in Figs. 2 and 3, one can see that the distribution is much different, yet localization occurs in both RVEs. These two softening mechanisms arise from the two different sources of porosity: those represented by the internal state variable and those from the two larger holes.

As a modification to this analysis, the direction of loading in the uniaxial calculation was changed to the x-direction in-line with the axis common to both holes. In the previous uniaxial calculation, the loading direction was perpendicular to the two holes. Figure 4 shows that the orientation of the holes in relation to the loading direction affects the hardening rate and localization within the RVE. Often, void volume fractions are treated as scalar quantities with no orientation distribution effects. These calculations expose this assumption as false when considering macroscale formulations. The hardening rate of the volume-averaged elements at the boundary was higher for the x-direction loading than for the y-direction loading for the same RVE strain levels for the case of no initial microporosity. The peak stress occurred earlier in time as did the maximum strain level for the x-direction case (strain = 1.0% for the x-direction and strain = 1.4% for the y-direction). The isotropic hardening rate was higher for this case than the perpendicular loading case.

When the equal-biaxial loading case was considered, the spatial orientations and gradients of the stresses, strains, and hardening parameters were quantitatively different than for the uniaxial case, although the qualitative trends were similar. The two holes grew together and the silicon particle really did not play a role in coalescence of the two larger holes. The orientation of the two holes changed the stress-strain response. The stress-time curve softened at 0.04 s for the elements loaded in the y-direction, where the elements loaded in the x-direction softened at 0.06 s.

When comparing the biaxial loading case with the two uniaxial cases, void coalescence occurred sooner and the two larger holes grew further inducing less material in the ligament between the two holes. Furthermore, the x-direction load at 0.075 s incurred less ligament

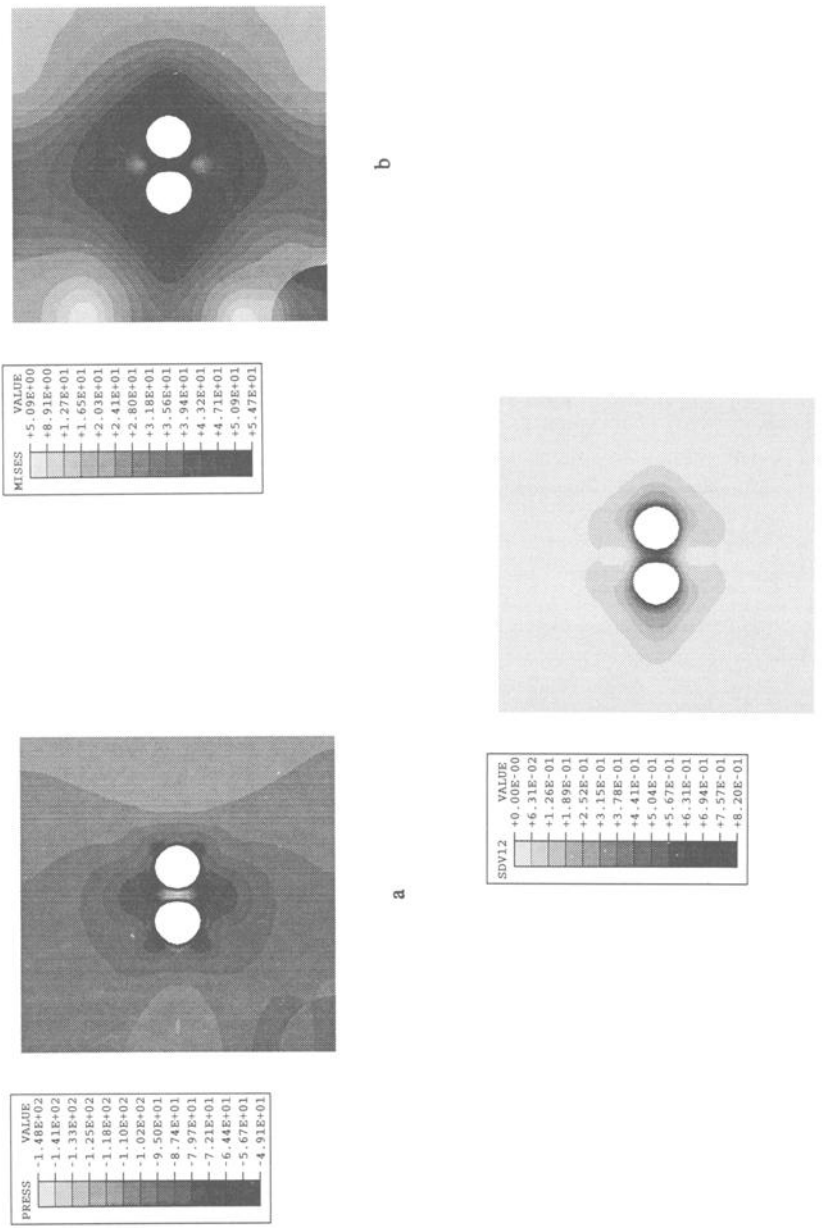

FIG. 3—*For the case with no initial porosity level within the aluminum matrix under biaxial loading conditions at localization:* (a) *hydrostatic pressure,* (b) *von Mises stress, and* (c) *effective plastic strain (SDV12).*

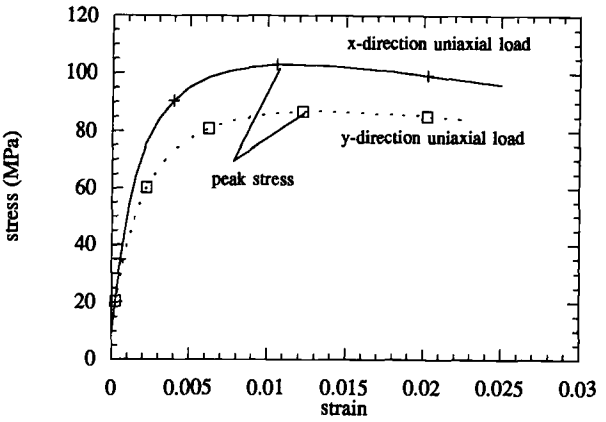

FIG. 4—*Stress-strain curve of RVE loaded in different directions under uniaxial conditions.*

material than the *y*-direction loaded case. These results show an important phenomena that has often been neglected: spatial orientation and distribution of holes under different stress states play a key role in determining volume-averaged response of the RVE.

When considering shear loads, the global stress triaxiality is zero, but a material like cast A356-T6 aluminum can fail in shear due to the second-phase particles interacting with the aluminum matrix inducing a local nonzero triaxial stress state. Figure 5 shows the volume-averaged stress-strain curve illustrating the localization experienced by the RVE under shear. This occurred whether $\phi_o = 0$ or $\phi_o = 10^{-5}$. The material simulated a fracture under this shearing mode causing localization of the RVE near the silicon-aluminum interface.

Initially Anisotropic Material

Mesoscale calculations were performed using the RVE method described earlier with different anisotropic initial states to give understanding about the anisotropic influence on localization and failure. Although cast A356 is typically isotropic in nature, some post-casting processes, such as forging, have been performed to eliminate microporosity but introduce anisotropy into the material. Furthermore, wrought materials are often extruded or rolled inducing

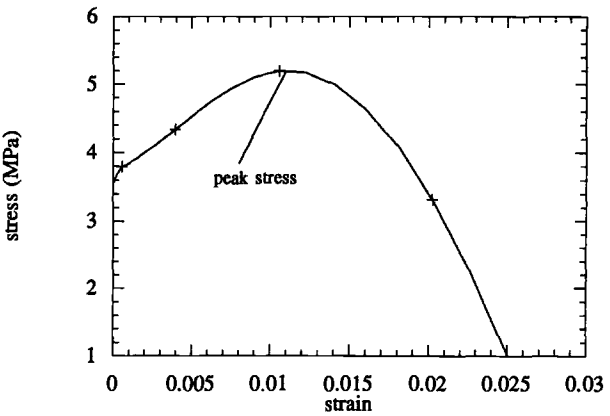

FIG. 5—*Stress-strain curve of RVE loaded under shear loads.*

anisotropy that is often ignored in a structural analysis calculation. In these calculations, the aluminum matrix is assumed to have no initial porosity.

For uniaxial loads in the y-direction, two different cases exist where the rolling direction can be parallel to the loading axis and perpendicular to the loading axis. For the former case, at a 50% prestrain, the component values for the kinematic and isotropic hardening variables were $\alpha_{xx} = -23.2$ MPa (-3360 psi), $\alpha_{yy} = -23.2$ MPa (3360 psi), and $R = 41.0$ MPa (5950 psi). These values were determined from Eqs 3 and 4, in which the components for the kinematic and isotropic hardening can be approximated when assuming that static recovery is negligible by

$$\alpha_{xx} = \sqrt{h/r_d}\tanh[\sqrt{hr_d}\varepsilon_{xx}],\ \alpha_{yy} = \sqrt{h/r_d}\tanh[\sqrt{hr_d}\varepsilon_{yy}] \tag{5}$$

and

$$R = \sqrt{H/R_d}\tanh[\sqrt{HR_d}\varepsilon] \tag{6}$$

The 50% strain values were inserted into the initial state of the material for the mesoscale calculations to simulate a prestrain. For the mesoscale calculation, the peak stress occurred at

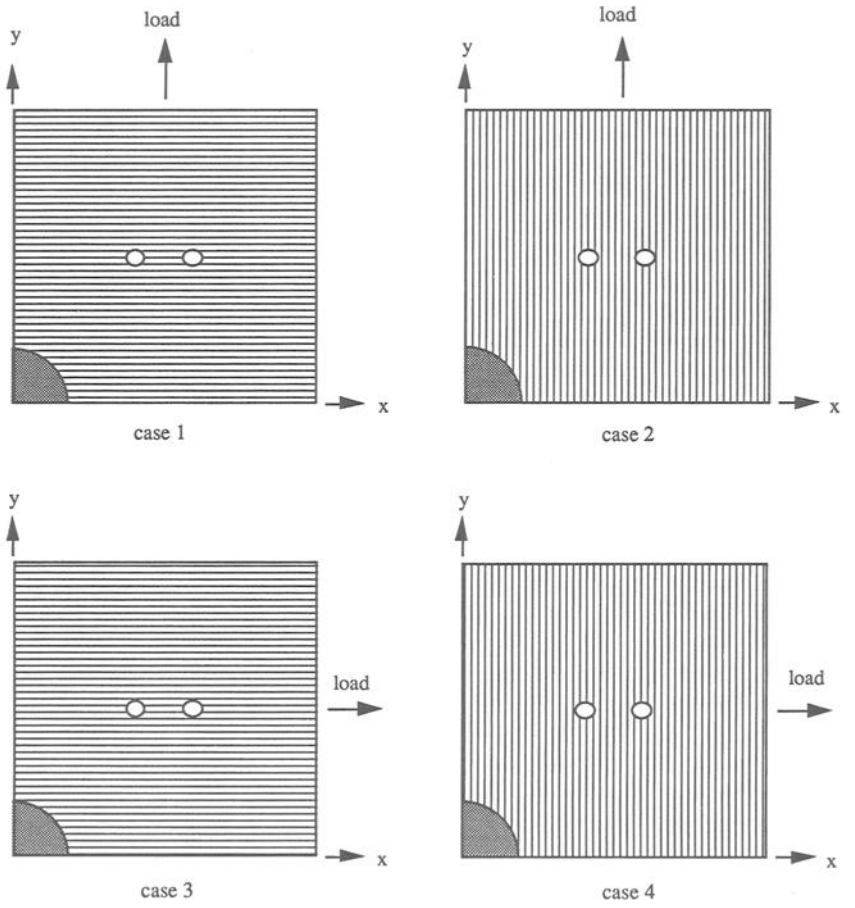

FIG. 6—*Four configurations showing different plane strain (two-dimensional) initial anisotropy cases.*

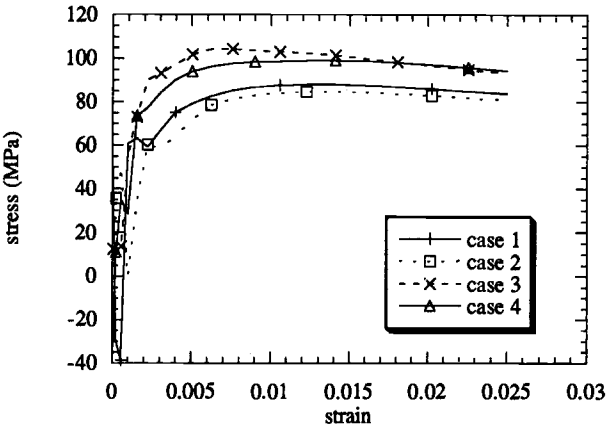

FIG. 7—*Stress-strain curves of loaded elements for the four different initial anisotropy cases.*

around 1.4% strain, which is the same as when no anisotropy was assumed. For the latter case, at a 50% prestrain with α_{xx} = 23.2 MPa (3360 psi), α_{yy} = −23.2 MPa (−3360 psi), and R = 41.0 MPa, (5950 psi), the peak stress occurred at 1.2% strain. This difference shows that some sensitivity exists in the constitutive model as related to orientation effects on localization.

For uniaxial loads in the x-direction, α_{xx} = 23.2 MPa (3360 psi), α_{yy} = −23.2 MPa (−3360 psi), and R = 41.0 MPa (5950 psi) represent 50% strain under plane strain rolling. For this case, the peak stress occurred at around 0.6% strain. Recall that when an isotropic initial state was assumed, the drop in localization strain level when loading from the y-direction to the x-direction was 1.4 to 1.0%. However, with this type of plastic anisotropy, the reduction decreases from 1.4 to 0.6%. For the anisotropic case with α_{xx} = −23.2 MPa (−3360 psi), α_{yy} = 23.2 MPa (3360), and R = 41.0 MPa (5950 psi), the strain at localization was at 1.4% when loaded in the x-direction. These four different geometries and loading conditions are shown in the schematic in Fig. 6. Case 3 was the only case were initial anisotropy was influential. This result indicates the importance of knowing the initial state of the material before trying to predict results via numerical calculations. Although no significant difference was exhibited in the localization strain for these four cases, the stress-strain curves were somewhat different as demonstrated by Fig. 7. Cases 1 and 4 yield the same localization strain (1.4%) and they exhibit different stress levels because of the initial conditions. Because Cases 2 and 3 have localization strains (1.2 and 0.7%, respectively) less than Cases 1 and 4, the initial anisotropy in the hard-

TABLE 1—*Effects of anisotropy on localization.*

Case	Load Axis	Anisotropy Axis	Localization Strain
1	y	x	1.4%
2	y	y	1.25%
3	x	x	0.75%
4	x	y	1.4%
No prestrain	y	...	1.4%
No prestrain	x	...	1.0%

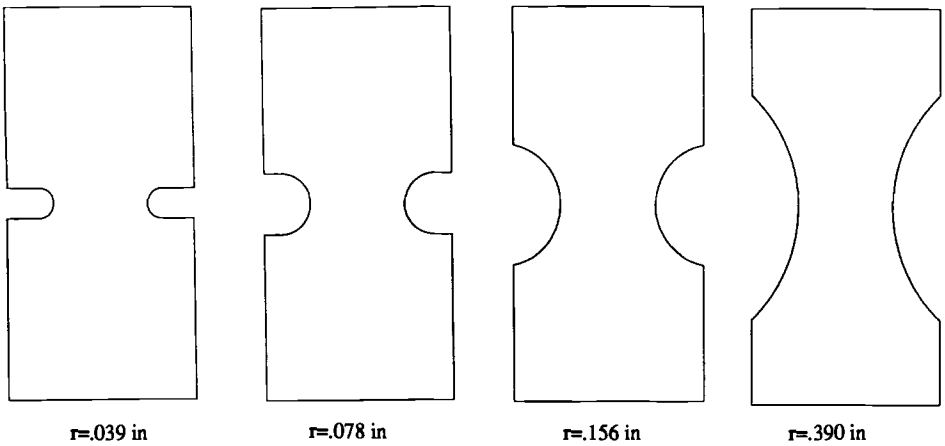

FIG. 8—*Schematic of four notch radii tested and used to correlate with damage model: 0.099 cm (0.039 in.), 0.198 cm (0.078 in.), 0.396 cm (0.0156 in.) and 0.99 cm (0.390 in.).*

ening parameters seems to play a more dominant role than the orientation of the holes (distribution effect). Table 1 summarizes the results.

Notch Tension Tests

Initially Isotropic Material

The results in this section build upon the work of Bammann et al. [*40*]. The damage parameter for the void growth rules in Eq 4 are determined from axisymmetric notched tensile specimens (Fig. 8). The notch specimens are useful because the radius of curvature of the notch strongly influences the evolution of damage, due to the significant tensile pressure that develops in the specimen as seen in Fig. 9. The damage parameter for void growth is determined from one of the notched tests, and the remaining tests are then used to verify the model. The progressive failure of a notched specimen grows from the center outward. At the beginning of the deformation, the stress triaxiality is highest at the edge of the notch but not enough to induce failure. As deformation proceeds, the peak stress triaxiality moves toward the center of the specimen where the tensile pressure is highest. The element on the axial line of symmetry failed first.

With a 0.635-cm (0.25-in.) diameter, the predicted effective plastic strain at failure ranged from 4.6%, for a notch radius of 0.0998 cm (0.0393 in.), to 32%, for a notch radius of 0.988 cm (0.389 in.). Table 2, taken from Bammann et al. [*40*], compares the predicted strain to failure with the test data. This "global" strain is the elongation over a 2.54 cm (1-in.) gage length at first observed material failure. The calculation values were volume-averaged over this distance. The model accurately predicts the strain to failure over the entire range of radii tested.

Calculations were also performed to analyze the initial material porosity levels. Figure 10 shows that as the initial porosity levels increase, the effective strain levels at failure increase linearly up to a certain porosity level (1.0%). The initial porosity below 0.1% affects the failure strain in a highly nonlinear fashion. Furthermore, at higher stress triaxialities (smaller notch radii), the initial porosity levels above 0.1% do not affect the failure strain significantly. At lower stress triaxialities (higher notch radii), the failure strains are much higher than the higher triaxiality cases. This sensitivity of the model to initial porosity levels needs further validation with experimental results but these results seem to fit our intuition.

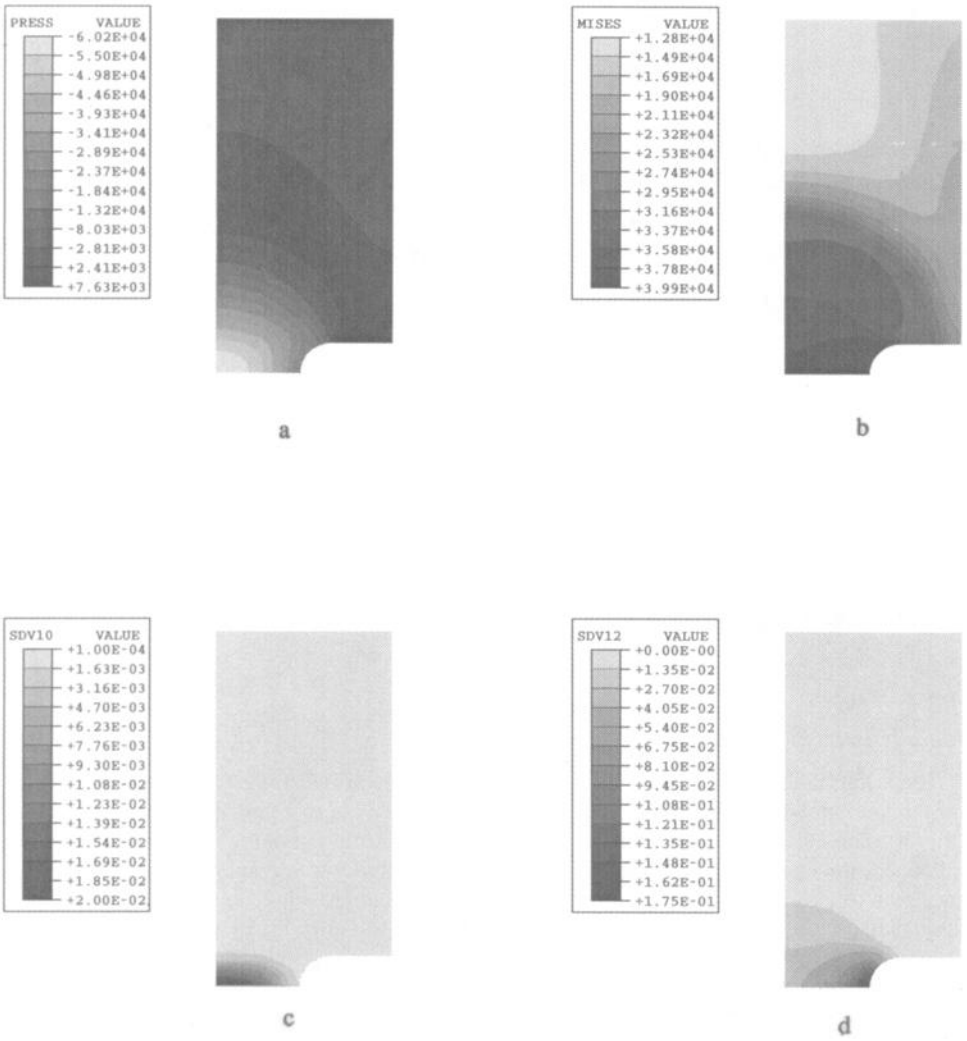

FIG. 9—*Contours of tensile pressure illustrating the highest value at the center of the specimen inducing void growth:* (a) *hydrostatic pressure,* (b) *von Mises stress,* (c) *porosity (SDV10), and* (d) *effective plastic strain (SDV12).*

Initially Anisotropic Material

Notch specimens are produced from stock that has experienced a variety of processing methods depending on the material. Notch aluminum specimens typically come from hot extruded billets and so anisotropies may exist. Notch steel tensile specimens typically come from hot-rolled plates and may incur different anisotropies. Although in both cases isotropy may occur at the center of the specimen, anisotropy may develop towards the edges and could play a role in determining the mechanical responses.

In the previous notch tensile calculations, the material was assumed to be initially isotropic.

TABLE 2—*Strain to failure: test versus prediction* [40].

Radius, cm (in.)	Number of Tests	Test Average	Calculation
0.988 (0.389)	3	0.043	0.044
0.399 (0.157)	5	0.021	0.023
0.200 (0.0787)	5	0.014	0.015
0.0998 (0.0393)	5	0.011	0.013

In order to gain insight into the effect of initial anisotropy on the notch tensile tests, calculations were performed that considered extrusion to understand the failure strain effects from initial anisotropy. Mackenzie et al. [*41*] showed from experimental data for several steels that under rolling conditions notch tension tests are sensitive to the direction of the loading. The kinematic hardening model used in this paper can capture the Bauschinger effect to first order but, does not include effects of orientation from texture. The saturation of the kinematic hardening was assumed to occur at about 6% strain. Hence, for processes, such as rolling, extrusion, and channel die compression, when the material experiences 6% strain or more, the maximum level for deformation-induced anistropy was reached for this material model. There is no mechanism currently to address evolving texture or dislocation substructure evolution for those levels above 6% strain.

A 50% prestrain was simulated by introducing α_{xx} = 23.2 MPa (3360 psi), α_{yy} = −23.2 MPa (−3360 psi), and R = 41.0 MPa (5950 psi) as an initial material state. The effective plastic strain at failure was 19.9% compared to the initially isotropic case of 18.1% for a notch radius of 0.099 cm (0.039 in). Also for this anisotropic case, the tensile pressure increased to 489 MPa (70.9 ksi) from 428 MPa (62.0 ksi) at failure. For both cases, the failure occurred at

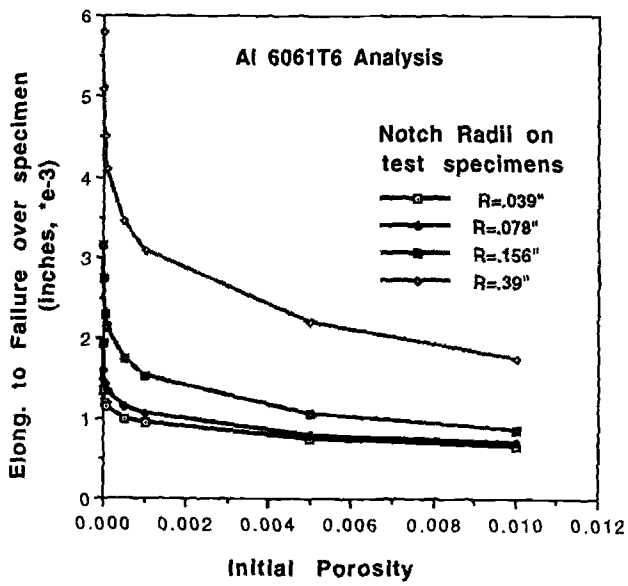

FIG. 10—*Failure strain versus initial porosity levels for different notch radii for 6061-T6 aluminum.*

the center of the specimen, but maximum values for the von Mises stress, the highest values for the components of $\tilde{\alpha}$, and maximum value for R was near the notch edge. When the direction of the extrusion axis and transverse axis were reversed in the notch specimen, the effective plastic strain to failure was 16.1% with the tensile pressure at 490 MPa (71.1 ksi). This trend was also observed by MacKenzie et al. [*41*]. Clearly, the directionality of the prestrain plays a role of damage evolution and void growth in ductile metals. These deformation-induced anisotropic features are many times not included in equations of state or isotropic material models. Furthermore, these investigations, as do many others, clearly point out that picking an effective plastic strain to failure is not the appropriate failure metric.

Forming Limit Diagrams (FLDs)

Initially Isotropic Material

The forming limits of sheet metal were first described by Keeler [*42*] in strain space by a forming limit diagram (FLD). Figure 11 shows a typical FLD that describes the localization (referred to as limit) and failure strains in two-dimensional strain space. Three-dimensional finite element analyses were performed to simulate the different stress states for biaxial tension, unbalanced biaxial tension (sometimes called stretch forming), plane strain, uniaxial, and shear (deep drawing). The details of the finite element analyses are explained in Horstemeyer et al. [*38*].

The material instability that was used in these calculations included two types. The first type was a geometric instability that is often used in numerical calculations that can occur due to machining and tolerance effects. A second type is that of porosity mismatch in adjacent material. Horstemeyer et al. [*38*] showed that these types of instabilities produce similar results.

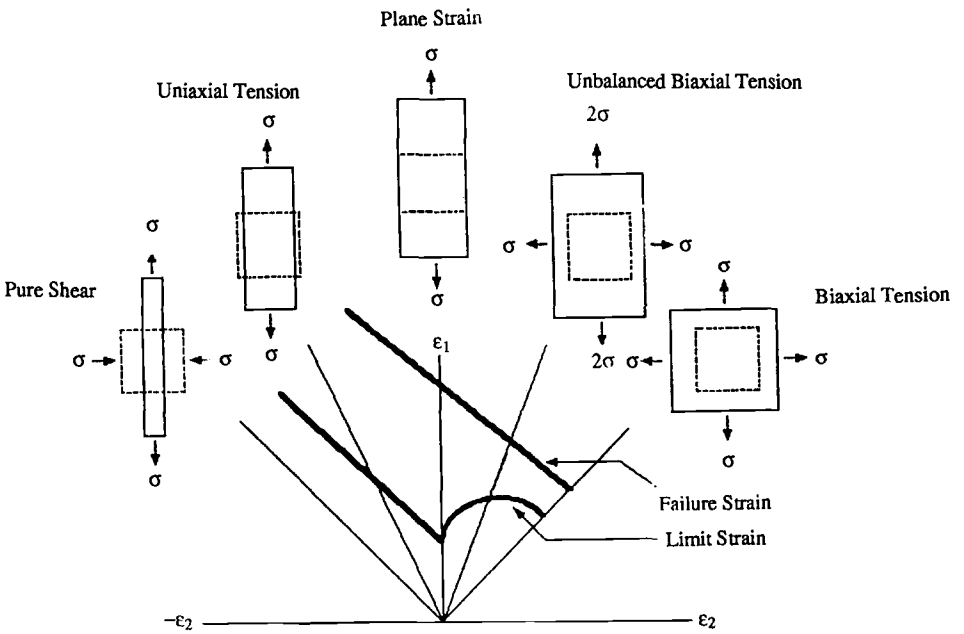

FIG. 11—*Schematic of forming limit diagram with limit (localization) and failure strain curves.*

TABLE 3—*Biaxial stretching results with different initial porosity levels.*

Case	Porosity Mismatch	% Localization Strain	% Failure Strain
1	0.1 times	5.2	10.6
2	0.5 times	5.2	10.6
3	1.0 times	4.8	9.3
4	10 times	3.4	7.0
5	100 times	2.6	3.9
6	1000 times	0.001	1.2

In this study, we chose different levels of porosity mismatches to show the different responses under biaxial stretching loading conditions. Table 3 summarizes the numerical results showing that as the porosity mismatch increased, the localization and failure strains decreased. The porosity mismatch is defined by the volume fraction of voids in one finite element compared to an adjacent element. The element near the center of the mesh was the one that was initialized differently while the rest of the mesh included a uniform distribution. Because of the equal-biaxial loading condition, the localization and failure strains in the x-direction are the same as that in the y-direction; hence, Table 3 only shows the localization and failure strain level that represents the x-direction and y-direction components. This trend corresponds directly to the different initial levels that were chosen in the notched tension test calculations.

Initially Anisotropic-Forming Limit Diagrams

The early investigation of Matsuoka and Sudo [*43*] revealed the various history effects for two-stage, nonproportional deformation. Combinations of simple deformation modes gave rise to a constant strain ratio ($\Delta\varepsilon_1/\Delta\varepsilon_2$). They discovered that higher limit strains result if the strain increment ratio is greater in the second stage loading than in the first stage. Conversely, lower limit strains result if the strain increment ratio is lower in the second stage loading than in the first stage. In other words, premature instabilities are observed for strain paths consisting of prior biaxial prestrain followed by plane strain loading. And prior plane strain preloading followed by biaxial loading increases the limit strains. Figure 12 demonstrates that our calculations followed these history effects. The evolutionary internal state variables picked up the directional hardening effects thus accurately describing the load history changes to produce the proper trends of the FLD.

Penetration Analysis

Initially Isotropic Material

A series of experiments was performed in which a gas gun shot a hardened steel rod into 6061-T6 aluminum disks at a range of velocities [*40*]. The disks were suspended in a manner so as to simulate a free boundary condition at the edges. In the experiments, impact velocities were measured with post-mortum inspection of each disk. Table 4 gives the pertinent geometric data for these tests, and Fig. 13 illustrates the finite element model and samples of iterative numerical analyses that were used to compare against the experimental results for two different velocity impact levels, with baseline material constants.

The failure velocity was defined as that which caused the first crack on the backside of the target disk (Fig. 13*b*, *c*, and *d*), but the perforation velocity was that needed to develop a crack

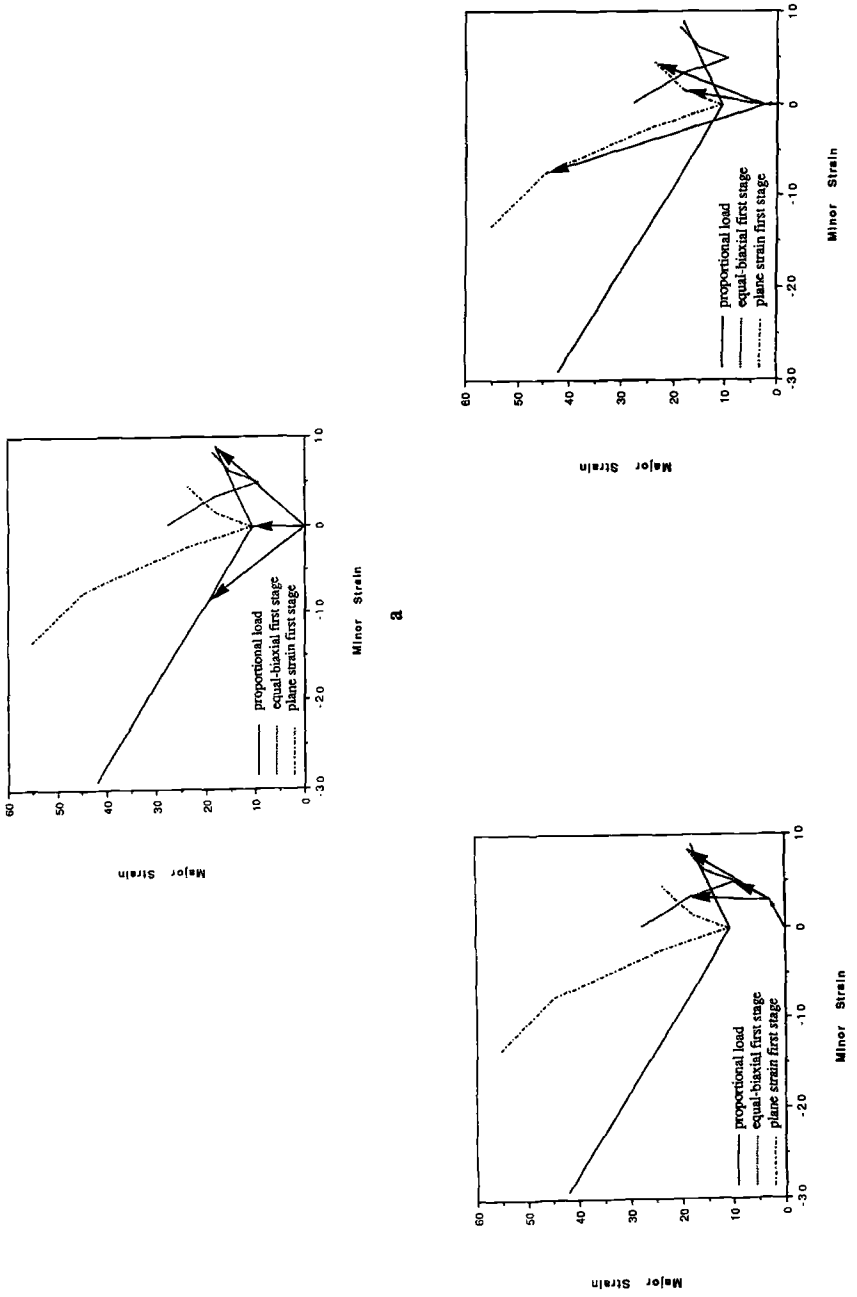

FIG. 12—*Comparison of single-stage, proportional loading case and two different two-stage, nonproportional loading cases:* (a) *the proportional case,* (b) *first-stage case started with equal-biaxial loads and followed by plane strain loads, and* (c) *first stage started with plane strain loads and followed by equal-biaxial loads. Strain is denoted in percent.*

TABLE 4—*Specimen dimensions.*

Feature	Dimension, cm (in.)
Disk radius	5.715 (2.25)
Disk thickness	0.3175 (0.125)
Impact rod diameter	1.27 (0.500)
Impact rod length	12.827 (5.05)

totally through the thickness of the disk (such as in Fig. 13*e*, *f*, and *g*), typically punching out or perforating a hole in the center of the disk. In addition to the finite element mesh, Fig. 13 illustrates the initiation of failure and full perforation. Numerical simulations compared well with test results, predicting the failure initiation velocity and perforation velocity to within 10% of the experimental results.

To investigate the porosity effect, the initial porosity level of 10^{-4} was increased to 5.0×10^{-4}. Increasing the initial material porosity by a factor of five for an initial penetrator velocity 80.3 m/s (3160 in./s), for which the baseline material produced only initiation of failure, resulted in weakening the material severely enough so that complete perforation was produced. The magnitude of the deformation and extent of failure in this case illustrates the highly nonlinear behavior of damage evolution, and thus initial porosity levels play a significant role in this type of boundary value problem.

To investigate the effect of variable porosity over the structure, a second analysis with an initial random distribution ($\pm 10\%$) of porosity was also conducted, but showed no significant difference from the baseline case. This implies that the void volume fraction, not the void distribution, is the driving factor for damage in this boundary value problem.

Initially Anisotropic Material

The 50% prestrain values for the kinematic and isotropic hardening variables, that is, $\alpha_{xx} = -23.2$ MPa (-3360 psi), $\alpha_{yy} = 23.2$ MPa (3360 psi), and $R = 41.0$ MPa (5950 psi), were placed as initial values in the material model for the penetration problem. In the case of the lower impact velocity, this degradation in material caused greater tearing—approximately through 50% of the disk thickness compared to only 10% in the baseline case, $v = 80.3$ m/s (3160 in./s). Interestingly, the greater propensity toward compression in the top portion of the disk induced a resistance such that tearing was difficult in this region. This was also shown in the higher initial impact velocity as well as can be seen in Fig. 14. The baseline case for the higher impact velocity, $v = 94.0$ m/s (3700 in./s), had produced a tear approximately through 80% of the disk. The anisotropic case at this impact velocity produced damage that was very similar.

The direction of the extrusion axis and transverse axis were reversed by changing the initial hardening constants in the x- and y-directions. Both impact velocities produced smaller damage resulting from the higher strength introduced in the in-plane direction of the disk retarding the tensile opening of the crack.

Consequently, these perturbations on the initial state of the material support the notion that anisotropy and directionality of the prestrain affect damage evolution. In comparing the magnitude of the effect, however, we note that the results are not necessarily intuitive because of the nonlinearities that arise.

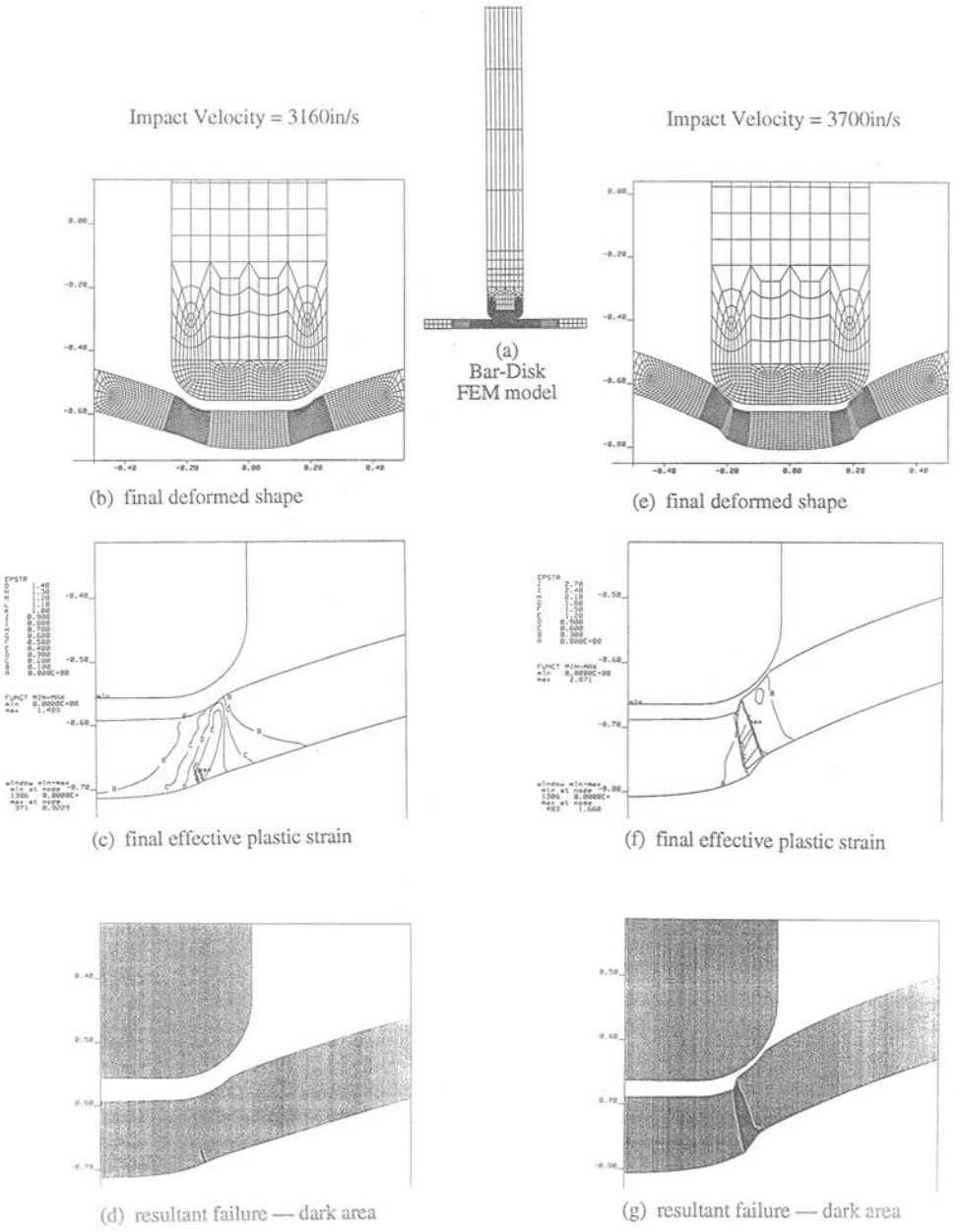

FIG. 13—*Comparison of numerical results for steel bar striking an aluminum disk at different velocities. The case on the left, the bar strikes at 80.3 m/s (3160 in./s), just initiating failure on the back side of the disk before it rebounds (the dark area in* d*). On the right, the bar strikes at 94 m/s (3700 in./s) resulting in complete perforation of the disk. The dark area in* g *represents void space between the disk and perforated disk center.*

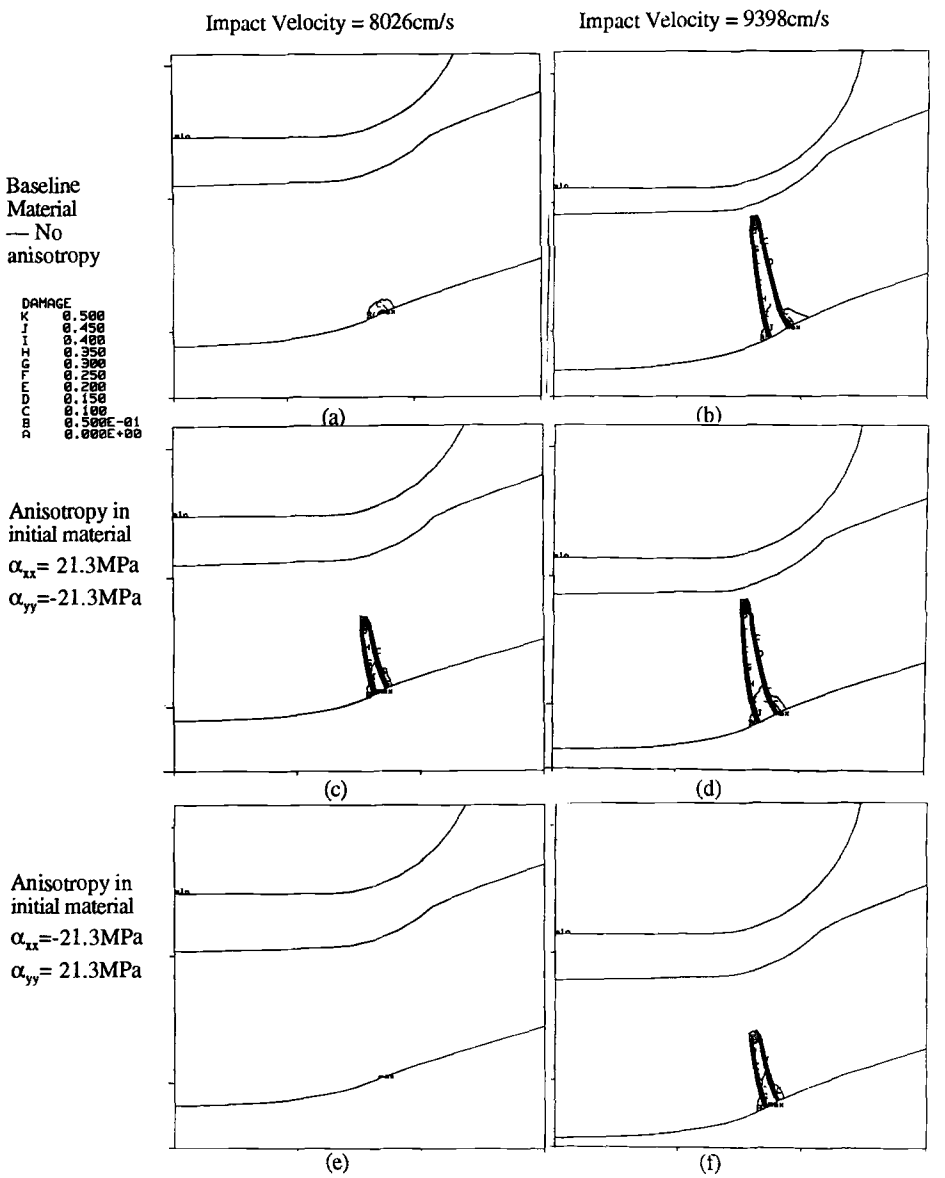

FIG. 14—*Comparison of analytic results for steel bar striking an aluminum disk with different initial material properties.*

Summary

In this numerical study, a number of initial material properties related to porosity and kinematic and isotropic hardening were varied to reflect the stress state and deformation history effects in different boundary value problems. Mesoscale calculations showed that initial "microporosity" changes the localization behavior dramatically from the case where no micro-

porosity is assumed with two larger voids. Anisotropy reflected in hardening equations shows small differences with the isotropic case. Macroscale notch tensile calculations showed some sensitivity to the initial porosity level and also to initial anisotropy of the hardening parameters. Forming limits also showed a sensitivity to prestrains and initial porosity differences. Also, high-speed penetration of aluminum disks showed sensitivities toward initial material properties. Further work needs to be performed with regard to orientation effects from texture within the context of continuum damage mechanics as well as including nucleation into the macroscale damage evolution.

Acknowledgments

This research was based upon the work supported by Sandia National Laboratories from the U.S. Department of Energy under Contract Number DE-AC04-76DP00789.

References

[1] Kachanov, L. M., "Time of the Rupture Process under Creep Conditions," *Ievestiva Akademii Navk SSSR Odtelemie Tekhniheskikh Nauk*, No. 8, 1958, pp. 26–31.

[2] Rabotnôv, I. N., "On the Equations of State for Creep," *Progress in Applied Mechanics—The Prager Anniversary Volume*, 1963, pp. 307–315.

[3] Lemaitre, J., "Evaluation of Dissipation and Damage in Metals," *Proceedings*, ICM Kyoto, Japan. Vol. 1, 1971.

[4] Chaboche, J. L., "Une loi differentielle d'endommagement de fatigue avec cumulation non lineaire," Revue Francaise de Mecanique No. 50–51, 1974.

[5] Hult, J., "Creep in Continua and Structures," *Topics in Applied Continuum Mechanics*, Springer, Vienna, 1974.

[6] Leckie, F. and Hayhurst, D., "Creep Rupture of Structures," *Proceedings*, Royal Society, London, Vol. A240, 1974, p. 323.

[7] Lemaitre, J., "Zniszcenie w zakresie lepkoplastycynym," *Mechanika Teoretyczna, i Stosowana*, Vol. 1/2, No. 20, 1982, pp. 29–48.

[8] Lemaitre, J. and Chaboche, J. L., "A Nonlinear Model of Creep-Fatigue Damage Cumulation and Interaction," *Proceedings*, IUTAM Symposium of Mechanics of Visoelastic Media and Bodies, Springer, Gothenburg, 1974.

[9] Lemaitre, J. and Plumtree, A., "Application of Damage Concept to Predict Creep-Fatigue Failures," *Journal of Engineering Materials and Technical Transactions*, ASME, Vol. 101, 1979, pp. 284–292.

[10] Lemaitre, J. and Dufailly, J., "Modelisation et identification de l'dendommagement plastique des metaux," *Proceedings*, 3eme Congres Francais de Mecanique, Grenoble, 1977.

[11] Dragon, A., "Plasticity and Ductile Fracture Damage: Study of Void Growth in Metals," *Engineering Fracture Mechanics*, Vol. 21, No. 4, 1985, pp. 875–885.

[12] Dragon, A. and Chihab, A., "On Finite Damage: Ductile Fracture-Damage Evolution," *Mechanics of Materials*, Vol. 4, 1985, pp. 95–106.

[13] Bammann, D. J. and Aifantis, E. C., "A Damage Model for Ductile Metals," *Nuclear Engineering and Design*, Vol. 116, 1989, pp. 355–362.

[14] Krajcinovic, D. and Fonseka, G. U., "The Continuous Damage Theory of Brittle Materials, Parts 1 and 2," *Journal of Applied Mechanics*, Vol. 48, 1981, pp. 809–824.

[15] Krajcinovic, D., "Constitutive Equations for Damaging Materials," *Journal of Applied Mechanics*, Vol. 50, 1983, pp. 355–360.

[16] Loland, K. E., "Continuous Damage Model for Load-Response Estimation of Concrete," *Cement and Concrete Research*, Vol. 10, 1980, pp. 395–402.

[17] Francois, D., "Fracture and Damage Mechanics of Concrete," *Application of Fracture Mechanics to Cementitious Composites*, NATO Advanced Research Workshop, 4–7 Sept., Northwestern University, Evanston, IL, 1984.

[18] Resende, L., "Constitutive Modeling and Finite Element Analysis in Geomechanics," PhD thesis, University of Cape Town, South Africa, 1984.

[19] Resende, L. and Martin, J. B., "A Progressive Damage Continuum Model for Granular Materials," *Computational Methods with Applicational Mechanical Engineering*, Vol. 42, 1984, pp. 1–18.

[20] Goods, S. H. and Brown, L. M., "The Nucleation of Cavities of Plastic Deformation," *Acta Metallurgica*, Vol. 27, 1979, pp. 1–15.
[21] Garrison, W. M. and Moody, N. R., "Ductile Fracture," *Journal of Physics and Chemistry of Solids*, Vol. 48, No. 11, 1987, pp. 1035–1074.
[22] Cocks, A. C. F. and Ashby, M. G., "Intergranular Fracture During Power-Law Creep Under Multiaxial Stresses," *Metal Science*, Aug.–Sept. 1980, pp. 395–402.
[23] Onsager, L., "Reciprocal Relations in Irreversible Processes," *Physics Review*, Vol. 37, 1931, p. 405; Vol. 38, p. 2265.
[24] Eckart, C., "Thermodynamics of Irreversible Processes, I. The Simple Fluid," *Physics Review*, Vol. 58, 1940, p. 267.
[25] Eckart, C., "Theory of Elasticity and Anelasticity," *Physical Review*, Vol. 73, 1948, p. 373.
[26] Coleman, B. D. and Gurtin, M. E., "Thermodynamics with Internal State Variables," *Journal of Chemistry and Physics*, Vol. 47, 1967, p. 597.
[27] Rice, J. R., "Inelastic Constitutive Relations for Solids: An Internal-Variable Theory and Its Application to Metal Plasticity," *Journal of the Mechanics and Physics of Solids*, Vol. 9, 1971, pp. 433–455.
[28] Davidson, L., Stevens, A. L., and Kipp, M. E., "Theory of Spall Damage Accumulation in Ductile Metals," *Journal of the Mechanics and Physics of Solids*, Vol. 25, 1977, pp. 11–28.
[29] Fremond, M. and Nedjar, B., "Damage, Gradient of Damage, and Principle of Virtual Power," *International Journal of Solids Structures*, Vol. 33, No. 8, 1996, pp. 1083–1103.
[30] Miller, A., "An Inelastic Constitutive Model for Monotonic, Cyclic, and Creep Deformation: Part 1–Equations Development and Analytical Procedures," *Journal of Engineering and Materials Technology*, Vol. 98, 1976.
[31] Chaboche, J. L. and Caullitaud, G., "On the Calculation of Structures in Cyclic Plasticity or Viscoplasticity," Vol. 23, No. 1, 1986, pp. 23–31.
[32] Bammann, D. J., "Modelling the Large Strain-High Temperature Response of Metals," *Modelling and Control of Casting and Welding Processes IV*, A. F. Giamei and G. J. Abbaschian, Eds., TMS Publications, Warrendale, PA 1988.
[33] Bammann, D. J., "Modelling Temperature and Strain Rate Dependent Large Deformations of Metals," *Applied Mechanics Review*, Vol. 1, 1990, pp. 312–318.
[34] Freed, A. D. and Walker, K. P., "Visoplasticity with Creep and Plasticity Bounds," *International Journal of Plastics*, Vol. 9, No. 2, 1993.
[35] Bammann, D. J., Chiesa, M. L., Horstemeyer, M. F., and Weingarten, L. I., "Failure in Ductile Materials Using Finite Element Methods," *Structural Crashworthiness and Failure*, N. Jones and T. Weirzbicki, Eds., Elsevier Applied Science, London, 1993.
[36] Horstemeyer, M. F., "Damage of HY100 Steel Plates from Oblique Constrained Blast Waves," *Advances in Local Fracture/Damage Models for the Analysis of Engineering Problems*, AMD-Vol. 137, J. H. Giovanola and A. J. Rosakis, Eds., American Society of Mechanical Engineers, New York, 1992.
[37] Horstemeyer, M. F., "Structural Analysis of a Submarine Using Statistical Design of Experiments," Advances in Numerical Simulation Techniques for Penetration and Perforation of Solids, ASME-AMD-Vol. 171, E. P. Chen and V. K. Luk, Eds., American Society of Mechanical Engineering, New York, 1993, pp. 189–200.
[38] Horstemeyer, M. F., Chiesa, M. L., and Bammann, D. J. "Predicting Forming Limit Diagrams with Explicit and Implicit Codes," *Analysis of Autobody Stamping Technology*, Society of Automotive Engineers, Warrendale, PA, 1994, pp. 11–25.
[39] Cocks, A. C. F., "Inelastic Deformation of Porous Materials," *Journal of Mechanics and Physics of Solids*, Vol. 37, No. 6, 1989, pp. 693–715.
[40] Bammann, D. J., Chiesa, M. L., McDonald, A. Kawahara, W. A., Dike, J. J., and Revelli, V. D., "Prediction of Ductile Failure in Metal Structures," *Failure Criteria and Analysis in Dynamic Response*, H. E. Lindberg, Ed., ASME AMD, Vol. 107, Nov. 1990, pp. 7–12.
[41] MacKenzie, A. C., Hancock, J. W., and Brown, D. K., "On the Influence of State of Stress on Ductile Failure Initiation in High Strength Steels," *Engineering Fracture Mechanics*, Vol. 9, 1977, pp. 167–188.
[42] Keeler, S. P., "Plastic Instability and Fracture in Sheets Stretched Over Rigid Punches," ScD. thesis, Massachusetts Institute of Technology, Cambridge, 1961.
[43] Matsuoka, M. and Sudo, C., *The Sumito Search*, No. 1, 1967, p. 71.